UNIVERSITY OF CALIFORNIA SAN DIEGO

Control Over Precursor Conversion for the Synthesis of Tailored Group-VI Transition Metal Dichalcogenide Nanocrystals

A Dissertation submitted in partial satisfaction of the requirements
for the degree Doctor of Philosophy

in

Chemistry

by

Jessica Quinn Geisenhoff

Committee in charge:

Professor Alina M. Schimpf, Chair
Professor Ertugrul Cubukcu
Professor Judy E. Kim
Professor Clifford P. Kubiak
Professor Michael J. Sailor
Professor Wei Xiong

2022

The Dissertation of Jessica Quinn Geisenhoff is approved, and it is acceptable in quality and form for publication on microfilm and electronically.

University of California San Diego

2022

DEDICATION

To Mom, Dad, Kevin, and Ian.

TABLE OF CONTENTS

DISSERTATION APPROVAL PAGE iii

DEDICATION iv

TABLE OF CONTENTS v

LIST OF FIGURES viii

LIST OF TABLES xiii

LIST OF ABBREVIATIONS xv

ACKNOWLEDGEMENTS xvii

VITA xix

ABSTRACT OF THE DISSERTATION xx

Chapter 1. Introduction to transition metal dichalcogenides and the colloidal synthesis thereof 1

1.1 Introduction 1

1.2 Polymorphism of transition metal dichalcogenides 2

1.2.1 Crystal structure of thermodynamically favored 2H phase 3

1.2.2 Crystal structure of the metastable 2M phase 6

1.2.3 Access to the metastable phase through reduction 9

1.2.4 Crystal phase stability 11

1.2 Colloidal synthesis 13

1.2.1 Precursor conversion chemistry 14

1.2.2 Thermodynamics and kinetics in nanocrystal synthesis 14

1.4 Colloidal synthesis of TMD nanocrystals 19

1.4.1 Metal precursor speciation and reactivity 19

1.4.2. Size, shape, and layer control of TMD nanocrystals 21

1.4.3 Monolayer nanocrystals via colloidal synthesis 24

1.4.4 Phase control of TMD nanocrystals 26

1.5 Scope of the dissertation 29

1.6 Acknowledgements 29

1.7 References 29

Chapter 2: Using ligands to control reactivity, size and phase in the colloidal synthesis of WSe_2 nanocrystals 46

2.1 Abstract 46

2.2 Introduction 46

2.3 Results and Analysis 47

2.4 Conclusions 55

2.5 Appendix: Supporting Information 55

2.6 Acknowledgements 61

2.7 References 62

Chapter 3: Manipulation of Precursor Reactivity for Facile Synthesis of Heterostructured and Hollow Metal Selenide Nanocrystals 66

3. 1 Abstract 66

3.2 Introduction 66

3.3 Results and Discussion 68

3.4 Summary and Conclusions 79

3.5 Experimental Methods 80

3.6 Appendix: Supporting Information 85

3.7 Acknowledgments 96

3.8 References 96

Chapter 4: Controlled CO Labilization of Tungsten Carbonyl Precursors for the Low-Temperature Synthesis of Tungsten Diselenide Nanocrystals 106

4.1 Abstract 106

4.2 Introduction 106

4.3 Results and Analysis 108

4.4 Discussion 117

4.5 Summary and Conclusions 118

4.6 Supplementary Information 119

4.7 Acknowledgments 132

4.8 References 132

Chapter 5: Insights into morphology control and the phase conversion pathway of colloidally synthesized WSe_2 nanocrystals 140

5.1 Abstract 140

5.2 Introduction 140

5.3 Results and Analysis 142

5.4 Discussion 158

5.5 Summary and Conclusions 160

5.6 Supplementary Information 161

5.7 Acknowledgments 169

5.8 References 169

Chapter 6: Tightly bound trioctylphosphine ligands for monolayer transition metal dichalcogenides nanocrystals 172

6.1 Abstract 172

6.2 Introduction 172

6.3 Results and Discussion 175

6.5 Supplementary Information 191

6.6 Acknowledgments 200

6.7 References 200

LIST OF FIGURES

Figure 1. 1. Crystal structure of the 1H monolayer 4

Figure 1. 2. Bulk crystal structures of the 2H and 3R phases. 5

Figure 1. 3. Crystals structure of the 1T′ monolayer. 7

Figure 1. 4. Bulk crystal structure of the 2M phase. 8

Figure 1. 5. Computed reaction coordinate diagram illustrating the phase conversion of 1H to 1T' to 1T phase 12

Figure 1. 6. Reaction coordinate diagrams illustrating thermodynamic and kinetic control 15

Figure 1. 7. Reaction at room temperature of tungsten hexachloride with different ligands 20

Figure 1. 8. Colloidal synthesis of $MoSe_2$ nanocrystals with different lateral sizes. 23

Figure 1. 9. Colloidally synthesized MoS_2 nanocrystals with different number of layers. 24

Figure 1. 10. Colloidal synthesis of monolayer WS_2 nanocrystals. 25

Figure 1. 11. Colloidal synthesis of metastable phase of WSe_2 nanocrystals 27

Figure 2. 1. TEM images of WSe_2 nanocrystals synthesized with 2, 10, 100, and 1000 eq OA/W 48

Figure 2. 2. HRTEM images and corresponding FFTs for WSe_2 synthesized with 2 eq OA/W and 1000 eq OA/W. 51

Figure 2. 3. Raman spectra of WSe_2 nanocrystals synthesized with 2, 10, 100, and 1000 eq OA/W. 52

Figure 2. 4. Raman spectra of WSe_2 nanocrystals synthesized with 2 eq OA/W. Aliquots were taken at 5, 10 and 20 min following Ph2Se2 injection. 54

Figure S2. 1. Colloidal stability of WSe_2 nanocrystals synthesized with 2eq and 1000 eq OA/W. 56

Figure S2. 2. Powder X-ray diffraction patterns of WSe_2 nanocrystals synthesized with 2, 10, 100 and 1000 OA/W 57

Figure S2. 3. Reaction of W(CO)6 in all TOPO (0 eq OA) heated to temperatures above 260 °C. 58

Figure S2. 4. Reaction of W(CO)6 in TOPO with 2 eq OA at 330 °C 58

Figure S2. 5. X-ray photoelectron spectra of nanocrystals synthesized with 2, 10, 100 and 1000 OA/W 59

Figure S2. 6. TEM image of nanocrystals synthesized with 2 eq OA/W at early times of the reaction. 59

Figure 3. 1. Characterization of Ni_3Se_4 and Ni_3Se_4/WSe_2 core/shell heterostructures synthesized in a single step with 1000 eq OA/W. 70

Figure 3. 2. Characterization of Ni_3Se_4 nanoplatelets and Ni_3Se_4/WSe_2 heterostructures grown in a two-step synthesis with 1000 eq OA/W and with 100 eq OA/W 73

Figure 3. 3. Characterization of Ni_3Se_4/WSe_2 core/shell heterostructures and hollow WSe_2 nanocrystals formed after removal of Ni_3Se_4 cores 75

Figure 3. 4. Characterization of Co_3Se_4 cores and Co_3Se_4/WSe_2 core/shell heterostructures synthesized in a single step with 1000 eq OA/W. 77

Figure 3. 5. Characterization of $Cu_{2-x}Se$ cores and $Cu_{2-x}Se/Cu_2WSe_4$ core/shell heterostructures synthesized in a single step with 1000 eq OA/W 78

Figure S3. 1. Line-scan of STEM-EDS mapping images of Ni_3Se_4/WSe_2 heterostructures. 85

Figure S3. 2. Additional STEM-EDS mapping images of Ni_3Se_4/WSe_2 heterostructures 85

Figure S3. 3. High-resolution TEM images of Ni_3Se_4/WSe_2 heterostructures 86

Figure S3. 4. TEM image showing gradual WSe_2 shell-growth on Ni_3Se_4 nanocrystals 86

Figure S3. 5. Statistical analysis of Ni_3Se_4 core nanocrystals 87

Figure S3. 6. STEM-EDS mapping images of small particles. 87

Figure S3. 7. Statistical analysis of WSe_2 shells 88

Figure S3. 8. Ni_3Se_4/WSe_2 heterostructures synthesized in the presence of 100 eq OA/W 88

Figure S3. 9. TEM images of WSe_2 shell-growth on Ni_3Se_4 in the absence of OA 89

Figure S3. 10. Line-scan of STEM-EDS mapping images showing preferred edge-growth. 89

Figure S3. 11. TEM of 5-min aliquot for shell-growth in the presence of 100 eq OA 90

Figure S3. 12. Ni_3Se_4/WSe_2 heterostructures synthesized in the presence of 100 eq PAA/W 90

Figure S3. 13. STEM-EDS mapping images of hollow WSe_2. 91

Figure S3. 14. IR absorption showing $Et_2N_2H_4$ intercalation into hollow WSe_2. 92

Figure S3. 15. Powder X-ray diffraction patterns showing $Et_2N_2H_4$ intercalated into WSe_2 ... 92

Figure S3. 16. Electronic absorption spectrum of $[Ni(Et_2N_2H_4)_3]^{2+}$ 93

Figure S3. 17. Co_3Se_4 synthesis with analogous conditions to Ni heterostructures 93

Figure S3. 18. STEM-EDS mapping images of Co_3Se_4/WSe_2 heterostructures. 94

Figure S3. 19. STEM-EDS mapping images of $Cu_{2-x}Se/Cu_2WSe_4$ heterostructures 95

Figure S3. 20. Cu_2WSe_4/WSe_2 heterostructures 96

Figure 4. 1. Characterization of WSe_2 nanocrystal synthesis in TOPO at 150 °C 110

Figure 4. 2. Crystal structures and IR spectra of $W(CO)_5$TPPO and *cis*-$W(CO)_4(TPPO)_2$. .. 112

Figure 4. 3. Characterization of WSe_2 nanocrystal synthesis in TOPO + TOP 114

Figure 4. 4. Crystal structure and IR spectra of $W(CO)_5$TPP. 116

Figure 4S. 1. IR spectrum of $W(CO)_6$ dissolved in THF. 119

Figure 4S. 2. TEM image of WSe_2 nanocrystals synthesized in TOPO at 150 °C). 120

Figure 4S. 3. XPS of WSe_2 nanocrystals synthesized in TOPO at 150 °C 120

Figure 4S. 4. Powder X-ray diffraction pattern of *cis*-$W(CO)_4(TPPO)_2$. 122

Figure 4S. 5. Crystal structure of *fac*-$W(CO)_3(TPPO)_3$. 122

Figure 4S. 6. IR spectra of $W(CO)_6$ heated in varying amounts of TOPO. 123

Figure 4S. 7. IR spectra of $W(CO)_6$ heated in TOPO with evacuation 124

Figure 4S. 8. Powder X-ray diffraction pattern of WSe_2 nanocrystals synthesized in TPPO 124

Figure 4S. 9. Characterization of WSe_2 nanocrystal synthesis in TOPO + TPP 126

Figure 5. 1. Characterization of timed aliquots from WSe_2 synthesis 145

Figure 5. 2. WSe_2 synthesized with constant $[W(CO)_6]$/varied $[Ph_2Se_2]$ 149

Figure 5. 3. WSe_2 synthesized with constant $[W(CO)_6]+[Ph_2Se_2]$/varied $Ph_2Se_2/W(CO)_6$ ... 152

Figure 5. 4. WSe_2 synthesized with constant $Ph_2Se_2/W(CO)_6$/varied $[W(CO)_6]+[Ph_2Se_2]$ ... 154

Figure 5. 5. WSe2 synthesized with constant $[Ph_2Se_2]$/varied $[W(CO)_6]$ 156

Figure 5. 6. Powder X-ray diffraction for WSe_2 nanocrystals synthesized at high concentrations followed by a dilution. 157

Figure S5. 1. Crystal structures of the thermodynamically favored 2H phase (P63/mmc) and the metastable 2M phase (C2/m). 161

Figure S5. 2. Typical heating curve and aliquots of a standard reaction..... 162

Figure S5. 3. Number of layers and phase conversion for standard WSe_2 reaction. 162

Figure S5. 4. Duplicate reactions for standard WSe_2 reactions..... 163

Figure S5. 5. TEM images for nanocrystals synthesized with constant $[W(CO)_6]$/varied $[Ph_2Se_2]$..... 164

Figure S5. 6. Raman spectra for nanocrystals synthesized at high concentration followed by a dilution..... 166

Figure 6. 1. Powder X-ray diffraction patterns and TEM images for WSe_2 synthesized in all TOPO and with 10 eq TOP. 176

Figure 6. 2. FTIR spectra for WSe_2 synthesized in all TOPO and with 10 eq TOP 179

Figure 6. 3. Proton NMR spectra of WSe_2 nanocrystals synthesized with 10 eq TOP 180

Figure 6. 4. Characterization of $MoSe_2$, WS_2 and MoS_2 nanocrystals synthesized with and without TOP 183

Figure 6. 5. Absorbance spectra for nanocrystals synthesized with and without TOP 186

Figure 6. 6. XPS spectra for TOP-bound WSe_2 and WS_2..... 188

Figure S6. 1. Powder X-ray diffraction patterns for WSe_2 synthesized in all TOPO and with 10 eq TOP. 191

Figure S6. 2. Characterization of aliquots taken from a reaction of TOP-bound WSe_2..... 192

Figure S6. 3. TGA of WSe_2 nanocrystals synthesized in all TOPO and with 10 eq TOP..... 192

Figure S6. 4. Characterization of molecular tungsten intermediates formed during the reaction. 193

Figure S6. 5. Characterization of molecular Se intermediates formed during the reaction with Ph_2Se_2. 193

Figure S6. 6. Attempt at post-synthetic intercalation of TOP into WSe_2 nanocrystals..... 194

Figure S6. 7. Characterization of WSe_2 nanocrystals synthesized with 1 eq and 2 eq TOP. . 194

Figure S6. 8. Absorbance spectra of complex formed from reaction performed in 200 eq TOP and no TOPO. 195

Figure S6. 9. Characterization of WSe_2 nanocrystals synthesized with 10 eq TOP with TOP=Se injection 195

Figure S6. 10. Characterization of TOP-bound WSe_2 nanocrystals synthesized in docosane. 196

Figure S6. 11. Characterization of molecular molybdenum intermediates formed during the reaction 196

Figure S6. 12. Characterization of molecular S intermediates formed during the reaction with Bn_2S_2 197

LIST OF TABLES

Table 1. 1. Crystal structure parameters for some known single crystals of group-VI TMDs. . 5

Table 1. 2. Relative total energy per ME_2 for 1H, 1T′, and 1T phases. 11

Table S2. 1. Amounts of ligand present in the reactions (A) before and (B) after Ph_2Se_2 injection. 56

Table 4S. 1. CO vibrations observed when $W(CO)_6$ in 100 eq TOPO is heated to 150 °C for 15 min. 119

Table 4S. 2. Crystallographic parameters of $W(CO)_{6-x}(TPPO)_x$. 121

Table 4S. 3. CO vibrations of $W(CO)_5TPPO$ 123

Table 4S. 4. CO vibrations of *cis*-$W(CO)_4(TPPO)_2$ 123

Table 4S. 5. CO vibrations observed when $W(CO)_6$ is heated in 100 eq TOPO + 1 eq TOP to 150 °C for 15 min. 124

Table 4S. 6. CO vibrations of $W(CO)_5TPP$ 125

Table 4S. 7. CO vibrations observed when $W(CO)_5TPP$ is heated in 100 eq TOPO to 150 °C for 15 min. 125

Table 4S. 8. Chemicals 127

Table S5. 1. Reaction parameters and data obtained for aliquots taken from reaction synthesized with 5eq Ph2Se2 to W(CO)6 at total concentration of 73 mM 163

Table S5. 2. Reaction parameters for repeated reactions synthesized with 5eq Ph_2Se_2 to $W(CO)_6$ at total concentration of 73 mM 163

Table S5. 3. Reaction parameters for nanocrystals synthesized keeping amount of $W(CO)_6$ added constant and varying amount of Ph_2Se_2. 164

Table S5. 4. Reaction parameters for nanocrystals synthesized keeping the total concentration constant and varying the equivalents of Ph_2Se_2 165

Table S5. 5. Reaction parameters for nanocrystals synthesized keeping the equivalents of Ph_2Se_2 to $W(CO)_6$ constant and varying the total concentration. 165

Table S5. 6. Reaction parameters for nanocrystals synthesized keeping the amount of Ph_2Se_2 injected constant and varying the amount of $W(CO)_6$ added.. 165

Table S5. 7. Reaction parameters and data for dilution reaction 165

Table 6. 1. Exciton absorption energies for WSe_2, WS_2, $MoSe_2$, and MoS_2 synthesized with and without TOP 185

Table S6. 1. Chemicals 197

Table S6. 2. Details for reaction conditions and parameters. 199

LIST OF ABBREVIATIONS

2D	Two dimensional
Bn	Benzyl
DFT	Density functional theory
EDS	Energy dispersive X-ray spectroscopy
eq	Equivalent
FFT	Fast Fourier transform
FTIR	Fourier-transform infrared spectroscopy
HRTEM	High resolution transmission electron microscopy
IBE	Interlayer binding energy
IR	Infrared
LRTEM	Low resolution transmission electron microscopy
NC	Nanocrystals
NMR	Nuclear magnetic resonance
OAm	Oleylamine
OA	Oleic acid
PAA	Phenylacetic acid
Ph	Phenyl
PXRD	Powder X-ray Diffraction
STEM	Scanning transmission electron microscopy
TMD	Transition metal dichalcogenide
TOPO	Trioctylphosphine oxide

TOP	Trioctylphosphine
TPPO	Triphenylphosphine oxide
TPP	Triphenylphosphine
TEM	Transmission electron microscopy
XRD	X-ray diffraction
XPS	X-ray photoelectron spectra

ACKNOWLEDGEMENTS

First and foremost, I would like to acknowledge my advisor Alina M. Schimpf. She has been incredibly supportive throughout my graduate school experience and her guidance has been vital to my development as a scientific researcher, writer, and mentor.

I would like to acknowledge all the Schimpf lab members I had the pleasure of working with during my time at UCSD. Each of you made our shared work experience so much better with fruitful scientific discussions, jokes, and general comradery.

I would like to acknowledge my family. The unlimited love and support from my parents and brother always helped keep me going in graduate school.

Finally, I would like to acknowledge my partner, Ian. His constant support, feedback, and love throughout graduate school helped keep me sane.

Chapter 1, in part, is currently being prepared for submission for publication of the material. The dissertation author was the primary author of this paper and gratefully acknowledges the contributions of coauthor Alina M. Schimpf.

Chapter 2, in full, is a reprint of the material as it appears in "Using ligands to control reactivity, size and phase in the colloidal synthesis of WSe_2 nanocrystals." Chem. Commun. 2019, *55*, 8856-8859. The dissertation author was the primary author of this paper and gratefully acknowledges the contributions of coauthors Ashley K. Tamura and Alina M. Schimpf.

Chapter 3, in full, is a reprint of the material as it appears in "Manipulation of Precursor Reactivity for the Facile Synthesis of Heterostructured and Hollow Metal Selenide Nanocrystals." Chem. Mater. 2022, *32,* 2304-2312. The dissertation author was the primary author of this paper and gratefully acknowledges the contributions of coauthors Ashley K. Tamura and Alina M. Schimpf.

Chapter 4, in full, is a reprint of the material as it appears in "Controlled CO Labilization of Tungsten Carbonyl Precursors for the Low-Temperature Synthesis of Tungsten Diselenide Nanocrystals." Front. Nanotech. 2022. The dissertation author was a primary author of this paper and gratefully acknowledges the contributions of coauthors Hang Yin, Natacha Oget, Haeun Chang, Linfeng Chen and Alina M. Schimpf.

Chapter 5, in part, is currently being prepared for submission for publication of the material. The dissertation author was the primary author of this paper and gratefully acknowledges the contributions of coauthor Alina M. Schimpf.

Chapter 6, in part, is currently being prepared for submission for publication of the material. The dissertation author was the primary author of this paper and gratefully acknowledges the contributions of coauthors Hang Yin, Natacha Oget, and Alina M. Schimpf.

VITA

2016 Bachelor of Science in Chemistry, Colorado State University

2018 Master of Science in Chemistry, University of California San Diego

2022 Doctor of Philosophy in Chemistry, University of California San Diego

PUBLICATIONS

Geisenhoff, J. Q., Yin, H., Oget, N., Chang, H., Chen, L., and Schimpf, A. M. "Controlled CO Labilization of Tungsten Carbonyl Precursors for the Low-Temperature Synthesis of Tungsten Diselenide Nanocrystals" *Submitted*

Geisenhoff, J. Q., Tamura, A. K., and Schimpf, A. M. "Manipulation of Precursor Reactivity for the Facile Synthesis of Heterostructured and Hollow Metal Selenide Nanocrystals" *Chem. Mater.* **2020**, 32, 6, 2304.

Geisenhoff, J. Q., Tamura, A. K., and Schimpf, A. M. "Using Ligands to Control Reactivity, Size and Phase in the Colloidal Synthesis of WSe_2 Nanocrystals" *Chemical Communications* **2019**, 55, 8856

Whitcomb, K. J., ***Geisenhoff, J. Q.,*** Duncan, R. P., Gelfand, M. P., Van Orden, A. "Photon Antibunching in Small Clusters of CdSe/ZnS Core/Shell Quantum Dots" *J. Phys. Chem. B,* **2015**, 119, 9020.

ABSTRACT OF THE DISSERTATION

Control Over Precursor Conversion for the Synthesis of Tailored Group-VI Transition Metal Dichalcogenide Nanocrystals

by

Jessica Quinn Geisenhoff

Doctor of Philosophy in Chemistry

University of California San Diego, 2022

Professor Alina M. Schimpf, Chair

Transition metal dichalcogenides are a class of materials that are built from two-dimensional layers held together via Van der Waals interactions. These materials are structurally diverse and can adopt multiple phases. In particular, the group VI TMDs (MoS2, MoSe2, WS2, WSe2) exist in either a metastable 2M phase or the thermodynamically favored

2H phase. Material properties can be tuned by controlling the phase or the number of layers in the crystal, making controllable syntheses of these materials highly desired.

Colloidal synthesis offers a solution-phase route to solid-state materials. Conducting the synthesis in the solution phase allows a synthetic chemist to access a diverse parameter space that is usually not afforded with more traditional solid-state syntheses. This includes being able to tune reaction temperature, ligand environment, and precursor reactivity, which can easily lead to kinetically controlled reaction regimes and direct synthesis of metastable phases. This dissertation demonstrates that colloidal synthesis is a viable tool for phase tunable syntheses of TMDs, as well as investigating aspects that govern phase conversion.

The coordination and reactivity of the tungsten precursor used can be influenced via the ligands used. Reactions performed in solutions of either the strongly coordinating oleic acid, or the weakly coordinating trioctylphosphine oxide are detailed in chapter 2. The size and phase of the nanocrystals are tuned, where increased amounts of oleic acid decrease the reactivity leading to large nanocrystals of the metastable 2M phase.

Building upon the work outlined in chapter 2, chapter 3 leverages the reduced reactivity of the metal precursor in great amounts of oleic acid to synthesize metal selenide/tungsten diselenide heterostructures via a one-pot method. The delayed reactivity in oleic acid allows for nucleation of other metal selenides prior to the secondary growth of WSe_2.

How the coordination environment of tungsten influences reactivity and nanocrystal formation is more rigorously evaluated in chapter 4. Heating $W(CO)_6$ in the presence of either trioctylphosphine oxide or trioctylphosphine forms $W(CO)_{6-x}(L)_x$ intermediates. Phosphine oxides promote CO labilization while phosphines hinder this process. Thus, performing

reactions in TOPO lead to low-temperature syntheses of the metastable 2M phase, while those with TOP require additional heating.

Insights into how morphology impacts phase conversion from the metastable 2M phase to the thermodynamically favored 2H phase are investigated in chapter 5. Reactions performed in trioctylphosphine oxide with differing concentration results in WSe_2 nanocrystals with differing layer numbers. Here, high precursor concentrations lead to nanocrystals with increased number of layers without changing the lateral size of the nanocrystals. This change in nanocrystal morphology is accompanied by a reduction in the phase conversion rate from the 2M phase to the 2H phase. Phase conversion is likely slowed with increased interlayer binding energies.

Finally, a synthetic route to monolayer TMD nanocrystals is outlined in chapter 6. Controlled heat-ups in the presence of excess trioctylphosphine result in ligands tightly bound to the basal plane of the TMDs. These ligands permanently separate the layers from one another, producing monolayers, and influence the electronic properties of the nanocrystals. Additionally, phase conversion is rapid in these monolayer-like systems.

Chapter 1. Introduction to transition metal dichalcogenides and the colloidal synthesis thereof

1.1 Introduction

Transition metal dichalcogenides (TMDs) are a class of layered two-dimensional (2D) materials with the stoichiometry of ME_2, where M is a transition metal and E is a chalcogen (S, Se, or Te). The individual layers are just three atoms thick, where a layer of metal atoms is sandwiched between two layers of chalcogen atoms. Within an individual layer, strong covalent bonds are formed between the metal and chalcogen atoms, while bonding between layers is weak as the layers are primarily held together via Van der Waals interactions.[1-4] The weak interlayer interactions allow for layers to be easily cleaved from one another accessing few- to monolayer crystals.[5-7]

Many transition metals are available to select from that form layered lamellar crystal structures of ME_2. This includes metal atoms in group IV (Ti, Zr, Hf), group V (V, Nb, Ta), group VI (Mo, W), group VII (Re), and group X (Pd, Pt) and the identity of the metal atom plays a large role in governing the properties of the material.[1-4] For instance, the group-VI TMDs, with chalcogens atoms S or Se (MoS_2, $MoSe_2$, WS_2, WSe_2) can exist in various phases with unique properties to that group. For instance, the thermodynamically favored crystal structure, known as the 2H phase, is a semiconductor[8] that has a layer-dependent band structure that converts from an indirect to a direct bandgap at the monolayer.[9-10] The thinness and properties of these materials make them of great interest for many optoelectronic and spintronic applications.[11-12] These TMDs can also exist in their metastable 2M phase, which converts from a semimetal[13] to a small-bandgap[14] material during the multilayer[13]-to-monolayer[14] transition. The bulk structure behaves as a topological

superconductor[13, 15] and the monolayer as a topological insulator[14, 16] making both forms useful in quantum computation.

The unique properties of the 2M and 2H phases of MoS_2, $MoSe_2$, WS_2, and WSe_2 have driven intense interest in developing syntheses that can select between these two phases and can control for layer number. Accessing the thermodynamically favored 2H phase is more common, especially for more traditional solid-state synthesis, as typical syntheses rely on high reaction temperatures to overcome atom diffusion and spontaneously form the thermodynamically favored phase.[17-18] Synthesizing the metastable 2M phase requires a more targeted approach. Many methods rely on a multi-step process in which the 2H phase is post-synthetically converted to the metastable phase.[19-25] Alternatively, direct synthetic methods offer a way to obtain the metastable phase via a single synthetic step. Solution-phase synthesis, or colloidal synthesis, has emerged as a useful tool to directly synthesize metastable phases,[26] including the 2M phases of group VI TMDs.[27] Conducting syntheses in the solution phase affords control over multiple synthetic parameters, such as temperature, precursor speciation, precursor concentration, and ligand environment.[17, 26, 28-32] This degree of synthetic control readily allows access to kinetically controlled reaction regimes in which the metastable phase will crystallize before the stable phase.[17, 26, 30-31]

The work presented in this dissertation focuses on progress made in the colloidal synthesis of TMD nanocrystals. This solution-based technique is leveraged to directly synthesize the metastable 2M phase and is used as a tool to study the phase conversion processes and factors that favor the metastable phase. This introduction serves to introduce the TMDs of interest (section 1.2), colloidal chemistry and its thermodynamic and kinetic considerations (section 1.3), and finally, colloidal synthesis of TMDs will be discussed (section 1.4).

1.2 Polymorphism of transition metal dichalcogenides

Describing the crystal structure, or phase, of TMDs can be distilled down to two structural components: the arrangement of atoms within a single layer (monolayer type) and the stacking of layers into a three-dimensional structure (bulk structure). The variability of these two parameters leads to a very complex phase space. This introduction aims to describe the phases relevant to the group VI TMDs where M = W, Mo and E = Se, S, which are the metastable 2M phase and the thermodynamically favored 2H phase. Synthesis and characterization of the metastable 2M phase have been challenging and have only recently been fully realized. To obtain a perspective on relative instabilities between the phases and how the metastable phase is stabilized we will first introduce the 2H phase and then discuss important discoveries and insights that allowed the synthesis of the metastable phase to be accessed in these materials.

1.2.1 Crystal structure of thermodynamically favored 2H phase

The most well-understood crystal structure for the group-VI TMDs is built from trigonal prismatic coordination of the metal center by the chalcogen atoms (Figure 1.1a). The local trigonal prismatic coordination results in the formation of a hexagonal lattice (Figure 1.1b). The hexagonal unit cell with lattice parameter a is highlighted in figure 1.1b. In its monolayer form, this structure is referred to as 1H, where "1" denotes a monolayer and "H" indicates the hexagonal symmetry of the lattice. Although a simplification,[8] for group VI TMDs the *s* and *p* orbitals of the chalcogen atoms are sufficiently stabilized relative to the *d* orbitals where ligand field theory can be used to qualitatively understand the stability of different phases.[33-34] For the trigonal prismatic coordination, the d orbitals split into a low-energy singlet, a_1, and two higher-energy doublets e and e′ (Figure 1.1c).[35-36] ME_2 with a formal oxidation state of $M^{4+}(E^{2-})_2$ results in two *d*-electrons for the group-VI TMDs and a filled a_1 subband which makes it semiconducting.[36]

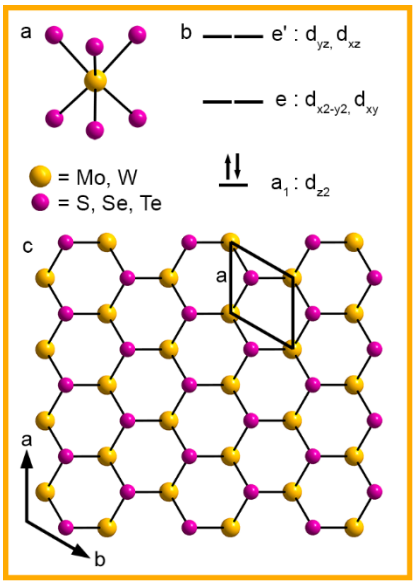

Figure 1. 1. (a) Trigonal prismatic coordination of metal atom within the 1H layer. 1H monolayer viewed along the c-direction. **(b)** Hexagonal unit cell in black with lattice parameter, a, highlighted. **(c)** Transition metal d orbital splitting for trigonal prismatic coordination.

These 1H monolayers can stack and crystallize in different bulk structures (Figure 1.2). In the thermodynamically favored form, these layers stack where each layer is rotated 180° with respect to the next layer (Figure 1.2a).[37-41] This results in ABAB stacking with 2 layers in the unit cell and a hexagonal bulk structure in the space group *P*63/*mmc*.[37-41] This phase is referred to as 2H. For MoS_2, WS_2, and $MoSe_2$, another metastable bulk structure can be formed from the 1H layers (Figure 1.2b).[38, 42-43] Here the layers are translationally shifted by 1/3a along the *a*- and *b*-directions, resulting in a rhombohedral space group (*R*/3*m*) with 3 layers per unit cell. [38, 42-43] This phase is referred to as 3R. For MoS_2, WS_2, and $MoSe_2$, the 3R phase is less stable than the 2H phase.[44] For WS_2 and MoS_2 the 2H phase is found naturally and the 3R phase of only MoS_2 is naturally occurring.[45] Structures of the 2H phase are also known for both $MoTe_2$ and WTe_2. For $MoTe_2$ the 2H phase is thermodynamically favored, however, it is metastable for WTe_2.[14, 46] A summary of the crystal structure information for the 2H and 3R phases can be found in Table 1.1.

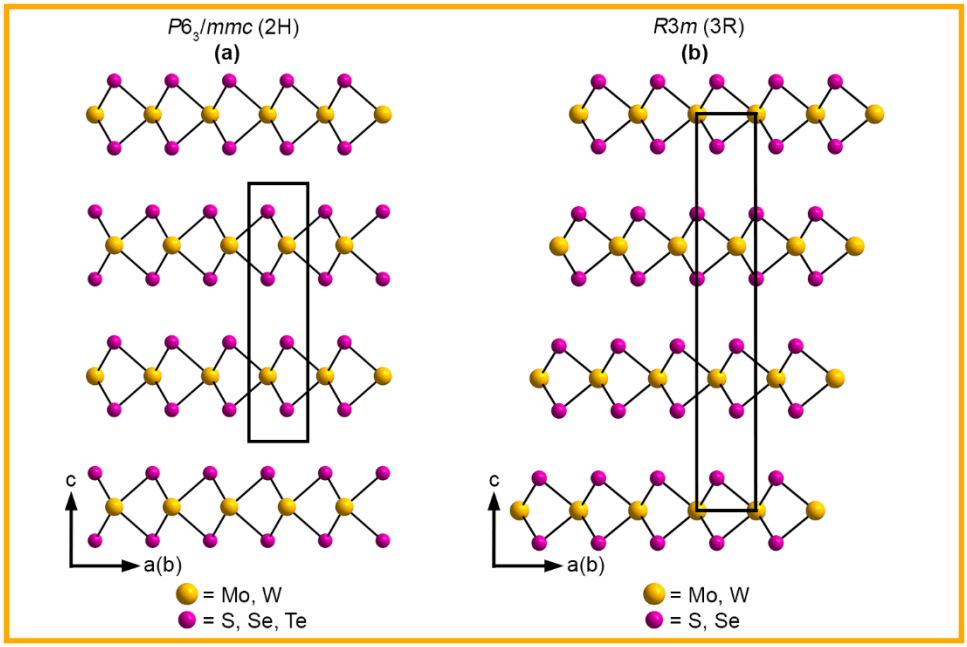

Figure 1. 2. Bulk structures built from staked 1H layers in the **(a)** 2H phase and **(b)** in the 3R phase.

Table 1. 1. Crystal structure parameters for some known single crystals of group-VI TMDs.

Material	Phase			Lattice Constants				Ref.
	Monolayer form	Bulk Structure		*a* (Å)	*b* (Å)	*c* (Å)	*β* (°)	
		Name	Space group					
MoS_2	1H	2H	*P*63/*mmc*	3.15		12.32		[37]
	1H	3R	*R*3/*m*	3.16		18.37		[42]
	1T'	2M	*C*2/*m*	5.66	3.18	12.84	113.70	[47]
WS_2	1H	2H	*P*63/*mmc*	3.18		12.50		[38]
	1H	3R	*R*3/*m*	3.16		18.49		[38]
	1T'	2M	*C*2/*m*	5.69	3.22	12.85	112.85	[13, 47]
$MoSe_2$	1H	2H	*P*63/*mmc*	3.29		12.9		[39]
	1H	3R	*R*3/*m*	3.29		19.39		[43]
	1T'	2M	*C*2/*m*	5.90	3.27	13.74	112.34	[47]
WSe_2	1H	2H	*P*63/*mmc*	3.29		12.97		[38]
	1T'	2M	*C*2/*m*	5.86	3.27	13.74	111.51	[47-48]
$MoTe_2$	1H	2H	*P*63/*mmc*	3.52		13.96		[40]
	1T'	1T′	$P2_1/m$	6.33	3.47	13.86	93.92	[49]
	1T'	T_d	$Pnm2_1$	6.33	3.469	13.83	90	[41]
WTe_2	1H	2H	*P*63/*mmc*	3.49		14.31		[41]
	1T'	T_d	$Pnm2_1$	6.27	3.48	14.04	90	[50]

It is important to note that the stability of the 1H monolayers and subsequent bulk structures is unique to the group-VI TMDs and can be attributed to the *d*-electron count of the metal. If instead the *d*-electron count is changed, such as if it is lowered, group IV and V TMDs, or

increased, group VII TMDs the trigonal prismatic coordination is no longer favored.[1-4] Instead, octahedral coordination or distorted octahedral coordination is preferred.[1-4] Lattices built from pristine octahedra are referred to as 1T, as the bulk structure has one layer in the unit cell and typically adopts a trigonal space group (P-3m1).[51-53] Lattices built from the distorted octahedra are referred to as 1T′ in the monolayer form to denote the distortion from the octahedral lattice.

1.2.2 Crystal structure of the metastable 2M phase

The group VI TMDs can also adopt the 1T′ monolayer form (Figure 1.3). The distorted octahedra (Figure 1.3a) lead to the formation of metal-metal bonds and infinite zigzagging chains of bonded metal atoms throughout the lattice (Figure 1.3b). A superstructure is formed from the distortion with a rectangular unit cell $a \times \sqrt{3}a$. Distortion from the pristine octahedral 1T lattice is favored in the group VI TMDs via a Peierls (Jahn–Teller-like) transition (Figure 1.3c).[14, 54-57] The spontaneous lattice distortion to open a small band gap is driven by the metal-metal bonding formed in the 1T′ monolayers which splits the t_{2g} states into bonding, nonbonding, and antibonding subbands (Figure 1.3c).[57] With only 2 d-electrons, the partially filled t_{2g} orbitals of the 1T phase convert to a filled bonding t_{2g} orbital with the distortion that is lowered in energy, resulting in the 1T′ monolayer being energetically favored compared to the 1T monolayer.[57] It should be noted that the d orbital splitting is insufficient to describe the band structure of the 1T′ structure. For the sulfide and selenide group, VI TMDs p-d type band inversion occurs where p bands are pulled below d bands.[54] This band inversion is the origin of the topological properties of the 1T′ phase.[54]

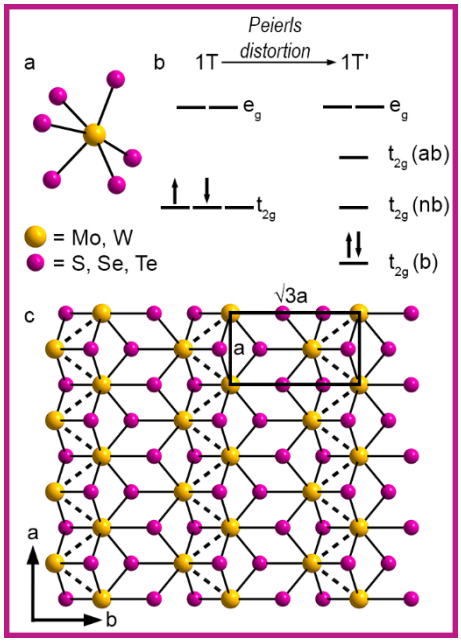

Figure 1. 3. (a) Distorted octahedral coordination of metal atom within the 1T′ layer. **(b)** 1T′ monolayer viewed along the c-direction, zigzagging metal–metal bonds shown with dotted lines. The monoclinic unit cell ($a \times \sqrt{3}a$) is in black. **(c)** Transition metal d orbital splitting for octahedral 1T and change to the ligand field splitting upon distortion to the 1T′ lattice.

Only recently have crystals of high enough quality been produced to determine the stacking of 1T′ layers of group-VI S and Se TMDs. These crystals were obtained through controlled oxidation and deintercalation of potassium-intercalated TMDs.[13, 47-48] First, the potassium-intercalated structure was synthesized either via a direct synthesis with K_2WO_4 and elemental sulfur or selenium or by heating the 2H TMD crystal in the presence of K. The K_xME_2 crystals were then soaked in a solution containing either $K_2Cr_2O_7$ or I_2 to oxidize and induce deintercalation. The bulk crystal structure of the stacked 1T′ layers is shown in figure 1.4. There is no rotation between the layers, but rather only translational shifts. The translational shift along the *a*-direction by *a*/2 results in two layers per unit cell, (Figure 1.4a). Along the *b*-direction, the layers are staggered from one another forming an angle of β = ~112° of the unit cell (specific crystal

parameters summarized in table 1.1). The bulk lattice is in the monoclinic space group *C*2/*m* and is referred to as 2M.

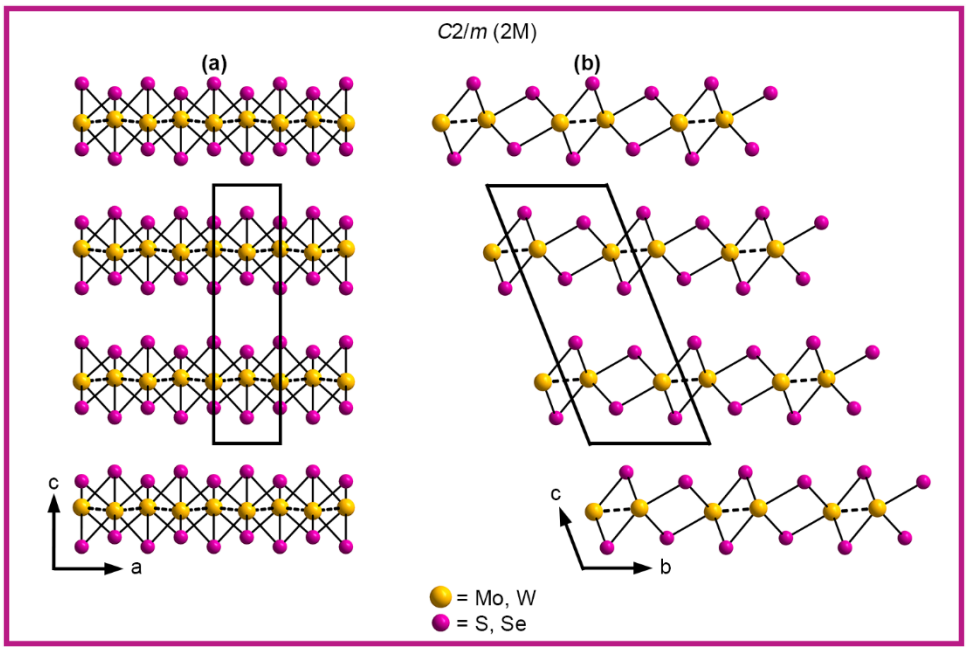

Figure 1. 4. 2M bulk structure built from staked 1T′ layers viewed along the **(a)** *b* axis and **(b)** the *a* axis.

Interestingly, despite the relatively recent discovery of the 2M phases of the sulfide and selenide group VI TMDs, the group-VI tellurides have been known to adopt structures built from 1T′ monolayers, such as the bulk structures 1T′ and T_d (Table 1.1).[49-50] These structures differ from the 2M phase as each layer is rotated 180° with respect to the next layer and has smaller angles that form between the stacked 1T′ layers. We suspect that these crystallographic differences likely come from the difference in sizes of the chalcogen atoms. The ease of forming the distorted octahedral lattice with the tellurides compared to the sulfides and selenides is credited to the increased covalency. Tellurium has a greater propensity to adopt oxidation states between −1 and −2 compared to sulfur and selenium which results in tellurium forming short Te-Te contacts in the lattice.[58-61] These short contacts serve to raise the energy of the *p* orbitals resulting in overlap and

mixing of the *p* and *d* orbitals, yielding partial electron transfer from the tellurium atoms to the metal centers.[58-61] This effectively lowers the formal *d*-electron count of the metal and destabilizes the trigonal prismatic coordination.[62] Unsurprisingly, a common method to synthesize the 2M phase for the sulfide and selenide group-VI TMDs is via reduction. Like in the synthesis of the 2M single crystals, the K_xME_2 intermediate results in excess electrons added to the TMD layers stabilizing the distorted octahedral coordination by lowering the valency of the metal atom.

1.2.3 Access to the metastable phase through reduction

A popular method of synthesizing the metastable phase is via phase conversion from the 2H phase to the 2M phases. Charge doping of either holes or electrons should induce this phase conversion,[55, 63] but reduction is the more common method as intercalation of strongly reducing species into the two-dimensional lattice is a known phenomenon. [19, 63] Interestingly, group-IV and -V TMDs can support intercalation of weak electron donors, such as many Lewis-basic ligands,[64] without a phase change, while the 2H phase of the group VI TMDs has a low electron affinity[2, 65] and only strong electron donors are capable of intercalation.[19, 63] Electron donation into the lattice accompanies intercalation and results in electron transfer to empty *d* orbitals stabilizing the octahedral structure and causing a phase conversion.

Typically crystals of 2H group-VI TMDs are soaked in a solution containing a strong, lithium-based reducing agent, such as *n*-butyl-lithium (*n*-BuLi), $LiBH_4$, or LiH, which results in Li insertion between the layers and electron injection into the material.[20, 66-72] This method has induced phase conversion for MoS_2, $MoSe_2$, WS_2, and WSe_2,[73] but MoS_2 has been most intensely studied and will be used for the discussion here. After lithium insertion into 2H MoS_2, $LiMoS_2$ is formed as an intermediate. The poor crystallinity of the $LiMoS_2$ intermediate has precluded structural determination from single-crystal XRD, but structural characterization has been

performed via PDF analysis.[67, 70, 74] Conversion to octahedral coordination has been observed, and even in this highly reduced state, a distortion is already present. Rather than forming an infinite zigzagging chain a metal–metal bonds, a tetramerization occurred in which the metal atoms clustered together in groups of four, forming a unit cell with dimensions $2a \times 2a$.[70, 74] In a fully reduced state, with 3 *d* electrons per metal, this distortion is predicted to be more stable than the idealized octahedral coordination.[57] To oxidize the material and remove the intercalated Li the $LiMoS_2$ was transferred to water.[66] The Li reacted with the water to generate H_2 gas and LiOH.[66] The generation of H_2 gas was shown to forcibly cleave the layers from one another and form relatively stable suspensions of mono-/few-layer MoS_2. These layers were then washed and allowed to restack, either through centrifugation or drying. Through this violent reaction, the crystalline quality became too poor for single-crystal X-ray diffraction, but structural insights can be gained via electron diffraction in HRTEM imaging[66, 68] or with PDF analysis.[69] After restacking, there is no evidence of pristine 1T lattices, but multiple distortions within the layer could be identified. This includes the tetramerization discussed earlier as well as a trimerization, in which the metal atoms cluster in groups of 3, forming a unit cell that is $\sqrt{3}a \times \sqrt{3}a$.[48] Most of the product, however, was restacked 1T′ layers.[48] This phase was noted to be more resistant to phase conversion back to the 2H phase, compared to the tetramerization and trimerization distortions.[66] Due to the 2D nature of the platelets formed after restacking, results in preferred orientation and made it difficult to determine the layer arrangement. Originally analysis was done to try to match the structures with the known 1T′ or T_d lattices of the telluride TMDs,[66-68] however powder X-ray diffraction patterns match better with the now-known 2M structure. Additionally, Rietveld-like refinements on Li intercalated MoS_2, with Li removed and restacked with ethylene diamine between the layers also show the 2M stacking rather than the 1T′ or T_d strcutures.[75]

Due to the success of lithium intercalation, many other reductant-based syntheses have been developed to access the metastable 2M phase or 1T′ monolayers. These methods typically rely on adding a reductant post-synthetically[23, 76] or during the synthesis.[77-80] For instance, 2H MoS_2 can be layered on top of the 2D electride material of dicalcium nitride, $[Ca_2N]^+ \cdot e^-$.[76] The dicalcium nitride has a low work function, enabling rapid injection of electrons into MoS_2 and resulting in phase conversion to the 1T′ layers. Recently, CVD synthesis has emerged as a reliable method to synthesize this metastable phase directly. In a typical synthesis, the reductant is added during the synthesis by using K_2MoS_4 as the starting material as well as conducting the synthesis under the flow of a reductive gas (H_2 and Ar mixture).[77] This results in monolayers of the 1T′ phase of K_xMoS_2.

1.2.4 Crystal phase stability

The reduction-based methods all rely on electron injection to stabilize the metastable 2M phase. Some syntheses add mild oxidants to remove intercalants, but it is difficult to interpret if the final material is neutral or slightly reduced. Calculations can help elucidate if the synthesis of the neutral structure is feasible or if the addition of excess electrons is necessary to stabilize the structure. Calculations to determine ground state energies and the phase conversion pathway have been performed on monolayers of the 1H, 1T′, and 1T phases of group VI TMDs.

Table 1. 2. Relative total energy per ME_2 for 1H, 1T′, and 1T phases. Adapted from ref. [46].

Material	*H* (eV per ME_2)		
	1H	1T'	1T
MoS_2	0	0.55	0.84
$MoSe_2$	0	0.33	0.71
$MoTe_2$	0	0.04	0.52
WS_2	0	0.54	0.89
WSe_2	0	0.27	0.78
WTe_2	0	-0.09	0.57

Table 1.2 lists the calculated ground-state energies of the 1T and 1T′ monolayers of the group-VI TMDs relative to the 1H monolayer counterparts. Calculations were performed under ambient conditions.[46] Unsurprisingly, the 1T layer has the highest ground-state energy among all the phases. The energy of the 1T′ monolayer depends on the chalcogen atoms and becomes more stable as S > Se >Te due to increased covalency.[41, 60] Only in the case of WTe_2, the ground state energy of the 1T′ layer is lower in energy than that of the 1H layer. The data in Table 2 shows that the difference in energy is relatively small between the 1H and 1T′ phases, where MoS_2 has the highest energy difference of 0.55 eV per ME_2 unit.

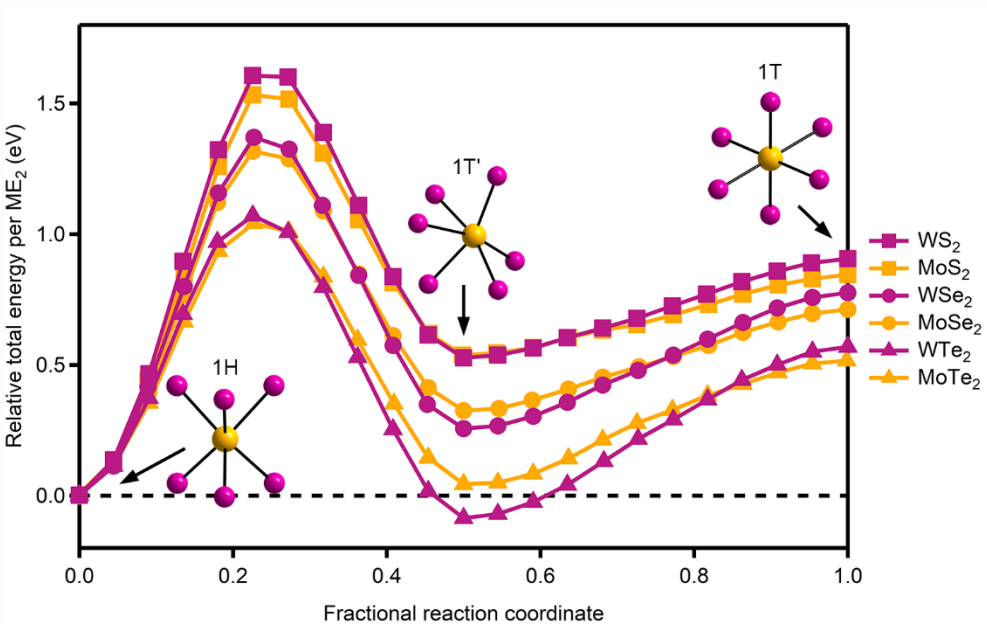

Figure 1. 5. Computed reaction coordinate diagram for monolayer TMD phases in the conversion of 1H to 1T' to 1T, adapted from ref. [14].

To determine the feasibility of the synthesis of 1T′ monolayers, conversion of the 1H phase to the 1T′ was modeled,[14] (Figure 1.5) Importantly, there exists a large (>1 eV/ME_2) energy barrier between the 1H and the 1T′ phase, which suggests it should be possible to stabilize the 1T′ phase without spontaneous conversion to the 1H phase. The 1T′ phase also exists at an energy minimum,

further supporting its metastability. The 1T phase, on the other hand, exists at a local energy maximum, causing it to spontaneously convert to the 1T′ phase via a Peierls distortion. This corroborates that the 1T phase is likely only stabilized via extrinsic factors, such as the addition of excess electrons and concomitant intercalation of charge-compensating cations. To further support the metastability of the 1T′ phase and instability of the 1T phase, phonon dispersion curves have also been calculated. [46, 56, 81] In the case of the 1T phase, a phonon mode with an imaginary frequency arises indicating the unstable nature of this phase.[46, 56, 81] The greatest instability is also located at a point in the lattice that leads to a distortion to the 1T′ phase.[56, 81] In contrast, there are no imaginary frequencies in the phonon dispersion curves for the 1T′ phase, supporting its structural stability.[14, 82]

The small energy differences between the 1T′ and 1H phases and the existence of a large energy barrier between the two phases support the possibility of direct synthesis of the metastable phase via syntheses under kinetic control. Indeed, molecular beam epitaxy syntheses support the ability to synthesize neutral structures via kinetic control as 1T′ monolayers of WSe_2 have been grown by reducing the reaction temperature (500 K instead of 675 K).[16, 83]

1.2 Colloidal synthesis

Colloidal synthesis of nanocrystalline materials relies on precursor decomposition in the presence of organic surfactant capping ligands resulting in colloidally stable nanocrystals. The principles of the modern methodology originated with the pioneering work by Murray, Norris, and Bawendi in which cadmium chalcogenide nanocrystals were synthesized at high temperatures in the presence of the coordinating ligands trioctylphosphine oxide (TOPO) and trioctylphosphine (TOP).[84] Overall, the formation of nanocrystals requires two steps: nucleation and growth. To achieve nucleation and growth, one must select suitable precursors that decompose at the given

reaction temperature. These precursors first convert to solutes of the nanocrystal (soluble units of the nanocrystal). Then, these solutes accumulate until supersaturation is reached and nuclei are formed. After this, a period of growth is entered in which any remaining solutes in the solution deposit on the surfaces of the nuclei. Using classical nucleation theory as a guiding model,[85] many refinements in nano synthesis have been achieved and one can tailor nanocrystal size, shape, composition, and phase of many metal chalcogenide semiconductor nanocrystals. However, classical nucleation theory makes multiple assumptions that may not apply to the given crystal system, and thus it might not be sufficient to explain the resultant product.[86]

1.2.1 Precursor conversion chemistry

One of the most important factors in dictating nucleation and growth of crystallites is controlling the solute concentration over the course of the reaction. The rate that solutes are introduced can be controlled via precursor conversion kinetics.[87]

$$P \rightarrow S \leftrightarrow NC$$

Typically, precursors (P) are converted to solutes (S) slowly, then the solutes come together to form nanocrystals (NC). Precursors convert to solutes irreversibly, while for relatively weakly bound systems (such as ionic systems) nanocrystals can dissolve and reform solutes during the reaction. The rate of precursor conversion to solutes can be controlled by the reactivity of the selected precursors. For instance, rapid conversion to solutes from highly reactive precursors results in high supersaturations of solutes, a greater number of nuclei formed during the nucleation step, and small nanocrystal sizes. This has been demonstrated nicely for metal chalcogenide nanocrystals (CdSe, CdS, PbSe) where size can be controlled via the reactivity of the chalcogenourea precursor.[88-91]

1.2.2 Thermodynamics and kinetics in nanocrystal synthesis

In a thermodynamically controlled reaction, the resulting product is obtained because it is in its most stable state (Figure 1.6), while a kinetically controlled reaction regime selects the product that has the lowest energy barrier.[17, 29] Identifying thermodynamic or kinetically controlled reaction pathways in nanocrystal synthesis can provide great insights into the design of complex nanomaterials. Doing such analysis is common practice for molecular reactions but is more challenging on the nanoscale. Sometimes the intermediates formed during the reaction are not well understood which makes it challenging to evaluate relative stabilities.[29] Despite these challenges, it has been observed that many nanocrystal reactions fall under kinetic control where cluster intermediates, different sizes, shapes, and phases can be observed as metastable products formed during the reaction.

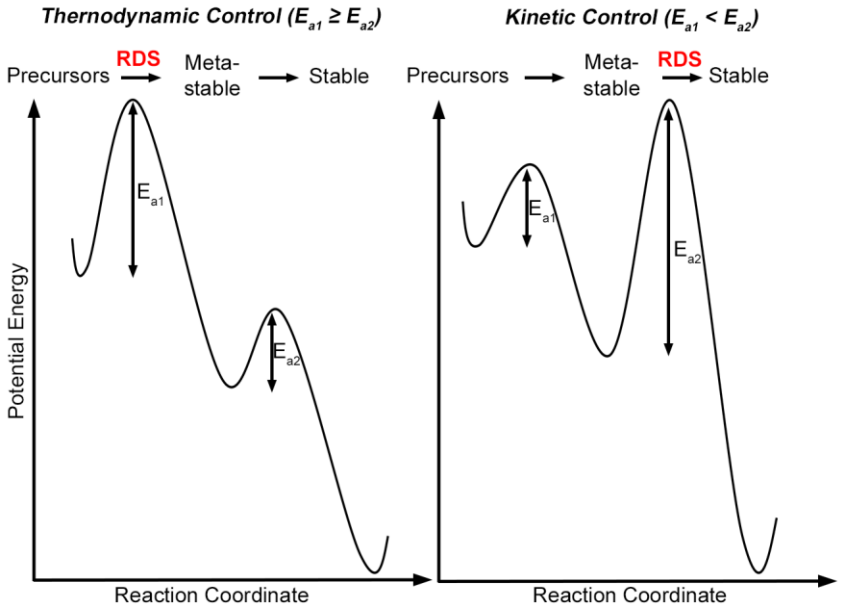

Figure 1. 6. Reaction coordinate diagrams indicating thermodynamic control (left) where the stable product forms spontaneously and kinetic control (right) metastable intermediates can be accessed.

Molecular intermediates

In some systems, metastable molecular intermediates are formed that precede the formation of nanocrystals, like amorphous or cluster intermediates.[92-98] These intermediates are typically formed when highly reactive precursors are used that lower the energy barrier, E_{a1}. These intermediates are sometimes referred to as "kinetically persistent" as they can require long reaction times to overcome the second energy barrier, E_{a2}, and convert to nanocrystals.[92] Formation of such intermediates is common in the synthesis of indium phosphide nanocrystals. The precursors used are highly reactive, such as $P(SiMe_3)_3$, and rapidly convert to solutes, which readily aggregate into clusters or amorphous particles.[96] For some reactions magic-sized indium phosphide clusters are formed as intermediates that have been crystallized.[97-98]

Nanocrystal Size

Generally, due to high surface-to-volume ratios, small nanocrystals are metastable. In a thermodynamically driven process, Ostwald ripening will occur to lower the energy of the system by increasing the total nanocrystal size. Here, small nanocrystals are dissolved and then deposited at the surfaces of larger nanocrystals, overall increasing the crystallite size.[99] This process can lead to broad distributions of nanocrystal sizes which lowers the quality of the material properties of the batch of nanocrystals.[100] A kinetically controlled size-focusing growth regime can be accessed by tuning the precursor conversion kinetics.[87] If the reactions rate-limiting step is the precursor conversion to solutes, the solutes will be actively generated over the course of the reaction.[101] High solute concentrations prevent the dissolution of the small nanocrystals and favor growth at the nanocrystal surface.[102] Since small nanocrystals have a higher surface energy growth will selectively occur at the surfaces of small nanocrystals, resulting in size focusing, sharpening the size distribution.[102]

Nanocrystal Shape

Finding conditions that favor kinetically controlled growth regimes for nanocrystals of controlled size and polydispersity laid the groundwork to access nanocrystals with metastable shapes. The Wulff construction can be used to determine a material's equilibrium crystal shape and for many crystal systems (such as metal chalcogenides) the thermodynamically favored shape is a sphere.[103] Unsurprisingly, the slow growth rate regimes that occur during Ostwald ripening result in spherically shaped nanocrystals.[104] Spherical nanocrystals are also obtained during size-focusing conditions.[104] If the growth rate is increased metastable nanocrystals with non-equilibrium, highly anisotropic shapes can be obtained as rapid growth regimes favor growth along high-energy facets.[104-107] In the case of rhodium nanocrystals, Different metastable shapes can be obtained by controlling the growth rate, including octahedrons, cuboctahedrons, and cubes.[107] Upon further heating the shape will convert to the thermodynamically preferred spheres.[107]

Nanocrystal Phase

In a similar vein, the nanocrystal phase can also be dictated by reaction kinetics. In the late 1800s, Ostwald observed that less stable polymorphs crystallize before the most stable ones.[108] In other words, under kinetically controlled reactions, the phase with the lowest kinetic barrier will form first. Many efforts have been made to explain why nucleation occurs in the metastable phase. At small sizes, when the critical nuclei are formed, the metastable phase can lower the surface energy.[109] The interfacial tension between the metastable phase and the solution is lowered because it is the more soluble phase.[110] Since the metastable phase is more soluble, the solution must be supersaturated concerning both phases to ensure nucleation in first the metastable phase.[31] Theoretically, at low enough supersaturations nucleation of the metastable phase can be circumvented and crystals will nucleate and grow only in the thermodynamically favored phase.[31] If the metastable phase is desired, one should also select conditions that favor its growth.

Conditions where the metastable phase grows more rapidly than the stable phase ensure a population of nanocrystals predominantly in the metastable phase.[111] These high supersaturations lower the first activation energy barrier, E_{a1}, allowing access to the metastable phase. In kinetically controlled reaction regimes, the kinetics of the phase transformation process will depend on the second energy barrier, E_{a2}. In the solution phase, phase transformations happen either in the solid state where atoms rearrange themselves in the lattice, or via a solvent-mediated route where the metastable crystals dissolve and then nucleate in the thermodynamically favored phase.[112] The colloidal synthesis of CdSe has shown to be kinetically controlled and crystallized via Ostwald's stages where the zinc blende structure nucleates first and then converts to the wurtzite phase.[30] Interestingly, at high precursor concentrations more of the thermodynamically favored wurtzite phase is formed.[30] Rapid nucleation and growth at high supersaturations result in a higher defect concentration facilitating the phase transition from the metastable to the stable phase.[30] With higher defects atom migration is assisted effectively lowering E_{a2}.[30]

Effect of ligands

Ligands included in nanocrystal synthesis can also serve as an instrumental component in the stabilization of metastable sizes, shapes, and phases. Based on the functional group of the ligand different nanocrystal facets can be stabilized when the ligands are bound, lowering the surface energy at that interface. For instance, the sizes of gold nanocrystals can be tuned post-synthetically due to the strong covalent bonds that are formed between the nanocrystal surface and thiol ligands.[113] The size of the nanocrystals is reduced when the concentration of the added thiol ligand is increased to optimize for surface interactions with these ligands.[113] Flat CdSe nanoplatelets can be formed in the presence of short-chain carboxylates.[114] These ionic ligands strongly bind to cadmium terminated (001) or (111) facets of zinc blende CdSe arresting growth

at these planes but allowing growth at the exposed edges.[114] The phase of CdSe can also be controlled with ligand interactions. In the presence of phosphonates the wurtzite crystal structure is stabilized, while in the presence of carboxylates the zincblende structure is favored.[32]

1.4 Colloidal synthesis of TMD nanocrystals

The colloidal synthesis of TMD nanocrystals is still in its infancy. Additionally, applying the analysis done for more traditional nanocrystal systems (section 1.3) can be complicated by the anisotropic nature of the crystal structure and the Van der Waals interactions holding the layers together. Despite these differences, colloidal synthesis has been successfully leveraged to obtain size, shape, and phase-controlled TMD nanocrystals. The synthetic parameters used and how they impact the resulting nanocrystal will be discussed in the following section.

1.4.1 Metal precursor speciation and reactivity

Many syntheses have been developed to access colloidal group VI TMD nanocrystals. Some syntheses make use of single source precursors, such as ammonium tetra thiomolybdate or tetra thiotungstate, that decompose to MoS_2 or WS_2.[115-116] The majority of reactions use a hot-injection method where a chalcogen precursor (elemental sulfur/selenium, sulfur/selenium well dissolved in a solvent, diorganyl dichalcogenides, CS_2, thioureas, and TOP-E) is injected at high temperatures into a solution containing the metal precursor.[117-146] The most used metal precursors are either metal carbonyls or metal chlorides as they are relatively cheap and readily available. Assessing the reactivity of the metal precursors is complicated by reactivity with common nanocrystal solvents/ligands. Tungsten and molybdenum chlorides are highly oxidizing[147] and likely react with the available ligands before injection of the chalcogen precursor.[132] Coordination of ligands/reaction with the solvent is indicated by color changes as the metal chloride is dissolved in the solvent (Figure 1.7). Tungsten and molybdenum carbonyls should not be as reactive as the

metal chlorides, but nanocrystal synthesis reactions typically exceed the reaction temperatures at which the M–C bond is cleaved.[148] With heat these precursors readily decompose to their elemental form, some other byproduct, or forming intermediates with the ligands available during the nanocrystal synthesis.[144]

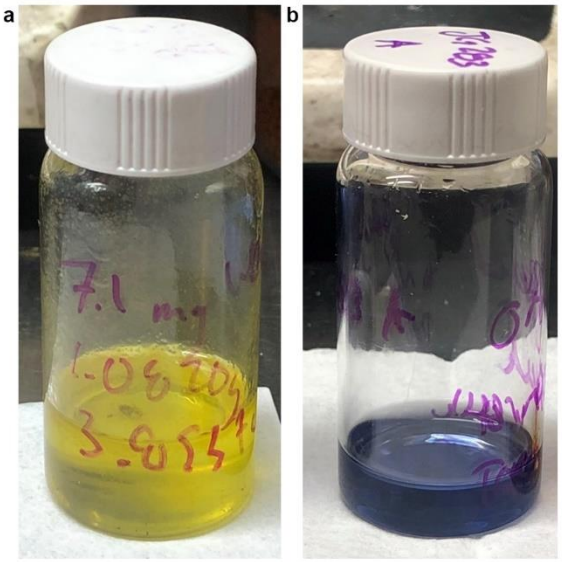

Figure 1. 7. Tungsten hexacarbonyl dissolved in mixtures of **(a)** oleic acid and TOP, and **(b)** oleic acid and TOPO at room temp.

Due to the reaction of the metal precursors with the available ligands, the reactivity and precursor conversion rate can be tuned via the ligand environment. For instance, Zhou et al. found that the reaction rate for WSe_2 synthesized in OAm versus OA differed greatly.[144] Here, $W(CO)_6$ was heated in OAm or OA to 330 °C, upon which elemental selenium was injected into the flask.[144] The reaction in OAm proceeded about 3 times more slowly than the one in OA.[144] Due to the change in the CO stretching frequency of the FTIR spectrum after heating $W(CO)_6$ in the ligands, the hypothesized intermediates formed were of the form $W(CO)_{6-x}L_x$.[144]

We observed a similar phenomenon with the reaction of WSe_2 in OA or TOPO (chapter 2). With a similar reaction scheme $W(CO)_6$ was heated to 330 °C in mixtures of OA or TOPO after

which Ph_2Se_2 was injected as the selenium source. The reactivity is rapid in reactions where the ligand environment is dominated by TOPO, nanocrystals nucleate immediately following the injection of the Ph_2Se_2. In contrast, when the ligand environment is mostly oleic acid the reactivity is sluggish, and nucleation of nanocrystals is delayed minutes after the injection. Reactions of $W(CO)_6$ with carboxylates are known to make metal oxo clusters that should be highly stable species,[149] while TOPO should be a weakly coordinating ligand that promotes CO labilization leading to rapid reactivity.[150]

To further investigate how ligands influence reactivity in TOPO, heat-ups of the $W(CO)_6$ in TOPO were performed at lower temperatures (chapter 4). At 150 °C $W(CO)_5$TOPO and cis-$W(CO)_4(TOPO)_2$ are formed as intermediates during the heat-up. The coordination of phosphine oxides to metal carbonyls is known to promote CO labilization which can explain the highly reactive nature of these metal intermediates.[150] These intermediates can be exploited to synthesize WSe_2 at very low temperatures. Injection of Ph_2Se_2 at 150 °C leads to the formation of WSe_2 after just 10 minutes. To demonstrate that reactivity can be influenced by the CO labilization capabilities of the included ligand, 1eq TOP is added to the ligand mixture. Here, $W(CO)_5$TOP is formed as the intermediate and requires higher temperatures for nanocrystals to nucleate. Phosphines hinder CO labilization which slows down the precursor conversion step.[151]

1.4.2. Size, shape, and layer control of TMD nanocrystals

Typically nanocrystal size can be controlled via precursor reactivity: faster conversion to solutes leads to a greater extent of nucleation and smaller nanocrystal sizes. The difference in reactivity of $W(CO)_6$ in mostly TOPO versus mostly OA (chapter 2) manifests itself in the nanocrystal size. The rapid reactivity in TOPO leads to smaller WSe_2 nanocrystals (~20 nm laterally) while the slow reactivity in OA leads to much larger nanocrystal sizes (~600 nm

laterally). Despite the underlying anisotropy of the two-dimensional crystals, growth is increased in all directions as the nanocrystals synthesized in OA have an increased number of layers as well as larger lateral sizes. It is also worth mentioning that the slow reactivity of the metal precursor in oleic acid allows for the facile synthesis of one-pot heterostructure nanocrystals (chapter 3) as WSe_2 can be selectively nucleated at later times following the formation of different metal selenide seed nanocrystals.

Nanocrystal size does not always align with metal precursor reactivity. As the trend of slower reactivity producing larger nanocrystals is not followed for Zhou et. al. Here, reactions in oleylamine showed slow reactivity but very small crystal sizes.[144] The small crystal sizes may be accounted for by the different binding affinity of the ligands to the nanocrystal surface. TOPO and OA should not have a strong binding affinity for either the surfaces or edges of the layers and therefore do not impede nanocrystal growth.[123, 125] On the other hand, oleylamine is known to interact strongly with both surfaces and edges.[125, 132] Therefore, the incorporation of oleylamine can slow down crystal growth at those facets, leading to smaller nanocrystals.

Control of size and layer number with ligand binding to edge sites

The binding of ligands to the basal plane of TMDs is challenging, but multiple sites are available at the exposed edges of nanosheets where dangling bonds are formed.[152] This typically leads to a much smaller surface area available for ligand binding that hampers the colloidal stability of the nanocrystals.[143] However, binding at the nanocrystal edges can be used to direct growth. For instance, in the case of $MoSe_2$ and WSe_2 lateral size and layer number are tied to the binding affinity of the ligands to the edge site of the nanocrystals (Figure 1.8).[123, 125] Oleylamine leads to smaller lateral sizes and increased layer number due to its strong binding affinity to edge sites, while weaker binding ligands such as OA and TOPO will allow more lateral growth of the

nanocrystals.[123, 125] Furthermore, the lateral versus layer growth can be controlled by the amount of highly binding to weakly binding ligands.[123]

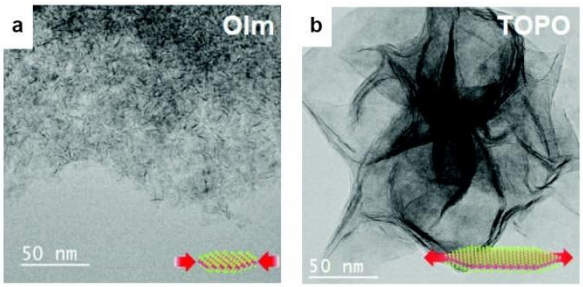

Figure 1. 8. LRTEM images of $MoSe_2$ nanocrystals synthesized in **(a)** oleylamine versus **(b)** TOPO. Nanocrystals synthesized in oleylamine have much smaller lateral sizes than those synthesized in TOPO. Figure reproduced from ref. [123].

Control of size and layer number with precursor concentration and ratio

Additionally, lateral sizes and layer numbers of TMD nanocrystals can be controlled by varying the precursor concentration and the precursor ratios.[117, 130] In the synthesis of MoS_2 and WS_2 the lateral sizes can be tuned with the precursor ratio, where the lateral sizes are increased as the ratio of M:S is lowered.[117] The number of layers can be increased by doing multiple injections and the solutes are replenished multiple times during the reaction. [117] Layer growth can also be controlled via concentration, where higher precursor concentrations lead to more layers in the resulting nanocrystals (Figure 1.9 a).[130] Increase in layer number by introducing more solute species fits with the layer growth model observed by Hansen et. al.[153] Growth of single MoS2 nanocrystals was monitored with HRTEM.[153] Here, it was observed that layer growth does not occur through a particle coalescence method, but rather via the deposition of solutes at the basal plane leading to multiple layer growth (Figure 1.9 b).[153]

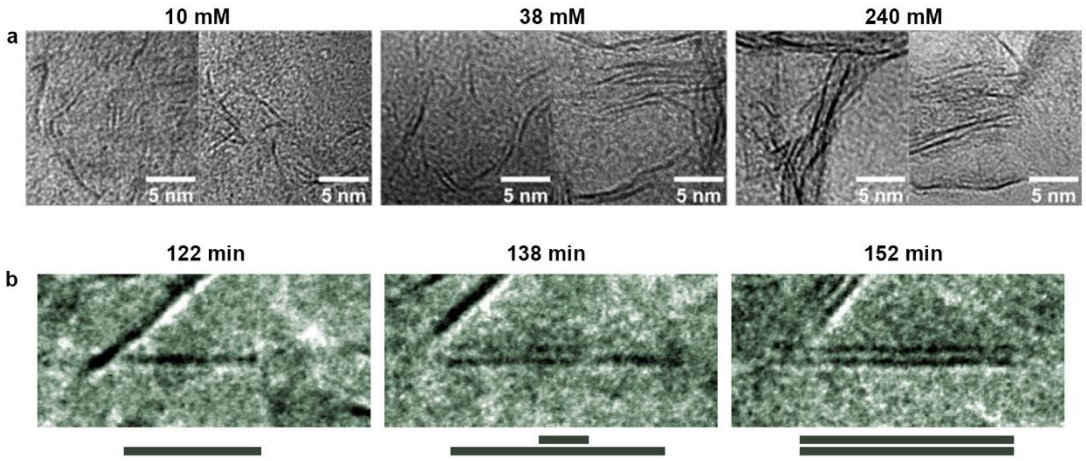

Figure 1. 9. (a) LRTEM images of MoS_2 synthesized with different precursor concentrations. **(b)** HRTEM image of single MOS_2 nanocrystal showing growth from monolayer to bilayer. (a) reproduced from ref. [130] and (b) reproduced from ref. [153].

We also showed that layer numbers can be controlled in the synthesis of WSe_2 nanocrystals by changing the precursor concentration and precursor ratio (chapter 5). In general, higher precursor concentrations lead to an increase in the number of layers in the nanocrystal without significantly changing the lateral sizes of the nanocrystals. Higher precursor concentrations push the reaction into kinetically controlled growth regimes that can lead to rapid directional growth. This tied with the layer-by-layer growth mechanism can lead to nanocrystals with increased layer number.

1.4.3 Monolayer nanocrystals via colloidal synthesis

Due to the layer-dependent properties of TMDs, being able to synthesize solution-processable monolayer materials is of great interest. Because layer number is tied to concentration some syntheses have been able to obtain the distribution of nanocrystals that highly skew to monolayers by lowering the concentration or changing the precursor ratio.[117, 130] For instance, we found that lowering the concentration leads to distributions that highly favor monolayers (chapter 5). Additionally, using a precursor ratio of $W(CO)_6$:Ph_2Se_2 = 1:1 always leads to distributions with

a great number of monolayers independent of the concentration. However, without something to permanently separate the layers from one another, there will always likely be some number of few-layer species in the distribution. One method to obtain a strict set of monolayer nanocrystals is to bind ligands along the basal plane of the material.

Oleylammonium ligands

For some nanocrystal syntheses of TMDs highly reducing intermediates can be formed that inject electrons into the nanocrystal lattice. This process is known for WS_2 synthesized in oleylamine.[122, 131-132, 135-136, 145-146] In oleylamine, many common sulfur precursors (CS_2, thiourea) will react with the excess oleylamine to generate the highly reducing H_2S gas.[135] The excess charges in the nanosheets are then compensated by the coordination of oleylammonium ligands along the basal plane of the TMD nanocrystals via electrostatic interaction.[132, 136] The nanocrystals can be dispersed in solution to obtain monolayers (Figure 1.10a).[132, 145] When the nanocrystals are dried there is an increase in the interlayer spacing between the nanosheets to 2.4 nm which is 1.8 nm greater than the normal Van der Waals spacing (Figure 1.10 b and c).[132] This method has recently been generalized to synthesize monolayers of WSe_2, MoS_2, and $MoSe_2$ as well.[122]

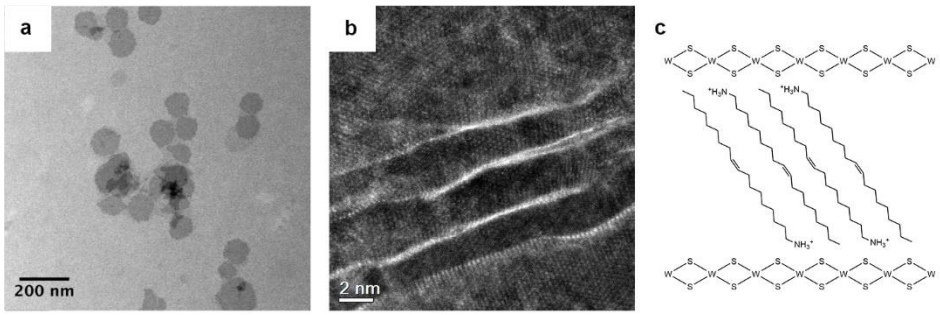

Figure 1. 10. WS_2 synthesized under conditions that led to oleylammonium bound nanocrystals. **(a)** LRTEM of WS_2 nanodisks, **(b)** STEM image showing the interlayer distance between nanosheets, and **(c)** schematic showing WS_2 layers with oleylammonium between. a and b reproduced from reference [132].

Phosphine ligands

In chapter 6 we demonstrate a method that leads to phosphines binding along the basal planes of the nanosheets. Here, phosphines, diorganyl dichalcogenides, and the metal carbonyl precursor are combined at low temperatures and then heated. The resulting nanocrystals have an increased interlayer distance than the Van der Waals distance due to the phosphine being bound. The binding of phosphines to the basal plane can also be generalized to multiple TMD nanocrystal systems such as MoS_2, $MoSe_2$, WS_2, and WSe_2.

1.4.4 Phase control of TMD nanocrystals

Reduction based

Like in the bulk, the metastable 2M phase of TMDs can be accessed via reduction-based methods. For instance, the reducing conditions that lead to the oleylammonium bound monolayers result in the metastable distorted octahedral structure.[122, 131-132, 135-136, 145-146] Upon oxidation and phase conversion to the 2H phase these ligands are removed from the surface as they are no longer needed for charge compensation.[136] Accessing metastable phases through a similar route can be used with ammonium,[137] other alkylammonium ligands,[131, 135] or ionic liquids[154] used to charge-stabilize the metastable phase.

The metastable phase can also be accessed by heterostructure formation between a metallic nanocrystal and TMDs. For instance, the growth of $MoSe_2$ onto gold nanocrystals results in the stabilization of the metastable phase, as electrons are easily transferred from the gold to $MoSe_2$.[155]

Kinetically Controlled

For many nanocrystal syntheses of WSe_2, it has been observed that the materials first nucleate in the metastable 2M phase and then convert to the thermodynamically favored 2H phase with time.[27, 143-144] This occurs over a broad range of metal and chalcogen precursors indicating

that many colloidal synthesis reactions fall within a kinetically controlled reaction regime. This is likely due to the comparatively low reaction temperatures used for solution phase reactions compared to traditional solid-state synthesis, and the broad range of precursors available. For instance, Sokolikova et. al has shown that synthesizing WSe_2 at 300 °C resulted in nanoflowers (Figure 1.11 a) of the 2M phase (Figure 1.11 b).[27] At this temperature the metastable phase was always obtained even with the use of various precursors with differing reactivity.[27] The metastable phase can be converted to the thermodynamically favored 2H phase by annealing the nanocrystals at 395 °C (Figure 1.11 c).[27]

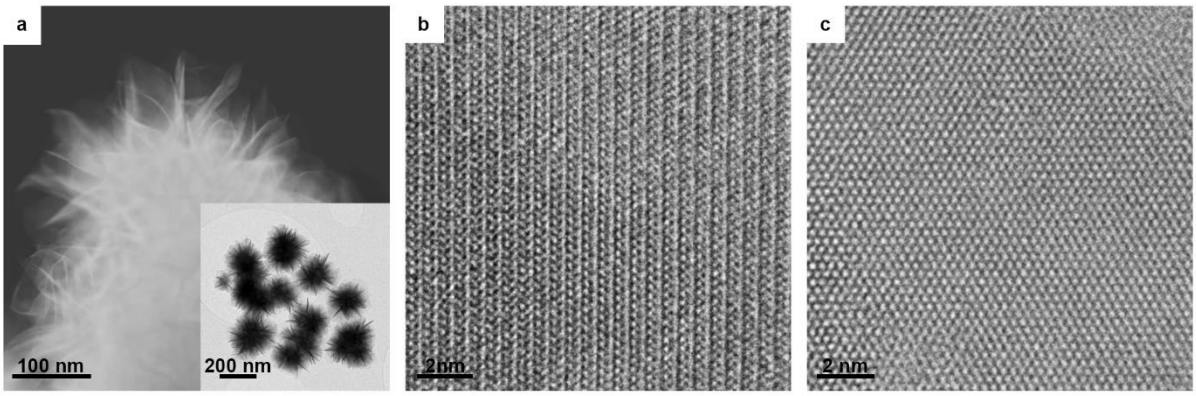

Figure 1. 11. (a) Annular dark-field scanning TEM image of single WSe_2 nanoflower. The inset shows an LRTEM image of multiple nanoflowers. **(b)** HRTEM image of as-synthesized nanoflowers. Lattice fringes show zigzag chains of tungsten atoms through the lattice indicating the metastable phase. **(c)** HRTEM image of nanocrystals annealed at 395 °C. The hexagonal arrangement of tungsten atoms indicates the thermodynamically preferred phase. Reproduced from ref [27].

Once in a kinetically controlled reaction regime prolonging the duration of the metastable phase can be tuned by controlling the reactivity of the precursors. For instance, in the synthesis of WSe_2 outlined in chapter 2, the slow reactivity in oleic acid leads to large amounts of 2M phase for greater amounts of time, while the syntheses in TOPO result in rapid phase conversion to the 2H phase. Given that both reactions are stopped after the same amount of time, slower reactivity would more likely isolate a kinetically favored product by allowing less time for reverse reactions,

such as nanocrystal dissolution or migration in the lattice. In contrast, a faster reaction would allow for sufficient time for the reaction to reach equilibrium and form the thermodynamically favored phase.[144] In other words, the rapid nucleation in TOPO may result in defect generation that facilitates atom migration in the lattice, or the fast reactivity may allow for the necessary time for the metastable nanocrystals to dissolve then nucleate and grow in the thermodynamically preferred phase, while the slow reactivity in oleic acid hinders both these processes.

Since controlling the extent of supersaturation is also a useful tool to enter kinetically controlled reaction regimes, we performed reactions at varying concentrations to synthesize WSe_2 (chapter 5). At high precursor concentrations, nanocrystals of an increased number of layers are produced with a markedly slower phase conversion process compared to the few-layer nanocrystals formed at lower concentrations. The precursor ratio was also varied and showed that increased concentrations of the selenium precursor yield slower phase conversion from the 2M phase. It is hard to completely disentangle increased layer number and increased selenium precursor concentration from one another, but likely both play a role in preventing phase conversion. Importantly, we also show that the phase conversion is going through a direct solid-state transition rather than through a solvent-mediated transition. This suggests that phase conversion is hindered by aspects that prevent atom migration in the lattice, such as an increased number of layers and fewer defects.

How layer number impacts phase conversion is further explored in chapter 6. When phosphine ligands are bound to the basal planes of WSe_2 and WS_2 nanocrystals very rapid phase conversion is observed compared to the few-layer nanocrystals. Reduction of the interlayer interactions from the bound phosphine ligands allows for facile atom migration in the lattice and thus increased amounts of the thermodynamically preferred phase.

1.5 Scope of the dissertation

This dissertation focuses on how colloidal synthesis can be used to control the size, shape/number of layers, and phase of TMD nanocrystals. As highlighted in section 1.4, chapter 2 will discuss how ligands used in the synthesis of WSe_2 nanocrystals can vary both size and phase. Chapter 3 highlights how the delayed reactivity of tungsten precursors can be exploited to produce W-based heterostructures. Chapter 4 details how controlling the CO labilization rate of the tungsten carbonyl precursor can be used to control the temperature at which WSe_2 nanocrystals of the metastable phase will nucleate. Chapter 5 describes a synthetic method to control the number of layers in WSe_2 nanocrystals, and how this morphology change impacts the phase conversion rate from the 2M phase to the 2H phase. Finally, chapter 6 discusses a method to synthesize monolayer TMD nanocrystals via tightly bound phosphine ligands at the basal plane.

1.6 Acknowledgements

Chapter 1, in part, is currently being prepared for submission for publication of the material. The dissertation author was the primary author of this paper and gratefully acknowledges the contributions of coauthor Alina M. Schimpf.

1.7 References

1. Wilson, J. A.; Yoffe, A. D., Transition Metal Dichalcogenides Discussion and Interpretation of Observed Optical, Electrical and Structural Properties. *Adv Phys* **1969,** *18* (73), 193-+.

2. Chhowalla, M.; Shin, H. S.; Eda, G.; Li, L. J.; Loh, K. P.; Zhang, H., The chemistry of two-dimensional layered transition metal dichalcogenide nanosheets. *Nat Chem* **2013,** *5* (4), 263-275.

3. Manzeli, S.; Ovchinnikov, D.; Pasquier, D.; Yazyev, O. V.; Kis, A., 2D transition metal dichalcogenides. *Nat Rev Mater* **2017,** *2* (8).

4. Whittingham, M. S., Chemistry of Intercalation Compounds - Metal Guests in Chalcogenide Hosts. *Prog Solid State Ch* **1978,** *12* (1), 41-99.

5. Liu, F.; Wu, W. J.; Bai, Y. S.; Chae, S. H.; Li, Q. Y.; Wang, J.; Hone, J.; Zhu, X. Y., Disassembling 2D van der Waals crystals into macroscopic monolayers and reassembling into artificial lattices. *Science* **2020,** *367* (6480), 903-+.

6. Zhang, Q. Y.; Mei, L.; Cao, X. H.; Tang, Y. X.; Zeng, Z. Y., Intercalation and exfoliation chemistries of transition metal dichalcogenides. *J Mater Chem A* **2020,** *8* (31), 15417-15444.

7. Li, H.; Wu, J. M. T.; Yin, Z. Y.; Zhang, H., Preparation and Applications of Mechanically Exfoliated Single-Layer and Multi layer MoS2 and WSe2 Nanosheets. *Accounts Chem Res* **2014,** *47* (4), 1067-1075.

8. Mattheis.Lf, Energy-Bands for 2h-Nbse2 and 2h-Mos2. *Phys Rev Lett* **1973,** *30* (17), 784-787.

9. Sun, Y. J.; Wang, D.; Shuai, Z. G., Indirect-to-Direct Band Gap Crossover in Few-Layer Transition Metal Dichalcogenides: A Theoretical Prediction. *J Phys Chem C* **2016,** *120* (38), 21866-21870.

10. Pandey, S. K.; Das, R.; Mahadevan, P., Layer-Dependent Electronic Structure Changes in Transition Metal Dichalcogenides: The Microscopic Origin. *Acs Omega* **2020,** *5* (25), 15169-15176.

11. Ajayan, P.; Kim, P.; Banerjee, K., Two-dimensional van der Waals materials. *Phys Today* **2016,** *69* (9), 39-44.

12. Schaibley, J. R.; Yu, H. Y.; Clark, G.; Rivera, P.; Ross, J. S.; Seyler, K. L.; Yao, W.; Xu, X. D., Valleytronics in 2D materials. *Nat Rev Mater* **2016,** *1* (11).

13. Fang, Y.; Pan, J.; Zhang, D.; Wang, D.; Hirose, H. T.; Terashima, T.; Uji, S.; Yuan, Y.; Li, W.; Tian, Z.; Xue, J.; Ma, Y.; Zhao, W.; Xue, Q.; Mu, G.; Zhang, H.; Huang, F., Discovery

of Superconductivity in 2M WS2 with Possible Topological Surface States. *Adv Mater* **2019,** *31* (30), e1901942.

14. Qian, X. F.; Liu, J. W.; Fu, L.; Li, J., Quantum spin Hall effect in two-dimensional transition metal dichalcogenides. *Science* **2014,** *346* (6215), 1344-1347.

15. Li, Y. W.; Zheng, H. J.; Fang, Y. Q.; Zhang, D. Q.; Chen, Y. J.; Chen, C.; Liang, A. J.; Shi, W. J.; Pei, D.; Xu, L. X.; Liu, S.; Pan, J.; Lu, D. H.; Hashimoto, M.; Barinov, A.; Jung, S. W.; Cacho, C.; Wang, M. X.; He, Y.; Fu, L.; Zhang, H. J.; Huang, F. Q.; Yang, L. X.; Liu, Z. K.; Chen, Y. L., Observation of topological superconductivity in a stoichiometric transition metal dichalcogenide 2M-WS2. *Nat Commun* **2021,** *12* (1).

16. Ugeda, M. M.; Pulkin, A.; Tang, S. J.; Ryu, H.; Wu, Q. S.; Zhang, Y.; Wong, D.; Pedramrazi, Z.; Martin-Recio, A.; Chen, Y.; Wang, F.; Shen, Z. X.; Mo, S. K.; Yazyev, O. V.; Crommie, M. F., Observation of topologically protected states at crystalline phase boundaries in single-layer WSe2. *Nat Commun* **2018,** *9*.

17. Martinolich, A. J.; Neilson, J. R., Toward Reaction-by-Design: Achieving Kinetic Control of Solid State Chemistry with Metathesis. *Chem Mater* **2017,** *29* (2), 479-489.

18. Kanatzidis, M. G.; Poeppelmeier, K. R., Report from the third workshop on future directions of solid-state chemistry: The status of solid-state chemistry and its impact in the physical sciences. *Prog Solid State Ch* **2008,** *36* (1-2), 1-133.

19. Xia, J.; Wang, J.; Chao, D. L.; Chen, Z.; Liu, Z.; Kuo, J. L.; Yan, J. X.; Shen, Z. X., Phase evolution of lithium intercalation dynamics in 2H-MoS2. *Nanoscale* **2017,** *9* (22), 7533-7540.

20. Sun, L. F.; Yan, X. X.; Zheng, J. Y.; Yu, H. D.; Lu, Z. X.; Gao, S. P.; Liu, L. N.; Pan, X. Q.; Wang, D.; Wang, Z. G.; Wang, P.; Jiao, L. Y., Layer-Dependent Chemically Induced Phase Transition of Two-Dimensional MoS2. *Nano Lett* **2018,** *18* (6), 3435-3440.

21. Cho, S.; Kim, S.; Kim, J. H.; Zhao, J.; Seok, J.; Keum, D. H.; Baik, J.; Choe, D. H.; Chang, K. J.; Suenaga, K.; Kim, S. W.; Lee, Y. H.; Yang, H., Phase patterning for ohmic homojunction contact in MoTe2. *Science* **2015,** *349* (6248), 625-628.

22. Zhu, J. Q.; Wang, Z. C.; Yu, H.; Li, N.; Zhang, J.; Meng, J. L.; Liao, M. Z.; Zhao, J.; Lu, X. B.; Du, L. J.; Yang, R.; Shi, D.; Jiang, Y.; Zhang, G. Y., Argon Plasma Induced Phase Transition in Monolayer MoS2. *J Am Chem Soc* **2017,** *139* (30), 10216-10219.

23. Yin, X. M.; Wang, Q. X.; Cao, L.; Tang, C. S.; Luo, X.; Zheng, Y. J.; Wong, L. M.; Wang, S. J.; Quek, S. Y.; Zhang, W. J.; Rusydi, A.; Wee, A. T. S., Tunable inverted gap in monolayer quasi-metallic MoS2 induced by strong charge-lattice coupling. *Nat Commun* **2017,** *8*.

24. Song, S.; Keum, D. H.; Cho, S.; Perello, D.; Kim, Y.; Lee, Y. H., Room Temperature Semiconductor-Metal Transition of MoTe2 Thin Films Engineered by Strain. *Nano Lett* **2016,** *16* (1), 188-193.

25. Tong, X.; Qi, Y. H.; Chen, J.; Wang, N.; Xu, Q., Supercritical CO2-Assisted Reverse-Micelle-Induced Solution-Phase Fabrication of Two-Dimensional Metallic 1T-MoS2 and 1T-WS2. *Chemnanomat* **2017,** *3* (7), 466-471.

26. Tappan, B. A.; Brutchey, R. L., Polymorphic Metastability in Colloidal Semiconductor Nanocrystals. *Chemnanomat* **2020,** *6* (11), 1567-1588.

27. Sokolikova, M. S.; Sherrell, P. C.; Palczynski, P.; Bemmer, V. L.; Mattevi, C., Direct solution-phase synthesis of 1T' WSe2 nanosheets. *Nat Commun* **2019,** *10* (1), 712.

28. Soderholm, L.; Mitchell, J. F., Perspective: Toward "synthesis by design": Exploring atomic correlations during inorganic materials synthesis. *Apl Mater* **2016,** *4* (5).

29. Wang, Y. W.; He, J. T.; Liu, C. C.; Chong, W. H.; Chen, H. Y., Thermodynamics versus Kinetics in Nanosynthesis. *Angew Chem Int Edit* **2015,** *54* (7), 2022-2051.

30. Washington, A. L.; Foley, M. E.; Cheong, S.; Quffa, L.; Breshike, C. J.; Watt, J.; Tilley, R. D.; Strouse, G. F., Ostwald's Rule of Stages and Its Role in CdSe Quantum Dot Crystallization. *J Am Chem Soc* **2012,** *134* (41), 17046-17052.

31. Cardew, P. T.; Davey, R. J., The Kinetics of Solvent-Mediated Phase-Transformations. *P Roy Soc Lond a Mat* **1985,** *398* (1815), 415-428.

32. Gao, Y.; Peng, X. G., Crystal Structure Control of CdSe Nanocrystals in Growth and Nucleation: Dominating Effects of Surface versus Interior Structure. *J Am Chem Soc* **2014,** *136* (18), 6724-6732.

33. Goodenough, J. B., Band Model for Transition-Metal Chalcogenides Having Layer Structures with Occupied Trigonal-Bipyramidal Sites. *Mater Res Bull* **1968,** *3* (5), 409-+.

34. Voiry, D.; Mohite, A.; Chhowalla, M., Phase engineering of transition metal dichalcogenides. *Chem Soc Rev* **2015,** *44* (9), 2702-2712.

35. Huisman, R.; Dejonge, R.; Haas, C.; Jellinek, F., Trigonal-Prismatic Coordination in Solid Compounds of Transition Metals. *J Solid State Chem* **1971,** *3* (1), 56-&.

36. Ding, X.; Zhang, S.; Zhao, M.; Xiang, Y.; Zhang, K. H. L.; Zu, X. T.; Li, S.; Qiao, L., NbS2 : A Promising p-Type Ohmic Contact for Two-Dimensional Materials. *Phys Rev Appl* **2019,** *12* (6).

37. Dickinson, R. G.; Pauling, L., The crystal structure of molybdenite. *J Am Chem Soc* **1923,** *45*, 1466-1471.

38. Schutte, W. J.; Deboer, J. L.; Jellinek, F., Crystal-Structures of Tungsten Disulfide and Diselenide. *J Solid State Chem* **1987,** *70* (2), 207-209.

39. James, P. B.; Lavik, M. T., The crystal structure of MoSe2. *Acta Crystallographica* **1963,** *16* (11), 1183-1183.

40. Puotinen, D.; Newnham, R. E., The crystal structure of MoTe2. *Acta Crystallographica* **1961,** *14* (6), 691-692.

41. Dawson, W. G.; Bullett, D. W., Electronic-Structure and Crystallography of Mote2 and Wte2. *J Phys C Solid State* **1987,** *20* (36), 6159-6174.

42. Bell, R. E.; Herfert, R. E., Preparation and Characterization of a New Crystalline Form of Molybdenum Disulfide. *J Am Chem Soc* **1957,** *79* (13), 3351-3354.

43. Towle, L. C.; Oberbeck, V.; Brown, B. E.; Stajdoha.Re, Molybdenum Diselenide - Rhombohedral High Pressure - High Temperature Polymorph. *Science* **1966,** *154* (3751), 895-&.

44. Strachan, J.; Masters, A. F.; Maschmeyer, T., 3R-MoS2 in Review: History, Status, and Outlook. *Acs Appl Energ Mater* **2021,** *4* (8), 7405-7418.

45. Frisenda, R.; Niu, Y.; Gant, P.; Munoz, M.; Castellanos-Gomez, A., Naturally occurring van der Waals materials. *Npj 2d Mater Appl* **2020,** *4* (1).

46. Duerloo, K. A. N.; Li, Y.; Reed, E. J., Structural phase transitions in two-dimensional Mo- and W-dichalcogenide monolayers. *Nat Commun* **2014,** *5*.

47. Lai, Z.; He, Q.; Tran, T. H.; Repaka, D. V. M.; Zhou, D. D.; Sun, Y.; Xi, S.; Li, Y.; Chaturvedi, A.; Tan, C.; Chen, B.; Nam, G. H.; Li, B.; Ling, C.; Zhai, W.; Shi, Z.; Hu, D.; Sharma, V.; Hu, Z.; Chen, Y.; Zhang, Z.; Yu, Y.; Renshaw Wang, X.; Ramanujan, R. V.; Ma, Y.; Hippalgaonkar, K.; Zhang, H., Metastable 1T'-phase group VIB transition metal dichalcogenide crystals. *Nat Mater* **2021,** *20* (8), 1113-1120.

48. Fang, Y. Q.; Dong, Q.; Pan, J.; Liu, H. Y.; Liu, P.; Sun, Y. Y.; Li, Q. J.; Zhao, W.; Liu, B. B.; Huang, F. Q., Observation of superconductivity in pressurized 2M WSe2 crystals. *J Mater Chem C* **2019,** *7* (28), 8551-8555.

49. Brown, B. E., The crystal structures of WTe2 and high-temperature MoTe2. *Acta Crystallographica* **1966,** *20* (2), 268-274.

50. Mentzen, B. F.; Sienko, M. J., Preparation and X-Ray Study of Mixed-Anion Tungsten Dichalcogenides. *Inorg Chem* **1976,** *15* (9), 2198-2202.

51. Tian, C.; Gao, Y. P.; Tian, F. B.; Wang, X.; Zhang, Z. H.; Duan, D. F.; Huang, X. L.; Cui, T., Dimensionality switching and superconductivity transition in dense 1T-HfSe2. *Phys Rev B* **2022,** *105* (18).

52. Pal, S.; Debnath, K.; Gupta, S. N.; Harnagea, L.; Muthu, D. V. S.; Waghmare, U. V.; Sood, A. K., Pressure-induced 1T to 3R structural phase transition in metallic VSe2: X-ray diffraction and first-principles theory. *Phys Rev B* **2021,** *104* (1).

53. Hu, K.; Lian, J. C.; Zhu, L.; Chen, Q. J.; Xie, S. Y., Prediction of Fe2P-type TiTe2 under pressure. *Phys Rev B* **2020,** *101* (13).

54. Choe, D. H.; Sung, H. J.; Chang, K. J., Understanding topological phase transition in monolayer transition metal dichalcogenides. *Phys Rev B* **2016,** *93* (12).

55. Chen, K. Y.; Deng, J. K.; Shi, Q.; Ding, X. D.; Sun, J.; Yang, S.; Liu, J. Z., Charge doping induced reversible multistep structural phase transitions and electromechanical actuation in two-dimensional 1T '-MoS2. *Nanoscale* **2020,** *12* (23), 12541-12550.

56. Keum, D. H.; Cho, S.; Kim, J. H.; Choe, D. H.; Sung, H. J.; Kan, M.; Kang, H.; Hwang, J. Y.; Kim, S. W.; Yang, H.; Chang, K. J.; Lee, Y. H., Bandgap opening in few-layered monoclinic MoTe2. *Nat Phys* **2015,** *11* (6), 482-U144.

57. Pasquier, D.; Yazyev, O. V., Unified picture of lattice instabilities in metallic transition metal dichalcogenides. *Phys Rev B* **2019,** *100* (20).

58. Jobic, S.; Deniard, P.; Brec, R.; Rouxel, J.; Jouanneaux, A.; Fitch, A. N., Crystal and Electronic Band-Structure of Irte2 - Evidence of Anionic Bonds in a Cdi2-Like Arrangement. *Z Anorg Allg Chem* **1991,** *598* (7-8), 199-215.

59. Canadell, E.; Jobic, S.; Brec, R.; Rouxel, J.; Whangbo, M. H., Importance of Short Interlayer Te-Te Contacts for the Structural Distortions and Physical-Properties of Cdi2-Type Layered Transition-Metal Ditellurides. *J Solid State Chem* **1992,** *99* (1), 189-199.

60. Mar, A.; Jobic, S.; Ibers, J. A., Metal Metal Vs Tellurium Tellurium Bonding in Wte2 and Its Ternary Variants Tairte4 and Nbirte4. *J Am Chem Soc* **1992,** *114* (23), 8963-8971.

61. Wang, Z. G., 2H -> 1T phase transformation in Janus monolayer MoSSe and MoSTe: an efficient hole injection contact for 2H-MoS2. *J Mater Chem C* **2018,** *6* (47), 13000-13005.

62. Enyashin, A. N.; Yadgarov, L.; Houben, L.; Popov, I.; Weidenbach, M.; Tenne, R.; Bar-Sadan, M.; Seifert, G., New Route for Stabilization of 1T-WS2 and MoS2 Phases. *J Phys Chem C* **2011,** *115* (50), 24586-24591.

63. Gao, G. P.; Jiao, Y.; Ma, F. X.; Jiao, Y. L.; Waclawik, E.; Du, A. J., Charge Mediated Semiconducting-to-Metallic Phase Transition in Molybdenum Disulfide Monolayer and Hydrogen Evolution Reaction in New 1T' Phase. *J Phys Chem C* **2015,** *119* (23), 13124-13128.

64. Gamble, F. R.; Osiecki, J. H.; Cais, M.; Pisharody, R.; Disalvo, F. J.; Geballe, T. H., Intercalation complexes of lewis bases and layered sulfides: a large class of new superconductors. *Science* **1971,** *174* (4008), 493-7.

65. Kuo, D. Y.; Cossairt, B. M., Direct intercalation of MoS2 and WS2 thin films by vacuum filtration. *Mater Horiz* **2022,** *9* (1), 360-367.

66. Heising, J.; Kanatzidis, M. G., Exfoliated and restacked MoS2 and WS2: Ionic or neutral species? Encapsulation and ordering of hard electropositive cations. *J Am Chem Soc* **1999,** *121* (50), 11720-11732.

67. Rocquefelte, X.; Bouessay, I.; Boucher, F.; Gressier, P.; Ouvrard, G., Synergetic theoretical and experimental structure determination of nanocrystalline materials: study of LiMoS2. *J Solid State Chem* **2003,** *175* (2), 380-383.

68. Heising, J.; Kanatzidis, M. G., Structure of restacked MoS2 and WS2 elucidated by electron crystallography. *J Am Chem Soc* **1999,** *121* (4), 638-643.

69. Petkov, V.; Billinge, S. J. L.; Heising, J.; Kanatzidis, M. G., Application of atomic pair distribution function analysis to materials with intrinsic disorder. Three-dimensional structure of exfoliated-restacked WS2: Not just a random turbostratic assembly of layers. *J Am Chem Soc* **2000,** *122* (47), 11571-11576.

70. Rocquefelte, X.; Boucher, F.; Gressier, P.; Ouvrard, G.; Blaha, P.; Schwarz, K., Mo cluster formation in the intercalation compound LiMoS2. *Phys Rev B* **2000,** *62* (4), 2397-2400.

71. Tan, S. J.; Abdelwahab, I.; Ding, Z.; Zhao, X.; Yang, T.; Loke, G. Z.; Lin, H.; Verzhbitskiy, I.; Poh, S. M.; Xu, H.; Nai, C. T.; Zhou, W.; Eda, G.; Jia, B.; Loh, K. P., Chemical Stabilization of 1T' Phase Transition Metal Dichalcogenides with Giant Optical Kerr Nonlinearity. *J Am Chem Soc* **2017,** *139* (6), 2504-2511.

72. Leng, K.; Chen, Z. X.; Zhao, X. X.; Tang, W.; Tian, B. B.; Nai, C. T.; Zhou, W.; Loh, K. P., Phase Restructuring in Transition Metal Dichalcogenides for Highly Stable Energy Storage. *Acs Nano* **2016,** *10* (10), 9208-9215.

73. Ambrosi, A.; Sofer, Z.; Pumera, M., 2H -> 1T phase transition and hydrogen evolution activity of MoS2, MoSe2, WS2 and WSe2 strongly depends on the MX2 composition. *Chem Commun* **2015,** *51* (40), 8450-8453.

74. Petkov, V.; Billinge, S. J. L.; Larson, P.; Mahanti, S. D.; Vogt, T.; Rangan, K. K.; Kanatzidis, M. G., Structure of nanocrystalline materials using atomic pair distribution function analysis: Study of LiMoS2. *Phys Rev B* **2002,** *65* (9).

75. Ushakov, I. E.; Goloveshkin, A. S.; Lenenko, N. D.; Ezernitskaya, M. G.; Korlyukov, A. A.; Zaikovskii, V. I.; Golub, A. S., Hydrogen Bond-Driven Self-Assembly between Single-Layer MoS2 and Alkyldiamine Molecules. *Cryst Growth Des* **2018,** *18* (9), 5116-5123.

76. Dhakal, K. P.; Ghimire, G.; Chung, K.; Duong, D. L.; Kim, S. W.; Kim, J., Probing Multiphased Transition in Bulk MoS2 by Direct Electron Injection. *Acs Nano* **2019,** *13* (12), 14437-14446.

77. Liu, L.; Wu, J.; Wu, L.; Ye, M.; Liu, X.; Wang, Q.; Hou, S.; Lu, P.; Sun, L.; Zheng, J.; Xing, L.; Gu, L.; Jiang, X.; Xie, L.; Jiao, L., Phase-selective synthesis of 1T' MoS2 monolayers and heterophase bilayers. *Nat Mater* **2018,** *17* (12), 1108-1114.

78. Zhang, X.; Zhang, Y. Y.; Zhang, Y.; Jiang, W. J.; Zhang, Q. H.; Yang, Y. G.; Gu, L.; Hu, J. S.; Wan, L. J., Phase-Controlled Synthesis of 1T-MoSe2/NiSe Heterostructure Nanowire Arrays via Electronic Injection for Synergistically Enhanced Hydrogen Evolution. *Small Methods* **2019,** *3* (2).

79. Yu, Y.; Nam, G. H.; He, Q.; Wu, X. J.; Zhang, K.; Yang, Z.; Chen, J.; Ma, Q.; Zhao, M.; Liu, Z.; Ran, F. R.; Wang, X.; Li, H.; Huang, X.; Li, B.; Xiong, Q.; Zhang, Q.; Liu, Z.; Gu, L.; Du, Y.; Huang, W.; Zhang, H., High phase-purity 1T'-MoS2- and 1T'-MoSe2-layered crystals. *Nat Chem* **2018,** *10* (6), 638-643.

80. Gao, B.; Zhao, Y. W.; Du, X. Y.; Li, D.; Ding, S. J.; Li, Y. H.; Xiao, C. H.; Song, Z. X., Electron injection induced phase transition of 2H to 1T MoS2 by cobalt and nickel substitutional doping. *Chem Eng J* **2021,** *411*.

81. Calandra, M., Chemically exfoliated single-layer MoS2: Stability, lattice dynamics, and catalytic adsorption from first principles. *Phys Rev B* **2013,** *88* (24).

82. Liu, Y. C.; Wang, V.; Xia, M. G.; Zhang, S. L., First-principles study on structural, thermal, mechanical and dynamic stability of T'-MoS2. *J Phys-Condens Mat* **2017,** *29* (9).

83. Litwin, P. M.; Sales, M. G.; Nilsson, V.; Balachandran, P. V.; Constantin, C.; McDonnell, S., The effect of growth temperature and metal-to-chalcogen on the growth of WSe2 by molecular beam epitaxy. *Proc Spie* **2019,** *11085*.

84. Murray, C. B.; Norris, D. J.; Bawendi, M. G., Synthesis and Characterization of Nearly Monodisperse Cde (E = S, Se, Te) Semiconductor Nanocrystallites. *J Am Chem Soc* **1993,** *115* (19), 8706-8715.

85. Lamer, V. K.; Dinegar, R. H., Theory, Production and Mechanism of Formation of Monodispersed Hydrosols. *J Am Chem Soc* **1950,** *72* (11), 4847-4854.

86. Whitehead, C. B.; Ozkar, S.; Finke, R. G., LaMer's 1950 model of particle formation: a review and critical analysis of its classical nucleation and fluctuation theory basis, of competing models and mechanisms for phase-changes and particle formation, and then of its application to silver halide, semiconductor, metal, and metal-oxide nanoparticles. *Mater Adv* **2021,** *2* (1), 186-235.

87. Owen, J. S.; Chan, E. M.; Liu, H. T.; Alivisatos, A. P., Precursor Conversion Kinetics and the Nucleation of Cadmium Selenide Nanocrystals. *J Am Chem Soc* **2010,** *132* (51), 18206-18213.

88. Bennett, E.; Greenberg, M. W.; Jordan, A. J.; Hamachi, L. S.; Banerjee, S.; Billinge, S. J. L.; Owen, J. S., Size Dependent Optical Properties and Structure of ZnS Nanocrystals Prepared from a Library of Thioureas. *Chem Mater* **2022,** *34* (2), 706-717.

89. Campos, M. P.; Hendricks, M. P.; Beecher, A. N.; Wslravens, W.; Swain, R. A.; Cleyeland, G. T.; Hens, Z.; Sfeir, M. Y.; Owen, J. S., A Library of Selenourea Precursors to PbSe Nanocrystals with Size Distributions near the Homogeneous Limit. *J Am Chem Soc* **2017,** *139* (6), 2296-2305.

90. Hamachi, L. S.; Plante, I. J. L.; Coryell, A. C.; De Roo, J.; Owen, J. S., Kinetic Control over CdS Nanocrystal Nucleation Using a Library of Thiocarbonates, Thiocarbamates, and Thioureas. *Chem Mater* **2017,** *29* (20), 8711-8719.

91. Hendricks, M. P.; Campos, M. P.; Cleveland, G. T.; Jen-La Plante, I.; Owen, J. S., A tunable library of substituted thiourea precursors to metal sulfide nanocrystals. *Science* **2015,** *348* (6240), 1226-1230.

92. Cossairt, B. M., Shining Light on Indium Phosphide Quantum Dots: Understanding the Interplay among Precursor Conversion, Nucleation, and Growth. *Chem Mater* **2016,** *28* (20), 7181-7189.

93. Zhang, T. H.; Liu, X. Y., Nucleation: What Happens at the Initial Stage? *Angew Chem Int Edit* **2009,** *48* (7), 1308-1312.

94. Lee, J.; Yang, J.; Kwon, S. G.; Hyeon, T., Nonclassical nucleation and growth of inorganic nanoparticles. *Nat Rev Mater* **2016,** *1* (8).

95. Kudera, S.; Zanella, M.; Giannini, C.; Rizzo, A.; Li, Y. Q.; Gigli, G.; Cingolani, R.; Ciccarella, G.; Spahl, W.; Parak, W. J.; Manna, L., Sequential growth of magic-size CdSe nanocrystals. *Advanced Materials* **2007,** *19* (4), 548-+.

96. Allen, P. M.; Walker, B. J.; Bawendi, M. G., Mechanistic Insights into the Formation of InP Quantum Dots. *Angew Chem Int Edit* **2010,** *49* (4), 760-762.

97. Gary, D. C.; Flowers, S. E.; Kaminsky, W.; Petrone, A.; Li, X. S.; Cossairt, B. M., Single-Crystal and Electronic Structure of a 1.3 nm Indium Phosphide Nanocluster. *J Am Chem Soc* **2016,** *138* (5), 1510-1513.

98. Gary, D. C.; Terban, M. W.; Billinge, S. J. L.; Cossairt, B. M., Two-Step Nucleation and Growth of InP Quantum Dots via Magic-Sized Cluster Intermediates. *Chem Mater* **2015,** *27* (4), 1432-1441.

99. Lifshitz, I. M.; Slyozov, V. V., The Kinetics of Precipitation from Supersaturated Solid Solutions. *J Phys Chem Solids* **1961,** *19* (1-2), 35-50.

100. Peng, X. G.; Wickham, J.; Alivisatos, A. P., Kinetics of II-VI and III-V colloidal semiconductor nanocrystal growth: "Focusing" of size distributions. *J Am Chem Soc* **1998,** *120* (21), 5343-5344.

101. Clark, M. D.; Kumar, S. K.; Owen, J. S.; Chan, E. M., Focusing Nanocrystal Size Distributions via Production Control. *Nano Lett* **2011,** *11* (5), 1976-1980.

102. Sugimoto, T., Preparation of Monodispersed Colloidal Particles. *Adv Colloid Interfac* **1987,** *28* (1), 65-108.

103. Marks, L. D.; Peng, L., Nanoparticle shape, thermodynamics and kinetics. *J Phys-Condens Mat* **2016,** *28* (5).

104. Yin, Y.; Alivisatos, A. P., Colloidal nanocrystal synthesis and the organic-inorganic interface. *Nature* **2005,** *437* (7059), 664-670.

105. Smith, J. D.; Scanlan, M. M.; Chen, A. N.; Ashberry, H. M.; Skrabalak, S. E., Kinetically Controlled Sequential Seeded Growth: A General Route to Crystals with Different Hierarchies. *Acs Nano* **2020,** *14* (11), 15953-15961.

106. Strach, M.; Mantella, V.; Pankhurst, J. R.; Iyengar, P.; Loiudice, A.; Das, S.; Corminboeuf, C.; van Beek, W.; Buonsanti, R., Insights into Reaction Intermediates to Predict Synthetic Pathways for Shape-Controlled Metal Nanocrystals. *J Am Chem Soc* **2019,** *141* (41), 16312-16322.

107. Zhao, M.; Chen, Z. T.; Shi, Y. F.; Hood, Z. D.; Lyu, Z. H.; Xie, M. H.; Chi, M. F.; Xia, Y. A., Kinetically Controlled Synthesis of Rhodium Nanocrystals with Different Shapes and a Comparison Study of Their Thermal and Catalytic Properties. *J Am Chem Soc* **2021,** *143* (16), 6293-6302.

108. ten Wolde, P. R.; Frenkel, D., Homogeneous nucleation and the Ostwald step rule. *Phys Chem Chem Phys* **1999,** *1* (9), 2191-2196.

109. McHale, J. M.; Auroux, A.; Perrotta, A. J.; Navrotsky, A., Surface energies and thermodynamic phase stability in nanocrystalline aluminas. *Science* **1997,** *277* (5327), 788-791.

110. Sohnel, O., Electrolyte Crystal Aqueous-Solution Interfacial-Tensions from Crystallization Data. *J Cryst Growth* **1982,** *57* (1), 101-108.

111. Black, J. F. B.; Cardew, P. T.; Cruz-Cabeza, A. J.; Davey, R. J.; Gilks, S. E.; Sullivan, R. A., Crystal nucleation and growth in a polymorphic system: Ostwald's rule, p-aminobenzoic acid and nucleation transition states. *Crystengcomm* **2018,** *20* (6), 768-776.

112. Davey, R. J.; Cardew, P. T.; Mcewan, D.; Sadler, D. E., Rate Controlling Processes in Solvent-Mediated Phase-Transformations. *J Cryst Growth* **1986,** *79* (1-3), 648-653.

113. Shimpi, J. R.; Sidhaye, D. S.; Prasad, B. L. V., Digestive Ripening: A Fine Chemical Machining Process on the Nanoscale. *Langmuir* **2017,** *33* (38), 9491-9507.

114. Li, Z.; Peng, X. G., Size/Shape-Controlled Synthesis of Colloidal CdSe Quantum Disks: Ligand and Temperature Effects. *J Am Chem Soc* **2011,** *133* (17), 6578-6586.

115. Lin, H. H.; Wang, C. X.; Wu, J. P.; Xu, Z. Z.; Huang, Y. J.; Zhang, C., Colloidal synthesis of MoS2 quantum dots: size-dependent tunable photoluminescence and bioimaging. *New J Chem* **2015,** *39* (11), 8492-8497.

116. Pang, Y. P.; Uddin, M. N.; Chen, W.; Javaid, S.; Barker, E.; Li, Y. G.; Suvorova, A.; Saunders, M.; Yin, Z. Y.; Jia, G. H., Colloidal Single-Layer Photocatalysts for Methanol-Storable Solar H-2 Fuel. *Advanced Materials* **2019,** *31* (49).

117. Zhou, M.; Zhang, Z. L.; Huang, K. K.; Shi, Z.; Xie, R. G.; Yang, W. S., Colloidal preparation and electrocatalytic hydrogen production of MoS2 and WS2 nanosheets with controllable lateral sizes and layer numbers. *Nanoscale* **2016,** *8* (33), 15262-15272.

118. Li, X.; Tang, A. W.; Li, J. T.; Guan, L.; Dong, G. Y.; Teng, F., Heating-up Synthesis of MoS2 Nanosheets and Their Electrical Bistability Performance. *Nanoscale Res Lett* **2016,** *11*.

119. Son, D.; Chae, S. I.; Kim, M.; Choi, M. K.; Yang, J.; Park, K.; Kale, V. S.; Koo, J. H.; Choi, C.; Lee, M.; Kim, J. H.; Hyeon, T.; Kim, D. H., Colloidal Synthesis of Uniform-Sized Molybdenum Disulfide Nanosheets for Wafer-Scale Flexible Nonvolatile Memory. *Advanced Materials* **2016,** *28* (42), 9326-+.

120. Gong, Q. F.; Cheng, L.; Liu, C. H.; Zhang, M.; Feng, Q. L.; Ye, H. L.; Zeng, M.; Xie, L. M.; Liu, Z.; Li, Y. G., Ultrathin MoS2(1-x)Se2x Alloy Nanoflakes For Electrocatalytic Hydrogen Evolution Reaction. *Acs Catal* **2015,** *5* (4), 2213-2219.

121. Barrera, D.; Wang, Q. X.; Lee, Y. J.; Cheng, L. X.; Kim, M. J.; Kim, J.; Hsu, J. W. P., Solution synthesis of few-layer 2H MX2 (M = Mo, W; X = S, Se). *J Mater Chem C* **2017,** *5* (11), 2859-2864.

122. Liu, Z. Q.; Nie, K. K.; Qu, X. Y.; Li, X. H.; Li, B. J.; Yuan, Y. L.; Chong, S. K.; Liu, P.; Li, Y. G.; Yin, Z. Y.; Huang, W., General Bottom-Up Colloidal Synthesis of Nano-MonolayerTransition-Metal Dichalcogenides with High 1T '-Phase Purity. *J Am Chem Soc* **2022,** *144* (11), 4863-4873.

123. Cho, Y.; Le, T. A.; Kim, H.; Hong, Y.; Hwang, H.; Park, G. H.; Seo, S.; Lee, H., Unveiling surface charge on chalcogen atoms toward the high aspect-ratio colloidal growth of two-dimensional transition metal chalcogenides. *Nanoscale* **2021,** *13* (2), 1291-1302.

124. Sun, D.; Feng, S. M.; Terrones, M.; Schaak, R. E., Formation and Interlayer Decoupling of Colloidal MoSe2 Nanoflowers. *Chem Mater* **2015,** *27* (8), 3167-3175.

125. Jung, W.; Lee, S.; Yoo, D.; Jeong, S.; Miro, P.; Kuc, A.; Heine, T.; Cheon, J., Colloidal synthesis of single-layer MSe2 (M = Mo, W) nanosheets via anisotropic solution-phase growth approach. *J Am Chem Soc* **2015,** *137* (23), 7266-9.

126. Guo, W. B.; Chen, Y. Z.; Wang, L. S.; Xu, J.; Zeng, D. Q.; Peng, D. L., Colloidal synthesis of MoSe2 nanonetworks and nanoflowers with efficient electrocatalytic hydrogen-evolution activity. *Electrochim Acta* **2017,** *231*, 69-76.

127. Zhou, X. L.; Jiang, J.; Ding, T.; Zhang, J. J.; Pan, B. C.; Zuo, J.; Yang, Q., Fast colloidal synthesis of scalable Mo-rich hierarchical ultrathin MoSe2-x nanosheets for high-performance hydrogen evolution. *Nanoscale* **2014,** *6* (19), 11046-11051.

128. Hassan, M. S.; Jana, A.; Gahlawat, S.; Bhandary, N.; Bera, S.; Ingole, P. P.; Sapra, S., Colloidally synthesized defect-rich MoSe2 nanosheets for superior catalytic activity. *B Mater Sci* **2019,** *42* (2).

129. Ndala, Z.; Shumbula, N.; Nkabinde, S.; Kolokoto, T.; Nchoe, O.; Shumbula, P.; Tetana, Z. N.; Linganiso, E. C.; Gqoba, S. S.; Moloto, N., Evaluating the Effect of Varying the Metal Precursor in the Colloidal Synthesis of MoSe2 Nanomaterials and Their Application as Electrodes in the Hydrogen Evolution Reaction. *Nanomaterials-Basel* **2020,** *10* (9).

130. Niebur A, S. A., Haizmann P, Strolka O, Rudolph D, Peisert H, Lauth J, Untangling the Intertwined: Metallic to Semiconducting Phase Transition in Colloidal MoS2 Nanoplatelets and Nanosheets. *ChemRxiv* **2022,** (Cambridge: Cambridge Open Engage).

131. Jiang, M.; Zhang, J. J.; Wu, M. H.; Jian, W. J.; Xue, H. T.; Ng, T. W.; Lee, C. S.; Xu, J., Synthesis of 1T-MoSe2 ultrathin nanosheets with an expanded interlayer spacing of 1.17 nm for efficient hydrogen evolution reaction. *J Mater Chem A* **2016,** *4* (39), 14949-14953.

132. Mahler, B.; Hoepfner, V.; Liao, K.; Ozin, G. A., Colloidal synthesis of 1T-WS2 and 2H-WS2 nanosheets: applications for photocatalytic hydrogen evolution. *J Am Chem Soc* **2014,** *136* (40), 14121-7.

133. Zhou, P.; Tanghe, I.; Schiettecatte, P.; van Thourhout, D.; Hens, Z.; Geiregat, P., Ultrafast carrier dynamics in colloidal WS2 nanosheets obtained through a hot injection synthesis. *J Chem Phys* **2019,** *151* (16).

134. Zhang, H.; Hock, A. S., Crystalline WS2 via Room Temperature, Solution-Phase Synthesis. *Inorg Chem* **2017,** *56* (1), 106-109.

135. Scarfiello, R.; Cesari, A.; Altamura, D.; Masi, S.; Nobile, C.; Balzano, F.; Giannini, C.; Grillo, V.; Tavabi, A. H.; Dunin-Borkowski, R. E.; Uccello-Barretta, G.; Cozzoli, P. D.; Rizzo, A., Mechanistic insight into the formation of colloidal WS2 nanoflakes in hot alkylamine media. *Nanoscale Adv* **2019,** *1* (7), 2772-2782.

136. Liu, Z. Q.; Li, N.; Su, C.; Zhao, H. Y.; Xu, L. L.; Yin, Z. Y.; Li, J.; Du, Y. P., Colloidal synthesis of 1T ' phase dominated WS2 towards endurable electrocatalysis. *Nano Energy* **2018,** *50*, 176-181.

137. Liu, Q.; Li, X. L.; Xiao, Z. R.; Zhou, Y.; Chen, H. P.; Khalil, A.; Xiang, T.; Xu, J. Q.; Chu, W. S.; Wu, X. J.; Yang, J. L.; Wang, C. M.; Xiong, Y. J.; Jin, C. H.; Ajayan, P. M.; Song, L., Stable Metallic 1T-WS2 Nanoribbons Intercalated with Ammonia Ions: The Correlation between Structure and Electrical/Optical Properties. *Advanced Materials* **2015,** *27* (33), 4837-4844.

138. Antunez, P. D.; Webber, D. H.; Brutchey, R. L., Solution-Phase Synthesis of Highly Conductive Tungsten Diselenide Nanosheets. *Chem Mater* **2013,** *25* (12), 2385-2387.

139. Jin, H.; Ahn, M.; Jeong, S.; Han, J. H.; Yoo, D.; Son, D. H.; Cheon, J., Colloidal Single-Layer Quantum Dots with Lateral Confinement Effects on 2D Exciton. *J Am Chem Soc* **2016,** *138* (40), 13253-13259.

140. Kadam, S. R.; Enyashin, A. N.; Houben, L.; Bar-Ziv, R.; Bar-Sadan, M., Ni-WSe2 nanostructures as efficient catalysts for electrochemical hydrogen evolution reaction (HER) in acidic and alkaline media. *J Mater Chem A* **2020,** *8* (3), 1403-1416.

141. Zhang, B. Q.; Chen, J. S.; Niu, H. L.; Mao, C. J.; Song, J. M., Synthesis of ultrathin WSe2 nanosheets and their high-performance catalysis for conversion of amines to imines. *Nanoscale* **2018,** *10* (43), 20266-20271.

142. Henckel, D. A.; Lenz, O.; Cossairt, B. M., Effect of Ligand Coverage on Hydrogen Evolution Catalyzed by Colloidal WSe2 (vol 7, pg 2815, 2017). *Acs Catal* **2017,** *7* (10), 6699-6699.

143. Geisenhoff, J. Q.; Tamura, A. K.; Schimpf, A. M., Using ligands to control reactivity, size and phase in the colloidal synthesis of WSe2 nanocrystals. *Chem Commun (Camb)* **2019,** *55* (60), 8856-8859.

144. Zhou, P. S.; Schiettecatte, P.; Vandichel, M.; Rousaki, A.; Vandenabeele, P.; Hens, Z.; Singh, S., Synthesis of Colloidal WSe2 Nanocrystals: Polymorphism Control by Precursor-Ligand Chemistry. *Cryst Growth Des* **2021,** *21* (3), 1451-1460.

145. Shahmanesh, A.; Romanin, D.; Dabard, C.; Chee, S. S.; Greboval, C.; Methivier, C.; Silly, M. G.; Chaste, J.; Bugnet, M.; Pierucci, D.; Ouerghi, A.; Calandra, M.; Lhuillier, E.; Mahler, B., 2D Monolayer of the 1T' Phase of Alloyed WSSe from Colloidal Synthesis. *J Phys Chem C* **2021,** *125* (20), 11058-11065.

146. Pippia, G.; Van Hamme, D.; Martin-Garcia, B.; Prato, M.; Moreels, I., A colloidal route to semiconducting tungsten disulfide nanosheets with monolayer thickness. *Nanoscale* **2022,** *14* (42), 15859-15868.

147. Connelly, N. G.; Geiger, W. E., Chemical Redox Agents for Organometallic Chemistry. *Chem Rev* **1996,** *96* (2), 877-910.

148. Lewis, K. E.; Golden, D. M.; Smith, G. P., Organometallic Bond-Dissociation Energies - Laser Pyrolysis of Fe(Co)5, Cr(Co)6, Mo(Co)6, and W(Co)6. *J Am Chem Soc* **1984,** *106* (14), 3905-3912.

149. Bino, A.; Cotton, F. A.; Dori, Z.; Koch, S.; Kuppers, H.; Millar, M.; Sekutowski, J. C., New Class of Trinuclear Tungsten(Iv) Cluster Compounds with W-W Single Bonds. *Inorg Chem* **1978,** *17* (11), 3245-3253.

150. Darensbourg, D. J.; Walker, N.; Darensbourg, M. Y., Synthesis of Metal-Carbonyl-Complexes Highly Enriched in C-13 - Utilization of the Co-Labilizing Ability of (N-Bu)3p=O. *J Am Chem Soc* **1980,** *102* (3), 1213-1214.

151. Cotton, F. A.; Darensbourg, D. J.; Kolthammer, B. W. S.; Kudaroski, R., Solid-State and Solution Structures of [Pnp][W(Co)5o2cch3] and [Pnp][W(Co)4(Pet3)O2cch3] and the Co-Labilizing Ability of the Acetato Ligand in These Anionic Derivatives. *Inorg Chem* **1982,** *21* (4), 1656-1662.

152. Tsai, C.; Chan, K. R.; Abild-Pedersen, F.; Norskov, J. K., Active edge sites in MoSe2 and WSe2 catalysts for the hydrogen evolution reaction: a density functional study. *Phys Chem Chem Phys* **2014,** *16* (26), 13156-13164.

153. Hansen, L. P.; Johnson, E.; Brorson, M.; Helveg, S., Growth Mechanism for Single- and Multi-Layer MoS2 Nanocrystals. *J Phys Chem C* **2014,** *118* (39), 22768-22773.

154. Yang, J. N.; Xu, Q. C.; Zheng, Y. T.; Tian, Z. M.; Shi, Y. Y.; Ma, C. X.; Liu, G. Y.; Peng, B.; Wang, Z.; Zheng, W. J., Phase Engineering of Metastable Transition Metal Dichalcogenides via Ionic Liquid Assisted Synthesis. *Acs Nano* **2022**.

155. Liu, Z. Q.; Zhang, X.; Gong, Y.; Lu, Q. P.; Zhang, Z. C.; Cheng, H. F.; Ma, Q. L.; Chen, J. Z.; Zhao, M. T.; Chen, B.; Chen, Y.; Wu, X. J.; Yin, P. F.; Gu, L.; Du, Y. P.; Zhang, H., Synthesis of MoX2 (X = Se or S) monolayers with high-concentration 1T phase on 4H/fcc-Au nanorods for hydrogen evolution. *Nano Res* **2019,** *12* (6), 1301-1305.

Chapter 2: Using ligands to control reactivity, size and phase in the colloidal synthesis of WSe_2 nanocrystals

2.1 Abstract

Colloidal chemistry is leveraged for size- and phase-tuning of transition metal dichalcogenide nanomaterials. Specifically, nucleation and growth of colloidal WSe_2 nanocrystals are controlled via mixtures of oleic acid (OA) and trioctylphosphine oxide. Increased OA yields slower nucleation, larger nanocrystals and a shift from the 2H to 1T′ phase.

2.2 Introduction

The discovery of extraordinary properties in graphene has catalyzed an intense interest in two-dimensional (2D) nanomaterials, including a wide variety of elemental, binary and ternary inorganic nanostructures.[1-4] Among these 2D materials, transition metal dichalcogenides (TMDs) are extensively studied because of their unique electronic, optical, catalytic and mechanical properties.[5-7] TMDs can host a variety of phases that each have a unique electronic structure, allowing access to a compositionally and electronically diverse set of 2D materials.[8] Semiconducting TMDs (ME_2, M= Mo, W; E = S, Se) have a thermodynamically favoured 2H phase, known for its unique optical and optoelectronic properties, particularly at the monolayer.[9] Additionally, this class of materials can adopt the metallic 1T or small-bandgap 1T′ phases, which demonstrate promise for use in catalysis[10-13] or as topological insulators,[14-15] respectively. Due to its metastability, however, the 1T′ phase of these group VI TMDs remains relatively unexplored. Only recently have these materials been synthesized

using direct chemical methods that do not require charge intercalation or other post-synthetic modification.[16-20]

Colloidal chemistry offers a promising route to obtain metastable TMD phases through strategic choice of precursor or ligand identity, concentration, temperature or other reaction conditions to access kinetic growth regimes.[21-24] Indeed, colloidal chemistry has been exploited to access the metastable wurtzite phase of $CuInSe_2$ nanocrystals by choosing precursors with strong C–Se bonds that favor slow nucleation.[25-26] Similarly, organosulfur precursors with varying reactivity have been used to achieve highly selective and tunable phases of Fe_xS_y nanocrystals.[27] Recently, colloidal synthesis was used to obtain 1T′ phases of WS_2 and WSe_2,[16, 19] the latter of which has proven particularly challenging to access via traditional methods. Herein, we show that coordinating ligands greatly influence the precursor reactivity and resultant nanocrystal size and phase in colloidally synthesized WSe_2. Specifically, when synthesized in mixtures of oleic acid (OA) and trioctylphosphine oxide, inclusion of increasing amounts of OA hinders the reactivity of the precursor, leading to fewer nucleation events and larger nanocrystals. This trend is accompanied by a change in the phase composition, from 2H when minimal OA is present, to 1T′ when OA is introduced in higher concentrations. These results demonstrate the promise of using colloidal chemistry to tune the size and phase of WSe_2 and other TMD nanocrystals.

2.3 Results and Analysis

WSe_2 nanocrystals (Figure 2.1) were synthesized via hot injection of diphenyl diselenide (Ph_2Se_2) into a solution containing $W(CO)_6$ in a mixture of TOPO and OA. Specifically, nanocrystals were synthesized with OA/W molar equivalents (eq) of 2, 10, 100, and 1000. OA/TOPO amounts were varied while keeping the overall ligand/W ratio

consistent. Exact ligand amounts for each OA/W ratio are provided in Table 2S.1. In a typical synthesis, a degassed solution of 20 mg (0.057 mmol) $W(CO)_6$ in OA/TOPO was heated to 330 °C, at which point a solution containing 64 mg (0.2 mmol) Ph_2Se_2 in 1 ml OA or TOPO was rapidly injected. Following injection, a color change from yellow to black was observed within a few minutes. The solution was heated for 30 min, after which it was cooled to room-temperature and nanocrystals were collected via centrifugation. The resulting nanocrystals could be resuspended in toluene to form colloidal suspensions that were stable for several hours (Figure 2S.1).

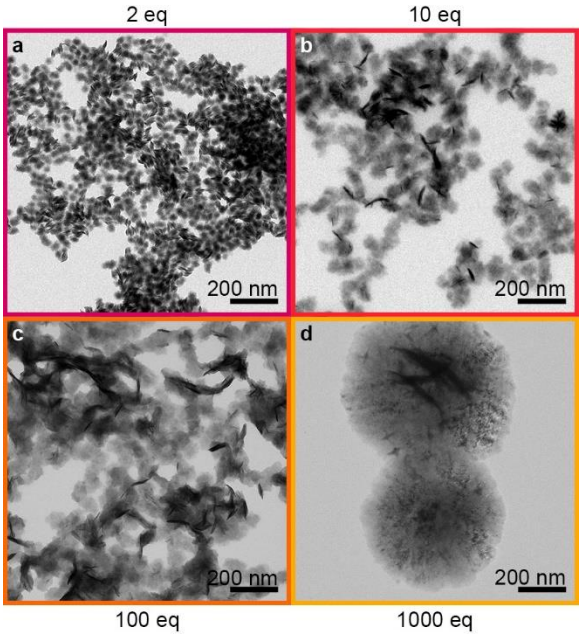

Figure 2. 1. TEM images of WSe_2 nanocrystals synthesized via injection of 1ml Ph_2Se_2 (0.04 M in TOPO or OA) into a solution of $W(CO)_6$ (0.02 mmol) in OA/TOPO. The final reaction mixtures contained (a) 2, (b) 10, (c) 100 or (d) 1000 eq OA/W. Exact ligand amounts are provided in Table 2S.1.

Figure 2.1 shows transmission electron microscope (TEM) images for nanocrystals synthesized with OA/W molar ratios of (a) 2, (b) 10, (c) 100, and (d) 1000. In each case, the nanocrystals are disk-like, with lateral dimensions (*xy*) larger than the heights (*z*

direction). Notably, as the relative amount of OA increases, so does the nanocrystal size. The powder X-ray diffraction patterns show a sharpening of the (002) reflection with increasing OA (Figure 2S.2a), indicating that larger nanocrystals also have more layers. For even the smallest sample (2 eq OA/W), the Raman peaks (*vide infra*) match those of bulk WSe_2, indicating multiple layers.

It has previously been reported that OA can be used to favor large lateral growth due to relatively weak binding to edge sites in 2H WSe_2.[28] Although TOPO is not expected to bind strongly to the nanocrystal surfaces, small particles are observed when very little OA is present. This trend may suggest that OA interacts strongly with the W precursor, and the absence of OA allows for rapid nucleation with more nucleation sites, ultimately yielding smaller nanocrystals. A similar trend is observed in the synthesis of CdSe nanocrystals in the presence of OA, where strong coordination to the Cd precursor reduces the active monomer concentration and leads to larger nanocrystals.[29]

Further evidence that OA hinders nucleation is observed qualitatively in the timescale of the color change following injection. Under high OA concentration conditions (1000 eq), the yellow precursor solution persists for minutes before turning black to indicate nanoparticle nucleation. Low OA concentration (2 eq) results in immediate color change from yellow to black, indicating fast onset of nucleation. These results together indicate that interaction with OA is inhibiting the reactivity of the tungsten precursor, despite allowing fast WSe_2 growth. The relatively weak size-dependence from 2–100 eq OA/W may reflect the fact that TOPO is still the dominant ligand in those reactions (Table 2S.1). It is important to note that reactions in all TOPO (0 eq OA) showed a nucleation event without the injection of Ph_2Se_2. Specifically, a solution of $W(CO)_6$ in TOPO becomes

turbid and black (Figure 2S.3a) when heated above 260 °C and amorphous nanoparticles could be isolated (Figure 2S.3b). Due to this additional nucleation event, WSe_2 nanocrystals synthesized in all TOPO (Figure 2S.3c) may be impure and are not included in further analysis. Inclusion of just 2 eq OA/W is enough to prevent this nucleation and the reaction mixture stays clear prior to injection of Ph_2Se_2 (Figure 2S.4).

Interestingly, the OA/W molar ratio has a significant effect on the phase of the WSe_2 nanocrystals synthesized here. Previous studies have reported colloidal syntheses of WSe_2 in both the 2H (Figure 2.2a) and 1T′ (Figure 2.2b) phases,[19, 28, 30-33] but the role of ligands, precursors and reaction conditions in promoting various phases has not been explored. Figures 2.2b and 2.2c show high-resolution TEM (HRTEM) images of the WSe_2 nanocrystals synthesized with OA/W mol ratios of 2 and 1000, respectively (corresponding to nanocrystals imaged in Figures 2.1a and 2.1d). The HRTEM for the nanocrystals synthesized with 2 eq OA/W show a hexagonal arrangement of the tungsten atoms (Figure 2.2c), characteristic of the hexagonal 2H lattice. The reflections present in the FFT (Figure 2.2e) correspond to interplanar spacings of $\boldsymbol{d_{100}}$ = 2.8 Å and $\boldsymbol{d_{2\bar{1}0}}$ = 1.6 Å, yielding the expected lattice parameter for 2H WSe_2 (a_{2H} = 3.3 Å). In contrast, nanocrystals synthesized in 1000 eq OA/W adopt a zig-zag arrangement of W atoms (Figure 2.2d), consistent with the 1T′ phase. This distorted octahedral coordination results in an elongation of the unit cell along the *x*-axis, while the *y*-axis remains unchanged ($a_{1T'}$ = 5.9 Å, $b_{1T'}$ = 3.3 Å, Figure 2.2f).

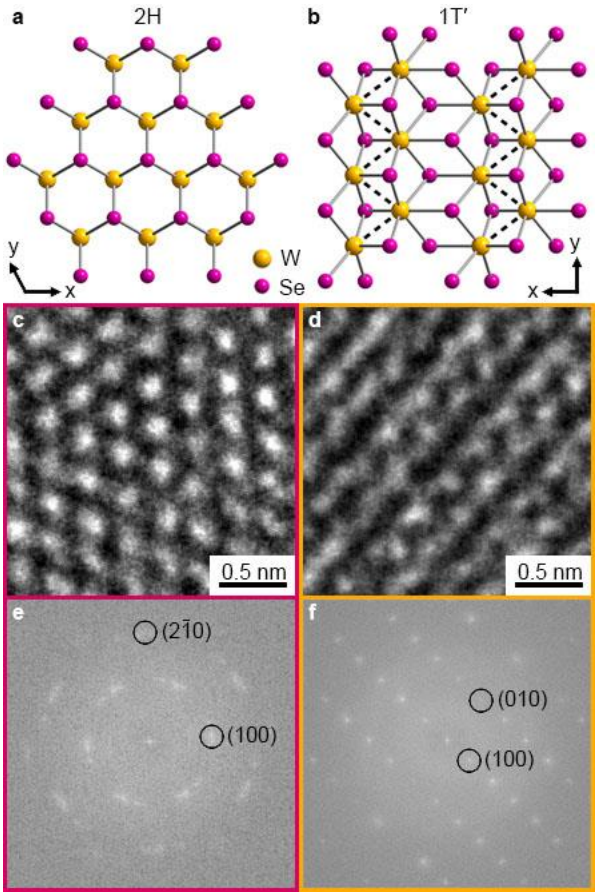

Figure 2. 2. Crystal structures showing the *xy*-plane of (a) 2H and (b) 1T′ WSe_2. HRTEM images for WSe_2 synthesized with (c) 2 eq OA/W and (d) 1000 eq OA/W and (e,f) corresponding FFTs. The electron beam is coincident with the (001) vector.

To probe the bulk phase of the nanocrystals synthesized with varying amounts of OA, Raman and X-ray photoelectron spectroscopies and powder X-ray diffraction were used. Figure 2.3a shows the Raman spectra of nanocrystals synthesized with (bottom to top) 2, 10, 100, and 1000 eq OA/W. The Raman spectrum of nanocrystals synthesized with 2 eq OA/W (Figure 2.3, bottom) is dominated by an intense peak centered at 251 cm^{-1}, formed by the unresolved combination of the A_{1g} and E_{2g} modes of multilayer 2H WSe_2.[34-35] When the OA/W ratio is increased to 10, this peak broadens and the peak at 219 cm^{-1} increases in relative intensity. When the OA/W ratio is increased to 100, the spectrum

displays 3 distinct peaks centered at 219 cm^{-1}, 240 cm^{-1}, and 260 cm^{-1}, which have been recently been assigned to the 1T′ phase of WSe_2.[19] Although there is little Raman data on 1T′ WSe_2, the emergence of 3 peaks is consistent with a break in the degeneracy of the E_{2g} mode, as no allowed point groups in the monoclinic space groups contain doubly degenerate representations. In addition, an underlying broad peak is observed, likely due to residual contributions from the A_{1g} and E_{2g} modes. At 1000 eq OA/W, the spectrum is composed only of the three distinct peaks with no underlying broadening. These Raman spectra suggest a gradual change from the 2H phase to the 1T′ phase with increasing amount of OA.

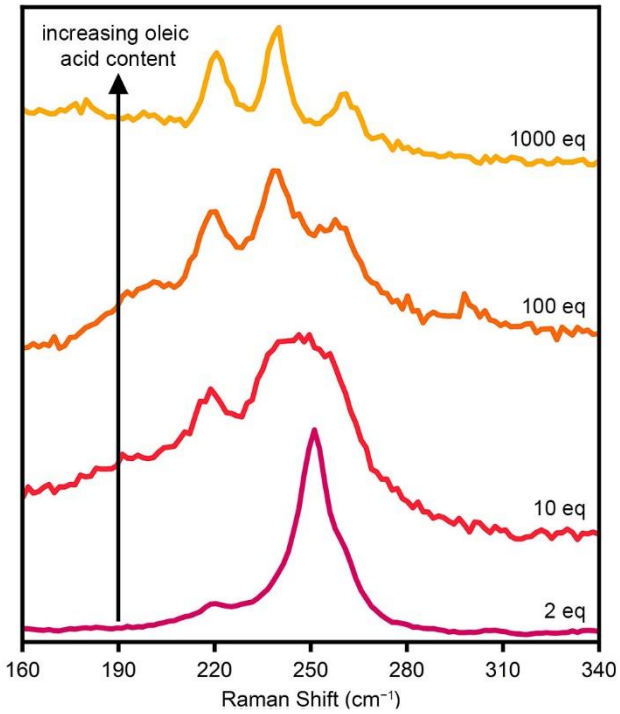

Figure 2. 3. Raman spectra of WSe_2 nanocrystals synthesized with (bottom to top) 2, 10, 100, and 1000 eq OA/W.

The change in phase with increasing OA content is also seen in the powder X-ray diffraction patterns (Figure 2S.2a). The powder patterns observed herein are similar to those

reported previously for both 2H and 1T′ WSe_2.[19, 28, 30-33] Increasing OA/W leads to a distinct loss of the (013) reflection (2H, 2$\boldsymbol{\theta}$ = 37.9 deg) and an increase in the reflection at 2 $\boldsymbol{\theta}$ = 34.8 deg. These characteristic differences have been seen previously for 2H vs 1T′ WSe_2, although the reflections for 1T′ WSe_2 have not been rigorously assigned. An initial estimate of the 1T′ WSe_2 powder pattern was simulated using the known Wyckoff positions for 1T′ $MoTe_2$ (*P2₁/m*, $\boldsymbol{\theta}$ = 93.917 deg),[36] with *a* and *b* obtained from TEM (Figure 2.2f), and *c* floated to match the (002) reflection (2 $\boldsymbol{\theta}$ = 13.92 deg, *c* = 12.74 Å). Although this method for predicting the 1T′ WSe_2 powder pattern has been used previously, the resulting pattern shows some discrepancies with the experimental pattern (Figure 2S.2a, top).[19] Le Bail fitting (Figure 2S.2b) of the 1000 eq pattern yielded similar unit cell parameters (*a* = 5.8543 Å, *b* = 3.2675 Å, *c* = 12.7884 Å, $\boldsymbol{\beta}$ = 93.9107 deg) and good agreement with the experimental powder pattern, indicating proper assignment of this phase to the monoclinic *P2₁/m* space group, consistent with the 1T′ phase observed for other TMDs.[36-37]

The gradual change in phase is corroborated by X-ray photoelectron spectroscopy (Figure 2S.5). Nanocrystals synthesized with 2 eq OA/W show W 4*f* binding energies matching that of 2H WSe_2 (Figure 2S.5a).[12, 28] As the OA/W ratio is increased, the W 4*f* peaks shift to lower binding energies, consistent with an increase in the W–Se bond distances expected for the 1T′ phase.[15, 19] A similar trend is also observed in the Se 3*d* binding energies with increasing OA/W ratios (Figure 2S.5b).

To gain further insight into the role of OA during nucleation and growth, WSe_2 nanocrystals were synthesized with 2 eq OA/W, and the phase monitored over time. Figure 2.4 shows the Raman spectra of aliquots taken at 5, 10 and 20 min following Ph_2Se_2 injection. Interestingly, the spectrum of the 5 min aliquot (Figure 2.4, bottom) shows the 3 peaks assigned

to the 1T′ phase. In the spectrum of the 10 min aliquot (Figure 2.4, middle), a broad peak centered around 250 cm^{-1} is observed in addition to a peak at 220 cm^{-1}, indicating the formation of a mixed phase. Finally, at 20 min (Figure 2.4, top) the signal is dominated by the peak at 251 cm^{-1}, diagnostic of the 2H phase. This time-dependence of the phase suggests that, under these conditions, WSe_2 nucleates in the metastable 1T′ phase and subsequently converts to the thermodynamically favourable 2H phase. This conversion may be hindered by large amounts of OA, leading to the trend observed at 30 min for increasing amounts of OA (Figure 2.3). Importantly, these results demonstrate that it is possible to obtain the 1T′ phase in small nanocrystals (Figure 2S.6) as well as in large ones (Figure 2.1d), suggesting that nanocrystal size and phase can be tuned independently.

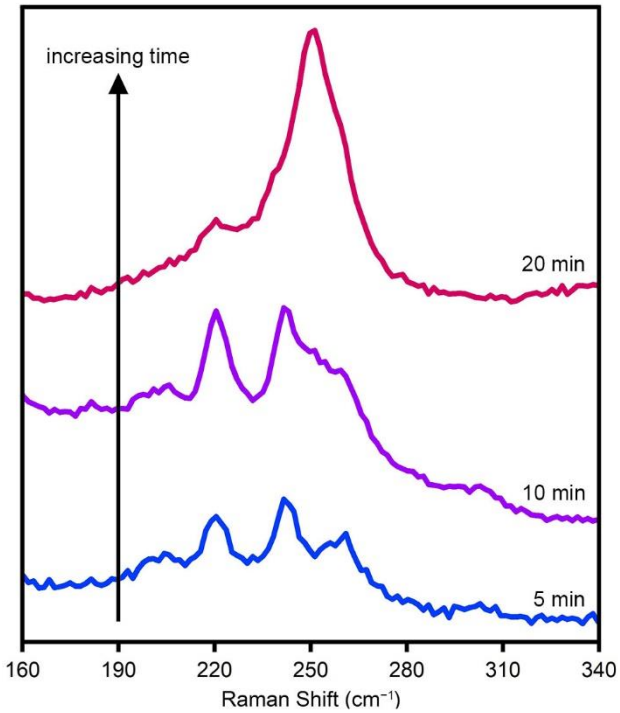

Figure 2. 4. Raman spectra of WSe_2 nanocrystals synthesized with 2 eq OA/W. Aliquots were taken at (bottom to top) 5, 10 and 20 min following Ph_2Se_2 injection.

2.4 Conclusions

The data presented herein show that ligand mixtures can be used to tune the precursor reactivity and resultant size of colloidally synthesized WSe_2 nanocrystals. Although neither ligand is expected to bind strongly to the nanocrystal surfaces, they lead to markedly different nanocrystal size and phase, suggesting that nucleation plays an important role in determining the final nanocrystal size. Specifically, increasing the amount of OA in OA/TOPO mixtures reduces the W precursor reactivity, leading to fewer nucleation events and larger nanocrystals. We hypothesize that W speciation prior to injection plays a major role in the rate of nucleation. For example, $W(CO)_6$ is known to be susceptible to oxidative addition by carboxylic acids,[38-39] suggesting that strong W–OA interactions may change W speciation prior to injection of Ph_2Se_2, and ultimately alter the nucleation event. TOPO, on the other hand, is expected to interact less strongly with the W precursor, facilitating rapid nucleation.

The change in precursor reactivity and final nanocrystal size is accompanied by a shift from the 2H to the 1T′ crystal phase when the reaction is stopped at 30 min. Inspection of the reaction over time suggests that, under these conditions, nanocrystals nucleate in the metastable 1T′ phase and may subsequently convert to the thermodynamically stable 2H phase. This conversion may depend on the coordinating ability of the ligands, among other factors. Further studies to elucidate the role of ligands in WSe_2 nucleation and growth are ongoing. Importantly, the data presented herein suggest it is possible to independently tune both nanocrystal size and phase. Overall, the results demonstrate the promise of using ligands to access a range of phases and sizes in colloidally synthesized TMD nanomaterials.

2.5 Appendix: Supporting Information

Table S2. 1. Amounts of ligand present in the reactions (A) before and (B) after Ph_2Se_2 injection.

OA/W		**mmol TOPO**		**mmol OA**		**OA/TOPO**		**TOPO/W**		**Ligand/W**	
A	B	A	B	A	B	A	B	A	B	A	B
948	1000	5.2	5.2	53.9	57.0	10.42	11	91	91	1039	1095
45	100	57	57	2.5	5.7	0.045	0.100	1001	1001	1046	1101
10	10	58	61	0.6	0.6	0.009	0.009	1029	1069	1039	1079
2	2	58	61	0.1	0.1	0.002	0.002	1029	1067	1031	1069
0	-	59	-	0	-	0	-	1038	-	1038	-

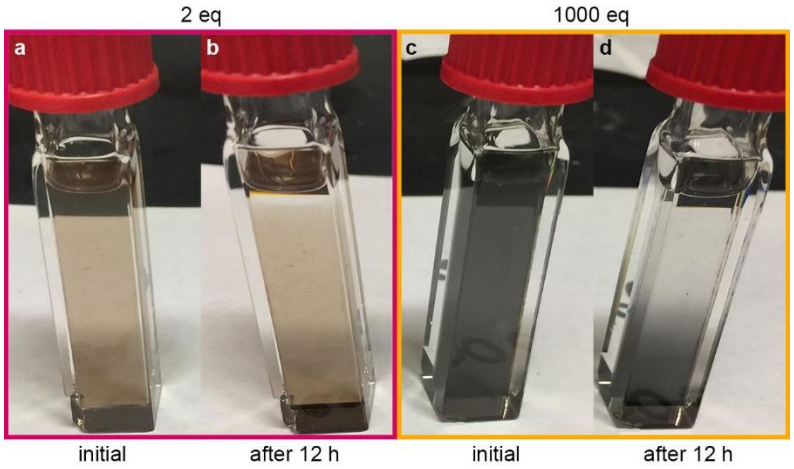

Figure S2. 1. Photographs of colloidal suspensions of nanocrystals synthesized with (a,b) 2 eq and (c,d) 1000 eq OA/W. Suspensions were prepared by adding ~12 ml toluene and 1 drop oleylamine to one of the two pellets collected from centrifugation. Photographs were taken (a,c) just after preparing suspensions and (b,d) after 12 h.

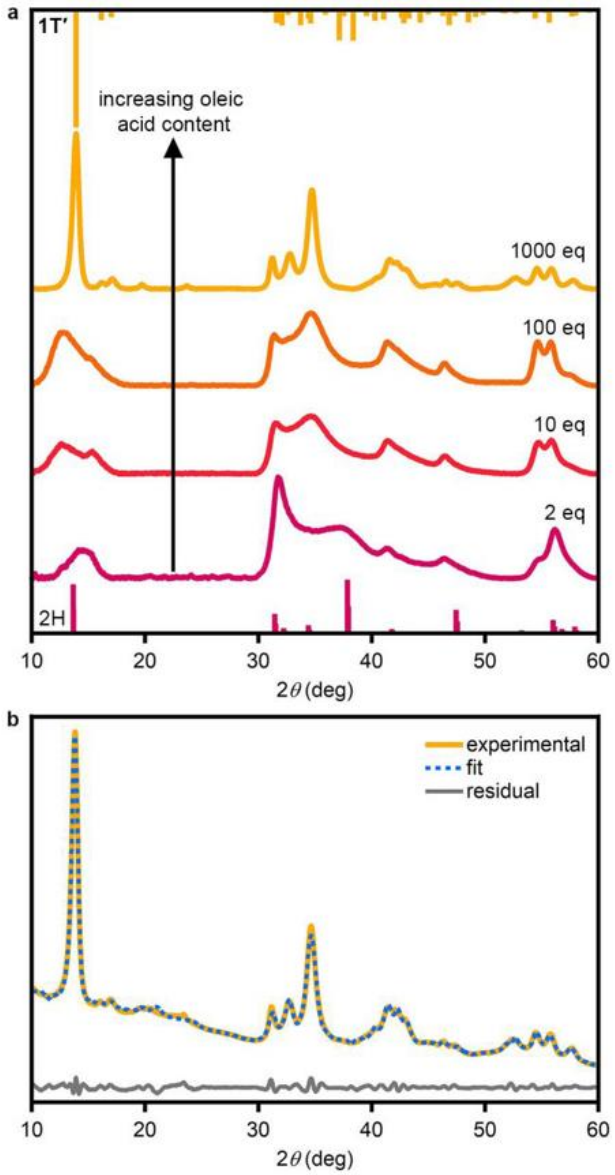

Figure S2. 2. (a) Powder X-ray diffraction patterns of nanocrystals synthesized with (bottom to top) 2, 10, 100 and 1000 OA/W. The 2H powder pattern is simulated from a published structure.[40] The 1T′ powder pattern was simulated using *a* and *b* parameters obtained from HRTEM (Figure 2.2f) and floating *c* to match the (002) reflection (2θ = 13.92 deg, c = 12.74 Å). (b) Le Bail fitting of the 1T′ (1000 eq) powder pattern in the $P2_1/m$ space group yields good agreement with the experimentally observed powder pattern with unit cell parameters *a* = 5.8543 Å, *b* = 3.2675 Å, *c* = 12.7884 Å, β = 93.9107 deg.

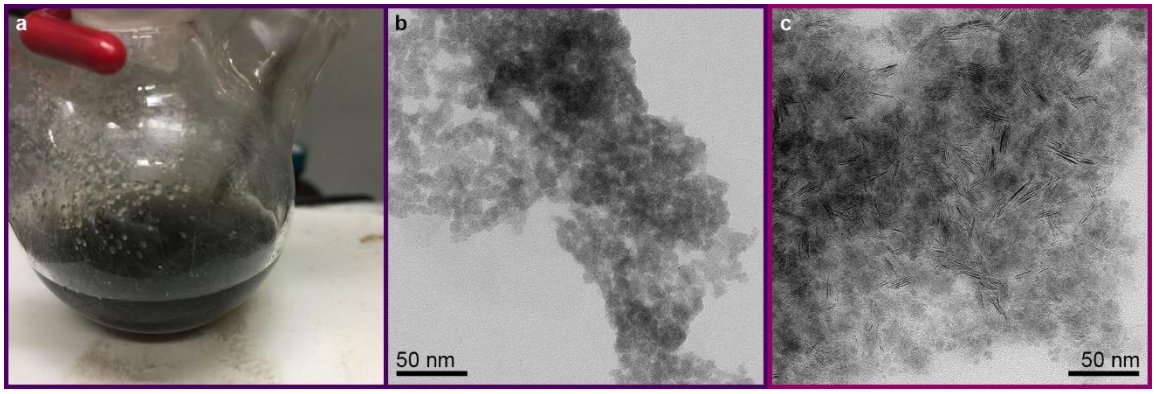

Figure S2. 3. (a) Photograph of the reaction of $W(CO)_6$ in TOPO, which results in rapid formation of a cloudy black solution above 260 °C, suggesting nucleation of nanoparticles from $W(CO)_6$ alone. TEM images of (b) amorphous nanoparticles isolated from the reaction of $W(CO)_6$ in TOPO and (c) WSe_2 synthesized in TOPO without added OA. The heterogeneity in (c) may be due to a separate nucleation event prior to Ph_2Se_2 injection. Because $W(CO)_6$ in all TOPO (0 eq OA) shows this nucleation without Ph_2Se_2 injection, WSe_2 nanocrystals synthesized with 0 eq OA/W are not included in the trends discussed in this study.

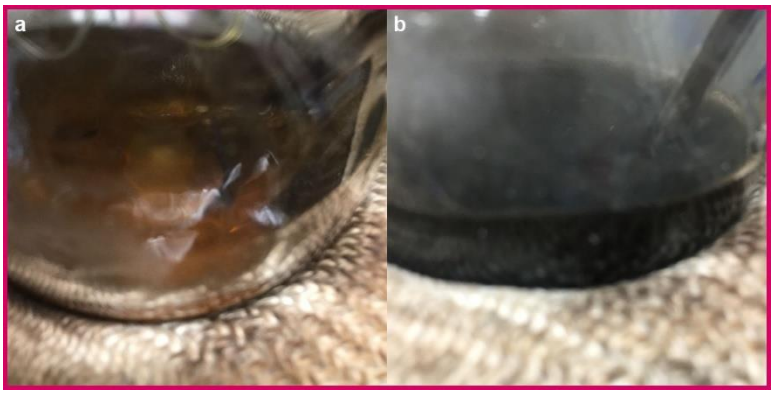

Figure S2. 4. Photograph of reaction of $W(CO)_6$ in TOPO with 2 eq OA at 320 °C (a) before and (b) after Ph_2Se_2 injection. The lack of cloudy solution prior to Ph_2Se_2 injection suggests that inclusion of 2 eq OA prevents nucleation of $W(CO)_6$ alone.

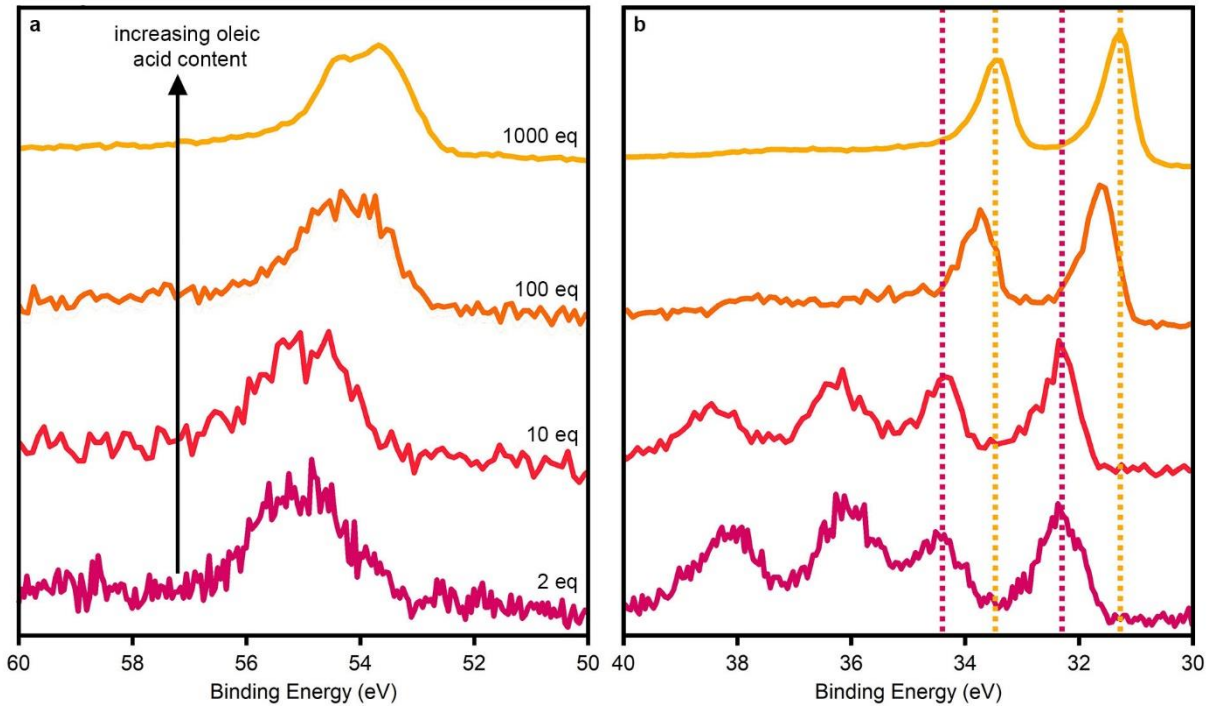

Figure S2. 5. (a) Se 3*d* and (b) W 4*f* X-ray photoelectron spectra of nanocrystals synthesized with (bottom to top) 2, 10, 100 and 1000 OA/W. The dashed vertical lines at 32.3 and 34.4 eV show the expected energies for the W $4f_{7/2}$ and W $4f_{5/2}$, respectively in 2H.[41] The dashed vertical lines at 31.8 and 33.5 eV show the energies observed in the nanocrystals synthesized with 1000 OA/W. The shift of these peaks to lower energies is consistent with a change to the 1T′ crystal phase.[42-43] The peaks at higher binding energies (~38 and ~36 eV) are consistent with oxidized W.[16, 44] These peaks are more prevalent in the samples synthesized with 2 and 10 eq, likely due to easier surface oxidation of smaller nanocrystals.

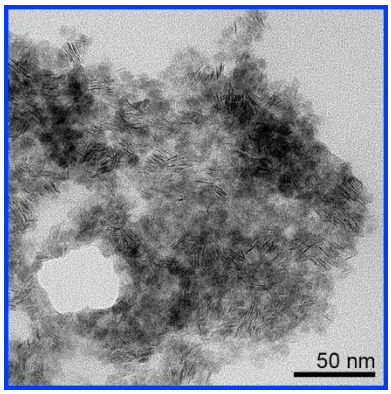

Figure S2. 6. TEM image of nanocrystals synthesized with 2 eq OA/W. Aliquot was taken 2 min following Ph_2Se_2 injection. The Raman spectrum (Figure 2.4, bottom) shows peaks indicative of the 1T′ phase, suggesting that nanocrystal size and phase can be tuned independently.

Experimental methods

Chemicals. Trioctylphosphine oxide (TOPO, 90%) was purchased from Strem Chemicals. Diphenyl diselenide (Ph_2Se_2, >96%) was purchased from TCI and stored in a vacuum desiccator. Tungsten hexacarbonyl ($W(CO)_6$, 99%) was purchased from Acros Organics and stored in a nitrogen-filled glovebox. Oleic acid (OA, 90%, stored in freezer), and hexanes (≥98.5%) were purchased from Sigma Aldrich. Toluene (tol, 99.9%), and methanol (MeOH, 99.9%) were purchased from Fischer Scientific. All chemicals were used without further purification. All chemicals were stored in ambient conditions unless otherwise noted.

All reactions were carried out using a glass sheath to prevent contamination from the temperature probe.

Synthesis of WSe_2 with 2 eq OA/W. In a 100 ml round bottom flask equipped with a Teflon-coated stir bar, 32 mg OA (0.11 mmol) and 22.6 g TOPO (58.5 mmol) were combined. Separately, a stock solution of Ph_2Se_2 was prepared by combining 256 mg Ph_2Se_2 (0.8 mmol) in 4.88 g (12.62 mmol) TOPO. Both solutions were degassed under vacuum at 100 °C for 1 hr, followed by 4 quick cycles of refilling the flask with argon and evacuating. The evacuated TOPO/OA mixture was brought into a nitrogen-filled glovebox, where 20 mg $W(CO)_6$ (0.057 mmol) was added. This solution was placed back on the Schlenck line and heated to 330 °C under argon, at which point 1 ml Ph_2Se_2 stock solution (0.15 mmol Ph_2Se_2, 2.3 mmol TOPO) was swiftly injected into the flask. The reaction proceeded for a total of 30 min, at which point the heating mantle was removed and the solution left to cool to room-temperature. The nanocrystals were collected by the addition of ~5 ml MeOH directly to the solution followed by centrifugation for 5 min at 3400 rpm. Nanocrystals were washed 2 additional times by dispersing in 10 ml 2:1 tol/MeOH followed by centrifugation for 5 min at 3400 rpm.

Synthesis of WSe_2 with 10, 100, and 1000 eq OA/W. Synthesis of WSe_2 with higher OAW was performed similarly to reaction above, with varying amounts of OA and TOPO. Table 2S.1 details the amounts of ligand used for each synthesis. For 10 eq OA/W Ph_2Se_2 was injected using 1 ml of the same stock solution described above. For 100 and 1000 eq OA/W, a new stock solution was prepared by adding 256 mg Ph_2Se_2 to 4 ml OA and degassing as described above. All other steps were performed as described above.

Characterization. TEM grids were prepared by drop-casting a suspension of nanocrystals in toluene onto a 100-mesh copper TEM grid coated with formvar and carbon (Electron Microscopy Sciences). TEM images were collected on a FEI Spirit operating at 120 keV and HRTEM images were collected using a JEOL JEM-2800 TEM operating at 200 keV. Raman and XPS samples were prepared by drop-casting a suspension of nanocrystals in hexanes onto a polished silicon substrate (Silicon Valley Microelectronics). Raman spectra were collected using a Renishaw inVia confocal Raman microscope with 10 mW of 532 nm laser excitation and a 50× objective lens. XPS measurements were acquired using a Kratos Analytical AXIS Supra surface analysis instrument at an emission current of 15 mA. Powder X-ray diffraction patterns were collected using a D8 Smart diffractometer with a Pt 135 detector equipped with a Rigaku MicroMax-007HF High-intensity Microfocus rotating anode with Cu Kα radiation (λ = 1.5478) at 40 kV, 25 mA and Varimax-HF double bounce optics. Diffraction images were merged/integrated in Diffrac.EVA V.4.3.0.1 (Bruker). Le Bail fitting[45] was performed using the FullProf software package.

2.6 Acknowledgements

Chapter 2, in full, is a reprint of the material as it appears in "Using ligands to control reactivity, size and phase in the colloidal synthesis of WSe_2 nanocrystals." Chem. Commun. 2019,

55, 8856-8859. The dissertation author was the primary author of this paper and gratefully acknowledges the contributions of coauthors Ashley K. Tamura and Alina M. Schimpf.

2.7 References

1. Bhimanapati, G. R.; Lin, Z.; Meunier, V.; Jung, Y.; Cha, J.; Das, S.; Xiao, D.; Son, Y.; Strano, M. S.; Cooper, V. R.; Liang, L. B.; Louie, S. G.; Ringe, E.; Zhou, W.; Kim, S. S.; Naik, R. R.; Sumpter, B. G.; Terrones, H.; Xia, F. N.; Wang, Y. L.; Zhu, J.; Akinwande, D.; Alem, N.; Schuller, J. A.; Schaak, R. E.; Terrones, M.; Robinson, J. A., Recent Advances in Two-Dimensional Materials beyond Graphene. *Acs Nano* **2015,** *9* (12), 11509-11539.

2. Tan, C. L.; Cao, X. H.; Wu, X. J.; He, Q. Y.; Yang, J.; Zhang, X.; Chen, J. Z.; Zhao, W.; Han, S. K.; Nam, G. H.; Sindoro, M.; Zhang, H., Recent Advances in Ultrathin Two-Dimensional Nanomaterials. *Chem Rev* **2017,** *117* (9), 6225-6331.

3. Burch, K. S.; Mandrus, D.; Park, J. G., Magnetism in two-dimensional van der Waals materials. *Nature* **2018,** *563* (7729), 47-52.

4. Cai, Z. Y.; Liu, B. L.; Zou, X. L.; Cheng, H. M., Chemical Vapor Deposition Growth and Applications of Two-Dimensional Materials and Their Heterostructures. *Chem Rev* **2018,** *118* (13), 6091-6133.

5. Chhowalla, M.; Shin, H. S.; Eda, G.; Li, L. J.; Loh, K. P.; Zhang, H., The chemistry of two-dimensional layered transition metal dichalcogenide nanosheets. *Nat Chem* **2013,** *5* (4), 263-275.

6. Chhowalla, M.; Liu, Z. F.; Zhang, H., Two-dimensional transition metal dichalcogenide (TMD) nanosheets. *Chem Soc Rev* **2015,** *44* (9), 2584-2586.

7. Choi, W.; Choudhary, N.; Han, G. H.; Park, J.; Akinwande, D.; Lee, Y. H., Recent development of two-dimensional transition metal dichalcogenides and their applications. *Mater Today* **2017,** *20* (3), 116-130.

8. Voiry, D.; Mohite, A.; Chhowalla, M., Phase engineering of transition metal dichalcogenides. *Chem Soc Rev* **2015,** *44* (9), 2702-2712.

9. Mak, K. F.; Shan, J., Photonics and optoelectronics of 2D semiconductor transition metal dichalcogenides. *Nat Photonics* **2016,** *10* (4), 216-226.

10. Lukowski, M. A.; Daniel, A. S.; Meng, F.; Forticaux, A.; Li, L. S.; Jin, S., Enhanced Hydrogen Evolution Catalysis from Chemically Exfoliated Metallic MoS2 Nanosheets. *J Am Chem Soc* **2013,** *135* (28), 10274-10277.

11. Voiry, D.; Salehi, M.; Silva, R.; Fujita, T.; Chen, M. W.; Asefa, T.; Shenoy, V. B.; Eda, G.; Chhowalla, M., Conducting MoS2 Nanosheets as Catalysts for Hydrogen Evolution Reaction. *Nano Lett* **2013,** *13* (12), 6222-6227.

12. Li, G. Q.; Zhang, D.; Qiao, Q.; Yu, Y. F.; Peterson, D.; Zafar, A.; Kumar, R.; Curtarolo, S.; Hunte, F.; Shannon, S.; Zhu, Y. M.; Yang, W. T.; Cao, L. Y., All The Catalytic Active Sites of MoS2 for Hydrogen Evolution. *J Am Chem Soc* **2016,** *138* (51), 16632-16638.

13. Mao, J.; Wang, Y.; Zheng, Z. L.; Deng, D. H., The rise of two-dimensional MoS2 for catalysis. *Front Phys-Beijing* **2018,** *13* (4).

14. Choe, D. H.; Sung, H. J.; Chang, K. J., Understanding topological phase transition in monolayer transition metal dichalcogenides. *Phys Rev B* **2016,** *93* (12).

15. Ugeda, M. M.; Pulkin, A.; Tang, S. J.; Ryu, H.; Wu, Q. S.; Zhang, Y.; Wong, D.; Pedramrazi, Z.; Martin-Recio, A.; Chen, Y.; Wang, F.; Shen, Z. X.; Mo, S. K.; Yazyev, O. V.; Crommie, M. F., Observation of topologically protected states at crystalline phase boundaries in single-layer WSe2. *Nat Commun* **2018,** *9*.

16. Mahler, B.; Hoepfner, V.; Liao, K.; Ozin, G. A., Colloidal Synthesis of 1T-WS2 and 2H-WS2 Nanosheets: Applications for Photocatalytic Hydrogen Evolution. *Journal of the American Chemical Society* **2014,** *136* (40), 14121-14127.

17. Liu, L.; Wu, J.; Wu, L.; Ye, M.; Liu, X.; Wang, Q.; Hou, S.; Lu, P.; Sun, L.; Zheng, J.; Xing, L.; Gu, L.; Jiang, X.; Xie, L.; Jiao, L., Phase-selective synthesis of 1T′ MoS2 monolayers and heterophase bilayers. *Nat. Mater.* **2018,** *17* (12), 1108-1114.

18. Yu, Y.; Nam, G.-H.; He, Q.; Wu, X.-J.; Zhang, K.; Yang, Z.; Chen, J.; Ma, Q.; Zhao, M.; Liu, Z.; Ran, F.-R.; Wang, X.; Li, H.; Huang, X.; Li, B.; Xiong, Q.; Zhang, Q.; Liu, Z.; Gu, L.; Du, Y.; Huang, W.; Zhang, H., High phase-purity 1T′-MoS2- and 1T′-MoSe2-layered crystals. *Nat Chem* **2018,** *10* (6), 638-643.

19. Sokolikova, M. S.; Sherrell, P. C.; Palczynski, P.; Bemmer, V. L.; Mattevi, C., Direct solution-phase synthesis of 1T' WSe_2 nanosheets. *Nat Commun* **2019,** *10* (1), 712.

20. Cheng, F.; Hu, Z. X.; Xu, H.; Shao, Y.; Su, J.; Chen, Z.; Ji, W.; Loh, K. P., Interface Engineering of Au(111) for the Growth of 1T '-MoSe2. *Acs Nano* **2019,** *13* (2), 2316-2323.

21. Yin, Y.; Alivisatos, A. P., Colloidal nanocrystal synthesis and the organic–inorganic interface. *Nature* **2005,** *437* (7059), 664-670.

22. Gao, Y.; Peng, X., Crystal structure control of CdSe nanocrystals in growth and nucleation: dominating effects of surface versus interior structure. *J Am Chem Soc* **2014,** *136* (18), 6724-32.

23. Thanh, N. T. K.; Maclean, N.; Mahiddine, S., Mechanisms of Nucleation and Growth of Nanoparticles in Solution. *Chem Rev* **2014,** *114* (15), 7610-7630.

24. Brutchey, R. L., Diorganyl Dichalcogenides as Useful Synthons for Colloidal Semiconductor Nanocrystals. *Accounts Chem Res* **2015,** *48* (11), 2918-2926.

25. Norako, M. E.; Brutchey, R. L., Synthesis of Metastable Wurtzite $CuInSe_2$ Nanocrystals. *Chem Mater* **2010,** *22* (5), 1613-1615.

26. Tappan, B. A.; Barim, G.; Kwok, J. C.; Brutchey, R. L., Utilizing Diselenide Precursors toward Rationally Controlled Synthesis of Metastable CuInSe2 Nanocrystals. *Chem Mater* **2018,** *30* (16), 5704-5713.

27. Rhodes, J. M.; Jones, C. A.; Thal, L. B.; Macdonald, J. E., Phase-Controlled Colloidal Syntheses of Iron Sulfide Nanocrystals via Sulfur Precursor Reactivity and Direct Pyrite Precipitation. *Chem Mater* **2017,** *29* (19), 8521-8530.

28. Jung, W.; Lee, S.; Yoo, D.; Jeong, S.; Miro, P.; Kuc, A.; Heine, T.; Cheon, J., Colloidal Synthesis of Single-Layer MSe_2 (M = Mo, W) Nanosheets via Anisotropic Solution-Phase Growth Approach. *J Am Chem Soc* **2015,** *137* (23), 7266-7269.

29. Bullen, C. R.; Mulvaney, P., Nucleation and growth kinetics of CdSe nanocrystals in octadecene. *Nano Lett* **2004,** *4* (12), 2303-2307.

30. Antunez, P. D.; Webber, D. H.; Brutchey, R. L., Solution-Phase Synthesis of Highly Conductive Tungsten Diselenide Nanosheets. *Chem Mater* **2013,** *25* (12), 2385-2387.

31. Jin, H.; Ahn, M.; Jeong, S.; Han, J. H.; Yoo, D.; Son, D. H.; Cheon, J., Colloidal Single-Layer Quantum Dots with Lateral Confinement Effects on 2D Exciton. *J Am Chem Soc* **2016,** *138* (40), 13253-13259.

32. Sun, Y. F.; Fujisawa, K.; Lin, Z.; Lei, Y.; Mondschein, J. S.; Terrones, M.; Schaak, R. E., Low-Temperature Solution Synthesis of Transition Metal Dichalcogenide Alloys with Tunable Optical Properties. *J Am Chem Soc* **2017,** *139* (32), 11096-11105.

33. Han, J. H.; Kwak, M.; Kim, Y.; Cheon, J., Recent Advances in the Solution-Based Preparation of Two-Dimensional Layered Transition Metal Chalcogenide Nanostructures. *Chem Rev* **2018,** *118* (13), 6151-6188.

34. Sahin, H.; Tongay, S.; Horzum, S.; Fan, W.; Zhou, J.; Li, J.; Wu, J.; Peeters, F. M., Anomalous Raman spectra and thickness-dependent electronic properties of WSe2. *Phys Rev B* **2013,** *87* (16).

35. Zhao, W. J.; Ghorannevis, Z.; Amara, K. K.; Pang, J. R.; Toh, M.; Zhang, X.; Kloc, C.; Tan, P. H.; Eda, G., Lattice dynamics in mono- and few-layer sheets of WS2 and WSe2. *Nanoscale* **2013,** *5* (20), 9677-9683.

36. Brown, B. E., Crystal Structures of WTe2 and High-Temperature Mote2. *Acta Crystallogr* **1966,** *20*, 268.

37. Keum, D. H.; Cho, S.; Kim, J. H.; Choe, D. H.; Sung, H. J.; Kan, M.; Kang, H.; Hwang, J. Y.; Kim, S. W.; Yang, H.; Chang, K. J.; Lee, Y. H., Bandgap opening in few-layered monoclinic MoTe2. *Nat Phys* **2015,** *11* (6), 482-U144.

38. Bino, A.; Cotton, F. A.; Dori, Z.; Koch, S.; Kueppers, H.; Millar, M.; Sekutowski, J. C., A new class of trinuclear tungsten(IV) cluster compounds with tungsten-tungsten single bonds. *Inorg. Chem.* **1978,** *17* (11), 3245-3253.

39. Cotton, F. A.; Mott, G. N., Susceptibility of the tungsten-tungsten quadruple bond to oxidative addition. Structure of a hydrogen chloride adduct. *J Am Chem Soc* **1982,** *104* (22), 5978-5982.

40. Glemser, V. O.; Sauer, H.; Konig, P., Uber wolframsulfide and wolframselenide. *Z. Anorg. Allg. Chem.* **1948,** *257*.

41. Zhang, Y.; Ugeda, M. M.; Jin, C.; Shi, S. F.; Bradley, A. J.; Martin-Recio, A.; Ryu, H.; Kim, J.; Tang, S.; Kim, Y.; Zhou, B.; Hwang, C.; Chen, Y.; Wang, F.; Crommie, M. F.; Hussain, Z.; Shen, Z. X.; Mo, S. K., Electronic structure, surface doping, and optical response in epitaxial WSe_2 thin films. *Nano Lett* **2016,** *16* (4), 2485-91.

42. Ugeda, M. M.; Pulkin, A.; Tang, S.; Ryu, H.; Wu, Q.; Zhang, Y.; Wong, D.; Pedramrazi, Z.; Martin-Recio, A.; Chen, Y.; Wang, F.; Shen, Z. X.; Mo, S. K.; Yazyev, O. V.; Crommie, M. F., Observation of Topologically Protected States at Crystalline Phase Boundaries in Single-Layer WSe_2. *Nat Commun* **2018,** *9* (1), 3401.

43. Sokolikova, M. S.; Sherrell, P. C.; Palczynski, P.; Bemmer, V. L.; Mattevi, C., Direct solution-phase synthesis of 1T′ WSe_2 nanosheets. *Nat. Comm.* **2019,** *10* (1), 712.

44. Xie, F. Y.; Gong, L.; Liu, X.; Tao, Y. T.; Zhang, W. H.; Chen, S. H.; Meng, H.; Chen, J., XPS studies on surface reduction of tungsten oxide nanowire film by Ar+ bombardment. *J Electron Spectrosc* **2012,** *185* (3-4), 112-118.

45. McCusker, L. B.; Von Dreele, R. B.; Cox, D. E.; Louer, D.; Scardi, P., Rietveld refinement guidelines. *J Appl Crystallogr* **1999,** *32*, 36-50.

Chapter 3: Manipulation of Precursor Reactivity for Facile Synthesis of Heterostructured and Hollow Metal Selenide Nanocrystals

3. 1 Abstract

We present a one-pot synthesis of nanocrystal heterostructures containing metal selenide cores shelled with tungsten-based metal selenides. This synthesis is enabled by the use of oleic acid as a W-coordinating ligand, which inhibits W reactivity and allows for formation of core nanocrystals prior to W-based selenide secondary growth. As a case study, we show that high amounts of oleic acid lead to slower, edge-preferred growth of WSe_2 on Ni_3Se_4, whereas lower amounts of oleic acid lead to uninhibited growth of WSe_2, fully covering the Ni_3Se_4 nanocrystals. The Ni_3Se_4 nanocrystal cores can readily be removed to access hollow WSe_2 nanocrystals. The manipulation of W-precursor reactivity can be extended to form Co_3Se_4/WSe_2, $Cu_{2-x}Se/Cu_2WSe_4$ and Cu_2WSe_4/WSe_2 core/shell heterostructures. These results demonstrate the exploitation of ligand coordination to enable easy, solution-phase synthesis of exotic or complex nanostructures.

3.2 Introduction

Colloidal chemistry offers the benefits of scalable, solution-phase methods that can be used to synthesize a diverse range of nanocrystals under relatively mild conditions.[1-4] In addition to facilitating the realization of new and tunable properties by enabling access to quantum-confined regimes,[5-9] colloidal syntheses can be tailored to access kinetically governed growth and to enable control over nanocrystal shape[10-17] and/or phase,[18-22] a feat not typically possible using conventional routes. One popular handle in the tuning of colloidal nanocrystal syntheses is the choice of ligand,[2] which can influence the resulting size,[13, 15] shape,[10, 13-17] phase[20-22] and

composition[23] via coordination to various nanocrystal facets or by altering the chemical potential, solubility or reactivity of precursors in the reaction. This synthetic control has been extended to the development of heterostructured or hybrid nanocrystals,[3, 24-30] which allow for the integration of complementary or multifunctional properties into a single system. Ligand coordination can be exploited to control secondary growth, [31-33] such as at the edges or on specific facets of a nanocrystal, allowing for fine-tuning of the properties and functionalities of hybrid nanostructures.

Secondary growth of shells onto nanocrystalline cores has been used to tailor and improve nanocrystal properties by passivating surface states, modulating carrier confinement or improving chemical stability.[3, 12, 27-28, 34-56] For example, the synthesis of core/shell nanocrystal heterostructures based on transition metal dichalcogenides has recently gained attention as a strategy for modulating their optical or electronic properties and for improving the catalytic or photocatalytic abilities.[57-62] Shell-growth in the synthesis of nanocrystal heterostructures relies on a complex balance of several reaction parameters, including ligand coordination and precursor reactivity, and is typically achieved with two- or multi-step syntheses in which a second set of precursors is added into a solution containing the core nanocrystals.[12, 34-43, 46, 48, 50-53, 63-64] Such methods are often time-consuming and difficult to scale-up, making design of one-step heterostructure syntheses highly desirable. Promisingly, recent studies have demonstrated that one-step seeded-growth is possible through carefully controlled precursor conversion and reaction kinetics,[65-66] although a diverse range of core/shell architectures has not yet been demonstrated. Here, we present a strategy for a one-step synthesis of core/shell heterostructures in which oleic acid (OA) ligands are used to modulate the reactivity of the W precursor for shell-growth, enabling secondary growth on various different nanocrystal cores.

Recently, we demonstrated that ligand identity greatly influences the reactivity of tungsten hexacarbonyl ($W(CO)_6$) in the synthesis of WSe_2 nanocrystals.[22] Specifically, injection of diphenyl diselenide (Ph_2Se_2) into a solution of $W(CO)_6$ in trioctylphosphine oxide (TOPO) results in rapid nucleation, yielding small WSe_2 nanocrystals. Inclusion of a large excess of OA, however, decreases the reactivity of the W precursor, delaying nucleation and resulting in large WSe_2 nanocrystals. This reduction in reactivity is accompanied by isolation of the metastable 1T′ (2M) phase,[67-71] likely due to coordination by OA preventing conversion to the thermodynamically favored 2H phase. Here, we exploit the reduction in W reactivity to develop a one-step colloidal synthesis of core/shell heterostructured nanocrystals. As a case study, we present the synthesis of Ni_3Se_4/WSe_2 core/shell heterostructures. OA is used to coordinate W in solution, slowing down the reactivity and enabling rapid Ni_3Se_4 nucleation formation followed by slow secondary growth of WSe_2. WSe_2 shows preferred edge-growth and can be tuned to deposit primarily on Ni_3Se_4 edges or to fully cover the Ni_3Se_4 cores via tuning of OA/W ratio. The Ni_3Se_4 can subsequently be removed by soaking in ethylenediamine ($Et_2N_2H_4$) and trioctylphosphine (TOP), enabling a relatively simple route to hollow WSe_2 nanocrystals. This synthetic strategy can be extended to access Co_3Se_4/WSe_2, $Cu_{2-x}Se/Cu_2WSe_4$ or Cu_2WSe_4/WSe_2 core/shell heterostructures, demonstrating that the crystal structure of the underlying core is not an important consideration for this secondary growth. Overall, these syntheses allow access to heterostructured or hollow nanostructures in just one or two steps and demonstrate a synthetic strategy to ultimately enable facile, solution-phase syntheses of exotic nanocrystals.

3.3 Results and Discussion

Ni_3Se_4/WSe_2 heterostructures were synthesized using a one-pot hot-injection method. In a typical synthesis, a solution of nickel acetylacetonate ($Ni(acac)_2$) and $W(CO)_6$ in OA/TOPO was

heated to 330 °C, at which point a solution of Ph_2Se_2 in OA was rapidly injected. Immediately following injection, a color change from yellow to black was observed. Transmission electron microscopy (TEM) of an aliquot taken at 2 min (Figure 3.1a) shows the formation of sharp-edged nanocrystalline polyhedra. Reaction for 30 min leads to overcoating of these polyhedra to form heterostructures (Figure 3.1b,c). The powder X-ray diffraction pattern (Figure 3.1d) of the 2-min aliquot matches that of Ni_3Se_4, suggesting that this material nucleates first and forms the cores of the heterostructures. The powder pattern of the 30-min aliquot shows additional peaks consistent with 1T′ (2M, space group *C*2/*m*) WSe_2,[22, 67] suggesting a Ni_3Se_4/WSe_2 core/shell architecture. Scanning TEM with energy dispersive X-ray spectroscopy (STEM-EDS) mapping (Figure 3.1c, Figure 3S.1, Figure 3S.2) and high-resolution TEM (Figure 3S.3) corroborate this assignment.

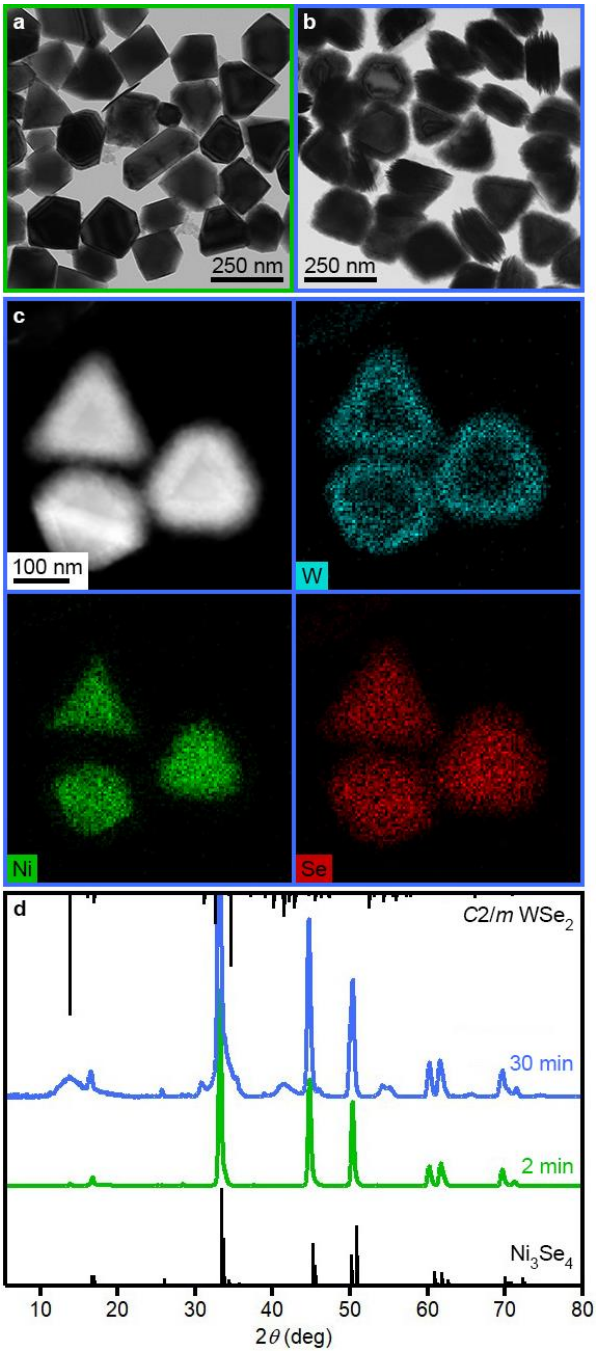

Figure 3. 1. Ni_3Se_4/WSe_2 core/shell heterostructures synthesized by rapid injection of 0.3 mmol Ph_2Se_2 in 1.5 ml OA into a solution of 0.1 mmol $Ni(acac)_2$ and 0.06 mmol $W(CO)_6$ in 17 ml OA and 2 g TOPO at 330 °C. TEM images of nanocrystals at **(a)** 2 and **(b)** 30 min following injection. **(c)** STEM-EDS mapping of heterostructures formed at 30 min. **(d)** Powder X-ray diffraction patterns of nanocrystals at 2 (green) and 30 (blue) min compared to those simulated for Ni_3Se_4 (bottom) and WSe_2 (top).

Incremental analysis of an analogous reaction shows that Ni_3Se_4 formation is complete within the first 2 min and WSe_2 shell-growth is gradual following Ph_2Se_2 injection (Figure 3S.4). Statistical analysis of the Ni_3Se_4 cores (Figure 3S.5) shows no measurable change in size between the first and last aliquots, suggesting that the Ni_3Se_4 core are fully formed within the first 2 min. STEM-EDS mapping of the small particles visible in the 2-min aliquot (Figure 3S.6) reveals the presence of extra W, but not Se, associated with these particles. Furthermore, no WSe_2 was detectable by Raman spectroscopy in the 2-min aliquot. We thus hypothesize that these impurities are due to W precursor that cannot be washed away but are not indicative of separate WSe_2 nucleation. Although the underlying Ni_3Se_4 seeds are polydisperse (Figure 3S.4, Figure 3S.5), the growth of the WSe_2 is surprisingly uniform (Figure 3S.7). Similar observations have been noted in non-epitaxial growth in which nuclei formed at a nanocrystal surface and subsequently merge into a shell.[40]

We hypothesize that WSe_2 shell-growth is modulated by the presence of OA. Indeed, when the amount of OA is lowered to 100 eq, more extensive shell-growth is observed (Figure 3S.8). To further evaluate the role of OA in shell-growth, Ni_3Se_4 nanocrystals were shelled with WSe_2 in varying amounts of OA. To avoid variations in the Ni_3Se_4 cores due to changing OA amount, we synthesized a single batch of Ni_3Se_4 cores (Figure 3.2a) and shelled them as an independent step (Figure 3.2b–e). Additionally, the Ni_3Se_4 cores were synthesized as platelets with the goal of evaluating the preference for edge-growth that is indicated by the TEM images of the original synthesis (Figure 3.1b,c, Figure 3S.3, Figure 3S.4). To obtain Ni_3Se_4 nanoplatelets, 0.1 mmol Ph_2Se_2 in 1 ml OA was added dropwise into a solution of 0.1 mmol $Ni(acac)_2$ in 17 ml OA and 2 g TOPO at 330 °C. The resulting Ni_3Se_4 nanocrystals were washed and a stock solution was prepared by suspension in 4 ml octadecene (ODE). Subsequent shell-growth was conducted with 1000 (Figure 3.2b,d), 100 (Figure 3.2c,e) and 0 (Figure 3S.9) eq OA/W, while the concentrations

of $W(CO)_6$ and of Ni_3Se_4 cores were kept constant. For the 1000 eq reaction, 0.06 mmol Ph_2Se_2 was added to 1 ml of the stock solution and this mixture was rapidly injected into a solution containing 0.03 mmol $W(CO)_6$, 8.5 ml OA, and 2 g TOPO. For other equivalents the OA content was adjusted accordingly and TOPO was added to keep total volume the same. All shells were grown for a total of 30 min.

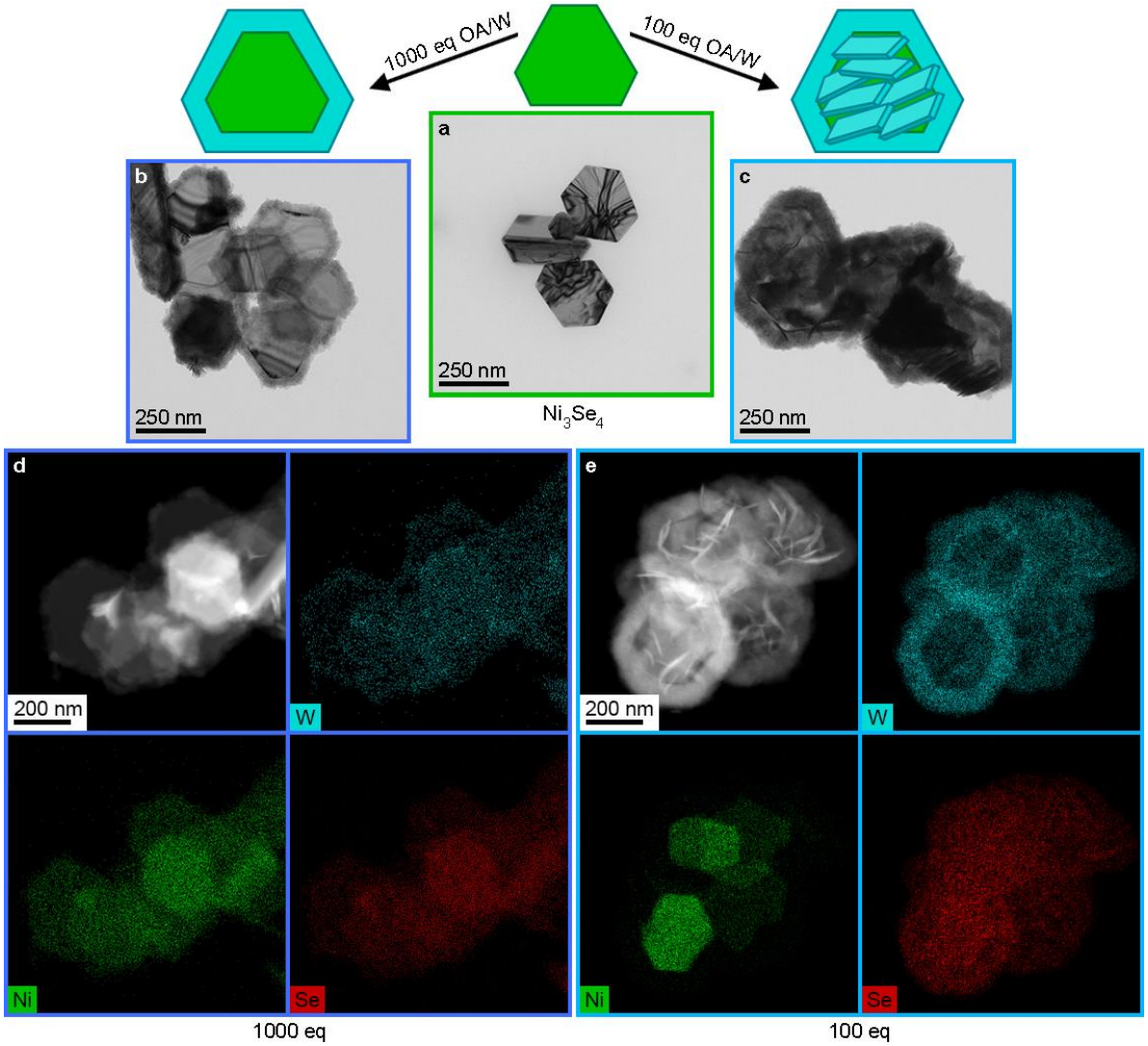

Figure 3. 2. TEM images of **(a)** Ni_3Se_4 nanoplatelets, **(b)** Ni_3Se_4/WSe_2 heterostructures grown with 1000 eq OA/W and **(c)** Ni_3Se_4/WSe_2 heterostructures grown with 100 eq OA/W. Both sets of shells were grown for 30 min. **(d, e)** STEM-EDS mapping of heterostructures in b, c.

For heterostructures synthesized in the presence of 1000 eq OA/W (Figure 3.2b,d), shell-growth is primarily around the edges of the hexagonal Ni_3Se_4. The ratio of W present on the edge compared to that on the face of the nanocrystals suggests that this trend is due to preferential growth and is not only an artifact of shell thickness (Figure 3S.10). When the amount of OA is decreased to 100 eq, the shell-growth around the edges becomes more substantial and is accompanied by obvious growth on the nanocrystal faces (Figure 3.2c,e). An aliquot taken 5 min

following injection shows that this growth occurs first on the nanocrystal edges (Figure 3S.11), followed by growth on the faces at later times. We hypothesize that this preferred growth is a result of the higher energy of the core nanocrystal edges. At high (1000 eq) ratios of OA/W, W reactivity is hindered and secondary growth occurs only on the nanocrystal edges with high surface energy.[72] When the ratio of OA/W is decreased (100 eq) more secondary nucleation of WSe_2 is enabled, leading to larger shells and growth on the less reactive nanocrystal faces. In the absence of OA, WSe_2 nucleation is much more rapid and occurs both at Ni_3Se_4 nanocrystal edges and as separate WSe_2 nanocrystals (Figure 3S.9). Similar core/shell heterostructures can be achieved using phenylacetic acid (100 eq OA/W, Figure 3S.12) instead of OA, further supporting that the carboxylic acid moiety is important for modulating W reactivity.[22]

Ni_3Se_4/WSe_2 nanocrystals can be further manipulated by removal of the Ni_3Se_4 cores to form hollow WSe_2 nanocrystals (Figure 3.3, Figure 3S.13). Specifically, treatment with $Et_2N_2H_4$ and TOP in chloroform results in dissolution of the Ni_3Se_4 core nanocrystals. The removal of Ni_3Se_4 cores is verified by powder X-ray diffraction (Figure 3.3b, teal), which shows no evidence of remaining Ni_3Se_4 after treatment. Furthermore, STEM-EDS mapping (Figure 3S.13) shows removal of Ni from the heterostructure core. Interestingly, the WSe_2 shells are insensitive to the removal of the Ni_3Se_4 cores, completely retaining their size (Figure 3S.7) and shape and allowing facile access to hollow WSe_2 nanocrystals.

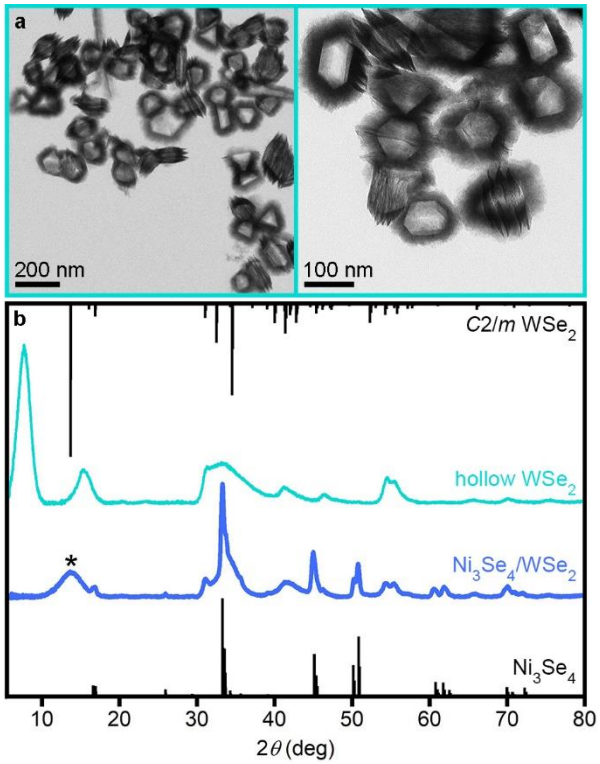

Figure 3. 3. (a) TEM images of hollow WSe_2 nanocrystals formed by anaerobic treatment of Ni_3Se_4/WSe_2 heterostructures with $Et_2N_2H_4$ and TOP in chloroform for 3 days. **(b)** Powder X-ray diffraction patterns of Ni_3Se_4/WSe_2 core/shell heterostructures (blue) and hollow WSe_2 nanocrystals (teal) formed after removal of Ni_3Se_4 cores compared to those simulated for Ni_3Se_4 and WSe_2.

The powder X-ray diffraction pattern of the hollow nanocrystals (Figure 3.3b, teal) suggests intercalation of $Et_2N_2H_4$ into the WSe_2 shells. Specifically, the (002) peak of WSe_2 (*) splits into two, with the more intense peak shifting to lower 2θ, indicative of an increase in the interlayer distance. The hollow WSe_2 nanocrystals exhibit an interlayer expansion, $d_{IE} = d_{intercalated} - d_{host}$ (where d_{host} and $d_{intercalated}$ are the interlayer distances of the host material before and after intercalation, respectively) of 0.50 nm, consistent with $Et_2N_2H_4$ intercalation observed in other transition metal dichalcogenides.[73-76] The presence of $Et_2N_2H_4$ in the washed hollow WSe_2 nanocrystals was verified by IR absorption spectroscopy (Figure 3S.14). STEM-EDS mapping (Figure 3S.13) shows a small amount of Ni remaining in the shells, likely co-intercalated with the

$Et_2N_2H_4$. Comparison to intercalation into WSe_2 nanocrystals alone, however, suggests that the presence of Ni cations is not necessary for $Et_2N_2H_4$ intercalation (Figure 3S.15).

Although TOP has been previously used to remove Se from metal selenide nanocrystals,[77] the selectivity for Ni_3Se_4 removal is likely enabled by the combination of reagents chosen. Specifically, $Et_2N_2H_4$ has high affinity for Ni and has been used in its extraction from ores,[78-79] but is not expected to remove W, as primary amines are generally poor at W extraction.[80] Only the case in which both elements (Ni and Se) are attacked results in dissolution of the material. Extraction of Ni^{2+} in the form of $[Ni(Et_2N_2H_4)_3]^{2+}$ was verified by electronic absorption spectroscopy (Figure 3S.16).

The non-epitaxial nature of WSe_2 growth suggests that this heterostructure growth strategy should be extendable to various nanocrystal cores, as long as the balance in precursor reactivity can be maintained. To explore the applicability of the method to other materials, $Ni(acac)_2$ was replaced with cobalt(III) acetylacetonate ($Co(acac)_3$), while all other conditions were kept analogous to those used for the synthesis of the heterostructures shown in in Figure 3.1. Although the TEM images of the resulting nanostructures showed small amounts of sheet-like growth off of the core Co_3Se_4 nanocrystals (Figure 3S.17a), WSe_2 was not observed in the powder X-ray diffraction pattern (Figure 3S.17b). In order to more easily observe WSe_2 shell-growth, the amount of W was increased and the reaction was allowed to proceed for 2 h. Figure 3.4a,b shows TEM images of an aliquot taken at 2 min and of the final nanocrystals, respectively. Similar to the Ni-based reaction, the 2-min aliquot shows sharp polyhedral nanocrystals, which have been overcoated in the final product. Analysis of the powder X-ray diffraction patterns of both nanocrystal sets reveals that the initial nanocrystals are Co_3Se_4 (Figure 3.4b, pink), and that WSe_2 is added in the final product (Figure 3.4b, purple). The Co_3Se_4/WSe_2 core/shell architecture is

confirmed with STEM-EDS mapping (Figure 3S.18). Overall these results suggest that this reaction proceeds similarly to the Ni-based one, where Co_3Se_4 nanocrystals are rapidly formed, followed by slow secondary growth of WSe_2. The necessity of using higher amounts of W precursor to observe WSe_2 shell-growth could suggest that some W is incorporated into the Co_3Se_4 cores, but the primary goal of Co_3Se_4/WSe_2 core/shell heterostructures is achieved with relatively little optimization of the reaction parameters.

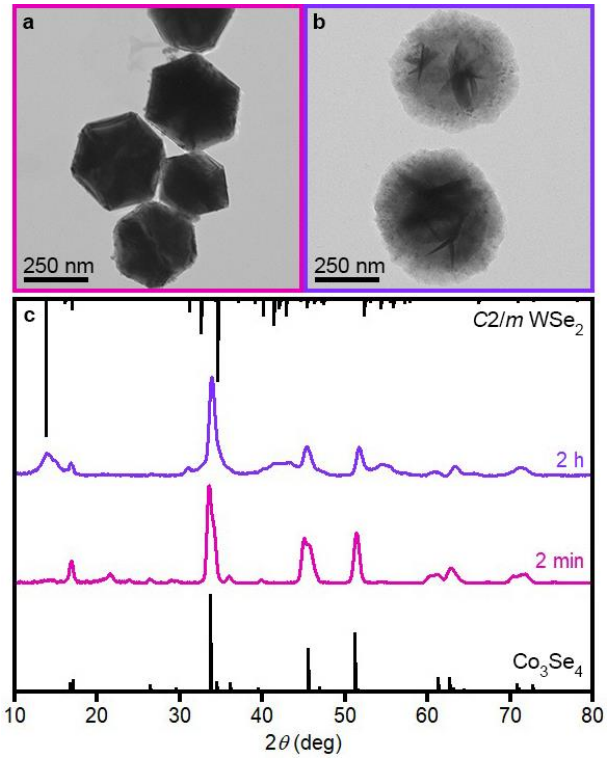

Figure 3. 4. TEM images of nanocrystals at **(a)** 2 min and **(b)** 2 h following injection of 0.5 mmol Ph_2Se_2 in 2.5 ml OA into 0.1 mmol $Co(acac)_3$ and 0.13 mmol $W(CO)_6$ in 17 ml OA and 4 g TOPO at 330 °C. **(c)** Powder X-ray diffraction patterns nanocrystals at 2 min (pink) and 2 h (purple) compared to those simulated for Co_3Se_4 (bottom) and WSe_2 (top).

Further extension of this strategy was explored by replacing $Ni(acac)_2$ with copper(I) chloride (CuCl). In this case, rapid injection of Ph_2Se_2 led to large, polydisperse, agglomerated $Cu_{2-x}Se$ nanocrystals. To improve the quality of $Cu_{2-x}Se$ core nanocrystals, a dropwise addition of

Ph_2Se_2 was used, with all other conditions analogous to those used for the heterostructures shown in Figure 3.1. Figure 3.5a,b shows TEM images of nanocrystals collected 2 and 30 min following Ph_2Se_2 injection, respectively. Similar to the Ni- and Co-based reactions, the aliquot taken at 2 min shows formation of polyhedral cores (Figure 3.5a), which are confirmed by powder X-ray diffraction to be $Cu_{2-x}Se$ (Figure 3.5c, yellow). At 60 min, shell-growth is observed (Figure 3.5b) and is determined by powder X-ray diffraction to be Cu_2WSe_4 (Figure 3.5c, orange). The $Cu_{2-x}Se$/ Cu_2WSe_4 core/shell architecture is confirmed by STEM-EDS mapping (Figure 3S.19).

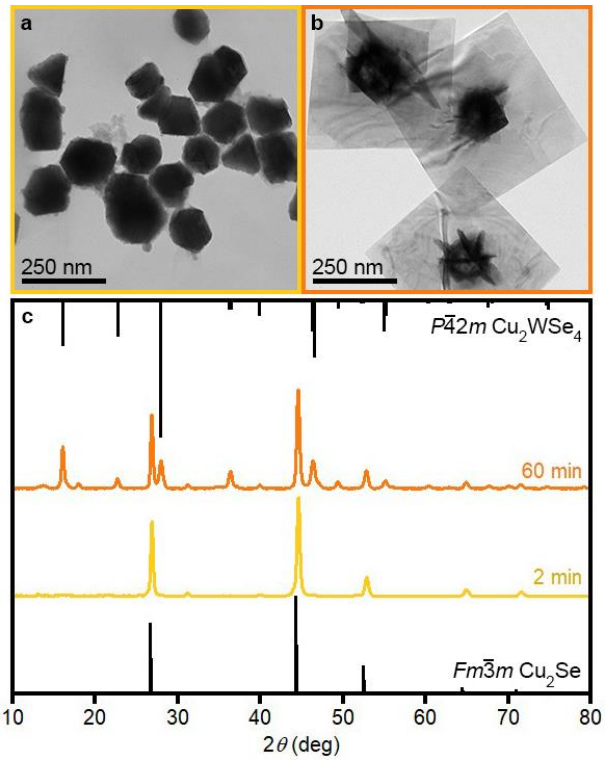

Figure 3. 5. TEM images of nanocrystals at **(a)** 2 and **(b)** 60 min following injection of 0.3 mmol Ph_2Se_2 in 1.5 ml OA into 0.1 mmol CuCl and 0.06 mmol $W(CO)_6$ in 17 ml OA and 2 g TOPO at 330 °C. **(c)** Corresponding powder X-ray diffraction patterns compared to those predicted for $Cu_{2-x}Se$ (bottom) and Cu_2WSe_4 (top).

Similar to the nickel-based reaction, inclusion of OA hinders WSe_2 nucleation, while allowing rapid formation of Cu_2Se. The Cu_2Se loses Cu upon exposure to air to form $Cu_{2-x}Se$,

leading to a shift of the powder pattern reflections to higher 2θ. Unlike the Ni-based reaction, however, WSe_2 secondary growth is not observed under these conditions and instead a shell of Cu_2WSe_4 is formed. The formation of this ternary material is likely enabled by the high mobility of copper in copper selenide,[81-83] which allows the core nanocrystals to deliver copper during seeded growth of Cu_2WSe_4. Similar results have been observed in Cu_2S-seed-mediated growth of Cu_3VS_4, although without retention of the original seed.[84] Inclusion of higher amounts of W allows for secondary growth of WSe_2 on the Cu_2WSe_4 (Figure 3S.20). These results show that our synthetic strategy can be easily extended to other materials without extensive optimization, demonstrating its promise as a general method to enable facile, one-step access to core/shell heterostructures not limited to binary shell materials. Additionally, future studies based on these results may provide insight into solution-phase syntheses of ternary copper chalcogenide nanocrystals, which are attractive for various applications, including solar energy harvesting and catalysis.[19, 82, 84-88]

3.4 Summary and Conclusions

The synthetic strategies proposed herein take advantage of different precursor reactivities to form exotic WSe_2-based heterostructured or hollow nanocrystals in just one or two steps. This difference in reactivity is imparted by coordination of W by OA, which slows down W reactivity to enable rapid formation of Ni_3Se_4, Co_3Se_4 or Cu_2Se cores, followed by secondary nucleation of WSe_2 or Cu_2WSe_4. Additionally, OA can be used to select for primarily edge-growth of WSe_2, allowing tunability between lateral heterostructures and fully covered core/shell structures by modulating reactivity of the shell material via ligand coordination. The ability to grow WSe_2 on Ni_3Se_4, Co_3Se_4 or Cu_2WSe_4 and to select for growth at the edges or over the full nanocrystal suggests that the underlying crystal structure of the core nanocrystals is not important. Thus,

extension of this strategy to a wide range of metal selenide cores should be possible by balancing precursor reactivities of the desired core and shell materials. Overall, these results demonstrate the promise of exploiting differences in precursor reactivities for facile, one-step syntheses of exotic nanocrystal heterostructures.

3.5 Experimental Methods

Chemicals. Oleic acid (OA, 90%), nickel(II) acetylacetonate ($Ni(acac)_2$, 95%) and cobalt(III) acetylacetonate ($Co(acac)_3$, 98%) were purchased from Sigma Aldrich. Tungsten hexacarbonyl ($W(CO)_6$, 99%) and octadecene (ODE, 90%) were purchased from Acros Organics. Diphenyl diselenide (Ph_2Se_2, >96%) and ethylenediamine ($Et_2N_2H_4$, >98%) were purchased from TCI. Copper(I) chloride (CuCl, 97%), trioctylphosphine oxide (TOPO, 90%) and trioctylphosphine (TOP, 97%) were purchased from Strem Chemicals. Phenylacetic acid (PAA, 99%) was purchased from Alfa Aesar. Toluene (tol, 99.9%), chloroform ($CHCl_3$, HPLC grade) and methanol (MeOH, ACS grade) were purchased from Fischer Scientific. Ethanol (EtOH, anhydrous, 200 proof) was purchased from Decon labs. All chemicals were used without further purification.

For all reactions the temperature probe was sheathed in a glass cover to avoid contamination.

Synthesis of Ni_3Se_4/WSe_2 core/shell nanocrystals. In a typical synthesis, 25.6 mg (0.1 mmol) of $Ni(acac)_2$ was dissolved in 17 ml of OA and 2 g of TOPO in a 100-ml 3-neck round-bottom flask. This solution was degassed by pulling vacuum at 120 °C for 2 h, and then pumped into a nitrogen-filled glovebox, where 20 mg (0.06 mmol) $W(CO)_6$ was added. This mixture was then placed back on the Schlenk line and heated under a nitrogen flow. Once the solution reached 330 °C, 96 mg (0.3 mmol) Ph_2Se_2 in 1.5 ml OA was quickly injected into the flask. The reaction proceeded for a total of 30 min, at which point the heating mantle was removed and the solution

left to cool to room-temperature. The nanocrystals were washed by dispersing in 10 ml 2:1 tol/EtOH and centrifuging for 5 min at 3400 rpm to collect the precipitated nanocrystals. Washing was repeated a total of 3 times.

Synthesis of Ni_3Se_4/WSe_2 core/shell nanocrystals in the presence of 100 eq carboxylic acid. OA: In a 50 ml 3-neck round-bottom flask 0.9 ml OA, 8.9 g TOPO and 12.8 mg $Ni(acac)_2$ were degassed at 120 °C for 2 h. The flask was brought into a nitrogen-filled glovebox and to it added 10 mg (0.03 mmol) $W(CO)_6$. This mixture was then placed back on the Schlenk line and heated under a nitrogen flow. Once the solution reached 330 °C, 48 mg (0.15 mmol) Ph_2Se_2 in 0.75 ml ODE was rapidly injected. The reaction proceeded for a total of 30 min, at which point the heating mantle was removed and the solution left to cool to room-temperature. The nanocrystals were washed by dispersing in 2:1 tol/EtOH and centrifuging for 5 min at 3400 rpm to collect the precipitate. The washing was repeated a total of 3 times.

PAA: Nanocrystals were synthesized in the same manner to the reaction above, replacing OA with 0.39 g PAA.

Synthesis of Ni_3Se_4 nanoplatelets. In a typical synthesis, 25.6 mg (0.1 mmol) of $Ni(acac)_2$ was dissolved in 17 ml of OA and 1.9 g of TOPO in a 100-ml 3-neck round-bottom flask. This solution was degassed by pulling vacuum at 120 °C for 2 h. The solution was then heated under a nitrogen flow. Once the solution reached 330 °C, 32 mg (0.1 mmol) Ph_2Se_2 in 1 ml OA was added into the flask dropwise over 1.5 minutes. The reaction proceeded for a total of 10 min, at which point the heating mantle was removed and the solution left to cool to room-temperature. Nanocrystals were washed by dispersion in 10 ml 2:1 tol/EtOH and collected via centrifugation for 5 min at 3400 rpm. The washing was repeated a total of 3 times, after which the pellets were

brought into a nitrogen-filled glovebox and dispersed in 4 ml ODE to serve as a stock solution for shelling with WSe_2.

Secondary growth of WSe_2. 1000 eq OA/W: To a 25-ml 3-neck round-bottom flask, 8.5 ml OA and 2 g TOPO were added and degassed at 120 °C for 2 h. The degassed setup was brought into a nitrogen-filled glovebox and to the flask was added 10 mg (0.03 mmol) $W(CO)_6$. Separately, 1 ml Ni_3Se_4 in ODE (stock solution) and 19 mg (0.06 mmol) Ph_2Se_2 were added to a 20 ml scintillation vial. Both solutions were placed on a Schlenk line under a nitrogen flow. The $W(CO)_6$ solution was heated to 330 °C, after which the Ni_3Se_4/Ph_2Se_2 solution was swiftly injected. The reaction proceeded for a total of 30 min, at which point the heating mantle was removed and the solution left to cool to room-temperature. Nanocrystals were washed by dispersion in 10 ml 2:1 tol/EtOH and collected via centrifugation for 5 min at 3400 rpm. The washing was repeated a total of 3 times.

Fully covered nanocrystals (100 eq OA/W) were synthesized in the same manner as with 1000 eq OA/W using 0.9 ml OA and 8.9 g TOPO for the $W(CO)_6$ solution. Nanocrystals with 0 eq OA/W were synthesized in the same manner as with 1000 eq OA/W using 10 g TOPO for the $W(CO)_6$ solution.

Removal of Ni_3Se_4 nanocrystal cores. Freshly washed core/shell nanocrystals were dried under vacuum for 1 hour and pumped into a nitrogen-filled glove box. In a 20-ml vial capped with a septum, 1 ml each of $Et_2N_2H_4$ and TOP and 5 ml $CHCl_3$ were added to the nanocrystals. This mixture was sonicated until nanocrystals dispersed and was placed on a Schlenk line under nitrogen flow. The solution was stirred at room-temperature for 3 days, after which the flask was open to air and 2 ml MeOH was added. Hollow nanocrystals collected via centrifugation for 5 min

at 3400 rpm. The black pellet was dispersed in 3 ml DI water with sonication and precipitated with 6 ml EtOH. The washing was repeated a total of 5 times.

To collect $[Ni(Et_2N_2H_4)_3]^{2+}$ following Ni_3Se_4 core removal the supernatant was placed under vacuum and solvents were removed until a yellow oil and a purple crystalline powder remained. The oil was removed by extraction with 3 ml each hexanes and water, keeping only the purple aqueous layer.

Synthesis of Co_3Se_4/WSe_2 core/shell nanocrystals. To a 100-ml 3-neck round-bottom flask 36.0 mg $Co(acac)_3$ (0.1 mmol), 17 ml OA, and 4 g TOPO were added. This mixture was degassed by under vacuum at 120 °C for 2 h, and brought into a nitrogen-filled glovebox, where 46.8 mg (0.13 mmol) $W(CO)_6$ was added. This mixture was placed back on the Schlenk line and heated under nitrogen flow. Once the solution reached 330 °C, 160 mg (0.5 mmol) Ph_2Se_2 in 2.5 ml OA was swiftly injected into the flask. The reaction proceeded for a total of 2 h, after which the heating mantle was removed and the solution left to cool to room-temperature. Nanocrystals were washed by dispersion in 10 ml 2:1 tol/EtOH and collected via centrifugation for 5 min at 3400 rpm. The washing was repeated a total of 3 times

Synthesis of $Cu_{2-x}Se/Cu_2WSe_4$ core/shell nanocrystals. In a 100-ml 3-neck round-bottom flask 9.9 mg (0.1 mmol) CuCl was dissolved in 17 ml OA and 2 g TOPO. This solution was degassed by pulling vacuum at 120 °C for 2 h, and then pumped into a nitrogen-filled glovebox, where 20 mg (0.06 mmol) $W(CO)_6$ was added. This mixture was then placed back on the Schlenk line and heated under a nitrogen flow. Once the solution reached 330 °C, 96 mg (0.3 mmol) Ph_2Se_2 in 1.5 ml OA was added dropwise over 2 min. The reaction proceeded for a total of 30 min, at which point the heating mantle was removed and the solution left to cool to room-temperature.

Nanocrystals were washed by dispersion in 10 ml 2:1 tol/EtOH and collected via centrifugation for 5 min at 3400 rpm. The washing was repeated a total of 3 times.

Synthesis of $Cu_{2-x}Se/Cu_2WSe_4/WSe_2$ core/shell nanocrystals. In a 100-ml 3-neck round-bottom flask 9.9 mg (0.1 mmol) CuCl was dissolved in 17 ml OA and 5 g TOPO. This solution was degassed by pulling vacuum at 120 °C for 2 h, and then pumped into a nitrogen-filled glovebox, where 80 mg (0.23 mmol) $W(CO)_6$ was added. This mixture was then placed back on the Schlenk line and heated under a nitrogen flow. Once the solution reached 330 °C, 160 mg (0.5 mmol) Ph_2Se_2 in 2.5 ml OA was added dropwise over 2 min. The reaction proceeded for a total of 30 min, at which point the heating mantle was removed and the solution left to cool to room-temperature. Nanocrystals were washed by dispersion in 10 ml 2:1 tol/EtOH and collected via centrifugation for 5 min at 3400 rpm. The washing was repeated a total of 3 times.

Characterization. TEM grids were prepared by drop-casting a suspension of nanocrystals in toluene onto a 100-mesh copper TEM grid coated with formvar and carbon (Electron Microscopy Sciences). TEM images were collected on a FEI Spirit operating at 120 keV. High resolution transmission electron microscopy, scanning transmission electron microscopy (STEM), and energy dispersive X-ray spectroscopy images were collected using a JEOL JEM-2800 TEM. Powder X-ray diffraction samples were prepared by drying the pellet produced from washing the nanocrystals a portion of this pellet was then attached to a loop and mounted on the instrument. The powder pattern of hollow WSe_2 nanocrystals was collected using a Bruker K3 Kappa Vantec 500 diffractometer. All other patterns were collected using a D8 Smart diffractometer with a Pt-135 detector equipped with a Rigaku MicroMax-007HF High-intensity Microfocus rotating anode at 40 kV, 25 mA and Varimax-HF double bounce optics. All patterns were collected under Cu K_α radiation. Diffraction images were merged/integrated in Diffrac.EVA V.4.3.0.1 (Bruker).

3.6 Appendix: Supporting Information

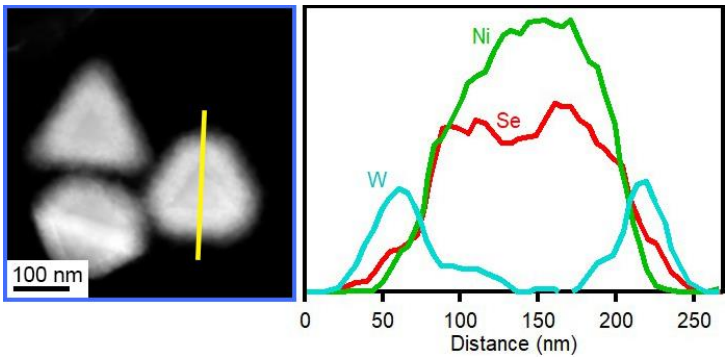

Figure S3. 1. Line-scan corresponding to STEM-EDS mapping images shown in Figure 3.1.

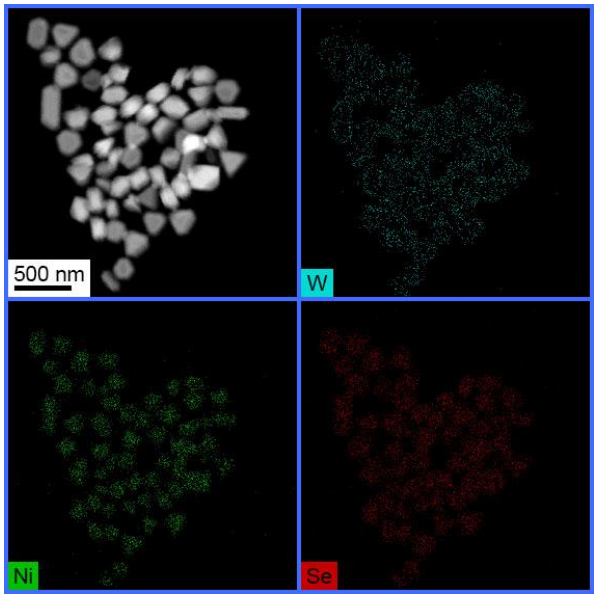

Figure S3. 2. STEM-EDS mapping images of Ni_3Se_4/WSe_2 heterostructures shown in Figure 3.1.

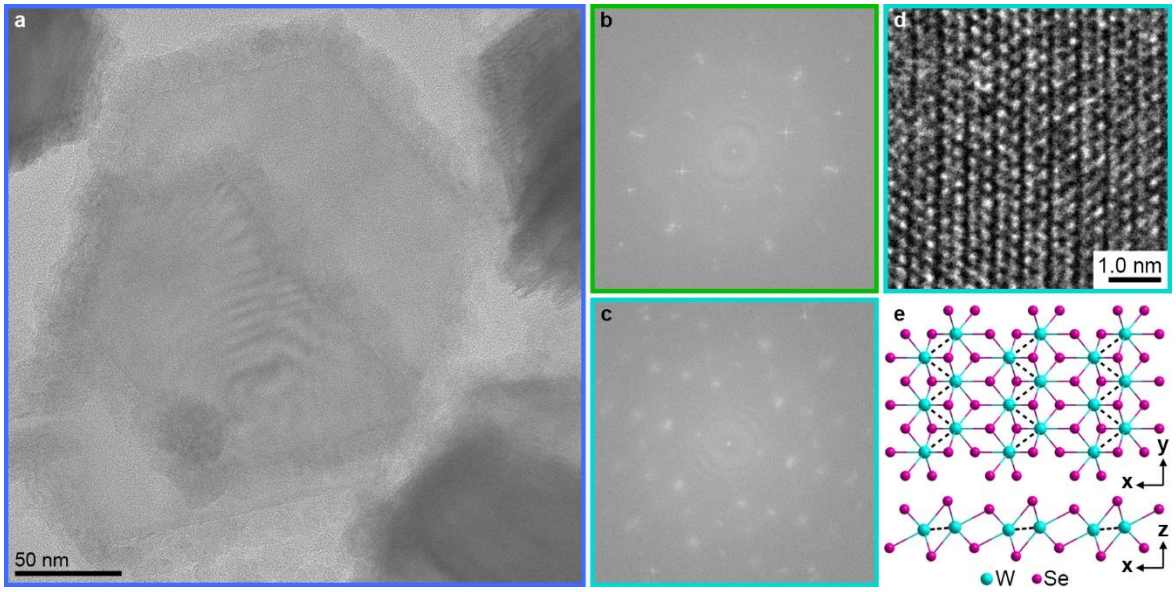

Figure S3. 3. (a) TEM image of Ni_3Se_4/WSe_2 heterostructures grown by rapid injection of 0.3 mmol Ph_2Se_2 in 1 ml OA into a solution of 0.1 mmol $Ni(acac)_2$ and 0.06 mmol $W(CO)_6$ in 17 ml OA and 2 g TOPO at 330 °C. Corresponding FFTs on selected regions of the **(b)** Ni_3Se_4 core and **(c)** WSe_2 shell. **(d)** High-resolution TEM of the WSe_2 shell displaying the zig-zag pattern characteristic of the 1T′ (2M) crystal phase. **(e)** Top and side views of a 1T′ layer of WSe_2 with the zig-zag pattern indicated in black dashed lines.

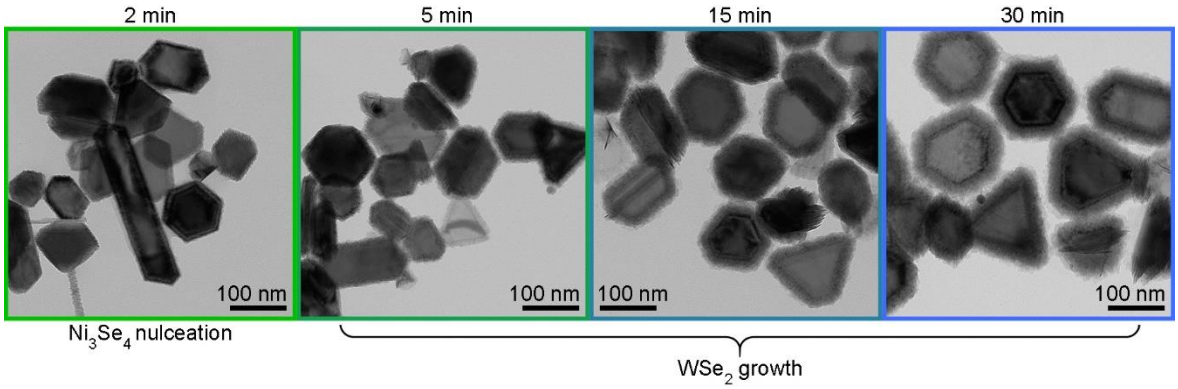

Figure S3. 4. One-pot synthesis of Ni_3Se_4/WSe_2 heterostructures grown by rapid injection of 0.3 mmol Ph_2Se_2 in 1.5 ml OA into a solution of 0.1 mmol $Ni(acac)_2$ and 0.06 mmol $W(CO)_6$ in 17 ml OA and 2 g TOPO at 330 °C. (a) TEM images of aliquots taken 2, 5, 15 and 30 min after injection of Ph_2Se_2, showing that WSe_2 shell thickness increases with time after injection.

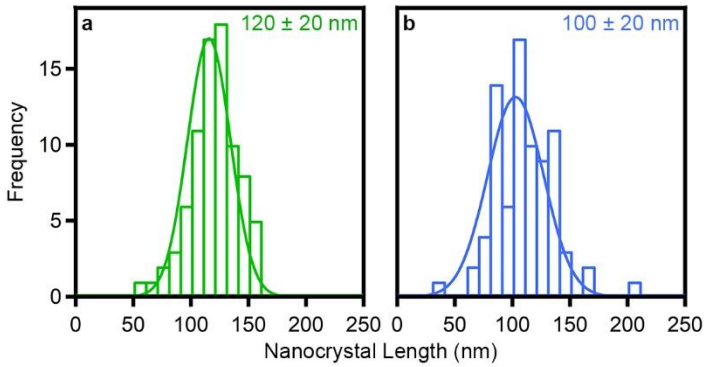

Figure S3. 5. Statistical analysis of Ni_3Se_4 nanocrystal cores shown in Figure 3.1. Aliquots taken **(a)** 5 and **(b)** 30 min after injection of Ph_2Se_2.

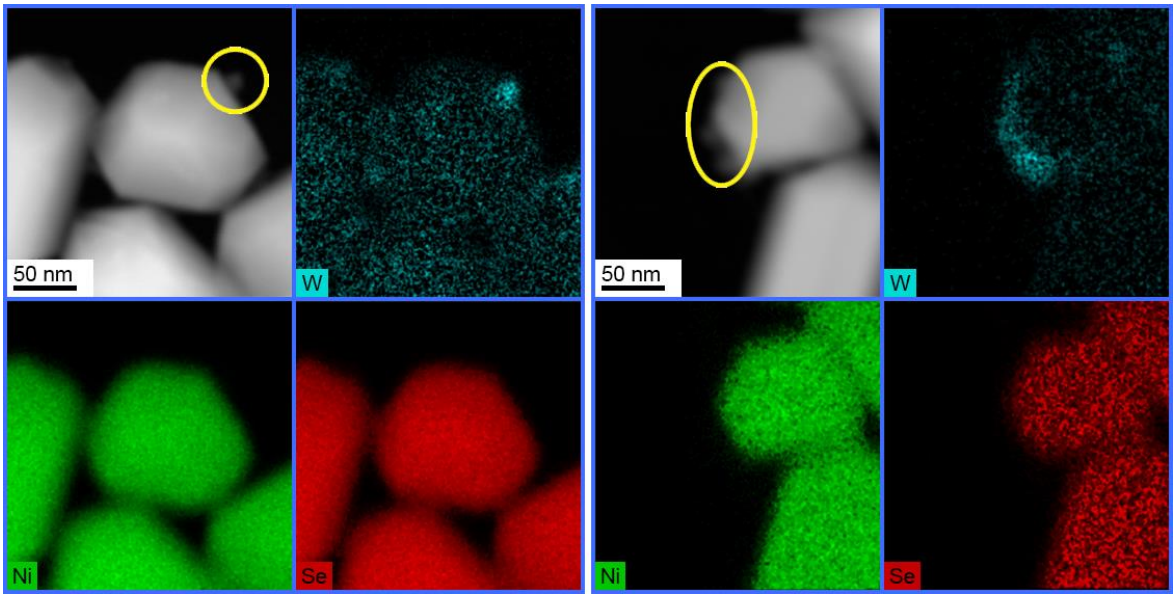

Figure S3. 6. STEM-EDS mapping images of Ni_3Se_4 nanocrystals from an aliquot taken 2 min following rapid injection of 0.3 mmol Ph_2Se_2 in 1.5 ml OA into a solution of 0.1 mmol $Ni(acac)_2$ and 0.06 mmol $W(CO)_6$ in 17 ml OA and 2 g TOPO at 330 °C.

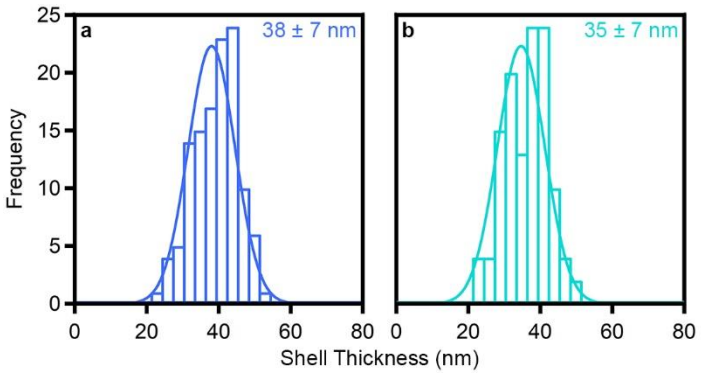

Figure S3. 7. Statistical analysis of WSe_2 shells shown in Figure 3S.4 **(a)** before and **(b)** after removal of Ni_3Se_4 cores.

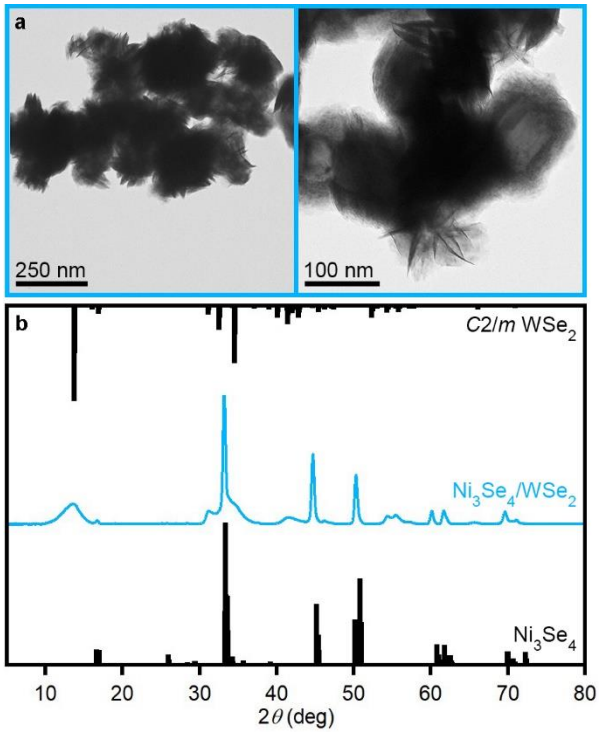

Figure S3. 8. (a) TEM images and **(b)** powder X-ray diffraction pattern of Ni_3Se_4/WSe_2 heterostructures synthesized in the presence of 100 eq OA/W. Specifically 0.15 mmol Ph_2Se_2 in 0.75 ml ODE was rapidly injected into a solution of 0.05 mmol $Ni(acac)_2$ and 0.03 mmol $W(CO)_6$ in 0.9 ml OA and 8.9 g TOPO at 330 °C.

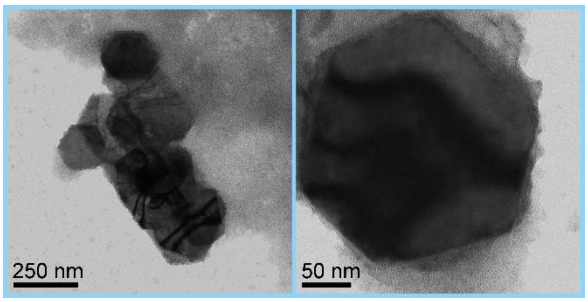

Figure S3. 9. TEM images of attempt to grow WSe_2 on Ni_3Se_4 without inclusion of OA. Specifically, 0.06 mmol Ph_2Se_2 was added to 1 ml Ni_3Se_4 nanocrystal (Figure 3.3a) stock solution in ODE. This solution was injected into 0.03 mmol $W(CO)_6$ in 10 g TOPO at 330 °C. The lack of OA or other coordinating ligand enables rapid, primary nucleation of small nanocrystals instead of only secondary nucleation onto the Ni_3Se_4 nanocrystals.

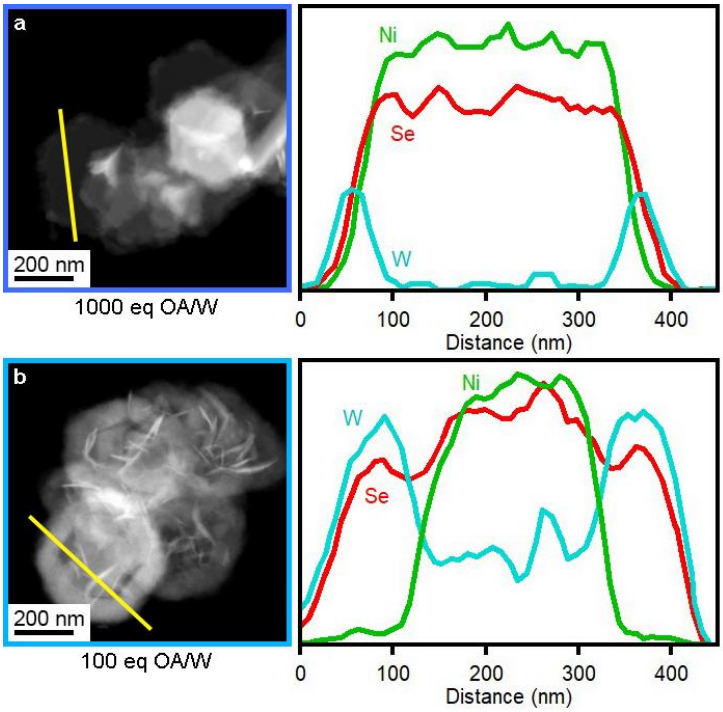

Figure S3. 10. Dark field TEM images and corresponding line-scans of WSe_2 grown onto Ni_3Se_4 nanoplatelets in the presence of **(a)** 1000 eq OA/W and **(b)** 100 eq OA/W. The line-scan of the 100-eq heterostructures reveals a ratio of ~2:1 W on the nanocrystal edge:face. The ratio of edge:face W is clearly much lower than 2:1 in the 1000-eq heterostructures, suggesting that edge growth is preferred.

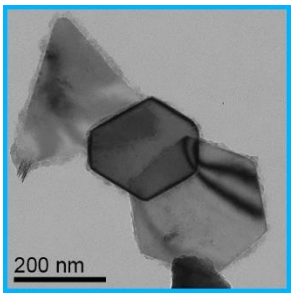

Figure S3. 11. TEM image of aliquot taken at 5 min of shell-growth of WSe_2 in the presence of 100 eq OA/W. Only deposition of the WSe_2 at the edges is observed.

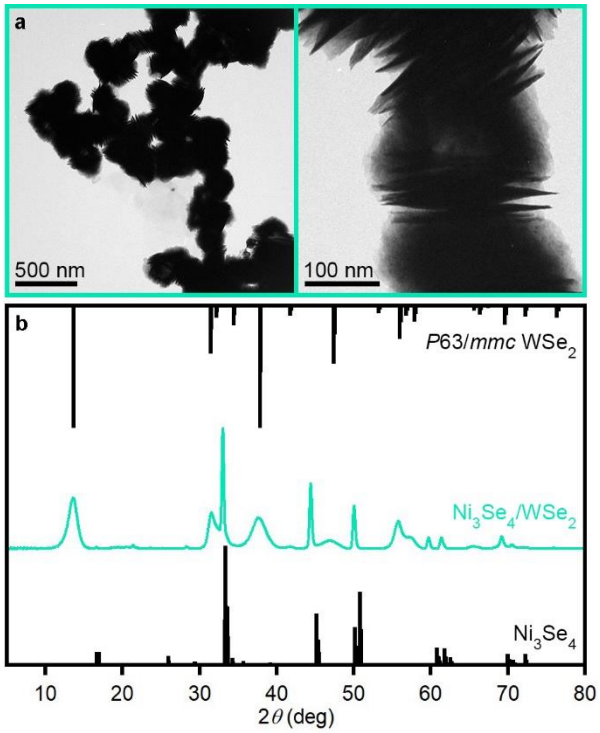

Figure S3. 12. (a) TEM images and **(b)** powder X-ray diffraction pattern of Ni_3Se_4/WSe_2 heterostructures synthesized in the presence of 100 eq phenylacetic acid (PAA). Specifically, 0.15 mmol Ph_2Se_2 in 0.75 ml ODE was rapidly injected into a solution of 0.05 mmol $Ni(acac)_2$ and 0.03 mmol $W(CO)_6$ in 0.39 g PAA and 8.9 g TOPO at 330 °C. This synthesis yields heterostructures shelled with the thermodynamically favored 2H phase of WSe_2, possibly due to greater mobility of the PAA ligand and/or to lower ligand amounts.[22] This synthesis could not be performed at 1000 eq PAA/W due to the lower boiling point of PAA.

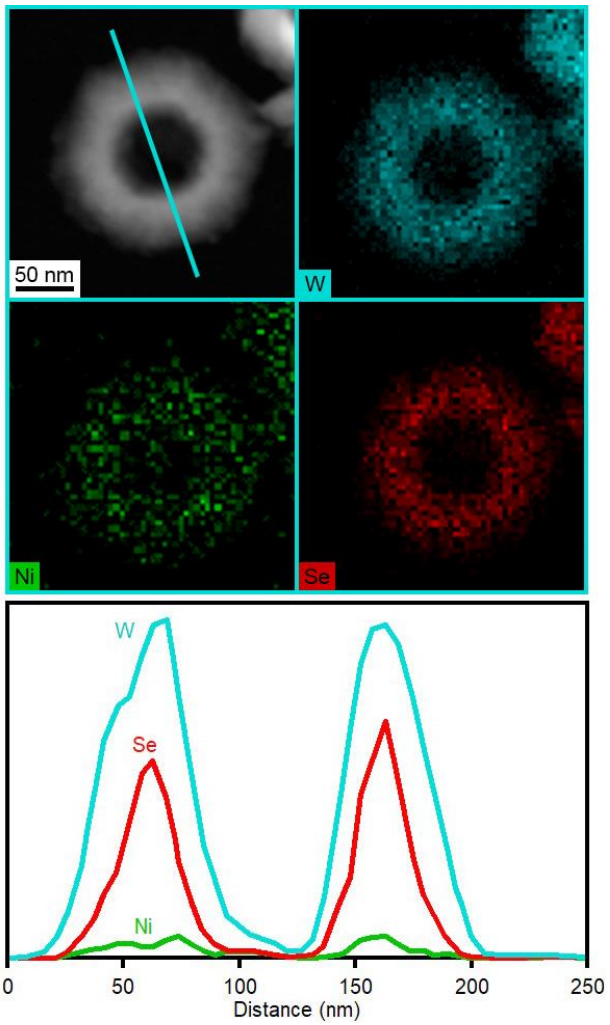

Figure S3. 13. STEM-EDS mapping images and corresponding line-scan of hollow WSe_2 nanocrystals formed by anaerobic treatment of heterostructures with $Et_2N_2H_4$ and TOP in chloroform for 3 days. Small amounts of Ni remaining in the shell are likely due to co-intercalation with $Et_2N_2H_4$.

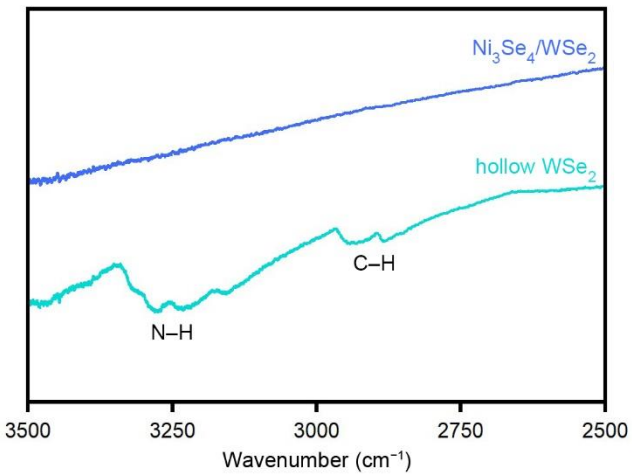

Figure S3. 14. IR absorption of Ni_3Se_4/WSe_2 heterostructures (top, blue) after 3 washes post-synthesis, showing no detectable ligands remaining. The heterostructures were soaked anaerobically with $Et_2N_2H_4$ and TOP in chloroform for 3 days, after which they were washed 5 times with 9 ml H_2O/EtOH (1:2). The IR absorption of the resulting hollow nanocrystals (bottom, teal) shows N–H and C–H stretches, indicative of $Et_2N_2H_4$ intercalation.

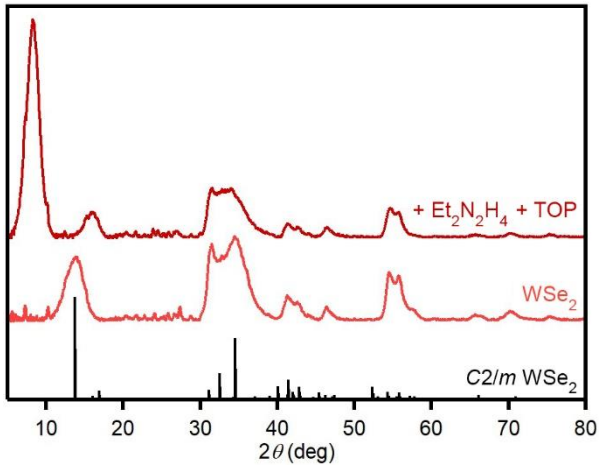

Figure S3. 15. Powder X-ray diffraction patterns of WSe_2 nanocrystals before (bottom) and after (top) anaerobic treatment with $Et_2N_2H_4$ and TOP in chloroform for 3 days. The WSe_2 nanocrystals were synthesized following a previously published procedure.[22] The WSe_2 interlayer expansion of 0.41 following intercalation is less than that observed when Ni is present, further supporting co-intercalation of Ni along with $Et_2N_2H_4$ in the case of the heterostructures.

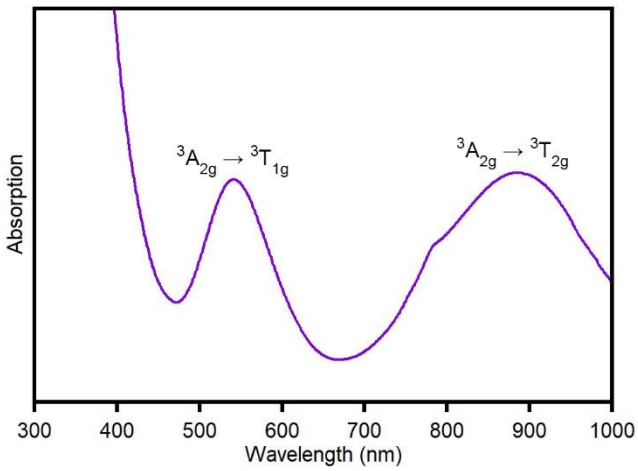

Figure S3. 16. Absorption spectrum of complex isolated from supernatant after Ni_3Se_4/WSe_2 heterostructures were anaerobically treated with $Et_2N_2H_4$ and TOP in chloroform for 3 days. The location of the $^3A_{2g} \rightarrow {}^3T_{2g}$ (884 nm) and $^3A_{2g} \rightarrow {}^3T_{1g}$ (541 nm) transitions are indicative of $[Ni(Et_2N_2H_4)_3]^{2+}$.[89]

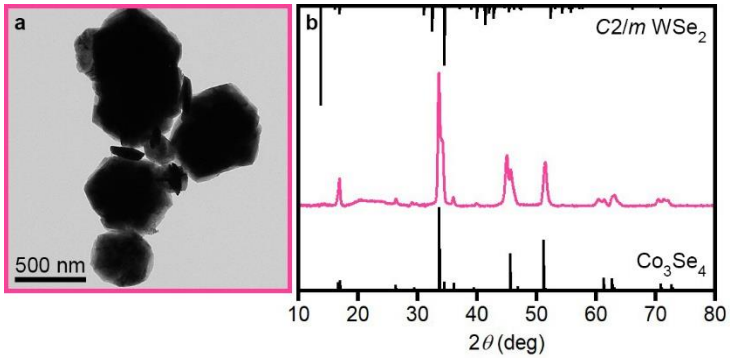

Figure S3. 17. (a) TEM image and **(b)** powder X-ray diffraction pattern of Co_3Se_4/WSe_2 heterostructures synthesized by injection of 0.3 mmol Ph_2Se_2 in 1.5 ml OA into a solution of 0.1 mmol $Co(acac)_3$ and 0.06 mmol $W(CO)_6$ in 17 ml OA and 2 g TOPO at 330 °C. Nanocrystals were grown for 30 min.

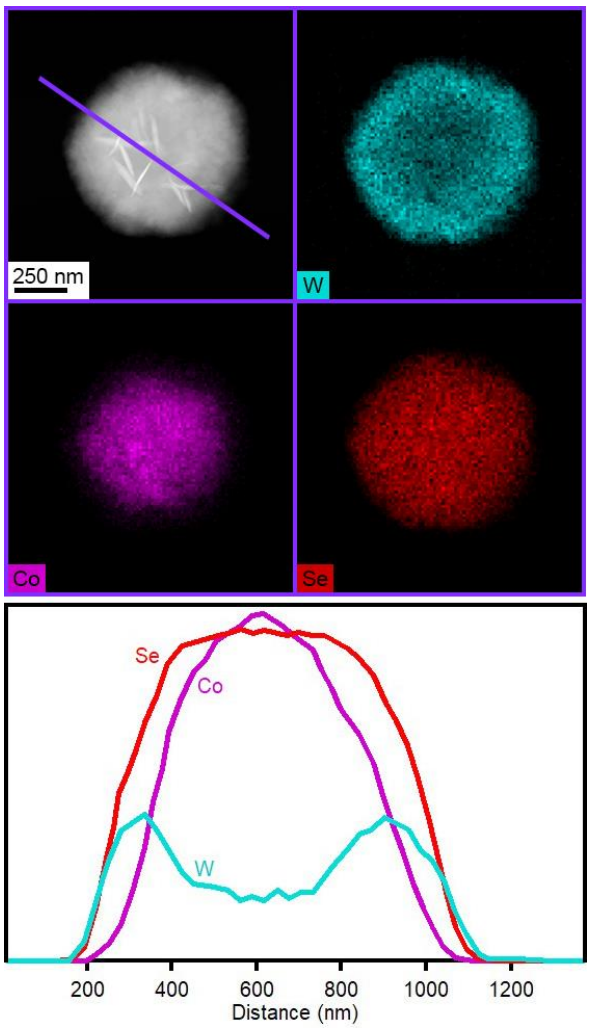

Figure S3. 18. STEM-EDS mapping images and corresponding line-scan of Co_3Se_4/WSe_2 heterostructures synthesized by rapid injection of 0.5 mmol Ph_2Se_2 in 2.5 ml OA into a solution of 0.1 mmol $Co(acac)_3$ and 0.13 mmol $W(CO)_6$ in 17 ml OA and 4 g TOPO at 330 °C. Nanocrystals were grown for 2 h.

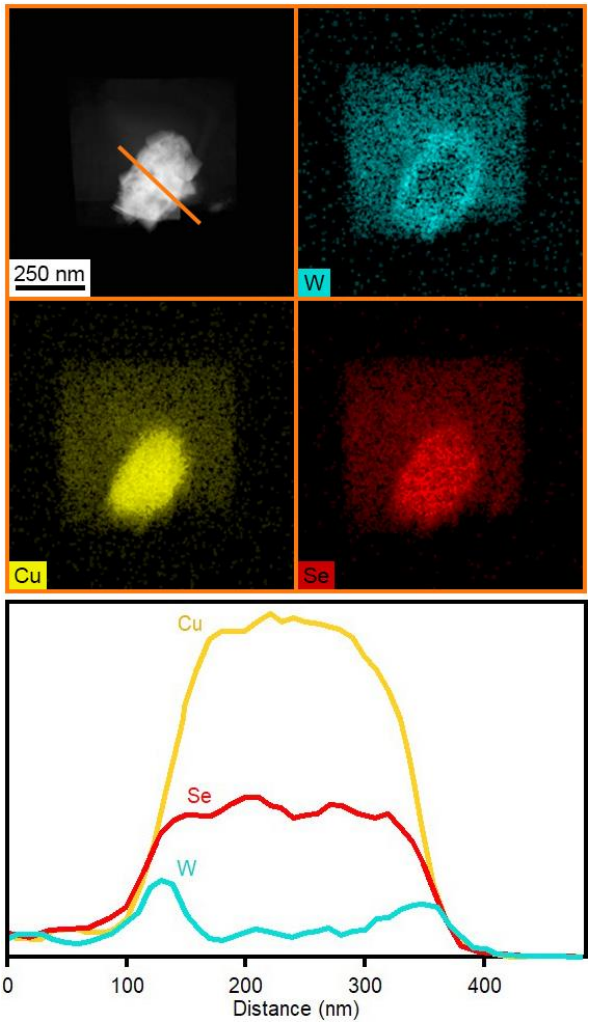

Figure S3. 19. STEM-EDS mapping images and corresponding line-scan of $Cu_{2-x}Se/Cu_2WSe_4$ heterostructures synthesized by rapid injection of 0.3 mmol Ph_2Se_2 in 1.5 ml OA into a solution of 0.1 mmol CuCl and 0.06 mmol $W(CO)_6$ in 17 ml OA and 2 g TOPO at 330 °C. Nanocrystals were grown for 60 min. Mapping reveals a $Cu_{2-x}Se$ with a shell of Cu_2WSe_4 surrounded by a thin sheet of Cu_2WSe_4.

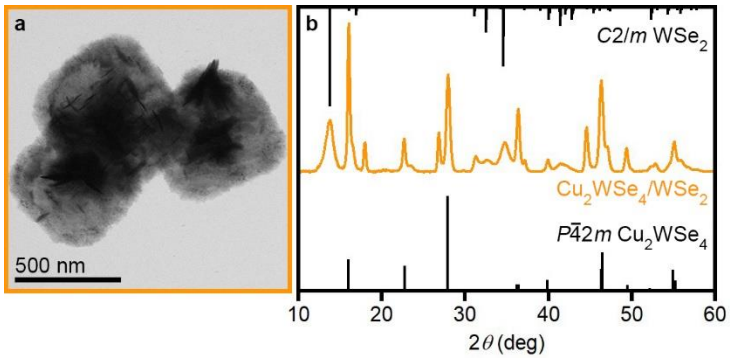

Figure S3. 20. (a) TEM image and **(b)** powder X-ray diffraction pattern of 60-min aliquot for synthesis of Cu_2WSe_4/WSe_2 heterostructures synthesized by dropwise addition of 0.5 mmol Ph_2Se_2 in 2.5 ml OA into a solution of 0.1 mmol CuCl and 0.23 mmol $W(CO)_6$ in 17 ml OA and 5 g TOPO at 330 °C.

3.7 Acknowledgments

Chapter 3, in full, is a reprint of the material as it appears in "Manipulation of Precursor Reactivity for the Facile Synthesis of Heterostructured and Hollow Metal Selenide Nanocrystals." Chem. Mater. 2022, *32*, 2304-2312. The dissertation author was the primary author of this paper and gratefully acknowledges the contributions of coauthors Ashley K. Tamura and Alina M. Schimpf.

3.8 References

1. Cushing, B. L.; Kolesnichenko, V. L.; O'Connor, C. J., Recent Advances in the Liquid-Phase Syntheses of Inorganic Nanoparticles. *Chem Rev* **2004,** *104* (9), 3893-3946.

2. Yin, Y.; Alivisatos, A. P., Colloidal Nanocrystal Synthesis and the Organic–Inorganic Interface. *Nature* **2005,** *437* (7059), 664-670.

3. Alvarado, S. R.; Guo, Y. J.; Ruberu, T. P. A.; Tavasoli, E.; Vela, J., Inorganic Chemistry Solutions to Semiconductor Nanocrystal Problems. *Coordin Chem Rev* **2014,** *263*, 182-196.

4. Pu, Y.; Cai, F. H.; Wang, D.; Wang, J. X.; Chen, J. F., Colloidal Synthesis of Semiconductor Quantum Dots toward Large Scale Production: A Review. *Ind Eng Chem Res* **2018,** *57* (6), 1790-1802.

5. Murray, C. B.; Norris, D. J.; Bawendi, M. G., Synthesis and Characterization of Nearly Monodisperse Cde (E = S, Se, Te) Semiconductor Nanocrystallites. *J Am Chem Soc* **1993,** *115* (19), 8706-8715.

6. Bawendi, M. G.; Steigerwald, M. L.; Brus, L. E., The Quantum-Mechanics of Larger Semiconductor Clusters (Quantum Dots). *Annu Rev Phys Chem* **1990,** *41*, 477-496.

7. Rossetti, R.; Nakahara, S.; Brus, L. E., Quantum Size Effects in the Redox Potentials, Resonance Raman-Spectra, and Electronic-Spectra of Cds Crystallites in Aqueous-Solution. *J Chem Phys* **1983,** *79* (2), 1086-1088.

8. Hines, M. A.; Scholes, G. D., Colloidal PbS Nanocrystals with Size-Tunable Near-Infrared Emission: Observation of Post-Synthesis Self-Narrowing of the Particle Size Distribution. *Adv. Mater.* **2003,** *15* (21), 1844-1849.

9. Murray, C. B.; Sun, S. H.; Gaschler, W.; Doyle, H.; Betley, T. A.; Kagan, C. R., Colloidal Synthesis of Nanocrystals and Nanocrystal Superlattices. *Ibm J Res Dev* **2001,** *45* (1), 47-56.

10. Peng, X. G.; Manna, L.; Yang, W. D.; Wickham, J.; Scher, E.; Kadavanich, A.; Alivisatos, A. P., Shape Control of CdSe Nanocrystals. *Nature* **2000,** *404* (6773), 59-61.

11. Manna, L.; Scher, E. C.; Alivisatos, A. P., Synthesis of Soluble and Processable Rod-, Arrow-, Teardrop-, and Tetrapod-Shaped CdSe Nanocrystals. *J Am Chem Soc* **2000,** *122* (51), 12700-12706.

12. Talapin, D. V.; Koeppe, R.; Gotzinger, S.; Kornowski, A.; Lupton, J. M.; Rogach, A. L.; Benson, O.; Feldmann, J.; Weller, H., Highly Emissive Colloidal CdSe/CdS Heterostructures of Mixed Dimensionality. *Nano Lett* **2003,** *3* (12), 1677-1681.

13. Puntes, V. F.; Krishnan, K. M.; Alivisatos, A. P., Colloidal Nanocrystal Shape and Size Control: The Case of Cobalt. *Science* **2001,** *291* (5511), 2115-2117.

14. Manna, L.; Milliron, D. J.; Meisel, A.; Scher, E. C.; Alivisatos, A. P., Controlled Growth of Tetrapod-Branched Inorganic Nanocrystals. *Nat. Mater.* **2003,** *2* (6), 382-385.

15. Yu, W. W.; Wang, Y. A.; Peng, X. G., Formation and stability of Size-, Shape-, and Structure-Controlled CdTe Nanocrystals: Ligand Effects on Monomers and Nanocrystals. *Chem Mater* **2003,** *15* (22), 4300-4308.

16. Jun, Y. W.; Casula, M. F.; Sim, J. H.; Kim, S. Y.; Cheon, J.; Alivisatos, A. P., Surfactant-Assisted Elimination of a High Energy Facet as a Means of Controlling the Shapes of TiO_2 Nanocrystals. *J Am Chem Soc* **2003,** *125* (51), 15981-15985.

17. Yang, T.-H.; Shi, Y.; Janssen, A.; Xia, Y., Surface Capping Agents and Their Roles in Shape-Controlled Synthesis of Colloidal Metal Nanocrystals. *Angew. Chem. Int. Edit.* **2019,** *0* (ja).

18. Rhodes, J. M.; Jones, C. A.; Thal, L. B.; Macdonald, J. E., Phase-Controlled Colloidal Syntheses of Iron Sulfide Nanocrystals via Sulfur Precursor Reactivity and Direct Pyrite Precipitation. *Chem Mater* **2017,** *29* (19), 8521-8530.

19. Tappan, B. A.; Barim, G.; Kwok, J. C.; Brutchey, R. L., Utilizing Diselenide Precursors toward Rationally Controlled Synthesis of Metastable CuInSe2 Nanocrystals. *Chem Mater* **2018,** *30* (16), 5704-5713.

20. Gao, Y.; Peng, X., Crystal structure control of CdSe nanocrystals in growth and nucleation: dominating effects of surface versus interior structure. *J Am Chem Soc* **2014,** *136* (18), 6724-32.

21. Mahler, B.; Hoepfner, V.; Liao, K.; Ozin, G. A., Colloidal Synthesis of 1T-WS_2 and 2H-WS_2 Nanosheets: Applications for Photocatalytic Hydrogen Evolution. *J Am Chem Soc* **2014,** *136* (40), 14121-7.

22. Geisenhoff, J. Q.; Tamura, A. K.; Schimpf, A. M., Using Ligands to Control Reactivity, Size and Phase in the Colloidal Synthesis of WSe_2 Nanocrystals. *Chem. Commun.* **2019,** *55* (60), 8856-8859.

23. Vlaskin, V. A.; Barrows, C. J.; Erickson, C. S.; Gamelin, D. R., Nanocrystal Diffusion Doping. *J Am Chem Soc* **2013,** *135* (38), 14380-14389.

24. Milliron, D. J.; Hughes, S. M.; Cui, Y.; Manna, L.; Li, J. B.; Wang, L. W.; Alivisatos, A. P., Colloidal Nanocrystal Heterostructures with Linear and Branched Topology. *Nature* **2004,** *430* (6996), 190-195.

25. Costi, R.; Saunders, A. E.; Banin, U., Colloidal Hybrid Nanostructures: A New Type of Functional Materials. *Angew. Chem. Int. Edit.* **2010,** *49* (29), 4878-97.

26. Donega, C. D., Synthesis and Properties of Colloidal Heteronanocrystals. *Chem Soc Rev* **2011,** *40* (3), 1512-1546.

27. Ji, B. T.; Giovanelli, E.; Habert, B.; Spinicelli, P.; Nasilowski, M.; Xu, X. Z.; Lequeux, N.; Hugonin, J. P.; Marquier, F.; Greffet, J. J.; Dubertret, B., Non-Blinking Quantum Dot with a Plasmonic Nanoshell Resonator. *Nat Nanotechnol* **2015,** *10* (2), 170-175.

28. Jang, Y. J.; Shapiro, A.; Horani, F.; Abu-Hariri, A.; Lifshitz, E., Recent Advances in Colloidal IV–VI Core/Shell Heterostructured Nanocrystals. *J Phys Chem C* **2018,** *122* (25), 13840-13847.

29. Tan, C. L.; Chen, J. Z.; Wu, X. J.; Zhang, H., Epitaxial Growth of Hybrid Nanostructures. *Nat Rev Mater* **2018,** *3* (2).

30. Fenton, J. L.; Steimle, B. C.; Schaak, R. E., Tunable Intraparticle Frameworks for Creating Complex Heterostructured Nanoparticle Libraries. *Science* **2018,** *360* (6388), 513-517.

31. Vinokurov, K.; Macdonald, J. E.; Banin, U., Structures and Mechanisms in the Growth of Hybrid Ru–Cu_2S Nanoparticles: From Cages to Nanonets. *Chem Mater* **2012,** *24* (10), 1822-1827.

32. Straney, P. J.; Diemler, N. A.; Smith, A. M.; Eddinger, Z. E.; Gilliam, M. S.; Millstone, J. E., Ligand-Mediated Deposition of Noble Metals at Nanoparticle Plasmonic Hotspots. *Langmuir* **2018,** *34* (3), 1084-1091.

33. Smith, J. D.; Bunch, C. M.; Li, Y. D.; Koczkur, K. M.; Skrabalak, S. E., Surface Versus Solution Chemistry: Manipulating Nanoparticle Shape and Composition Through Metal–Thiolate Interactions. *Nanoscale* **2019,** *11* (2), 512-519.

34. Hines, M. A.; Guyot-Sionnest, P., Synthesis and Characterization of Strongly Luminescing ZnS-Capped CdSe Nanocrystals. *J Phys Chem-Us* **1996,** *100* (2), 468-471.

35. Talapin, D. V.; Rogach, A. L.; Kornowski, A.; Haase, M.; Weller, H., Highly Luminescent Monodisperse CdSe and CdSe/ZnS Nanocrystals Synthesized in a Hexadecylamine–Trioctylphosphine Oxide–Trioctylphospine Mixture. *Nano Lett* **2001,** *1* (4), 207-211.

36. Li, J. J.; Wang, Y. A.; Guo, W. Z.; Keay, J. C.; Mishima, T. D.; Johnson, M. B.; Peng, X. G., Large-Scale Synthesis of Nearly Monodisperse CdSe/CdS Core/Shell Nanocrystals Using Air-Stable Reagents via Successive Ion Layer Adsorption and Reaction. *J Am Chem Soc* **2003,** *125* (41), 12567-12575.

37. Talapin, D. V.; Mekis, I.; Gotzinger, S.; Kornowski, A.; Benson, O.; Weller, H., CdSe/CdS/ZnS and CdSe/ZnSe/ZnS Core–Shell–Shell Nanocrystals. *J Phys Chem B* **2004,** *108* (49), 18826-18831.

38. Brumer, M.; Kigel, A.; Amirav, L.; Sashchiuk, A.; Solomesch, O.; Tessler, N.; Lifshitz, E., PbSe/PbS and PbSe/PbSe$_x$S$_{1-x}$ Core/Shell Nanocrystals. *Adv. Funct. Mater.* **2005,** *15* (7), 1111-1116.

39. Xie, R. G.; Kolb, U.; Li, J. X.; Basche, T.; Mews, A., Synthesis and Characterization of Highly Luminescent CdSe–Core CdS/Zn$_{0.5}$Cd$_{0.5}$S/ZnS Multishell Nanocrystals. *J Am Chem Soc* **2005,** *127* (20), 7480-7488.

40. Kim, H.; Achermann, M.; Balet, L. P.; Hollingsworth, J. A.; Klimov, V. I., Synthesis and Characterization of Co/CdSe Core/Shell Nanocomposites: Bifunctional Magnetic-Optical Nanocrystals. *J Am Chem Soc* **2005,** *127* (2), 544-6.

41. Chen, Y.; Vela, J.; Htoon, H.; Casson, J. L.; Werder, D. J.; Bussian, D. A.; Klimov, V. I.; Hollingsworth, J. A., "Giant" Multishell CdSe Nanocrystal Quantum Dots with Suppressed Blinking. *J Am Chem Soc* **2008,** *130* (15), 5026-5027.

42. Mahler, B.; Spinicelli, P.; Buil, S.; Quelin, X.; Hermier, J. P.; Dubertret, B., Towards Non-Blinking Colloidal Quantum Dots. *Nat. Mater.* **2008,** *7* (8), 659-664.

43. Capek, R. K.; Lambert, K.; Dorfs, D.; Smet, P. F.; Poelman, D.; Eychmuller, A.; Hens, Z., Synthesis of Extremely Small CdSe and Bright Blue Luminescent CdSe/ZnS Nanoparticles by a Prefocused Hot-Injection Approach. *Chem Mater* **2009,** *21* (8), 1743-1749.

44. Reiss, P.; Protiere, M.; Li, L., Core/Shell Semiconductor Nanocrystals. *Small* **2009,** *5* (2), 154-168.

45. Smith, A. M.; Nie, S. M., Semiconductor Nanocrystals: Structure, Properties, and Band Gap Engineering. *Accounts Chem. Res.* **2010,** *43* (2), 190-200.

46. Zhang, Y.; Dai, Q. Q.; Li, X. B.; Cui, Q. Z.; Gu, Z. Y.; Zou, B.; Wang, Y. D.; Yu, W. W., Formation of PbSe/CdSe Core/Shell Nanocrystals for Stable Near-Infrared High Photoluminescence Emission. *Nanoscale Res Lett* **2010,** *5* (8), 1279-1283.

47. Chaudhuri, R. G.; Paria, S., Core/Shell Nanoparticles: Classes, Properties, Synthesis Mechanisms, Characterization, and Applications. *Chem Rev* **2012,** *112* (4), 2373-2433.

48. Chen, O.; Zhao, J.; Chauhan, V. P.; Cui, J.; Wong, C.; Harris, D. K.; Wei, H.; Han, H. S.; Fukumura, D.; Jain, R. K.; Bawendi, M. G., Compact High-Quality CdSe–CdS Core–Shell Nanocrystals with Narrow Emission Linewidths and Suppressed Blinking. *Nat. Mater.* **2013,** *12* (5), 445-451.

49. Chen, O.; Wei, H.; Maurice, A.; Bawendi, M.; Reiss, P., Pure Colors from Ccore–Shell Quantum Dots. *Mrs Bull* **2013,** *38* (9), 696-702.

50. Jun, S.; Jang, E., Bright and Stable Alloy Core/Multishell Quantum Dots. *Angew. Chem. Int. Edit.* **2013,** *52* (2), 679-682.

51. Lim, J.; Jeong, B. G.; Park, M.; Kim, J. K.; Pietryga, J. M.; Park, Y.-S.; Klimov, V. I.; Lee, C.; Lee, D. C.; Bae, W. K., Influence of Shell Thickness on the Performance of Light-Emitting Devices Based on CdSe/$Zn_{1-x}Cd_xS$ Core/Shell Heterostructured Quantum Dots. *Adv. Mater.* **2014,** *26* (47), 8034-8040.

52. Jeong, B. G.; Park, Y. S.; Chang, J. H.; Cho, I.; Kim, J. K.; Kim, H.; Char, K.; Cho, J.; Klirnov, V. I.; Park, P.; Lee, D. C.; Bae, W. K., Colloidal Spherical Quantum Wells with Near-Unity Photoluminescence Quantum Yield and Suppressed Blinking. *Acs Nano* **2016,** *10* (10), 9297-9305.

53. Shapiro, A.; Jang, Y. J.; Rubin-Brusilovski, A.; Budniak, A. K.; Horani, F.; Sashchiuk, A.; Lifshitz, E., Tuning Optical Activity of IV–VI Colloidal Quantum Dots in the Short-Wave Infrared (SWIR) Spectral Regime. *Chem Mater* **2016,** *28* (17), 6409-6416.

54. Owens, J.; Brus, L., Chemical Synthesis and Luminescence Applications of Colloidal Semiconductor Quantum Dots. *J Am Chem Soc* **2017,** *139* (32), 10939-10943.

55. Jang, Y. J.; Shapiro, A.; Isarov, M.; Rubin-Brusilovski, A.; Safran, A.; Budniak, A. K.; Horani, F.; Dehnel, J.; Sashchiuk, A.; Lifshitz, E., Interface Control of Electronic and Optical Properties in IV–VI and II–VI Core/Shell Colloidal Quantum Dots: A Review. *Chem. Commun.* **2017,** *53* (6), 1002-1024.

56. Kortan, A. R.; Hull, R.; Opila, R. L.; Bawendi, M. G.; Steigerwald, M. L.; Carroll, P. J.; Brus, L. E., Nucleation and Growth of Cdse on Zns Quantum Crystallite Seeds, and Vice Versa, in Inverse Micelle Media. *J Am Chem Soc* **1990,** *112* (4), 1327-1332.

57. Meng, N. N.; Zhou, Y. F.; Nie, W. Y.; Song, L. Y.; Chen, P. P., CuS/MoS_2 Nanocomposite with High Solar Photocatalytic Activity. *J Nanopart Res* **2015,** *17* (7).

58. Xu, J.; Cui, J. B.; Guo, C.; Zhao, Z. P.; Jiang, R.; Xu, S. Y.; Zhuang, Z. B.; Huang, Y.; Wang, L. Y.; Li, Y. D., Ultrasmall Cu7S4@MoS2 Hetero-Nanoframes with Abundant Active Edge Sites for Ultrahigh-Performance Hydrogen Evolution. *Angew. Chem. Int. Edit.* **2016,** *55* (22), 6502-6505.

59. Cui, J. B.; Jiang, R.; Lu, W. L.; Xu, S. Y.; Wang, L. Y., Plasmon-Enhanced Photoelectrical Hydrogen Evolution on Monolayer MoS_2 Decorated $Cu_{1.75}S$–Au Nanocrystals. *Small* **2017,** *13* (8).

60. Maiti, P. S.; Ganai, A. K.; Bar-Ziv, R.; Enyashin, A. N.; Houben, L.; Bar Sadan, M., $Cu_{2-x}S$–MoS_2 Nano-Octahedra at the Atomic Scale: Using a Template To Activate the Basal Plane of MoS_2 for Hydrogen Production. *Chem Mater* **2018,** *30* (14), 4489-4492.

61. Chen, J. Z.; Wu, X. J.; Gong, Y.; Zhu, Y. H.; Yang, Z. Z.; Li, B.; Lu, Q. P.; Yu, Y. F.; Han, S. K.; Zhang, Z. C.; Zong, Y.; Han, Y.; Gu, L.; Zhang, H., Edge Epitaxy of Two-Dimensional $MoSe_2$ and MoS_2 Nanosheets on One-Dimensional Nanowires. *J Am Chem Soc* **2017,** *139* (25), 8653-8660.

62. DiStefano, J. G.; Li, Y.; Jung, H. J.; Hao, S. Q.; Murthy, A. A.; Zhang, X. M.; Wolverton, C.; Dravid, V. P., Nanoparticle@MoS_2 Core–Shell Architecture: Role of the Core Material. *Chem Mater* **2018,** *30* (14), 4675-4682.

63. Ghosh, Y.; Mangum, B. D.; Casson, J. L.; Williams, D. J.; Htoon, H.; Hollingsworth, J. A., New Insights into the Complexities of Shell Growth and the Strong Influence of Particle Volume in Nonblinking "Giant" Core/Shell Nanocrystal Quantum Dots. *J Am Chem Soc* **2012,** *134* (23), 9634-9643.

64. Nakonechnyi, I.; Sluydts, M.; Justo, Y.; Jasieniak, J.; Hens, Z., Mechanistic Insights in Seeded Growth Synthesis of Colloidal Core/Shell Quantum Dots. *Chem Mater* **2017,** *29* (11), 4719-4727.

65. Yang, H. R.; Hamachi, L. S.; Rreza, I.; Wang, W.; Chan, E. M., Design Rules for One-Step Seeded Growth of Nanocrystals: Threading the Needle between Secondary Nucleation and Ripening. *Chem Mater* **2019,** *31* (11), 4173-4183.

66. Hamachi, L. S.; Yang, H. R.; Jen-La Plante, I.; Saenz, N.; Qian, K.; Campos, M. P.; Cleveland, G. T.; Rreza, I.; Oza, A.; Walravens, W.; Chan, E. M.; Hens, Z.; Crowther, A. C.; Owen, J. S., Precursor Reaction Kinetics Control Compositional Grading and Size of $CdSe_{1-x}S_x$ Nanocrystal Heterostructures. *Chem Sci* **2019,** *10* (26), 6539-6552.

67. Fang, Y. Q.; Pan, J.; Zhang, D. Q.; Wang, D.; Hirose, H. T.; Terashima, T.; Uji, S.; Yuan, Y. H.; Li, W.; Tian, Z.; Xue, J. M.; Ma, Y. H.; Zhao, W.; Xue, Q. K.; Mu, G.; Zhang, H.; Huang, F. Q., Discovery of Superconductivity in 2M WS_2 with Possible Topological Surface States. *Adv. Mater.* **2019,** *31* (30).

68. Fang, Y. Q.; Dong, Q.; Pan, J.; Liu, H. Y.; Liu, P.; Sun, Y. Y.; Li, Q. J.; Zhao, W.; Liu, B. B.; Huang, F. Q., Observation of Superconductivity in Pressurized 2M WSe_2 Crystals. *J Mater Chem C* **2019,** *7* (28), 8551-8555.

69. Cotton, F. A.; Darensbourg, D. J.; Kolthammer, B. W. S.; Kudaroski, R., Solid-State and Solution Structures of $[PNP][W(CO)_5O_2CCH_3]$ and $[PNP][W(CO)_4(PEt_3)O_2CCH_3]$ and the CO-Labilizing Ability of the Acetato Ligand in These Anionic Derivatives. *Inorg. Chem.* **1982,** *21* (4), 1656-1662.

70. Duerloo, K. A.; Li, Y.; Reed, E. J., Structural Phase Transitions in Two-Dimensional Mo- and W-Dichalcogenide Monolayers. *Nat Commun* **2014,** *5*, 4214.

71. Voiry, D.; Mohite, A.; Chhowalla, M., Phase engineering of transition metal dichalcogenides. *Chem Soc Rev* **2015,** *44* (9), 2702-2712.

72. Mokari, T.; Rothenberg, E.; Popov, I.; Costi, R.; Banin, U., Selective Growth of Metal Tips onto Semiconductor Quantum Rods and Tetrapods. *Science* **2004,** *304* (5678), 1787-90.

73. Liyanage, A. U.; Lerner, M. M., Use of Amine Electride Chemistry to Prepare Molybdenum Disulfide Intercalation Compounds. *Rsc Adv* **2014,** *4* (87), 47121-47128.

74. Figueroa, E.; Brill, J. W.; Selegue, J. P., New Intercalation Compounds of Transition Metal Dichalcogenides. *J Phys Chem Solids* **1996,** *57* (6-8), 1123-1127.

75. Boller, H.; Blaha, H., Intercalation Phases of TiS_2, 2H-NbS_2, and 1T-TaS_2 with Ethylenediamine and Trimethylenediamine: A Crystal Chemical and Thermogravimetric Study. *J Solid State Chem* **1982,** *45* (1), 119-126.

76. Ogata, H.; Fujimori, H.; Miyajima, S.; Kobashi, K.; Chiba, T.; Taylor, R. E.; Endo, K., Modification of Electronic Structure by Charge Transfer and Molecular Motion in Titanium Disulfide–Ethylenediamine Intercalation Compound. *J Phys Chem Solids* **1997,** *58* (5), 701-710.

77. Sines, I. T.; Schaak, R. E., Phase-Selective Chemical Extraction of Selenium and Sulfur from Nanoscale Metal Chalcogenides: A General Strategy for Synthesis, Purification, and Phase Targeting. *J Am Chem Soc* **2011,** *133* (5), 1294-7.

78. Eresen, N.; Kammel, R., Nickel Extractions from Limonite Type Laterite Ores by Pressure Leaching with Aqueous-Solutions of Polyamines. *Hydrometallurgy* **1981,** *7* (1-2), 41-60.

79. Jacobs, J. J., *Nickel and Cobalt Extraction Using Organic Compounds*. Pergamon: Oxford, England, 1985.

80. Willersinn, S.; Bart, H. J., Reactive Extraction and Critical Raw Materials: Industrial Recovery of Tungsten. *Chem-Ing-Tech* **2017,** *89* (1-2), 82-91.

81. Celustka, B.; Ogorelec, Z., Electrical Conduction and Self-Diffusion in Cuprous Selenide at High Temperature. *J Phys Chem Solids* **1966,** *27* (6-7), 957-&.

82. van der Stam, W.; Berends, A. C.; Donega, C. D., Prospects of Colloidal Copper Chalcogenide Nanocrystals. *Chemphyschem* **2016,** *17* (5), 559-581.

83. Coughlan, C.; Ibanez, M.; Dobrozhan, O.; Singh, A.; Cabot, A.; Ryan, K. M., Compound Copper Chalcogenide Nanocrystals. *Chem Rev* **2017,** *117* (9), 5865-6109.

84. Mantella, V.; Ninova, S.; Saris, S.; Loiudice, A.; Aschauer, U.; Buonsanti, R., Synthesis and Size-Dependent Optical Properties of Intermediate Band Gap Cu3VS4 Nanocrystals. *Chem Mater* **2019,** *31* (2), 532-540.

85. Cahen, D.; Noufi, R., Special Issue: Adventures in Cu-Chalcogenide Solar Cells. *Prog. Photovoltaics* **2012,** *20*.

86. Aldakov, D.; Lefrancois, A.; Reiss, P., Ternary and Quaternary Metal Chalcogenide Nanocrystals: Synthesis, Properties and Applications. *J Mater Chem C* **2013,** *1* (24), 3756-3776.

87. Knowles, K. E.; Hartstein, K. H.; Kilburn, T. B.; Marchioro, A.; Nelson, H. D.; Whitham, P. J.; Gamelin, D. R., Luminescent Colloidal Semiconductor Nanocrystals Containing Copper: Synthesis, Photophysics, and Applications. *Chem Rev* **2016,** *116* (18), 10820-10851.

88. Gao, T.; Zhang, Q.; Li, L.; Zhou, X.; Li, L. G.; Li, H. Q.; Zhai, T. Y., 2D Ternary Chalcogenides. *Adv Opt Mater* **2018,** *6* (14).

89. Sun, K. Q.; Marceau, E.; Che, M., Evolution of Nickel Speciation During Preparation of Ni-SiO_2 Catalysts: Effect of the Number of Chelating Ligands in $[Ni(en)_x(H_2O)_{6-2x}]^{2+}$ Precursor Complexes. *Phys Chem Chem Phys* **2006,** *8* (14), 1731-1738.

Chapter 4: Controlled CO Labilization of Tungsten Carbonyl Precursors for the Low-Temperature Synthesis of Tungsten Diselenide Nanocrystals

4.1 Abstract.

We report a low-temperature colloidal synthesis of WSe_2 nanocrystals from tungsten hexacarbonyl and diphenyl diselenide in trioctylphosphine oxide (TOPO). We identify TOPO-substituted intermediates, $W(CO)_5$TOPO and *cis*-$W(CO)_4(TOPO)_2$ by infrared spectroscopy. To confirm these assignments, we synthesize aryl analogues of phosphine-oxide-substituted intermediates, $W(CO)_5$TPPO (synthesized previously, TPPO = triphenylphosphine oxide) and *cis*-$W(CO)_4(TPPO)_2$ and *fac*-$W(CO)_3(TPPO)_3$ (new structures reported herein). Ligation of the tungsten carbonyl by either the alkyl or aryl phosphine oxides results in facile labilization of the remaining CO, enabling low-temperature decomposition to nucleate WSe_2 nanocrystals. The reactivity in phosphine oxides is contrasted with syntheses containing phosphine ligands, where substitution results in decreased CO labilization and higher temperatures are required to induce nanocrystal nucleation.

4.2 Introduction

Colloidal synthesis provides an attractive route to solid-state nanomaterials because it can exploit the diverse reaction-parameter-space to obtain kinetic control, enabling access to products that are difficult or impossible to achieve via bulk synthetic methods. Understanding and manipulating the precursor chemistry has emerged as a vital tool for advancing nanocrystal syntheses, as precursor conversion governs the nucleation and growth of nanocrystals.[1-5] Differences in precursor reactivity have been used to tailor nanocrystal size,[6-9] morphology[10-12] and phase.[11, 13-20] For

example, the size and size-distributions of cadmium, lead, and zinc chalcogenides have been greatly tuned via a selection of thioureas and selenoureas to vary the kinetics of the chalcogen supply.[6-9] The shape of copper nanocrystals has been selected through manipulation of the ligand-bound copper intermediate to vary the rate of conversion to active monomers. Ligation with trioctylphosphine oxide results in rapid conversion and the kinetically favored cubic product, while trioctylphosphine yields the thermodynamically favored spherical nanocrystals.[10] In the synthesis of WSe_2 nanocrystals,[18, 20] inclusion of trioctylphosphine oxide, oleic acid or oleylamine ligands was shown to vary the precursor reactivity, concomitant with a change in the phase of the final products. We hypothesize that differences in the observed reactivity are due to differences in the decomposition of the tungsten carbonyl precursors, where substitution by ligands at the metal center serves to modulate the energy required for dissociation.

Metal carbonyls, including tungsten hexacarbonyl,[18, 20-27] molybdenum hexacarbonyl,[22, 28-30] iron pentacarbonyl,[31-35] dicobalt octacarbonyl,[32, 36-39] and dimanganese decacarbonyl[33, 40-42] are widely used in the solution-phase syntheses of metal,[21, 23-26, 29, 32, 36-41] metal carbide,[30, 35] metal phosphide[31] or metal chalcogenide nanocrystals, [18, 20, 22, 27-29, 33-34] where they are commonly used as a source of metal[18, 20-22, 27-28, 31-34, 36, 38-41] or as a reducing agent.[23-26, 37, 42] The use of metal carbonyl precursors generally requires temperatures high enough to force cleavage of the metal–carbonyl bonds[43] and induce nanocrystal nucleation. Metal carbonyls can decompose directly to form metal nanocrystals,[21, 32, 36, 38-40] or can undergo ligand exchange at the metal site.[44-48] Such ligand exchange is expected to be important in controlling the subsequent reactivity of the metal carbonyls, but its role in nanocrystal formation has not been explicitly explored. As CO alone has been shown to direct nanocrystal growth and morphology,[49-50] its labilization from metal carbonyls can also be expected to influence nanocrystal formation. Here, we show that the ligands/solvents

common in many nanocrystal syntheses play an important role in forming and dictating the reactivity of substituted tungsten carbonyls that are used to form WSe_2 nanocrystals.

We have previously synthesized WSe_2 nanocrystals by hot-injection of diphenyl diselenide (Ph_2Se_2) into tungsten hexacarbonyl ($W(CO)_6$) dissolved in mixtures of trioctylphosphine oxide (TOPO) and oleic acid (OA) at 330 °C.[18] When using this mixture of ligands, the reactivity is increased with a larger TOPO/OA ratio, leading to more nanocrystal nucleation and smaller nanocrystals that are readily converted to the thermodynamically favored phase.[18] Indeed, when OA is excluded, $W(CO)_6$ decomposes at 260 °C, prior to injection of Ph_2Se_2.[18] Here, we take advantage of this greater reactivity in TOPO by using a low-temperature injection of Ph_2Se_2 to form WSe_2 nanocrystals at 150 °C. We follow the reactivity and conversion of $W(CO)_6$ using IR spectroscopy and show that, prior to Ph_2Se_2 injection, one or two CO ligands are replaced by TOPO ligands, enabling facile CO labilization. In contrast, when just one eq trioctylphosphine (TOP) is included, the TOP-substituted tungsten carbonyl is exclusively formed. This intermediate has decreased ligand dissociation from the tungsten, such that nanocrystals cannot be nucleated below 180 °C. The assignment of the phosphine- and phosphine-oxide-substituted intermediates is verified by synthesis of the aryl analogs (TPP and TPPO, respectively; TPP = triphenylphosphine, TPPO = triphenylphosphine oxide), which can be crystallized for structural identification. These studies demonstrate the role that phosphines and phosphine oxides can play in nanocrystal nucleation and growth by dictating the conversion of metal carbonyl precursors.

4.3 Results and Analysis

WSe_2 nanocrystals were synthesized via injection of Ph_2Se_2 into $W(CO)_6$ dissolved in TOPO at 150 °C. Briefly, $W(CO)_6$ (20 mg, 0.057 mmol) was heated in TOPO (2.1975 g, 100

TOPO/W) to 150 °C and held for 15 min. Beginning at ~ 70° C, the colorless solution began to turn yellow and continued to darken as the temperature increased. This color change was accompanied by bubbling, indicative of some gas evolution. After 15 min at 150 °C, Ph_2Se_2 in hexadecane (115 mM, 1 ml, 4 Se/W) was rapidly injected into the W solution. Immediately after injection, the solution changed to brown/black and rapid gas evolution was observed, indicating nucleation of WSe_2 nanocrystals.

Figure 4.1a(0) shows the IR spectrum of an aliquot collected just before the Ph_2Se_2 injection. Here, multiple CO vibrations are observed between 1950 and 1850 cm^{-1} (Table 4S.1). These vibrations are all shifted to lower wavenumber relative to that of $W(CO)_6$ (1971 cm^{-1}, Figure 4S.1), suggesting that $W(CO)_6$ has undergone substitution by TOPO to form $W(CO)_{6-x}(TOPO)_x$ intermediates. Similar shifts are observed when the CO of $W(CO)_6$ is substituted by one, two or three phosphine oxide ligands.[51-53] Just one minute following Ph_2Se_2 injection, the original peaks disappear and are replaced by weak vibrations at 1937 and 1903 cm^{-1} (Figure 4.1a(i)), which likely arise from another intermediate formed by oxidative addition of Ph_2Se_2 to the $W(CO)_{6-x}(TOPO)_x$ complexes.[54-56] Within 10 min following Ph_2Se_2 injection, no CO vibrations are evident in the IR spectrum (Figure 4.1a(iii)), indicating complete conversion of the $W(CO)_{6-x}(TOPO)_x$ intermediates. The heating profile of this synthesis is provided in Figure 4.1b, with the x indicating nucleation and filled circles indicating when aliquots were taken. After 10 min following Ph_2Se_2 injection, the heating mantle was removed and the resultant nanocrystals were collected, washed and characterized.

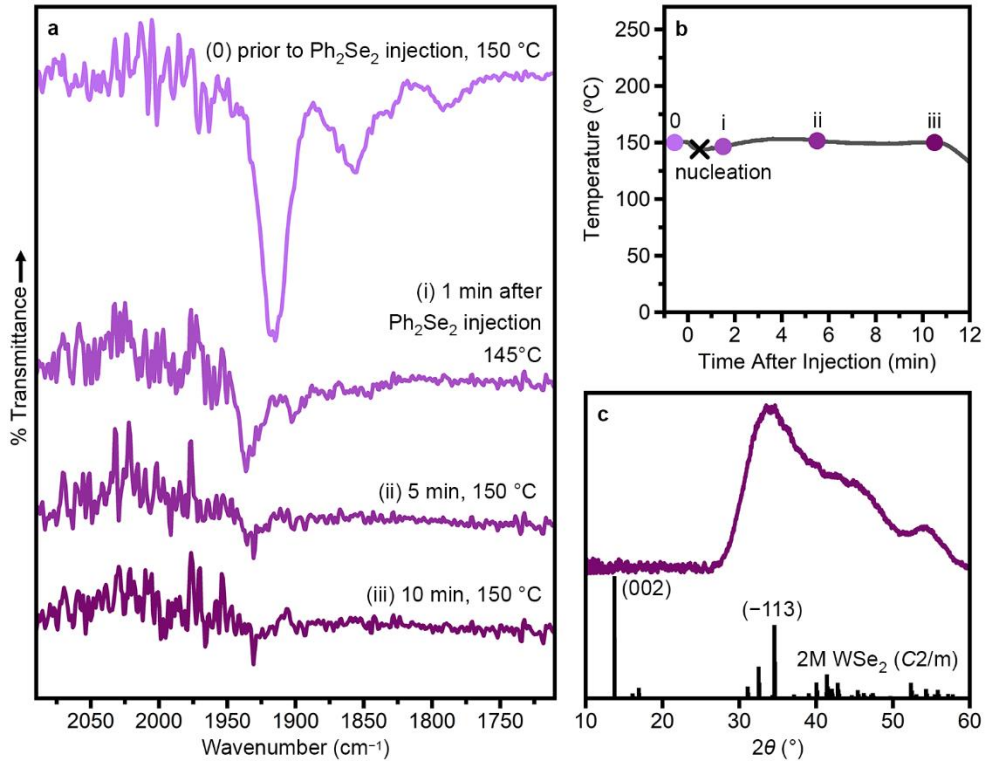

Figure 4. 1. Injection of Ph_2Se_2 into $W(CO)_6$ + TOPO (TOPO/Se/W = 100/4/1) at 150 °C. **(a)** FTIR spectra of aliquots taken prior to Se injection and approximately 1, 5 and 10 min after Se injection. **(b)** Temperature profile of the reaction with aliquots indicated by circles. The black x indicates the nucleation event, evidenced by a color-change of the reaction solution. **(c)** Powder X-ray diffraction pattern of nanocrystalline product compared to that simulated from single-crystal data for 2M WSe_2.[57]

Figure 4.1c shows the powder X-ray diffraction pattern of the resulting nanocrystals. The lack of a (002) reflection suggests very little interlayer stacking, which is confirmed by transmission electron microscopy (Figure 4S.2). The most intense reflection is observed at $2\theta \approx 34°$, consistent with the (−113) reflection of the metastable 2M phase of WSe_2.[18, 27, 57] This phase-assignment is verified by X-ray photoelectron spectroscopy (Figure 4S.3). We have previously shown that increased TOPO/OA leads to more 2H phase when WSe_2 nanocrystals are synthesized at 330 °C.[18] In this previous work, dominance of the thermodynamically favored phase was due to greater reactivity induced by TOPO, which led to more phase-conversion at high temperatures.[18] In contrast, the synthesis presented herein takes advantage of the TOPO-induced reactivity to

synthesize WSe_2 nanocrystals at lower temperatures, allowing preservation of the metastable 2M phase.

Since the bulky octyl groups of TOPO prohibit the isolation of single crystals, we used an aryl analog to corroborate the formation of $W(CO)_{6-x}(TOPO)_x$ intermediates. Specifically, we synthesized $W(CO)_{6-x}(TPPO)_x$ (x = 1, 2, 3). $W(CO)_5$TPPO (Figure 4.2a) was synthesized from photochemically prepared $W(CO)_5$THF (THF = tetrahydrofuran) following a previously reported procedure.[51] To synthesize $W(CO)_4(TPPO)_2$, $W(CO)_6$ and TPPO (10 eq) were combined in toluene and refluxed for ~1 h with stirring. Further addition of toluene resulted in a yellow precipitate, which was redissolved with heat. The resulting solution yielded yellow crystals in ~12 h. Single-crystal X-ray diffraction identified the crystals as *cis*-$W(CO)_4(TPPO)_2$ (Figure 4.2b, Table 4S.2) and powder X-ray diffraction confirmed this as the majority product (Figure 4S.4). We note, however, that a trace product of *fac*-$W(CO)_3(TPPO)_3$ (Table 4S.2, Figure 4S.5) was identified by single-crystal X-ray diffraction.

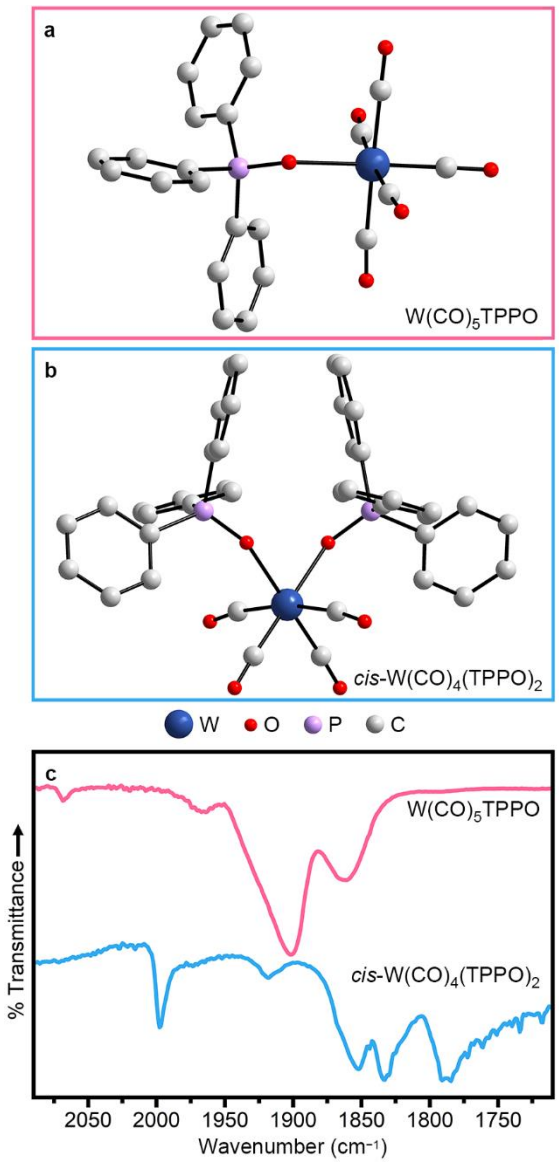

Figure 4. 2. Crystal structures of **(a)** $W(CO)_5TPPO$ and **(b)** *cis*-$W(CO)_4(TPPO)_2$. **(c)** FTIR spectra of $W(CO)_5TPPO$ (top) and of *cis*-$W(CO)_4(TPPO)_2$ (bottom) solids.

Figure 4.2c (top, pink) shows the IR spectrum of $W(CO)_5TPPO$. With pseudo-C_{4v} symmetry, this molecule has 4 IR-active CO vibrations (Table 4S.3).[51, 53] Figure 4.2c (bottom, blue) shows the IR spectrum of *cis*-$W(CO)_4(TPPO)_2$. With pseudo-C_{2v} symmetry, this molecule also has 4 IR-active CO vibrations (Table 4S.4), which are at similar positions to other tungsten carbonyls substituted with two phosphine oxide moieties.[52] Comparing the IR spectra of these two

molecules to that of the pre-injection aliquot (Figure 4.1a(0)), we conclude that heating $W(CO)_6$ in TOPO yields a mixture of the mono- and di-substituted species, $W(CO)_5$TOPO and *cis*-$W(CO)_4(TOPO)_2$, respectively (Table 4S.1). The lack of a peak at ~1970 cm^{-1} indicates little to no remaining $W(CO)_6$, suggesting that $W(CO)_5$TOPO and *cis*-$W(CO)_4(TOPO)_2$ are the reactive intermediates when Ph_2Se_2 is injected. Phosphine oxides are known to be particularly good at promoting CO labilization in metal carbonyls,[45, 58-59] which is likely the reason for increased reactivity when WSe_2 nanocrystals are synthesized in TOPO.

It is worth noting that both increased concentration of $W(CO)_6$ (Figure 4S.6) and the addition of a degassing step (Figure 4S.7) leads to more substitution by TOPO. When the synthesis is repeated using TPPO instead of TOPO, the reactivity is similar. Specifically, nucleation was observed immediately after the injection of Ph_2Se_2 and WSe_2 nanocrystals are formed within 10 min at 150 °C (Figure 4S.8). These observations corroborate that the higher reactivity is due to the phosphine oxides.

To contrast the rapid reactivity induced by TOPO, we sought a ligand with stronger binding and decreased CO labilization that would decrease reactivity in the nanocrystal synthesis. TOP is commonly used in nanocrystal syntheses and contains a strong σ-donating, π-accepting phosphine in contrast to the weak, hard oxygen donor of TOPO. Figure 4.3 shows the characterization of a WSe_2 synthesis performed similarly to that presented in Figure 4.1, but with just 1 eq TOP added to the reaction mixture. When $W(CO)_6$ is heated at 150 °C in the presence of 100 eq TOPO + 1 eq TOP for 15 min, IR spectroscopy reveals a new species (Figure 4.3a(0)), with vibrations that are distinct from both $W(CO)_6$ and $W(CO)_{6-x}(TOPO)_x$. We assign this species as primarily $W(CO)_5$TOP with a small amount of $W(CO)_4(TOP)_2$ (Table 4S.5, *vide infra*). Importantly, when

Ph_2Se_2 is injected into this mixture at 150 °C, no color change or gas evolution are observed over the course of 11 min and the CO vibrations remain largely unchanged (Figure 4.3a(i–iii)).

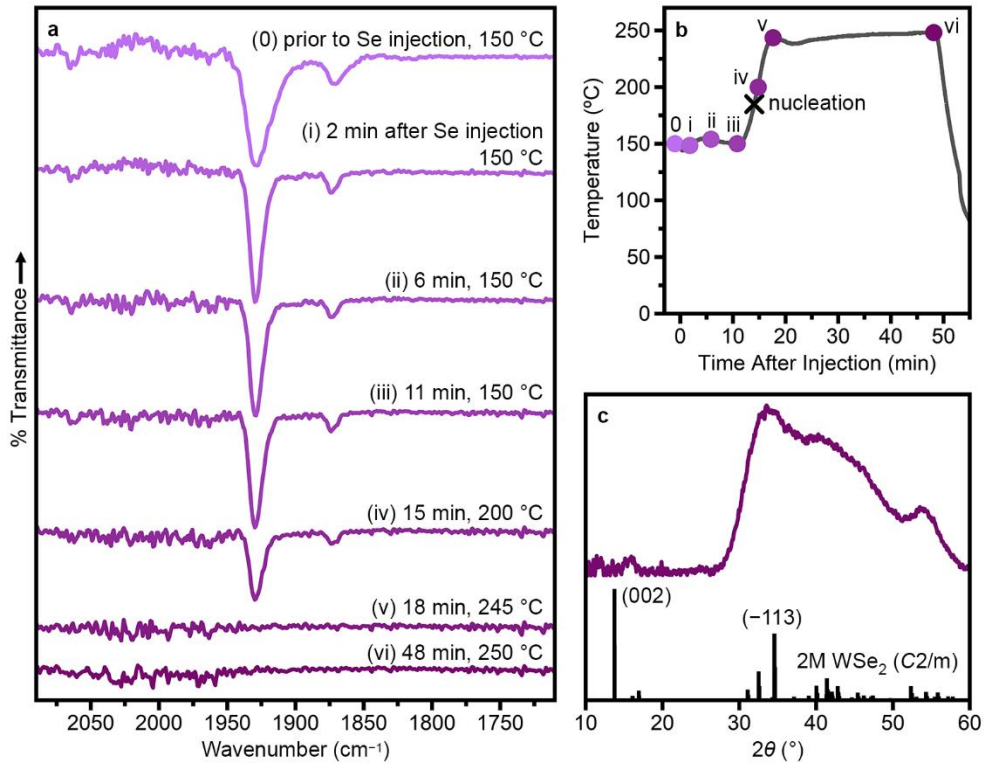

Figure 4. 3. Injection of Ph_2Se_2 into $W(CO)_6$ + TOPO + TOP (TOPO/TOP/Se/W = 100/1/4/1) at 150 °C. **(a)** FTIR spectra of aliquots taken prior to Se injection and approximately 2, 6, 11, 15, 18 and 48 min after Se injection. **(b)** Temperature profile of the reaction with aliquots indicated by circles. The black x indicates the nucleation event, evidenced by a color-change of the reaction solution. **(c)** Powder X-ray diffraction pattern of nanocrystalline product compared to that simulated from single-crystal data for 2M WSe_2.[57]

The low reactivity in the presence of TOP is in stark contrast to syntheses without TOP, in which a color-change, gas evolution and loss of CO are observed immediately upon injection (Figure 4.1a, b). To induce nanocrystal nucleation, the reaction was heated to 250 °C over ~10 min (Figure 4.3b). As the temperature was increased, the solution began to turn brown, indicating

nucleation of WSe_2. This color-change was accompanied by gas evolution, indicating liberation of CO. When the temperature reached 250 °C, the solution was very dark brown and gas evolution had slowed. Aliquots were collected shortly after nucleation (Figure 4.3a,b(iv)), once the temperature reached 250 °C (Figure 4.3a,b(v) and after 30 min at 250 °C (Figure 4.3a,b(vi)). The intensity of the $W(CO)_5$TOP CO vibration at 1930 cm^{-1} decreased following WSe_2 nucleation, and disappeared completely by the time the temperature reached 250 °C. Powder X-ray diffraction (Figure 4.3c) on the final nanocrystalline product reveals 2M WSe_2.

To confirm the assignment of $W(CO)_5$TOP, we synthesized the aryl analog, $W(CO)_5$TPP (Figure 4.4a) using previously reported methods.[60] Figure 4.4b(i) shows the IR spectrum of crystals of $W(CO)_5$TPP dissolved in THF. With pseaudo-C_{4v} symmetry, this molecule is expected to have 4 IR-active CO vibrations, but in this case the $A_1(2)$ and E modes are unresolvable (Table 4S.6).[61-62] Importantly, when $W(CO)_5$TPP is heated in 100 eq TOPO at 150 °C for 15 min (Figure 4.4b(ii)), the IR spectrum is comparable to that of the TOP-containing syntheses prior to injection of Ph_2Se_2 (Figure 3a(0)), and can be assigned primarily to $W(CO)_5$TPP with a small amount of $W(CO)_4(TPP)_2$ (Table 4S.7). All peaks are shifted to slightly higher wavenumber for TPP-substituted species relative to the TOP-substituted species due to the electron-withdrawing nature of the phenyl substituents.[63-64]

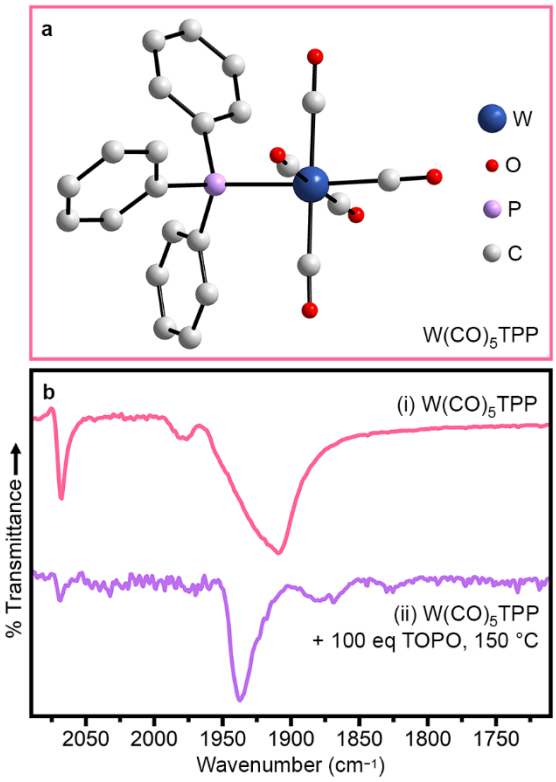

Figure 4. 4. (a) Crystal structure of $W(CO)_5TPP$. **(b)** IR spectra of (i) $W(CO)_5TPP$ dried solid and of (ii) that solid heated in 100 eq TOPO to 150 °C for 15 min (bottom). All spectra were collected at room-temperature.

When Ph_2Se_2 is injected into $W(CO)_5TPP$ + 100 eq TOPO at 150 °C, the reactivity is similar to that of the TOP-containing synthesis. Specifically, no color-change or gas evolution were observed over 10 min and the $W(CO)_5TPP$ CO vibration at 1937 cm^{-1} persisted, although with some decrease in intensity. We note that, in this synthesis, the CO vibration assigned to $W(CO)_4(TPP)_2$ disappears upon injection of Ph_2Se_2. We hypothesize that this is due to conversion of $W(CO)_4(TPP)_2$ to $W(CO)_5TPP$. This conversion results in formation of a small amount of TPP=Se and Ph_2Se (equation 4S.1), neither of which can react directly with $W(CO)_5TPP$ to nucleate nanocrystals at 150 °C. When the reaction is further heated, a color change is observed, indicating nucleation of WSe_2 (Figure 4S.9b). The reactivity of $W(CO)_5TPP$ is greater than that of

the TOP-containing synthesis, likely due to the electron-withdrawing nature of the phenyl substituents. Both phosphine-substituted species, however, show delayed reactivity compared to synthesis in TOPO alone. This observation confirms that carbonyl substitution with phosphines or phosphine oxides can be used to delay or induce nanocrystal nucleation, respectively.

4.4 Discussion

The decrease in reactivity observed with the phosphine substitution compared to phosphine-oxide substitution is likely two-fold. First, the phosphine is a stronger σ-donating and π-accepting ligand, making it less labile than the phosphine oxide ligand.[65] Second, phosphine- and phosphite-substitution in metal carbonyls have been shown to decrease CO labilization.[44, 46-48, 59, 66-69] In contrast, substitution with hard donor ligands,[44, 46, 48, 67-68, 70] including phosphine oxides,[45, 58-59] has been shown to increase CO labilization in metal carbonyls. This has been explained due to σ- and π-bonding effects between the donor and central metal atom, as well as a result of direct donation from the filled σ_z^b orbital of the donor to the π* orbitals of the carbonyls cis to the donor.[48, 68, 71] The low lability of both the phosphine and carbonyl ligands inhibits coordination by the Se precursor, thus requiring higher temperatures to force cleavage of the W–C and/or W–P bonds to initiate WSe_2 nucleation. We note that the substituents of the phosphine ligand also play a significant role in modifying the reactivity of the substituted metal carbonyls. With direct coordination to the donor, electron-withdrawing groups (e.g. phenyl substituents) decrease the P–W bond strength to allow for ligand dissociation at lower temperatures. This effect is not present in the phosphine oxides, as the substituents are not well-coupled to the donor.

In our hands, $W(CO)_6$ does not dissolve well in noncoordinating solvents used for nanocrystal synthesis, such as hexadecane. Thus, the influence on reactivity of a coordinating

solvent will likely be an important consideration. The reactivity trend observed with phosphine oxides vs phosphines can possibly be extended to other common nanocrystal ligands/solvents based on the known reactivity with metal carbonyls. For example, oleylamine would also be expected to be CO-labilizing due to the hard N donor, [44, 46, 48, 67-68, 70] and could facilitate metal carbonyl decomposition.[24] Variation of the substituents on the N donor could be used to further tune the reactivity. We note that we have not discussed the role of steric interactions, which could be used to further modify the metal carbonyl stability.

4.5 Summary and Conclusions

We present a low-temperature synthesis of WSe_2 nanocrystals by taking advantage of the modified reactivity of substituted tungsten carbonyls. When nanocrystals are synthesized in TOPO, $W(CO)_5$TOPO and *cis*-$W(CO)_4(TOPO)_2$ are identified as the reactive tungsten intermediates. This substitution with TOPO enables facile CO labilization, allowing for the ligand dissociation required to initiate reactivity of the tungsten carbonyls with the Se precursor at 150 °C. In contrast, when just 1 eq TOP is included, nanocrystals cannot be nucleated below 180 °C due to the non-labilizing nature of the phosphine. The reactivity of phosphine-containing syntheses can be further tuned via choice of phosphine substituent, where electron-withdrawing groups lead to increased reactivity. These results demonstrate the influence of common nanocrystal ligands on metal carbonyl reactivity and offer insight for fine-tuning the reactivity to manipulate nanocrystal nucleation and growth.

4.6 Supplementary Information

Table 4S. 1. CO vibrations observed when $W(CO)_6$ in 100 eq TOPO is heated to 150 °C for 15 min.

Wavenumber (cm^{-1})	Assignment
1915	$W(CO)_5$TOPO, E
1864	$W(CO)_5$TOPO, A_1(2)
1856	*cis*-$W(CO)_4(TOPO)_2$, E
1832	*cis*-$W(CO)_4(TOPO)_2$, B_1
1790	*cis*-$W(CO)_4(TOPO)_2$, B_2

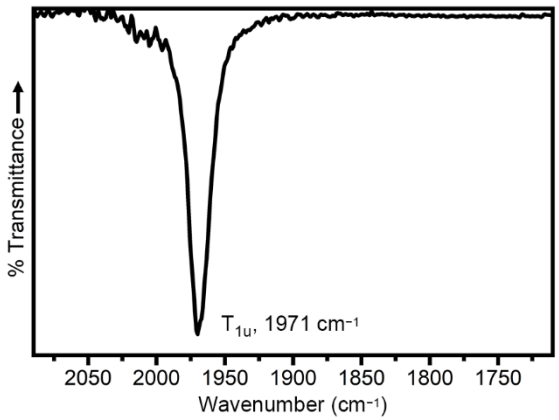

Figure 4S. 1. IR spectrum of $W(CO)_6$ dissolved in THF (~30 mM).

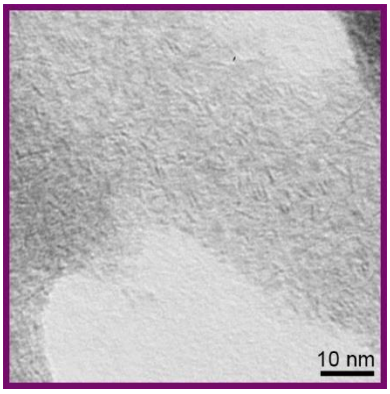

Figure 4S. 2. TEM image of WSe_2 nanocrystals synthesized via injection of Ph_2Se_2 into $W(CO)_6$ + TOPO (TOPO/Se/W = 100/4/1) at 150 °C (Figure 4.1).

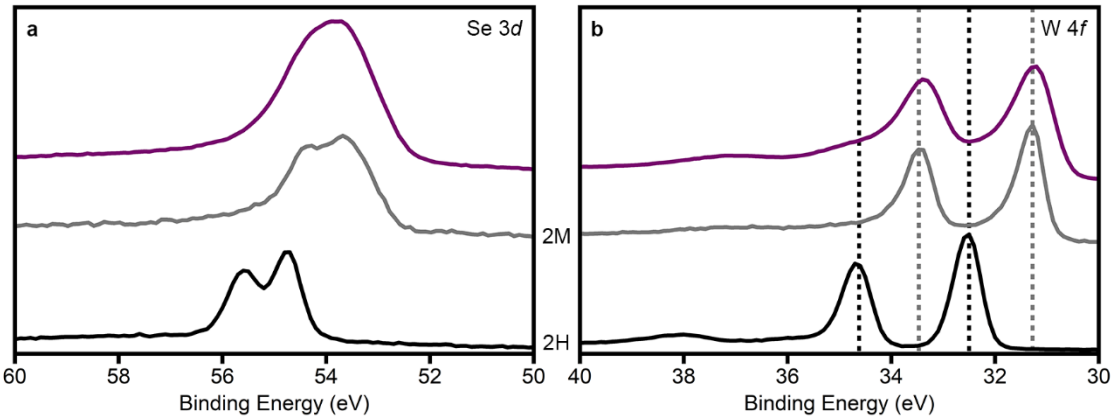

Figure 4S. 3. (a) Se 3*d* and **(b)** W 4*f* X-ray photoelectron spectra of WSe2 nanocrystals (purple, top). Spectra of bulk 2H and nanocrystalline 2M (reproduced from ref. [18]) WSe_2 samples are included for comparison. The lower binding energies of the nanocrystals synthesized herein are indicative of the smaller bandgap 2M phase.[18, 27, 72-73]

Table 4S. 2. Crystallographic parameters of $W(CO)_{6-x}(TPPO)_x$.

Structure	***cis*-W(CO)$_4$(TPPO)$_2$**	***fac*-W(CO)$_3$(TPPO)$_3$**
Empirical formula	$C_{40}H_{30}O_6P_2W$	$C_{57}H_{45}O_6P_3W$
Crystal system	monoclinic	monoclinic
Space group	C2/c	C2/c
Formula weight	852.43	1102.69
Crystal size (mm^3)	0.12 × 0.03 × 0.03	0.12 × 0.04 × 0.04
a (Å)	16.705(4)	19.9860(19)
b (Å)	12.169(4)	20.7140(12)
c (Å)	17.113(4)	23.3364(14)
α (°)	90	90
β (°)	103.891(9)	92.103(3)
γ (°)	90	90
Volume ($Å^3$)	3376.8(14)	9654.5(12)
Z	4	8
ρ_{calc} (g/cm^3)	1.677	1.517
μ (mm^{-1})	3.565	2.545
Goodness-of-fit on F^2	1.137	1.027
Reflections collected	19018	52863
Independent reflections	3464	9518
R_1	0.0263	0.0281
wR_2	0.0667	0.0519
CCDC #	2203214	2203215

Radiation: Mo K_α (λ = 0.71073 Å)
Temperature: 100 K

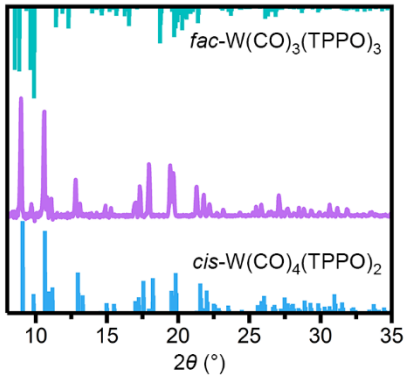

Figure 4S. 4. Powder X-ray diffraction pattern of crushed crystals synthesized via reflux of $W(CO)_6$ + TPPO (10 eq) in toluene (middle) compared to those simulated from single-crystal data for *fac*-$W(CO)_3(TPPO)_3$ (top) and *cis*-$W(CO)_4(TPPO)_2$ (bottom). The comparison indicates that the majority product is *cis*-$W(CO)_4(TPPO)_2$.

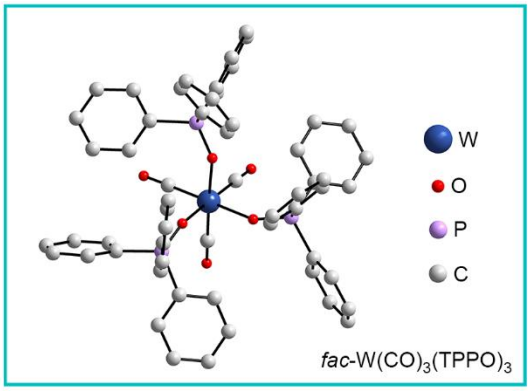

Figure 4S. 5. Crystal structure of *fac*-$W(CO)_3(TPPO)_3$.

Table 4S. 3. CO vibrations of $W(CO)_5TPPO$

Wavenumber (cm^{-1})	Symmetry
2067	$A_1(1)$
1966	B_1
1904	E
1862	$A_1(2)$

Table 4S. 4. CO vibrations of *cis*-$W(CO)_4(TPPO)_2$

Wavenumber (cm^{-1})	Symmetry
1996	$A_1(1)$
1852	$A_1(2)$
1834	B_1
1788	B_2
1917	*

*We hypothesize that this peak is due to $W(CO)_5TPPO$, which is expected to be in equilibrium with $W(CO)_4(TPPO)_2$.

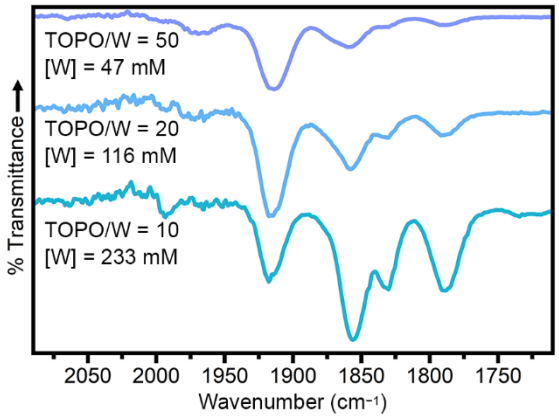

Figure 4S. 6. IR spectra of $W(CO)_6$ heated in varying amounts of TOPO at 150 °C for 15 min. All spectra were collected at room-temperature. Increased concentration (top to bottom) leads to more di-substituted species.

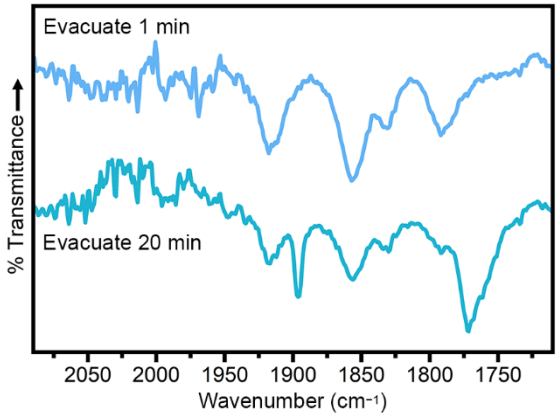

Figure 4S. 7. IR spectra of $W(CO)_6$ heated in TOPO (100 eq, [W] = 23 mM) at 150 °C for 15 min, followed by evacuation for 1 (top) and 20 (bottom) min. All spectra were collected at room-temperature. Evacuation leads to more TOPO substitution.

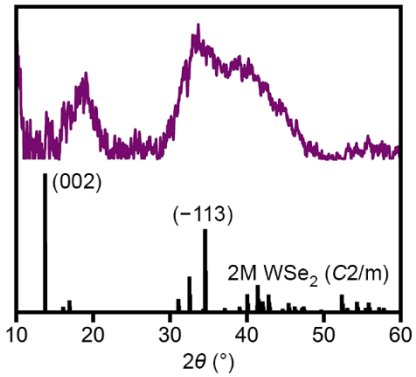

Figure 4S. 8. Powder X-ray diffraction pattern of WSe_2 nanocrystals synthesized in 100 eq TPPO compared to that simulated from single-crystal 2M WSe_2.[2] The broad reflection at 2θ = 20 ° is likely due to ligand.[74]

Table 4S. 5. CO vibrations observed when $W(CO)_6$ is heated in 100 eq TOPO + 1 eq TOP to 150 °C for 15 min.

Wavenumber (cm^{-1})	Assignment
2065	$W(CO)_5TOP$, $A_1(1)$
1930	$W(CO)_5TOP$, $A_1(2)$ + E
1873	*trans*-$W(CO)_4(TOP)_2$, E_u

Table 4S. 6. CO vibrations of $W(CO)_5TPP$

Wavenumber (cm^{-1})	**Symmetry**
2068	$A_1(1)$
1909	$A_1(2) + E$
1980	B_1

Table 4S. 7. CO vibrations observed when $W(CO)_5TPP$ is heated in 100 eq TOPO to 150 °C for 15 min.

Wavenumber (cm^{-1})	Assignment
2069	$W(CO)_5TPP$, $A_1(1)$
1937	$W(CO)_5TPP$, $A_1(2) + E$
1880	*trans*-$W(CO)_4(TPP)_2$, E_u

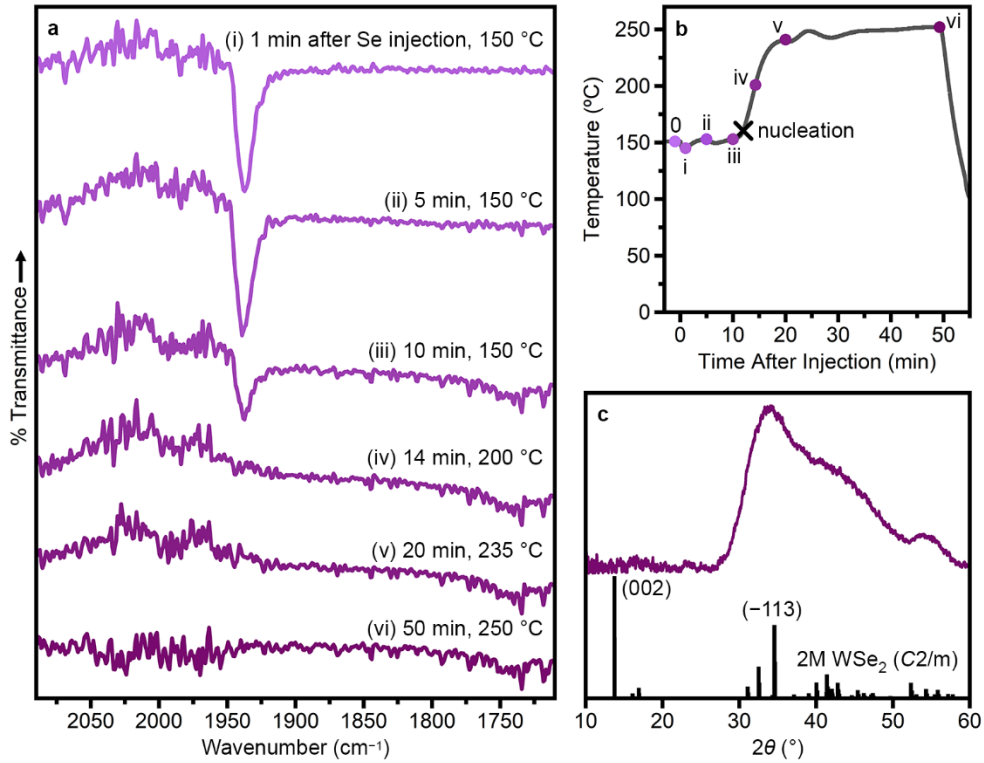

Figure 4S. 9. Injection of Ph_2Se_2 into $W(CO)_6$ + TOPO + TPP (TOPO/TPP/Se/W = 100/1/4/1) at 150 °C. **(a)** IR spectra of aliquots taken prior to Se injection and approximately 1, 5, 10, 14, 20 and 50 min after Se injection. **(b)** Temperature profile of the reaction with aliquots indicated by circles. The black x indicates the nucleation event, evidenced by a color-change of the reaction solution. The IR spectrum of aliquot 0 is shown in Figure 4.4b(ii). **(c)** Powder X-ray diffraction pattern of nanocrystalline product compared to that simulated from single-crystal data for 2M WSe_2.[57]

Equation 4S. 1. Possible side reactivity of $W(CO)_4(PR_3)_2$ (R = octyl, phenyl) upon injection of Ph_2Se_2:

$$W(CO)_4(PR_3)_2 + Ph_2Se_2 + CO \rightarrow W(CO)_5\,PR_3 + R_3P{=}Se + Ph_2Se$$

Experimental Methods

Chemicals

A list of chemicals, purities and manufacturers is provided in Table 4S.6. Molecular complexes were synthesized, crystallized, and washed using toluene, tetrahydrofuran (THF), and methanol from a solvent purification system. The solvents were transferred to a nitrogen-filled glovebox and stored over molecular sieves (3 Å). Solvents used in nanocrystal washing and suspension (Table 4S.6) were stored under ambient conditions. All chemicals were used without further purification.

Table 4S. 8. Chemicals

Chemical	**Purity**	**Manufacturer**
Tungsten hexacarbonyl ($W(CO)_6$)	99%	Acros
Trioctylphosphine oxide (TOPO)	99%	Strem
Triphenylphosphine oxide (TPPO)	99%	Alfa Aeser
Trioctylphosphine (TOP)	98%	Strem
Triphenylphosphine (TPP)	99%	Acros
Diphenyl diselenide (Ph_2Se_2)	>97%	TCI
Toluene (nanocrystals)	99.5%	Fisher Scientific
Methanol (nanocrystals)	99.8%	Fisher Scientific

Synthesis of WSe_2 Nanocrystals

TOPO/Se/W = 100/4/1 (Figure 4.1). In a nitrogen-filled glovebox, $W(CO)_6$ (20 mg, 0.057 mmol), TOPO (2.1975 g, 5.68 mmol) and a glass-coated stirbar were added to a 25-ml, 4-neck flask fitted with a condenser/flow adapter and 2 ceramic sheaths to hold thermocouples (one used to control the temperature, one used to log the temperature). Separately, Ph_2Se_2 (72.1 mg, 0.23 mmol) and hexadecane (1.54 g, 2 ml) were added to a 25-ml, 3-neck round-bottom flask containing a Teflon-coated stir bar. Both flasks were placed on a Schlenk line and evacuated and refilled with argon three times (repeated before and after opening the flow-adapters). Under argon, the 4-neck

flask was heated to 150 °C using a heating mantle attached to a proportional–integral–derivative controller. The 3-neck flask was heated to 70 °C using a heating mantle controlled by a Variac. Once the temperature of the 4-neck flask reached 150 °C, it was held for 15 min to ensure dissolution of the $W(CO)_6$. Then, 1 ml Ph_2Se_2 solution was injected into the 4-neck flask using a 1-ml plastic syringe fitted with a metal needle. Immediately following injection, the solution turned dark brown and rapid gas evolution was observed. Following injection, the reaction was held at 150 °C for 10 min. Aliquots were collected at 1 min prior to and 1, 5, and 10 min following the injection. After 10 min, the heating mantle was removed and the reaction allowed to cool. Once the temperature was <100 °C, toluene (2 ml) was added to the flask to prevent solidification. The mixture was transferred to 1.5-ml centrifuge tubes (0.5 ml per tube) and 1 ml MeOH was added to each tube. The mixture was centrifuged for 5 min at 8000 rpm. Nanocrystals were washed an additional two times by redispersing the resulting pellet in toluene, precipitating with MeOH (2:1 MeOH/toluene) and collecting via centrifugation.

TOPO/TOP/Se/W = 100/1/4/1. Nanocrystals were synthesized as described above with the addition of TOP (21.1 mg, 0.057 mmol) to the 4-neck flask. In this case, no reaction was observed following the Ph_2Se_2 injection. Instead, the temperature was held at 150 °C for 10 min, after which it was increased to 250 °C. The solution began to turn brown at ~180 °C, accompanied by some gas evolution. Once the temperature reached 250 °C, the solution was very dark brown and gas evolution had slowed. The reaction was held at 250 °C for an additional ~ 20 min. Aliquots were collected at 1 min prior to and 1, 5, 10, 14, 17 and 47 min following the injection. The heating mantle was removed after 47 min.

TOPO/TPP/Se/W = 100/1/4/1. Nanocrystals were synthesized as described in the section above, replacing TOP with TPP (14.9 mg, 0.057 mmol).

Aliquots. Aliquots were collected via syringe and needle. First, the syringe and needle were flushed 3 times by filling and expelling gas from the headspace of the reaction flask. Then, ~0.1 ml was extracted from the reaction solution and the aliquot was immediately dispensed into a plastic Eppendorf tube. The aliquot was transferred directly onto the ATR crystal for IR measurements.

Synthesis of Molecular Complexes with Aryl Analogs

Synthesis of $W(CO)_5THF$. The synthesis was adapted from a previously reported method.[51] In a nitrogen-filled glovebox, $W(CO)_6$ (100 mg, 0.28 mmol), THF (10 ml) and a stirbar were added to a 20-ml scintillation vial, which was sealed with a Teflon-lined cap. The solution was irradiated using a 365-nm LED with stirring for 1 h outside of the glovebox. The resulting yellow solution was transferred back into the glovebox.

Synthesis of $W(CO)_5TPPO$. The synthesis was adapted from a previously reported method.[51] In a nitrogen-filled glovebox, TPPO (0.28 mmol, 1 TPPO/W) was added to the THF solution of $W(CO)_5THF$ and stirred at room-temperature for 35 min.[5] Dried powder was collected via evaporation of the THF.

Synthesis of cis-$W(CO)_4(TPPO)_2$ and fac-$W(CO)_3(TPPO)_3$. In a nitrogen-filled glovebox, $W(CO)_6$ (100 mg, 0.28 mmol), TPPO (790 mg, 2.83 mmol, 10 TPPO/W), toluene (2 ml) and a stirbar were added to a 20-ml scintillation vial. The vial was sealed with a Teflon-lined cap and heated with stirring to reflux for 1 h. After the reaction cooled to room temperature, an additional 8 ml of toluene was added to the vial, which resulted in a yellow precipitate. The precipitate was redissolved with heat and yellow crystals were obtained after ~12 h. The crystals were washed with THF and methanol to remove excess $W(CO)_6$ and TPPO, respectively.

Synthesis of $W(CO)_5TPP$. The synthesis was adapted from a previously reported method.[75] In a nitrogen-filled glovebox, TPP (0.28 mmol, 1 TPP/W) was added to the THF solution of $W(CO)_5THF$ and stirred at room-temperature until the solution turned colorless (~4 h). THF was removed under vacuum and pentane (8 ml) was added. The resulting solution was stored at −33 °C and yellow crystals were observed after ~12 h.

Formation of $W(CO)_{6-x}(TOPO)_x$ via Heat-up

Varying the amount of TOPO. Heat-up reactions were performed following methods used for the nanocrystal syntheses prior to the Ph_2Se_2 injection. Reactions were performed in 3-neck flasks using an analogous setup without the thermocouple logger. The same amount of $W(CO)_6$ (20.0 mg, 0.057 mmol) was used for each reaction and the amount of TOPO was varied to obtain TOPO/W = 50, 20, and 10.

Influence of evacuation. This reaction was performed following the procedure described in the above section with the same amount of $W(CO)_6$ (20.0 mg, 0.057 mmol) and 100 eq TOPO. After holding the reaction at 150 °C for 10 min, the flask was evacuated for 20 min. After 1 min, the flask was refilled with argon and an aliquot was collected. The flask was then evacuated for an additional 19 min, after which it was refilled with argon and the heating mantle was removed. Once the temperature was <100 °C the septa were removed and a small amount of the resulting product was removed using a spatula.

Characterization

Single-crystal X-ray diffraction. Data were collected using a Bruker APEX-II Ultra CCD diffractometer equipped with a Mo K_α source (λ = 0.71073 Å). Crystals were mounted on a

Cryoloop with Fomblin Y oil. Data was collected under a nitrogen gas stream at 100(2) K using φ and ϖ scans. In a typical data-collection, the crystal-to-detector distance was 45 mm and the exposure time was 5 s per frame using a scan width of 0.75°. The data were integrated using the Bruker SAINT software program and scaled using the SADABS software program. Solution by direct methods (SHELXT)[76] produced a complete phasing model consistent with the proposed structure. All nonhydrogen atoms were refined anisotropically by full-matrix least-squares SHELXT-2014).[76]

Powder X-ray diffraction. Powder patterns of nanocrystals synthesized with 1 eq TOP were collected on a Bruker Apex II Single-Crystal X-ray Diffractometer equipped with a Mo Kα radiation source (λ = 0.7107Å). The pattern was converted to Cu Kα radiation (λ = 1.5406 Å) for consistency with other measurements. All other nanocrystal powder patterns were collected on a Bruker Microstar APEX II CCD diffractometer equipped with a Cu K_a source (λ = 1.54184 Å). Images were merged and processed with Diffrac EVA V4.3. Powder patterns of molecular solids were collected on a 2nd Gen Bruker D2 Phaser with a Cu K_a source (λ = 1.54184 Å, 0.2 s/step; 2578 steps, divergence slit = 1.0 mm, no air scatter screen, no air scatter slit, Söller slit = 2,5').

Infrared spectroscopy. IR spectra were collected on an Agilent Cary 630 ATR-FTIR (64 scans, resolution = 2 cm^{-1}, HappGenzel apodization, Mertz phase-correction). Aliquots from nanocrystal syntheses were transferred directly onto the ATR crystal for IR measurements. For measurements on the molecular aryl complexes, the product was solubilized in either THF or toluene and drop-cast onto the ATR crystal. Spectra were collected after the volatile solvent evaporated.

Transmission electron microscopy. TEM grids were prepared by drop-casting a suspension of nanocrystals in toluene as a single drop onto a 100-mesh copper TEM grid coated with formvar

and carbon (Electron Microscopy Sciences). Images were collected on a FEI Spirit operating at 120 keV.

X-ray photoelectron spectroscopy. XPS samples were prepared by drop-casting a suspension in toluene onto a Si wafer. The nanocrystal sample was prepared, transported and loaded into the instrument under a nitrogen atmosphere. Spectra were acquired using a Kratos Analytical AXIS Supra surface analysis instrument at an emission current of 15 mA.

4.7 Acknowledgments

Chapter 4, in full, is a reprint of the material as it appears in "Controlled CO Labilization of Tungsten Carbonyl Precursors for the Low-Temperature Synthesis of Tungsten Diselenide Nanocrystals." Front. Nanotech. 2022. The dissertation author was a primary author of this paper and gratefully acknowledges the contributions of coauthors Hang Yin, Natacha Oget, Haeun Chang, Linfeng Chen and Alina M. Schimpf.

4.8 References

1. Liu, H. T.; Owen, J. S.; Alivisatos, A. P., Mechanistic Study of Precursor Evolution in Colloidal Group II–VI Semiconductor Nanocrystal Synthesis. *J Am Chem Soc* **2007,** *129* (2), 305-312.

2. Steckel, J. S.; Yen, B. K. H.; Oertel, D. C.; Bawendi, M. G., On the Mechanism of Lead Chalcogenide Nanocrystal Formation. *J Am Chem Soc* **2006,** *128* (40), 13032-13033.

3. Garcia-Rodriguez, R.; Liu, H. T., Mechanistic Study of the Synthesis of CdSe Nanocrystals: Release of Selenium. *J Am Chem Soc* **2012,** *134* (3), 1400-1403.

4. Owen, J. S.; Chan, E. M.; Liu, H. T.; Alivisatos, A. P., Precursor Conversion Kinetics and the Nucleation of Cadmium Selenide Nanocrystals. *J Am Chem Soc* **2010,** *132* (51), 18206-18213.

5. Hendricks, M. P.; Cossairt, B. M.; Owen, J. S., The Importance of Nanocrystal Precursor Conversion Kinetics: Mechanism of the Reaction between Cadmium Carboxylate and Cadmium Bis(diphenyldithiophosphinate). *Acs Nano* **2012,** *6* (11), 10054-10062.

6. Bennett, E.; Greenberg, M. W.; Jordan, A. J.; Hamachi, L. S.; Banerjee, S.; Billinge, S. J. L.; Owen, J. S., Size Dependent Optical Properties and Structure of ZnS Nanocrystals Prepared from a Library of Thioureas. *Chem Mater* **2022,** *34* (2), 706-717.

7. Campos, M. P.; Hendricks, M. P.; Beecher, A. N.; Walravens, W.; Swain, R. A.; Cleveland, G. T.; Hens, Z.; Sfeir, M. Y.; Owen, J. S., A Library of Selenourea Precursors to PbSe Nanocrystals with Size Distributions near the Homogeneous Limit. *J Am Chem Soc* **2017,** *139* (6), 2296-2305.

8. Hamachi, L. S.; Plante, I. J. L.; Coryell, A. C.; De Roo, J.; Owen, J. S., Kinetic Control over CdS Nanocrystal Nucleation Using a Library of Thiocarbonates, Thiocarbamates, and Thioureas. *Chem Mater* **2017,** *29* (20), 8711-8719.

9. Hendricks, M. P.; Campos, M. P.; Cleveland, G. T.; Jen-La Plante, I.; Owen, J. S., A tunable library of substituted thiourea precursors to metal sulfide nanocrystals. *Science* **2015,** *348* (6240), 1226-1230.

10. Strach, M.; Mantella, V.; Pankhurst, J. R.; Iyengar, P.; Loiudice, A.; Das, S.; Corminboeuf, C.; van Beek, W.; Buonsanti, R., Insights into Reaction Intermediates to Predict Synthetic Pathways for Shape-Controlled Metal Nanocrystals. *J Am Chem Soc* **2019,** *141* (41), 16312-16322.

11. Mantella, V.; Varandili, S. B.; Pankhurst, J. R.; Buonsanti, R., Colloidal Synthesis of Cu-M-S (M = V, Cr, Mn) Nanocrystals by Tuning the Copper Precursor Reactivity. *Chem Mater* **2020,** *32* (22), 9780-9786.

12. Geisenhoff, J. Q.; Tamura, A. K.; Schimpf, A. M., Manipulation of Precursor Reactivity for the Facile Synthesis of Heterostructured and Hollow Metal Selenide Nanocrystals. *Chem Mater* **2020,** *32* (6), 2304-2312.

13. Norako, M. E.; Brutchey, R. L., Synthesis of Metastable Wurtzite $CuInSe_2$ Nanocrystals. *Chem Mater* **2010,** *22* (5), 1613-1615.

14. Tappan, B. A.; Barim, G.; Kwok, J. C.; Brutchey, R. L., Utilizing Diselenide Precursors toward Rationally Controlled Synthesis of Metastable CuInSe2 Nanocrystals. *Chem Mater* **2018,** *30* (16), 5704-5713.

15. Hernandez-Pagan, E. A.; Robinson, E. H.; La Croix, A. D.; Macdonald, J. E., Direct Synthesis of Novel $Cu_{2-x}Se$ Wurtzite Phase. *Chem Mater* **2019,** *31* (12), 4619-4624.

16. Rhodes, J. M.; Jones, C. A.; Thal, L. B.; Macdonald, J. E., Phase-Controlled Colloidal Syntheses of Iron Sulfide Nanocrystals via Sulfur Precursor Reactivity and Direct Pyrite Precipitation. *Chem Mater* **2017,** *29* (19), 8521-8530.

17. Lord, R. W.; Fanghanel, J.; Holder, C. F.; Dabo, I.; Schaak, R. E., Colloidal Nanoparticles of a Metastable Copper Selenide Phase with Near-Infrared Plasmon Resonance. *Chem Mater* **2020,** *32* (23), 10227-10234.

18. Geisenhoff, J. Q.; Tamura, A. K.; Schimpf, A. M., Using Ligands to Control Reactivity, Size and Phase in the Colloidal Synthesis of WSe_2 Nanocrystals. *Chem. Commun.* **2019,** *55* (60), 8856-8859.

19. Plummer, L. K.; Hutchison, J. E., Understanding the Effects of Iron Precursor Ligation and Oxidation State Leads to Improved Synthetic Control for Spinel Iron Oxide Nanocrystals. *Inorg. Chem.* **2020,** *59* (20), 15074-15087.

20. Zhou, P. S.; Schiettecatte, P.; Vandichel, M.; Rousaki, A.; Vandenabeele, P.; Hens, Z.; Singh, S., Synthesis of Colloidal WSe_2 Nanocrystals: Polymorphism Control by Precursor-Ligand Chemistry. *Cryst Growth Des* **2021,** *21* (3), 1451-1460.

21. Sahoo, P. K.; Kamal, S. S. K.; Premkumar, M.; Kumar, T. J.; Sreedhar, B.; Singh, A. K.; Srivastava, S. K.; Sekhar, K. C., Synthesis of Tungsten Nanoparticles by Solvothermal Decomposition of Tungsten Hexacarbonyl. *Int J Refract Met H* **2009,** *27* (4), 784-791.

22. Jung, W.; Lee, S.; Yoo, D.; Jeong, S.; Miro, P.; Kuc, A.; Heine, T.; Cheon, J., Colloidal Synthesis of Single-Layer MSe_2 (M = Mo, W) Nanosheets via Anisotropic Solution-Phase Growth Approach. *J Am Chem Soc* **2015,** *137* (23), 7266-7269.

23. Wang, Z. C.; Chen, Y. Z.; Zeng, D. Q.; Zhang, Q. F.; Peng, D. L., Solution Synthesis of Triangular and Hexagonal Nickel Nanosheets With the Aid of Tungsten Hexacarbonyl. *Crystengcomm* **2016,** *18* (8), 1295-1301.

24. Zhao, X. X.; Di, Q.; Wu, X. T.; Liu, Y. B.; Yu, Y. K.; Wei, G. J.; Zhang, J.; Quan, Z. W., Mild Synthesis of Monodisperse Tin Nanocrystals and Tin Chalcogenide Hollow Nanostructures. *Chem. Commun.* **2017,** *53* (80), 11001-11004.

25. Xiao, L.; Zhou, T.; Chen, Y. Z.; Wang, Z. C.; Zheng, H. F.; Xu, W. J.; Zeng, D. Q.; Peng, D. L., Tungsten Hexacarbonyl-Induced Growth of Nickel Nanorods and Nanocubes. *Mater Lett* **2018,** *229*, 340-343.

26. Zhao, X. X.; Di, Q.; Li, M. R.; Yang, Q.; Zhang, Z. Y.; Guo, X. Y.; Fan, X. K.; Deng, K. R.; Chen, W.; Zhang, J.; Fang, J. Y.; Quan, Z. W., Generalized Synthesis of Uniform Metal Nanoparticles Assisted with Tungsten Hexacarbonyl. *Chem Mater* **2019,** *31* (12), 4325-4329.

27. Sokolikova, M. S.; Sherrell, P. C.; Palczynski, P.; Bemmer, V. L.; Mattevi, C., Direct Solution-Phase Synthesis of 1T′ WSe_2 Nanosheets. *Nat Commun* **2019,** *10*.

28. Guo, W. B.; Chen, Y. Z.; Wang, L. S.; Xu, J.; Zeng, D. Q.; Peng, D. L., Colloidal Synthesis of $MoSe_2$ Nanonetworks and Nanoflowers With Efficient Electrocatalytic Hydrogen-Evolution Activity. *Electrochim Acta* **2017,** *231*, 69-76.

29. Liu, M.; Wang, Z. J.; Liu, J. X.; Wei, G. J.; Du, J.; Li, Y. P.; An, C. H.; Zhang, J., Synthesis of Few-Layer 1T'-$MoTe_2$ Ultrathin Nanosheets for High-Performance Pseudocapacitors. *J Mater Chem A* **2017,** *5* (3), 1035-1042.

30. Baddour, F. G.; Roberts, E. J.; To, A. T.; Wang, L.; Habas, S. E.; Ruddy, D. A.; Bedford, N. M.; Wright, J.; Nash, C. P.; Schaidle, J. A.; Brutchey, R. L.; Malmstadt, N., An Exceptionally Mild and Scalable Solution-Phase Synthesis of Molybdenum Carbide Nanoparticles for Thermocatalytic CO2 Hydrogenation. *J Am Chem Soc* **2020,** *142* (2), 1010-1019.

31. Qian, C.; Kim, F.; Ma, L.; Tsui, F.; Yang, P.; Liu, J., Solution-Phase Synthesis of Single-Crystalline Iron Phosphide Nanorods/Nanowires. *J Am Chem Soc* **2004,** *126* (4), 1195-8.

32. van Schooneveld, M. M.; Campos-Cuerva, C.; Pet, J.; Meeldijk, J. D.; van Rijssel, J.; Meijerink, A.; Erne, B. H.; de Groot, F. M. F., Composition Tunable Cobalt-Nickel and Cobalt-Iron Alloy Nanoparticles Below 10 NM Synthesized Using Acetonated Cobalt Carbonyl. *J. Nanopart. Res.* **2012,** *14* (8).

33. Kang, E.; Park, J.; Hwang, Y.; Kang, M.; Park, J. G.; Hyeon, T., Direct Synthesis of Highly Crystalline and Monodisperse Manganese Ferrite Nanocrystals. *J. Phys. Chem. B* **2004,** *108* (37), 13932-13935.

34. Hyeon, T.; Lee, S. S.; Park, J.; Chung, Y.; Bin Na, H., Synthesis of Highly Crystalline and Monodisperse Maghemite Nanocrystallites Without a Size-Selection Process. *J Am Chem Soc* **2001,** *123* (51), 12798-12801.

35. Meffre, A.; Mehdaoui, B.; Kelsen, V.; Fazzini, P. F.; Carrey, J.; Lachaize, S.; Respaud, M.; Chaudret, B., A Simple Chemical Route toward Monodisperse Iron Carbide Nanoparticles Displaying Tunable Magnetic and Unprecedented Hyperthermia Properties. *Nano Lett* **2012,** *12* (9), 4722-4728.

36. Puntes, V. F.; Krishnan, K. M.; Alivisatos, A. P., Colloidal Nanocrystal Shape and Size Control: The Case of Cobalt. *Science* **2001,** *291* (5511), 2115-2117.

37. Huang, L.; Zhang, X. P.; Wang, Q. Q.; Han, Y. J.; Fang, Y. X.; Dong, S. J., Shape-Control of Pt-Ru Nanocrystals: Tuning Surface Structure for Enhanced Electrocatalytic Methanol Oxidation. *J Am Chem Soc* **2018,** *140* (3), 1142-1147.

38. Lagunas, A.; Jimeno, C.; Font, D.; Sola, L.; Pericas, M. A., Mechanistic Studies on the Conversion of Dicobalt Octacarbonyl Into Colloidal Cobalt Nanoparticles. *Langmuir* **2006,** *22* (8), 3823-3829.

39. Puntes, V. F.; Zanchet, D.; Erdonmez, C. K.; Alivisatos, A. P., Synthesis of hcp-Co Nanodisks. *J Am Chem Soc* **2002,** *124* (43), 12874-12880.

40. Kang, Y. J.; Murray, C. B., Synthesis and Electrocatalytic Properties of Cubic Mn-Pt Nanocrystals (Nanocubes). *J Am Chem Soc* **2010,** *132* (22), 7568-+.

41. Lee, D. C.; Ghezelbash, A.; Stowell, C. A.; Korgel, B. A., Synthesis and Magnetic Properties of Colloidal MnPt3 Nanocrystals. *J. Phys. Chem. B* **2006,** *110* (42), 20906-20911.

42. Kang, Y.; Pyo, J. B.; Ye, X.; Diaz, R. E.; Gordon, T. R.; Stach, E. A.; Murray, C. B., Shape-Controlled Synthesis of Pt Nanocrystals: The Role of Metal Carbonyls. *Acs Nano* **2013,** *7* (1), 645-653.

43. Lewis, K. E.; Golden, D. M.; Smith, G. P., Organometallic Bond Dissociation Energies: Laser Pyrolysis of $Fe(CO)_5$, $Cr(CO)_6$, $Mo(CO)_6$, and $W(CO)_6$. *J Am Chem Soc* **1984,** *106* (14), 3905-3912.

44. Werner, H., Kinetic Studies on Substitution Reactions of Carbonylmetal Complexes. *Angew. Chem. Int. Edit.* **1968,** *7* (12), 930-&.

45. Darensbourg, D. J., Mechanistic Pathways for Ligand Substitution Processes in Metal Carbonyls. *Adv Organomet Chem* **1982,** *21*, 113-150.

46. Angelici, R. J., Kinetics and Mechanisms of Substitution Reactions of Metal Carbonyl Complexes. *Organomet Chem Rev A* **1968,** *3* (2), 173-226.

47. Atwood, J. D.; Brown, T. L., Cis Labilization of Ligand Dissociation. 3. Survey of Group 6 and 7 Six-Coordinate Carbonyl Compounds. The Site Preference Model for Ligand Labilization Effects. *J Am Chem Soc* **1976,** *98* (11), 3160-3166.

48. Howell, J. A. S.; Burkinshaw, P. M., Ligand Substitution-Reactions at Low-Valent 4-Coordinate, 5-Coordinate, and 6-Coordinate Transition-Metal Centers. *Chem Rev* **1983,** *83* (5), 557-599.

49. Kang, Y. J.; Ye, X. C.; Murray, C. B., Size- and Shape-Selective Synthesis of Metal Nanocrystals and Nanowires Using CO as a Reducing Agent. *Angew. Chem. Int. Edit.* **2010,** *49* (35), 6156-6159.

50. Wu, B. H.; Zheng, N. F.; Fu, G., Small Molecules Control the Formation of Pt Nanocrystals: A Key Role of Carbon Monoxide in the Synthesis of Pt Nanocubes. *Chem. Commun.* **2011,** *47* (3), 1039-1041.

51. Darensbourg, D. J.; Pala, M.; Simmons, D.; Rheingold, A. L., Chemical and Structural Characterization of $W(CO)_5OPPh_2NPPh_3$. A Novel Complex Containing a Phosphine Oxide Ligand Derived from the Bis(triphenylphosphine)nitrogen(1+) Cation. *Inorg. Chem.* **1986,** *25* (19), 3537-3541.

52. Planinić, P.; Meider, H., Synthesis and Characterization of Molybdenum(0) and Tungsten(0) Carbonyl Derivatives of Methylenebis[diphenylphosphine Oxide] And Bis[diphenylphosphinyl)methyl]phenylphosphine Oxide. *Polyhedron* **1989,** *8* (5), 627-632.

53. Cook, J. B.; Nicholson, B. K.; Smith, D. W., A structural, spectroscopic and theoretical study of the triphenylphosphine chalcogenide complexes of tungsten carbonyl, $[W(XPPh_3)(CO)_5]$, X = O, S, Se. *J Organomet Chem* **2004,** *689* (4), 860-869.

54. Lang, R. F.; Ju, T. D.; Kiss, G.; Hoff, C. D.; Bryan, J. C.; Kubas, G. J., Oxidative Addition of Disulfides to the Complex $W(CO)_3(phen)(EtCN)$. Synthesis, Structure, and Reactivity of $W(CO)_2(phen)(SR)_2$ (R = Ph, Me, CH_2Ph, ^tBu; phen = 1,10-Phenanthroline) Coordinatively Unsaturated Complexes of Tungsten(II) That Reversibly Bind CO and Other Ligands. *Inorg. Chem.* **1994,** *33* (18), 3899-3907.

55. Lang, R. F.; Ju, T. D.; Kiss, G.; Hoff, C. D.; Bryan, J. C.; Kubas, G. J., Oxidative Addition of Thiols, Disulfides, Iodine, and Hydrogen Iodide to $W(CO)_3(P^iPr_3)_2$. Preparation of Stable 17-Electron Tungsten Thiolate Radicals from Complexes with Weak W-H Bonds. *J Am Chem Soc* **1994,** *116* (17), 7917-7918.

56. Fortman, G. C.; Kegl, T.; Hoff, C. D., Kinetic, Thermodynamic, and Mechanistic Aspects of Oxidative Addition Reactions of RE-ER (E = S, Se, Te) and Transition Metal Complexes. *Curr Org Chem* **2008,** *12* (15), 1279-1297.

57. Fang, Y. Q.; Dong, Q.; Pan, J.; Liu, H. Y.; Liu, P.; Sun, Y. Y.; Li, Q. J.; Zhao, W.; Liu, B. B.; Huang, F. Q., Observation of Superconductivity in Pressurized 2M WSe_2 Crystals. *J Mater Chem C* **2019,** *7* (28), 8551-8555.

58. Darensbourg, D. J.; Walker, N.; Darensbourg, M. Y., Synthesis of Metal Carbonyl Complexes Highly Enriched in Carbon-13: Utilization of the CO-Labilizing Ability of $(n\text{-}Bu)_3P{=}O$. *J Am Chem Soc* **1980,** *102* (3), 1213-1214.

59. Darensbourg, D. J.; Darensbourg, M. Y.; Walker, N., Studies Using $(n\text{-}Bu)_3P{=}O$ as a Carbon Monoxide Labilizing Ligand in the Synthesis of Metal Carbonyl Complexes Highly Enriched in ^{13}CO. *Inorg. Chem.* **1981,** *20* (6), 1918-1921.

60. Aroney, M. J.; Buys, I. E.; Davies, M. S.; Hambley, T. W., Crystal-Structures of $[W(CO)_5(PPh_3)]$, $[M(CO)_5(AsPh_3)]$ and $[M(CO)_5(SbPh_3)]$ (M = Mo or W): A Comparative Study of Structure and Bonding in $[M(CO)_5(EPh_3)]$ Complexes (E = P, As or Sb; M = Cr, Mo or W). *J Chem Soc Dalton* **1994,** (19), 2827-2834.

61. Cotton, F. A.; Kraihanzel, C. S., Vibrational Spectra and Bonding in Metal Carbonyls. 1. Infrared Spectra of Phosphine-Substituted Group Vi Carbonyls in Co Stretching Region. *J Am Chem Soc* **1962,** *84* (23), 4432-+.

62. Angelici, R. J.; Malone, M. D., Infrared Studies of Amine Pyridine and Phosphine Derivatives of Tungsten Hexacarbonyl. *Inorg. Chem.* **1967,** *6* (9), 1731-&.

63. Cotton, F. A.; Darensbourg, D. J.; Ilsley, W. H., π Acidity of Tris(2-cyanoethyl)phosphine. X-ray Structural Studies of $M(CO)_5P(CH_2CH_2CN)_3$ (M = Cr, Mo) and $Mo(CO)_5P(C_6H_5)_3$. *Inorg. Chem.* **1981,** *20* (2), 578-583.

64. Honeychuck, R. V.; Hersh, W. H., Observation of a Novel ^{31}P NMR Cis-Influence Series: Implications for the Relative Basicity of PPh3 and PMe_3 in Tungsten Carbonyl Complexes. *Inorg. Chem.* **1987,** *26* (11), 1826-1828.

65. Wovkulich, M. J.; Atwood, J. D., Ligand Dissociation From Mono-Substituted Derivatives of Hexacarbonylchromium (Cr(CO)5L, L = $P(C_6H_5)_3$, $P(C_4H_9)_3$, $P(OCH_3)_3$, $P(OC_6H_5)_3$, and $As(C_6H_5)_3$). *J Organomet Chem* **1980,** *184* (1), 77-89.

66. Angelici, R. J.; Graham, J. R., Kinetic Studies of Group 6 Metal Carbonyl Complexes. I. Substitution Reactions of Dipyridyl Complexes of Chromium Hexacarbonyl. *J Am Chem Soc* **1965,** *87* (24), 5586-&.

67. Angelici, R. J.; Graham, J. R., Kinetic Studies of Group 6 Metal Carbonyl Complexes. IV. Substitution Reactions of O-Phenanthroline Complexes of Chromium Hexacarbonyl. *Inorg. Chem.* **1967,** *6* (5), 988-&.

68. Parker, P. J.; Wojcicki, A., Kinetic Studies of Carbonyl Substitution in Quinolinolatotetracarbonylmanganese(I) and Its Tricarbonyl Derivatives. *Inorg Chim Acta* **1974,** *11* (1), 17-23.

69. Cotton, F. A.; Darensbourg, D. J.; Kolthammer, B. W. S.; Kudaroski, R., Solid-State and Solution Structures of $[PNP][W(CO)_5O_2CCH_3]$ and $[PNP][W(CO)_4(PEt_3)O_2CCH_3]$ and the CO-Labilizing Ability of the Acetato Ligand in These Anionic Derivatives. *Inorg. Chem.* **1982,** *21* (4), 1656-1662.

70. Brown, R. A.; Dobson, G. R., Octahedral Metal Carbonyls. XXI. Carbonyl and Metal–Carbon Stretching Spectra of Monosubstituted Group Vib Metal Carbonyls. *Inorg Chim Acta* **1972,** *6*, 65-71.

71. Fenske, R. F.; Dekock, R. L., Electronic Structure and Bonding in Manganese Pentacarbonyl Halides and Hydride. *Inorg. Chem.* **1970,** *9* (5), 1053-&.

72. Ugeda, M. M.; Pulkin, A.; Tang, S.; Ryu, H.; Wu, Q.; Zhang, Y.; Wong, D.; Pedramrazi, Z.; Martin-Recio, A.; Chen, Y.; Wang, F.; Shen, Z. X.; Mo, S. K.; Yazyev, O. V.; Crommie, M. F., Observation of Topologically Protected States at Crystalline Phase Boundaries in Single-Layer WSe_2. *Nat Commun* **2018,** *9* (1), 3401.

73. Lai, Z.; He, Q.; Tran, T. H.; Repaka, D. V. M.; Zhou, D. D.; Sun, Y.; Xi, S.; Li, Y.; Chaturvedi, A.; Tan, C.; Chen, B.; Nam, G. H.; Li, B.; Ling, C.; Zhai, W.; Shi, Z.; Hu, D.; Sharma, V.; Hu, Z.; Chen, Y.; Zhang, Z.; Yu, Y.; Renshaw Wang, X.; Ramanujan, R. V.; Ma, Y.; Hippalgaonkar, K.; Zhang, H., Metastable 1T′-Phase Group VIB Transition Metal Dichalcogenide Crystals. *Nat. Mater.* **2021,** *20* (8), 1113-1120.

74. Calvin, J. J.; Kaufman, T. M.; Sedlak, A. B.; Crook, M. F.; Alivisatos, A. P., Observation of Ordered Organic Capping Ligands on Semiconducting Quantum Dots via Powder X-ray Diffraction. *Nat Commun* **2021,** *12* (1), 2663.

75. Aroney, M. J.; Buys, I. E.; Davies, M. S.; Hambley, T. W., Crystal-Structures of $[W(CO)_5(PPh_3)]$, $[M(CO)_5(AsPh_3)]$ and $[M(CO)_5(SbPh_3)]$ (M = Mo or W): A Comparative-Study of Structure and Bonding in $[M(CO)_5(EPh_3)]$ Complexes (E = P, As or Sb; M = Cr, Mo or W). *J Chem Soc Dalton* **1994,** (19), 2827-2834.

76. Sheldrick, G., SHELXT – Integrated Space-Group and Crystal-Structure Determination. *Acta Crystallogr. A* **2015,** *71* (1), 3-8.

Chapter 5: Insights into morphology control and the phase conversion pathway of colloidally synthesized WSe_2 nanocrystals

5.1 Abstract

We present a simple synthetic method that allows for morphological control of WSe_2 nanocrystals. Kinetic growth regimes are accessed by increasing the precursor concentration leading to nanocrystals with an increased number of layers. Under these kinetic growth regimes, the nanocrystals first nucleate in the metastable 2M phase and then convert to the thermodynamically favored 2H phase follows. Therefore, WSe_2 nanocrystals of controllable layer number and phase are produced. Using these syntheses, we obtain insights into the phase conversion pathway of the nanocrystals. The phase conversion progresses through a solid-state transformation where defects and interlayer binding energies impact the atom mobility in the lattice and the phase conversion rate.

5.2 Introduction

Solution-phase synthesis of solid-state materials (colloidal synthesis) is well known for its ability to access regimes of kinetic control. This kinetic control has been exploited to isolate nanocrystals of small sizes,[1-4] control shape,[5-8] and isolate materials in metastable phases.[9-13] This level of kinetic control for solid-state materials is unmatched in comparison to traditional solid-state syntheses, where high temperatures are necessary to overcome the barrier of atomic diffusion.[14-15]

For this reason, colloidal synthesis has become an emerging field to study phase control and phase conversion of materials.[9, 14, 16-18] Tungsten diselenide (WSe_2) poses an interesting system to study as it is biphasic and changes in the phase arise from relatively small differences in

coordination (Figure 5S.1). WSe_2 is a layered material where each layer is held together via van der Waals forces. The phase of the material is determined by how the individual layers stack, and the coordination of the metal within the layers. For WSe_2 the thermodynamically favored phase is built from trigonal prismatic coordination of the metal center to the chalcogen atoms. This leads to a hexagonal lattice (*P*63/*mmc*) and is referred to as 2H (2 layers per unit cell, hexagonal lattice).[19] This phase is semiconducting and is of interest due to its layer-dependent optical and electronic properties.[20-23] The metastable phase of WSe_2 is built from distorted octahedral coordination of the metal to the chalcogen atoms.[24-25] This distortion results in W-W bonds that form extended zig-zag chains through the lattice. This metastable phase is of lower symmetry and leads to a monoclinic lattice (*C*2/*m*).[24-26] Although this phase is sometimes referred to as 1T', here we adopt the label 2M (2 layers per unit cell, monoclinic lattice). This metastable phase has a small bandgap and is of interest due to its topologically insulating[27], and superconducting behavior.[25-26].

Indeed, colloidal chemistry has already been leveraged to synthesize WSe_2 in both the metastable and stable phases[16]. Under many colloidal chemistry conditions, it is observed that WSe_2 nucleates in the metastable 2M phase and then converts to its thermodynamically favored 2H phase.[11] In other words, the reactions are under kinetic control and follow Ostwald's rule of stages.[9, 28-29] Following the tenants of kinetically controlled reactions[30] the duration of the metastable phase can be prolonged by using less reactive precursors[11, 13] or lowering the reaction temperature.[10] However, multiple variables are changed during these reactions, such as ligand identity, precursor identity, and size and shape of the nanocrystals, which can make it challenging to identify specific factors governing the phase conversion process. Furthermore, it is unknown if the phase conversion is driven by a solvent-mediated transformation,[18] in which the 2M

nanocrystals dissolve and then recrystallize in the 2H phase, or a solid-state transformation[31] in which the 2H phase nucleates within the 2M lattice.

Herein we present a synthetic scheme in which variables can be systematically varied to understand the factors that influence phase conversion. This is done by using a single ligand system, trioctylphosphine oxide (TOPO), and hexadecane, and varying the concentration of the precursors used (tungsten hexacarbonyl ($W(CO)_6$) and diphenyl diselenide (Ph_2Se_2)). This allows us to eliminate the influence of changes in precursor identity or ligand environment and focus on how concentration alone impacts the reaction. To fully explore this reaction parameter space we vary the precursor concentration ([$W(CO)_6$] or [Ph_2Se_2]), total concentration ([$W(CO)_6$]+[Ph_2Se_2]), and equivalents of Ph_2Se_2 to $W(CO)_6$ (Ph_2Se_2/$W(CO)_6$). We find that increasing the total concentration yields nanocrystals with increased layer number with little change to lateral size. Additionally, we find that the phase conversion rate is tied to both layer number and the concentration of the Ph_2Se_2. Where at increased layer number and increased [Ph_2Se_2] there is slower phase conversion from the 2M phase to the 2H phase. Layer number and phase conversion rate being tied to concentration allows us to interrogate the phase conversion mechanism. We demonstrate that once formed the nanocrystals do not show much, if any, dissolution and recrystallization. Therefore, the phase converts via a crystal-to-crystal transformation process, and the phase conversion rate is governed by interlayer interactions and defect concentration. These findings give insight into the crystallization pathways for WSe_2 and identify the dominant phase conversion mechanism, and factors governing this phase conversion. The work presented herein will be useful in crafting phase-controlled syntheses of TMD materials and is of broad use for understanding phase conversion processes in colloidal synthesis.

5.3 Results and Analysis

Tungsten diselenide (WSe_2) nanocrystals were prepared via a reaction of diphenyl diselenide (Ph_2Se_2) with tungsten hexacarbonyl ($W(CO)_6$) in a mixture of triotylphosphine oxide (TOPO) and hexadecane (used for injection). Using this system multiple variables are changed to investigate how morphology and phase conversion is impacted. The variables investigated here are precursor concentration ([$W(CO)_6$] or [Ph_2Se_2]), total concentration ([$W(CO)_6$]+[Ph_2Se_2]), and equivalents of Ph_2Se_2 to $W(CO)_6$ ($Ph_2Se_2/W(CO)_6$). First, we will look at a reaction that uses intermediate values of those variables for this study; [$W(CO)_6$]=12, [Ph_2Se_2]=60, [$W(CO)_6$]+[Ph_2Se_2]=73, and $Ph_2Se_2/W(CO)_6$=5. Briefly, 0.06 mmol $W(CO)_6$ was heated in 4 ml TOPO to 150 °C. After sitting at this temperature for about 10 minutes, to fully solubilize the tungsten precursor, 0.30 mmol of Ph_2Se_2 in 1 ml hexadecane was swiftly injected into the solution. Immediately following injection, the mixture is heated to 330 °C. This ramp from 150 to 330 °C takes ten minutes and once the final temperature is reached the solution is held at this temperature for 3 hours. The heating profile of this reaction can be found in figure 5S.2a. We used a low-temperature injection followed by a heat-up as previous studies found that heating $W(CO)_6$ in TOPO to high temperatures can result in the decomposition of the tungsten precursor.[11] The low-temperature injection thus ensures the reactions proceed through molecular intermediates.

To monitor how nanocrystal morphology and phase change over the duration of the reaction aliquots are taken. Aliquot 1 is taken during the ramp step at 250 °C, 5 minutes after Ph_2Se_2 injection. Aliquots 2-8 are taken after the solution reaches 330 °C at 10, 15, 20, 40, 70, 130, and 190 minutes after injection (Figure 5S.2a and b). Powder X-ray diffraction is performed on all aliquots (Figure 5.1a). The metastable 2M phase and the thermodynamically favored 2H phase reference patterns are shown at the top and bottom of Figure 5.1a respectively. Some important reflections to take note of are the (002) reflection, which for both phases is at 13.7 2θ, the (-113)

reflection of the 2M phase at 34.5 2θ, and the (103) reflection of the 2H phase at 37.9 2θ. Previously we have demonstrated that the (-113) and (103) reflections of the 2M and 2H phases are useful to distinguish between the 2 phases.[11] At early reaction times and low temperatures (5 min after injection, 250 °C) the diffraction pattern lacks a peak at the (002) reflection, indicating little to no layer stacking. Starting at around 30 2θ some broad peaks arise that are indicative of a transition metal dichalcogenide material that is small in size. The first maximum is at 33.7 2θ shifted the expected (-113) of the 2M phases and there is no hump located at the (103) reflection of the 2H phase. The broadness and shifting of these peaks suggest the material has short-range order but more closely resembles the metastable 2M phase. When the reaction reaches 330 °C, 10 minutes after injection, a peak at the (002) reflection grows in and the peaks past 30 2θ sharpen. However, the first hump is still broadened and shifted to lower 2θ from the expected (-113) of the 2M phase. This shift still indicates a lack of crystallinity/small size of the material. After 5 minutes at 330 °C and 15 minutes after the Ph_2Se_2 injection (aliquot 3), there is an increase in the intensity of the (002) reflection indicating an increase in the number of layers of the nanocrystals. Aliquot 2 also shows a splitting of the broad hump at 34 2θ to a shoulder at 31 2θ and a sharpening and localization of the (-113) reflection of the 2M phase to its expected position at 34.5 2θ. This indicates that this aliquot is more crystalline and shows distinctly the metastable 2M phase.

All aliquots taken after 15 minutes (aliquots 3-8) show (002) reflections of similar sharpness and intensity indicating that the number of layers per particle stays consistent after 15 minutes. The FWHM of the (002) reflection for each aliquot is summarized in table 5S.1. The average (002) FWHM is 2.36 ± 0.04 for aliquots 2-8. Using the Scherrer equation we can estimate the number of layers giving an average of 6.2 ± 0.1 layers. To visualize the lack of change of layers with time the layer number for aliquots 2-8 are plotted versus time (Figure 5S.3a).

Using the (-113) and (103) reflections of the 2M and 2H phase we can analyze the change of phase over the course of the reaction. Overall, the (-113) becomes prominent 15 minutes after the injection of Ph_2Se_2 and persists at later times. The (103) reflection of the 2H phase gains some intensity with time but is hard to distinguish. To summarize this, we have defined an intensity ratio of $I_{38\ 2\theta}/\ I_{35\ 2\theta}$. This is used to depict the growth of the 2H phase especially when changes in the powder X-ray diffraction patterns are slight. The $I_{38\ 2\theta}/\ I_{35\ 2\theta}$ increases from 0.63 to 0.67 with time (Figure 5S.3b and Table 5S.1) indicating that some conversion to the 2H phase takes place.

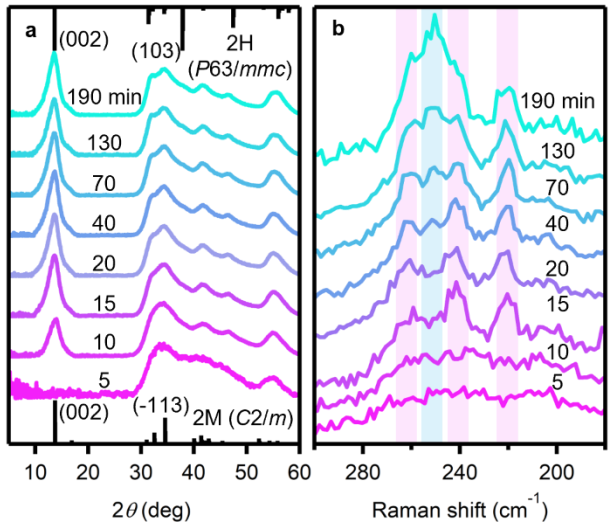

Figure 5. 1. PXRD (a) and Raman spectra (b) for aliquots taken during synthesis using nanocrystals synthesized by injecting 0.30 mM Ph_2Se_2 in 1ml hexadecane into a solution of 0.06 mM $W(CO)_6$ in 4 ml TOPO at 150 °C, followed by a heat-up to 330 °C. Aliquots were taken at 5, 10, 15, 20, 40, 70, 130, and 190 minutes. Pink bars in Raman spectra highlight 2M modes and blue bar highlights 2H modes.

It can be challenging to solely rely on the powder X-ray diffraction to determine relative amounts of phases in the sample as overlapping reflections between the phases and broadening from the nanocrystal samples can complicate the analysis. To overcome this, we use Raman spectroscopy (Figure 5.1b). Raman spectroscopy corroborates our analysis at early times and temperatures. At 5 and 10 minutes after the injection (aliquots 1 and 2), no Raman modes are

observed suggesting these aliquots lack crystallinity. At 15 minutes after the Ph_2Se_2 injection 3 peaks arise at 219 cm^{-1}, 240 cm^{-1}, and 260 cm^{-1} matching the known Raman modes of the 2M phase. As time progresses a peak grows at 251 cm^{-1} which is from the unresolved combination of the A_{1g} and E_{2g} Raman modes of the 2H phase. To better summarize the phase conversion observed here we can define an intensity ratio of 2H Raman modes over the selected 2M Raman mode at 219 cm^{-1}, $I_{251\ cm^{-1}}/I_{220\ cm^{-1}}$. This value starts at 0.64 and increases to 2.32 (Figure 5S.3c and Table 5S.1) explicitly showing the increase in the 2H phase with time. We note that the 2H phase is more sensitive to Raman spectroscopy due to greater interaction with the 532 nm light which likely results in an overestimation of the 2H phase.

To test the reproducibility of these results 2 more reactions with the same conditions were performed. Reaction conditions are summarized in Table 5S.4. The powder X-ray diffraction patterns taken at the 70-minute aliquot for all the reactions are shown in Figure 5S.4a. The (002) reflections for all samples are at similar intensities and broadness. The FWHM of the (002) reflections for each reaction are summarized in Table 5S.2, and the average (002) FWHM is 2.2 ± 0.2. The Raman spectra for the aliquot taken 190 minutes after injection is shown in Figure 5S.4b. A similar phase analysis detailed previously is performed. The ratio $I_{251\ cm^{-1}}/I_{220\ cm^{-1}}$ at the 190-minute aliquot gives an average of 2.2 ± 0.2 and the ratio $I_{38\ 2\theta}/\ I_{35\ 2\theta}$ gives an average of 0.63 ± 0.1 across all 3 reactions. This suggests that for the same reaction conditions we can reproducibly form nanocrystals with similar morphology and phase.

Importantly, the reaction outlined here has available methods to analyze the layer number and phase conversion of the nanocrystals, which makes this a good system to analyze how precursor concentration ($[W(CO)_6]$ or $[Ph_2Se_2]$), total concentration ($[W(CO)_6]+[Ph_2Se_2]$), and equivalents of Ph_2Se_2 to $W(CO)_6$ ($Ph_2Se_2/W(CO)_6$) will impact the layer number and phase conversion. Using

the previous reaction as an anchor ([$W(CO)_6$]=12, [Ph_2Se_2]=60, [$W(CO)_6$]+[Ph_2Se_2]=73, and $Ph_2Se_2/W(CO)_6$=5) we will systematically vary one variable at a time to discern which factors are most important to changing layer number and phase of the nanocrystals and to give insight into potential phase conversion mechanisms of WSe_2.

Constant [$W(CO)_6$], varied [Ph_2Se_2]

For the first set of reactions, the amount of $W(CO)_6$ added was held constant at 12 mM and the amount of Ph_2Se_2 injected was varied. Reaction conditions and data are summarized in Table 5S.3. Performing reactions in this way results in all 3 variables of [Ph_2Se_2], [$W(CO)_6$]+[Ph_2Se_2], and $Ph_2Se_2/W(CO)_6$ changing. The Raman spectra for aliquots 3-8 are shown in Figure 5.2. The reaction with the least amount of diphenyl diselenide injected is shown in Figure 5.2a; [Ph_2Se_2]=12 mM, [$W(CO)_6$]+[Ph_2Se_2]=24, $Ph_2Se_2/W(CO)_6$=1. The amount of diphenyl diselenide injected is increased in Figure 5.2b; [Ph_2Se_2]=24 mM, [$W(CO)_6$]+[Ph_2Se_2]=36, $Ph_2Se_2/W(CO)_6$=2. Raman for the anchor reaction is shown in Figure 5.2c; [Ph_2Se_2]=60 mM, [$W(CO)_6$]+[Ph_2Se_2]=73, $Ph_2Se_2/W(CO)_6$=5. Finally the reaction with the greatest amount of Ph_2Se_2 injected is in Figure 5.2d [Ph_2Se_2]=123 mM, [$W(CO)_6$]+[Ph_2Se_2]=132, $Ph_2Se_2/W(CO)_6$=10. A clear trend emerges where fewer equivalents and a lower concentration of the Ph_2Se_2 precursor results in more rapid conversion to the 2H phase. The 1 eq/12 mM case has a very intense peak in the Raman spectra at 250 cm^{-1}, well over any 2M Raman modes, at the end of the reaction. This trend gets weaker as the equivalents and concentration of Ph_2Se_2 increase, were for the final aliquot of the 10 eq/123 mM reaction, the 2H mode at 250 cm is barely formed compared to the 3 2M Raman modes. This phase conversion is summarized using the intensity ratio, $I_{251\ cm^{-1}}/I_{220\ cm^{-1}}$ (Figure 5.2f). For each of the reactions, the ratio of the 2H/2M phase starts in a similar position suggesting all reactions begin with nucleation in the metastable 2M phase. As time progresses, the 1 eq/12 mM reaction

increases in the 2H phase rapidly, and begins to level off around 130 minutes after the injection, then ends at 190 minutes with $I_{251\ cm}^{-1}/I_{220\ cm}^{-1}$=11.3, (green circles). The 2 eq/24 mM follows a similar trajectory but begins tailing off at a lower $I_{251\ cm}^{-1}/I_{220\ cm}^{-1}$ value, ending with a value of 4.8. The 5 eq/61 mM and 10 eq/123 mM reactions do not follow an exponential rise in the phase conversion, but rather are still in a linear regime suggesting the equilibrium amounts of 2H to 2M phase have not been reached. These reactions follow the same trend where the final $I_{251\ cm}^{-1}/I_{220\ cm}^{-1}$ value for the 5 eq/61 mM is 2.3 and for the 10 eq/123 mM is 1.3, showing that the amount of conversion to the 2H phase is reduced at higher amounts of Ph_2Se_2 added when the $W(CO)_6$ is held at the constant value of $[W(CO)_6]$= 12 mM.

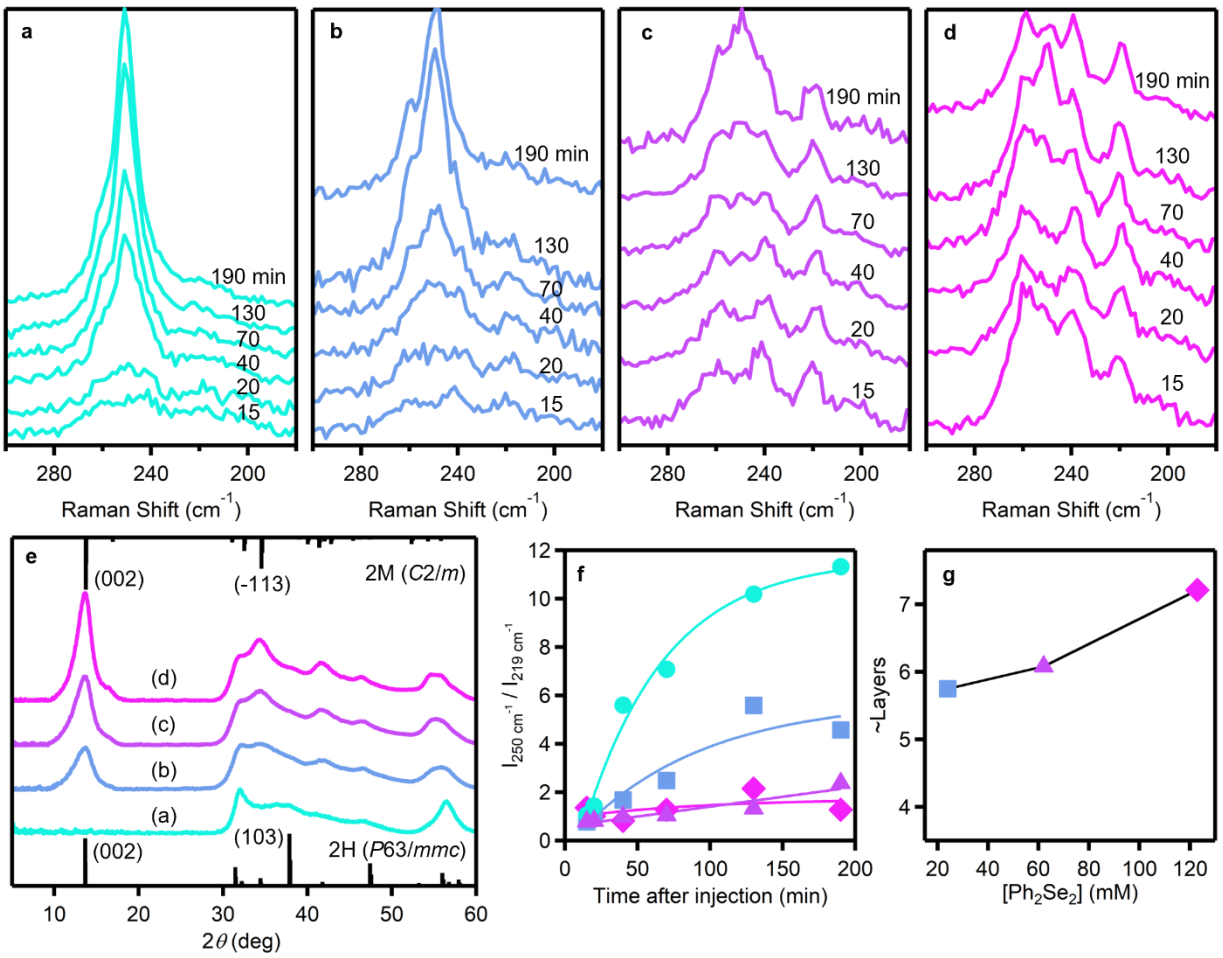

Figure 5. 2. Raman spectra at different reaction times for nanocrystals synthesized by keeping the amount of $W(CO)_6$ added constant (0.06 mmol) in 4 ml TOPO and a varying amount of Ph_2Se_2 injected in 1 ml hexadecane **(a)** 1eq (0.06 mmol), **(b)** 2eq (0.12 mmol), **(c)** 5 eq (0.30 mmol) and **(d)** 10 eq (0.60 mmol). pXRD for each of the corresponding reactions **(e)** including reference patterns for the 2M and 2H phase. The relative intensity of the 2H Raman modes over selected 2M Raman mode, $I_{251\ cm^{-1}}/I_{220\ cm^{-1}}$ plotted with time for the 1 eq (green circles), 2 eq (blue squares), 5 eq (purple triangles) and 10 eq (pink diamonds) reactions **(f)**. Layer number calculated using the Scherrer equation plotted against $[Ph_2Se_2]$ shown for the 2 eq, 5 eq, and 10 eq reactions.

Powder X-ray diffraction was performed on aliquot 6 (70 minutes after injection) for all reactions (Figure 5.2e). Here we can corroborate the increase in the 2H phase with lower amounts of Ph_2Se_2 that was seen in the Raman spectroscopy by using the intensity ratio defined earlier $I_{38\ 2\theta}/ I_{35\ 2\theta}$. This ratio is 1.1, 0.74, 0.64, and 0.56 for the 1 eq/12 mM, 2eq/24 mM, 5eq/61 mM, and

10 eq/123 mM reactions, respectively. The powder X-ray diffraction can also be used to analyze the nanocrystal layer number by looking at the FWHM of the (002) reflection. The 1 eq/12 mM reaction has no (002) peak, the 2 eq/24 mM reaction has a broad (002) peak with an FWHM of 2.6, the (002) of the 5 eq/61 mM reaction increases in intensity and sharpens to a FWHM of 2.4, finally the 10 eq/123 mM reaction continues this trend with a FWHM of 2.0. These values can be converted to layer numbers using the Scherrer equation to give 5.6, 6.1, and 7.4 for the 2, 5, and 10 eq reactions respectively (Table 5S.3, Figure 5.2g).

TEM images were taken on nanocrystals synthesized under a similar set of conditions but reacted for just an hour at 330 °C. TEM images for the 1 eq/12 mM, 2eq/24 mM, 5eq/61 mM, and 10 eq/123 mM reactions are shown in Figure 5S.5 a, b, c, and d respectively. It is clear that at lower diphenyl diselenide equivalents the particles have fewer layer numbers. Using the TEM images number of layers for the resulting sets of nanocrystals was analyzed (Figure 5S.5 j). With the increase of equivalents and concentration of Ph_2Se_2 we see an increase in the layer number; 1 eq 2±1, 2 eq 3±2, 5 eq 7±3, and 10 eq 9±5. However, the lateral sizes remain mostly unchanged; 1 eq 5±1 nm, 2 eq 5±1 nm, 5 eq 6±1 nm, and 10 eq 7±2 nm (Figure 5S.5 i).

Constant $[W(CO)_6]+[Ph_2Se_2]$, varied $Ph_2Se_2/W(CO)_6$

By holding the concentration of $W(CO)_6$ constant and changing the equivalents/concentration of Ph_2Se_2 the total concentration $[W(CO)_6]+[Ph_2Se_2]$, $[Ph_2Se_2]$, and $Ph_2Se_2/W(CO)_6$ are changed between each reaction. To tease out these competing effects we hold the $[W(CO)_6]+[Ph_2Se_2]$ at a constant value and vary the equivalents $Ph_2Se_2/W(CO)_6$. To keep the anchor reaction $[W(CO)_6]=12$, $[Ph_2Se_2]=60$, $[W(CO)_6]+[Ph_2Se_2]=73$, and $Ph_2Se_2/W(CO)_6=5$, we hold all reactions to $[W(CO)_6]+[Ph_2Se_2]=73$ and vary $Ph_2Se_2/W(CO)_6$ between 1, 2, 5, and 11 eq. Reaction conditions and data are summarized in Table 5S.4. The Raman spectra for aliquots 3-8 are shown

in Figure 5.2 a, b, c, and d, respectively. Here we see a similar phase conversion rate for the 1 eq reaction, where the 2H phase comes in very rapidly and ends with a great contribution of the 2H phase. The 2 eq reaction ends with only some 2H phase over the 2M modes and the 10 eq reaction shows the smallest amounts of 2H phase over the 2M phase modes. This is summarized using the intensity ratio $I_{251\ cm^{-1}}/I_{220\ cm^{-1}}$ and plotting this with time (Figure 5.3f). The reactions end at 190 minutes after injection with an intensity ratio of 8.3, 2.7, 2.3, and 1.6 for the 1, 2, 5, and 11 eq reactions respectively.

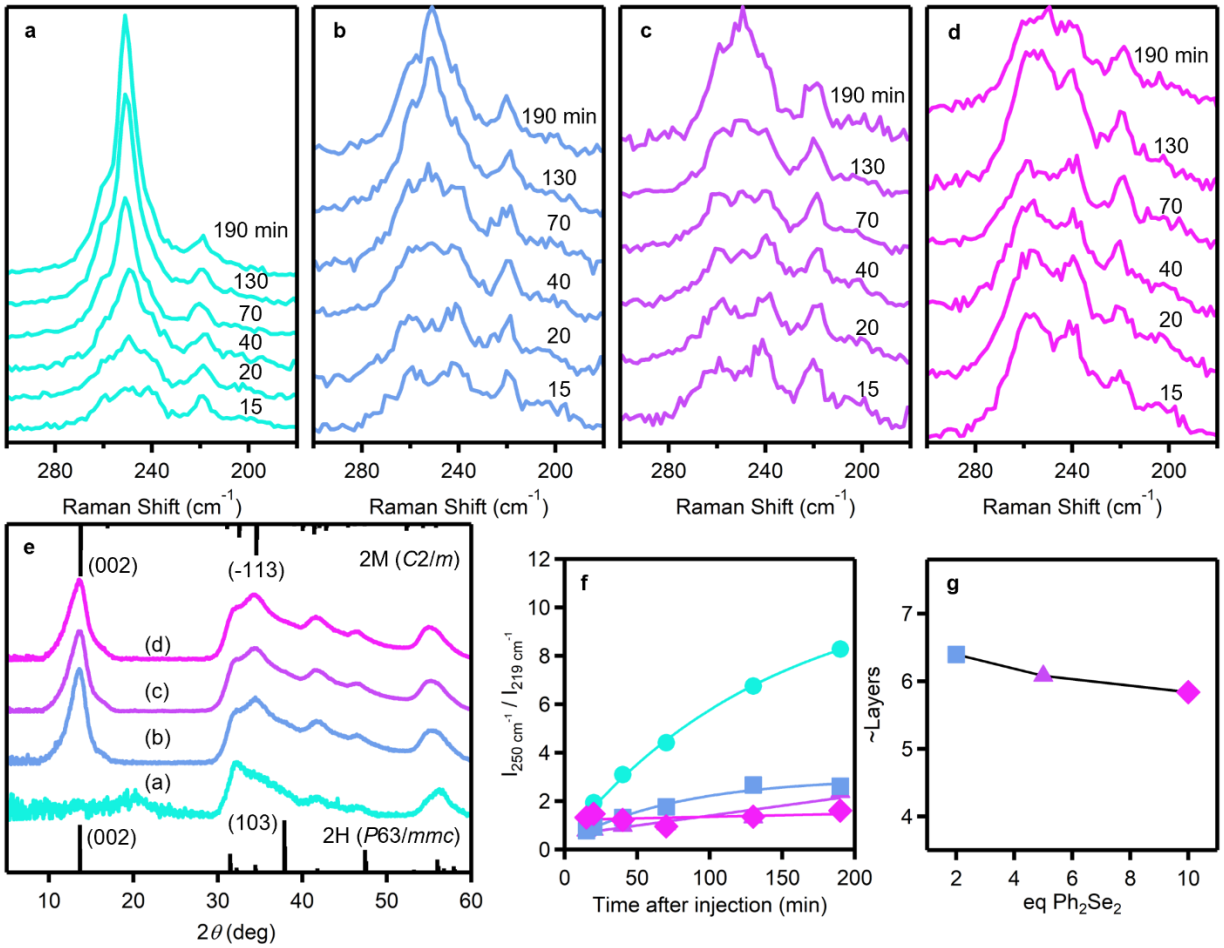

Figure 5. 3. Raman spectra at different reaction times for nanocrystals synthesized by keeping the total concentration, $[W(CO)_6]+[Ph_2Se_2]$, constant at 73 mM and varying the equivalents of $Ph_2Se_2/W(CO)_6$ **(a)** 1eq, **(b)** 2eq, **(c)** 5 eq and **(d)** 10 eq. pXRD for each of the corresponding reactions **(e)** including reference patterns for the 2M and 2H phase. The relative intensity of the 2H Raman modes over selected 2M Raman mode, $I_{251\ cm^{-1}}/I_{220\ cm^{-1}}$ plotted with time for the 1 eq (green circles), 2 eq (blue squares), 5 eq (purple triangles) and 10 eq (pink diamonds) reactions **(f)**. Layer number calculated using the Scherrer equation plotted against equivalents shown for the 2 eq, 5 eq, and 10 eq reactions.

The powder X-ray diffraction for the 70-minute aliquot of these reactions is shown in Figure 3e. Again, these mirror the phase conversion trend shown in the Raman data. The intensity ratio, $I_{38\ 2\theta}/ I_{35\ 2\theta}$, is 0.79, 0.66, 0.64, and 0.61 for the 1, 2, 5, and 11 eq reactions respectively. Looking at the (002) reflection we see that the 1 eq reaction again has no peak, indicating very few layers.

While the FWHM is 2.3, 2.4, and 2.5 for the 2, 5, and 11 eq reactions, this results in layer numbers of 6.3, 6.1, and 5.9. These results are not statistically significant from one another, suggesting there is little change in nanocrystal layer number between these reactions. All values are summarized in Table 5S.4.

Constant $Ph_2Se_2/W(CO)_6$, varied $[W(CO)_6]+[Ph_2Se_2]$

From the previous data set it appears that (for >2eq) holding the total concentration the same does not impact the number of layers in the nanocrystals, however, there is a slight change to the amount of phase conversion observed which may be coming directly from the eq of Ph_2Se_2 added. To further explore this we held the equivalents of $Ph_2Se_2/W(CO)_6$ at 5 and varied the total concentration $[W(CO)_6]+[Ph_2Se_2]$ between 23, 35, 73, and 147 mM. Reaction conditions and data are summarized in Table 5S.5. The Raman spectra for aliquots 3-8 of the reactions are shown in Figures 5.4 a, b, c, and d. In general, the amount of phase conversion decreases with increased concentration. At the low concentration of 23 mM, we see the most amount of 2H phase at the final time aliquot of 190 min, at the high concentration of 147 mM we see the least amount of 2H phase at the final time and 35 mM and 73 mM fall in between these two points. This is summarized using the intensity ratio $I_{251\ cm^{-1}}/I_{220\ cm^{-1}}$ and plotting this with time (Figure 5.4f). The reactions end at 190 minutes after injection with an intensity ratio of 4.9, 3.0, 2.3, and 1.4 for the 23, 35, 73, and 147 mM reactions respectively.

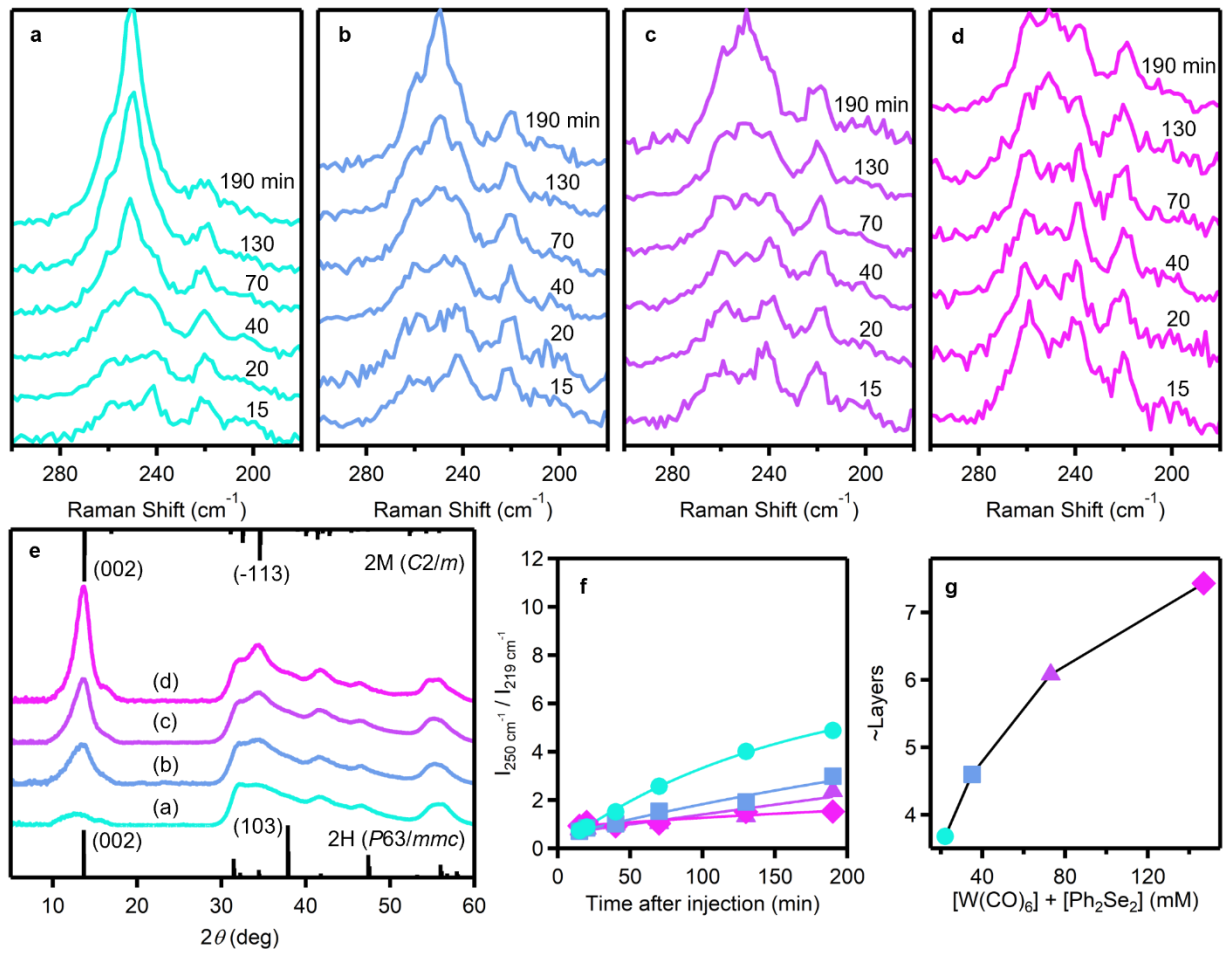

Figure 5. 4. Raman spectra at different reaction times for nanocrystals synthesized by keeping the equivalents of Ph_2Se_2 to $W(CO)_6$ constant at 5 eq and varying the total concentration, $[W(CO)_6]+[Ph_2Se_2]$, at **(a)** 23, **(b)** 35, **(c)** 72 and **(d)** 147 mM. pXRD for each of the corresponding reactions **(e)** including reference patterns for the 2M and 2H phase. The relative intensity of the 2H Raman modes over selected 2M Raman mode, $I_{251\ cm^{-1}}/I_{220\ cm^{-1}}$ plotted with time for the 23 mM (green circles), 35 mM (blue squares), 72 mM (purple triangles) and 147 mM (pink diamonds) reactions **(f)**. Layer number was calculated using the Scherrer equation plotted against equivalents shown for the 23, 35, 72, and 147 mM reactions.

The powder X-ray diffraction for the 70-minute aliquot of these reactions is shown in Figure 5.4e. The intensity ratio, $I_{38\ 2\theta}/ I_{35\ 2\theta}$, is 0.74, 0.65, 0.64, and 0.52 for the 23, 35, 73, and 147 mM reactions respectively. We also see a trend with layer number and concentration. The (002) for the 23 mM reaction is weak and broad, increasing the total concentration results in an increase in intensity and sharpening of the (002) that was seen previously in the first series. The FWHM is

3.7, 3.1, 2.4, and 2.0 for the 23, 35, 73, and 147 mM reactions respectively. This results in layer numbers 6.3, 6.1, and 5.9 e. All values are summarized in Table 5S.5.

Constant [Ph_2Se_2], varied [$W(CO)_6$]

From the previous trend, it appears that holding the equivalents constant does not keep the amount of phase conversion constant. The total amount of Ph_2Se_2 is also varied so finally, we study the effect of holding the concentration of [Ph_2Se_2] at a constant value, 60 mM, and varying the amount of [$W(CO)_6$] between 5, 12, 32, and 60 mM. Reaction conditions are summarized in Table 5S.6. The Raman spectra for aliquots 3-8 of the reactions are shown in Figures 5.5 a, b, c, and d. Here the 60 mM reaction results in using 1 eq of the $Ph_2Se_2/W(CO)_6$. The results in terms of phase conversion and morphology match the previous 1 eq reactions the phase conversion is very rapid, Figure 5.5a and f, giving an $I_{251\ cm^{-1}}/I_{220\ cm^{-1}}$=9.1. The other values of [$W(CO)_6$] of 5, 12, and 32 mM result in $Ph_2Se_2/W(CO)_6$ of 11, 5, and 2 respectively. For these conditions, the amount of 2H phase of the final Raman aliquot looks similar (Figure 5.5b, c, and d). This similarity can also be seen in the intensity ratio $I_{251\ cm^{-1}}/I_{220\ cm^{-1}}$ over time, where the traces for these 3 reactions lie on top of one another (Figure 5.5f). This similarity in the phase conversion is summarized by the $I_{251\ cm^{-1}}/I_{220\ cm^{-1}}$ at 190 min which is 2.0, 2.3, and 1.9 for the 5, 12, and 32 mM reactions respectively.

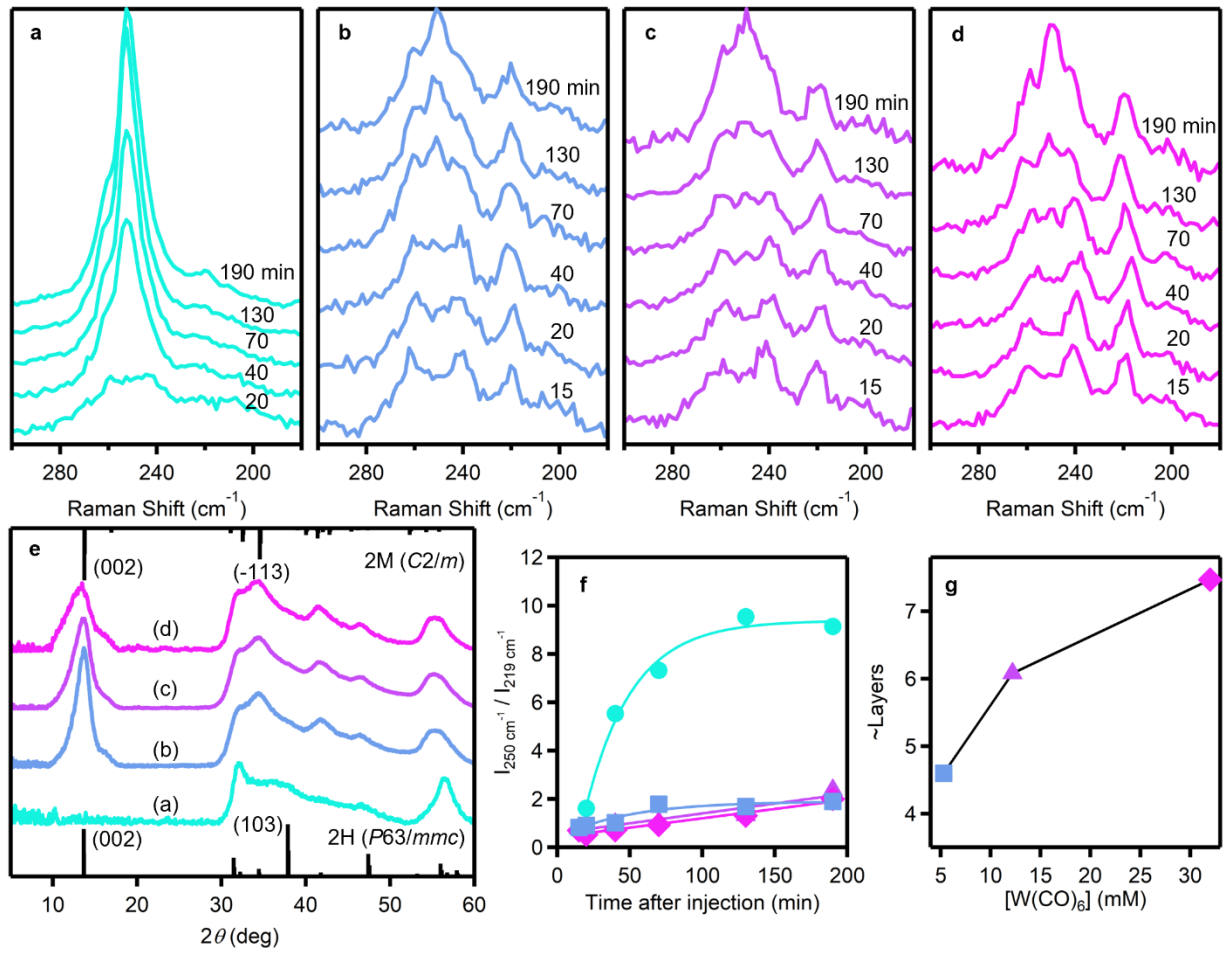

Figure 5. 5. Raman spectra at different reaction times for nanocrystals synthesized by keeping the amount of Ph_2Se_2 injected in 1ml hexadecane constant (0.30 mmol) and a varying amount of $W(CO)_6$ in 4 ml TOPO at **(a)** 1eq (0.30 mmol), **(b)** 2eq (0.16 mmol), **(c)** 5 eq (0.06 mmol) and **(d)** 10 eq (0.03 mmol). pXRD for each of the corresponding reactions **(e)** including reference patterns for the 2M and 2H phase. The relative intensity of the 2H Raman modes over selected 2M Raman mode, $I_{251\ cm^{-1}}/I_{220\ cm^{-1}}$ plotted with time for the 1 eq (green circles), 2 eq (blue squares), 5 eq (purple triangles) and 10 eq (pink diamonds) reactions **(f)**. Layer number calculated using the Scherrer equation plotted against $[W(CO)_6]$ shown for the 2 eq, 5 eq, and 10 eq reactions.

The powder X-ray diffraction for the 70-minute aliquot of these reactions is shown in Figure 5.5e. The intensity ratio, $I_{38\ 2\theta}/ I_{35\ 2\theta}$, for the 1 eq reaction is 0.91 showing high amounts of phase conversion. While for the $[W(CO)_6]$ of 5, 12, and 32 mM this value is 0.64, 0.64, and 0.65 respectively, showing little change in phase. When looking at a change in nanocrystal morphology,

we see that the 1 eq reaction remains an outlier even at these higher concentrations showing no (002) reflection indicating very few layers. While for the other reaction we see a similar trend in the layer number seen previously. At lower concentrations $[W(CO)_6]$=5 there is a broadened (002) and moving to increased concentrations results in an increase in intensity and sharpening of the (002). The FWHM is 3.1, 2.4, and 1.9 for the 5, 12, and 32 mM reactions respectively. This results in layer numbers 4.7, 6.1, and 7.7. All values are summarized in Table 5S.6.

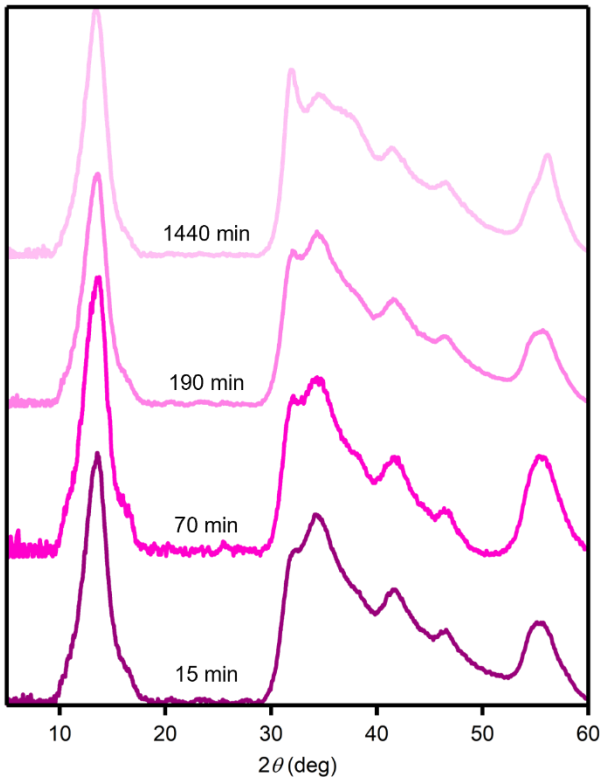

Figure 5. 6. Powder X-ray diffraction for nanocrystals synthesized with 5 eq Ph_2Se_2 at 72 mM total concentration at times, from bottom to top, 15, 75, and 195 minutes after injection **(a)**. pXRD for the reaction that used the same conditions (5 eq and 72 mM) but after 15 minutes 2 mls of the solution was injected into a second flask containing 6 ml of TOPO diluting the total concentration down to 24 mM. Aliquots take at 15 (before dilution), 75, and 195 minutes after injection shown **(b)**.

From the previously presented data, there seems to be a connection between the overall concentration and the layer number of the nanocrystals and a connection between the [Ph_2Se_2] and the phase conversion rate. To test if dissolution and recrystallization are occurring we performed a reaction where the concentration was reduced after the initial formation of the nanocrystals. Using the standard reaction; [$W(CO)_6$]=12, [Ph_2Se_2]=60, [$W(CO)_6$]+[Ph_2Se_2]=73, and $Ph_2Se_2/W(CO)_6$=5 as our base the nanocrystals were nucleated then the solution was diluted. The nanocrystals were allowed to grow for 15 minutes after injection, the point at that we noted full crystallization had occurred in figure 5.1. After 15 minutes, 2 mL of this solution was injected into a 330 °C solution of 6 mls TOPO. This dilution results in a solution of [$W(CO)_6$]=4, [Ph_2Se_2]=20, [$W(CO)_6$]+[Ph_2Se_2]=24, and $Ph_2Se_2/W(CO)_6$=5 mimicking the conditions used in the reaction shown in Figure 5.4a. A reaction ran directly at these lower concentrations has a significant reduction in the number of layers and increased phase conversion compared to the standard reaction. The powder X-ray diffraction pattern for this dilution reaction is shown at 15 minutes (before dilution), 70, 190, and 1440 minutes in Figure 5.6. Interestingly, we find that there is not a significant change in the FWHM of the (002) of the reaction after the dilution, even after 24 hours (Table 5S.7). Additionally, the phase conversion trends match that of the standard reaction. The $I_{38\ 2\theta}/ I_{35\ 2\theta}$ closely matches the standard reaction with time (Table 5S.7). Comparing the 190-minute aliquot Raman spectra we also see similar amounts of phase conversion (Figure 5S.6).

5.4 Discussion

Nanocrystal Morphology

The WSe_2 nanocrystals synthesized here first nucleate with few layers, then grow as the reaction is heated until they reach their final size, Figure 5.1. The final size and layer number of

the nanocrystals are reached quickly after the injection, 15 minutes after the injection, and 5 minutes after the reaction reaches 330 °C, after which growth is no longer observed. The nanocrystals likely grow via a layer-by-layer or monomer-by-monomer addition growth mechanism that has been observed previously for MoS_2.[32-33] Increasing the concentration of the reaction leads to more available monolayers accessing kinetically controlled growth regimes facilitating layer growth. Interestingly, the concentration of tungsten causes a more significant difference in the layer number of the nanocrystals per mM compared to the changing concentration of the diphenyl diselenide. We hypothesize that this may be due to the monomer intermediate having a greater amount of Se than W.

Reactions synthesized with $Ph_2Se_2/W(CO)_6$ =1, however, do not follow this trend. All reactions with 1 equivalent of the Ph_2Se_2 precursor result in very few layer nanocrystals as no (002) reflection is present in the powder X-ray diffraction pattern, showing no dependence on concentration. We hypothesize that this difference may be due to only 1 equivalent of Ph_2Se_2 increasing the concentration of Se defects in the nanocrystals which weakens the interlayer interactions and prevents layer stacking.

Phase Conversion

All reactions shown in this study are under kinetic control as the metastable phase is nucleated first, then conversion to the thermodynamic phase occurs, which is consistent with previous colloidal syntheses of WSe_2 nanocrystals. The low-temperature injection helps ensure nucleation in the metastable 2M phase and the precursors are fully consumed at these low temperatures. This suggests that an increase in 2H phase is due to phase conversion from the 2M phase rather than separate nucleation of the 2H phase. Both increases in a number of layers and [Ph_2Se_2] reduce the

amount of phase conversion. For equivalents of Ph_2Se_2 > 2 the dominant influence is [Ph_2Se_2] while for $Ph_2Se_2/W(CO)_6$ =1 the phase conversion is dependent on nanocrystal morphology.

The mechanism for Phase Conversion

In the solution phase, there are 2 possible phase conversion mechanisms: crystal-to-crystal where the 2H phase nucleates within the 2M nanocrystals and begins the phase transition process,[31] or solvent-mediated where the 2M nanocrystals dissolve and then 2H nanocrystals nucleate and grow.[18] With the dependence of the phase conversion on the [Ph_2Se_2], it may be tempting to assume the solvent-mediated case as increasing the concentration may serve to prevent dissolution and thus phase conversion. We tested the validity of this mechanism with the dilution reaction in Figure 6. Since we know that both layer number and phase are concentration-dependent, after the dilution we would expect a broadening of the (002) reflection and an increase in phase conversion if the nanocrystals were dissolving and recrystallizing. However, we see no change in the nanocrystal layer number or phase conversion rate after dilution. This suggests the solvent-mediated pathway is not strongly influencing the phase conversion. More strongly bonded covalent lattices prevent dissolution.[34]

A solid-state transformation is more likely for the WSe_2 nanocrystals synthesized here. Nucleation of the second phase is usually driven via defects or grain boundaries, and growth of this phase is facilitated via atom diffusion in the lattice. We hypothesize that both Se defects and the nanocrystal morphology are factors that affect the nucleation and growth of the 2H phase. The [Ph_2Se_2] could dictate Se defect concentration where more defects facilitate atom diffusion. The interlayer binding energy between the nanosheets is reduced with a smaller number of layers. Weak interlayer binding energies also serve to facilitate atom diffusion and phase conversion.

5.5 Summary and Conclusions

The syntheses presented herein show that nanocrystal morphology can be easily tuned by changing the precursor concentration, where increased concentrations lead to nanocrystals with an increased number of layers. Reactions using this colloidal synthesis are all under kinetic control where the metastable 2M phases of WSe_2 nucleates first then conversion to the thermodynamically favored 2H phase occurs. We also show that the phase conversion mechanism proceeds through a solid-state transformation where defects and interlayer binding energies impact the phase conversion rate.

5.6 Supplementary Information

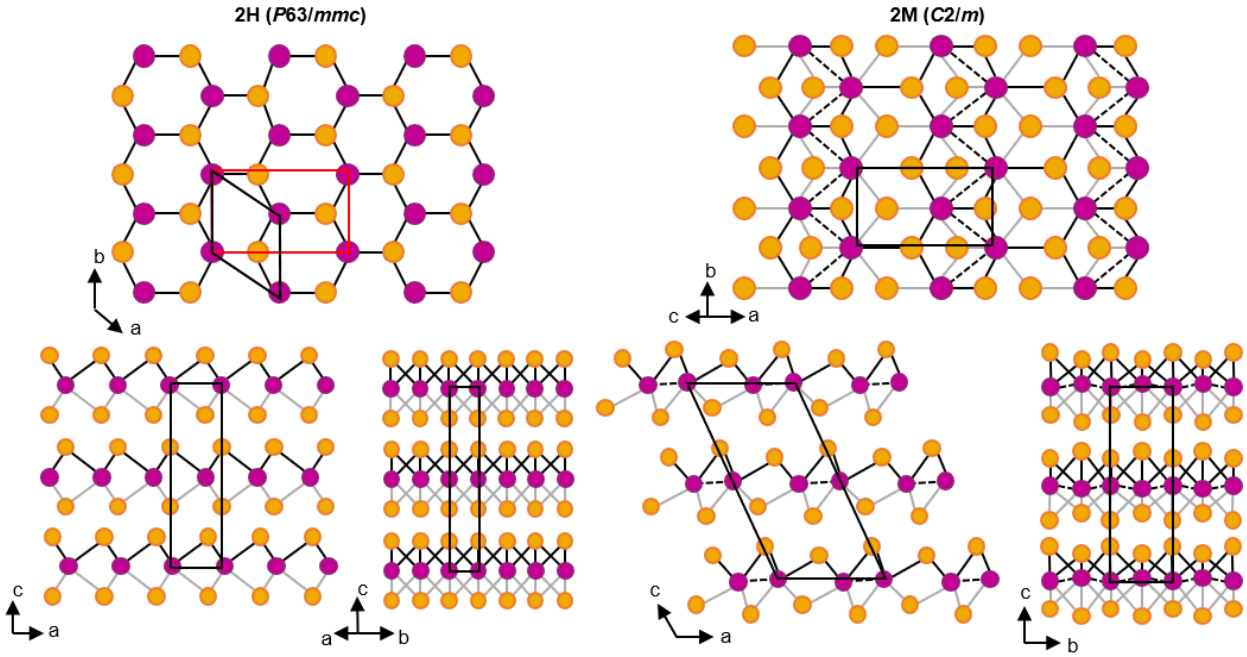

Figure S5. 1. Crystal structures of the thermodynamically favored 2H phase (p63/mmc) and the metastable 2M phase (C2/m). Unit cells for phases highlighted in black.

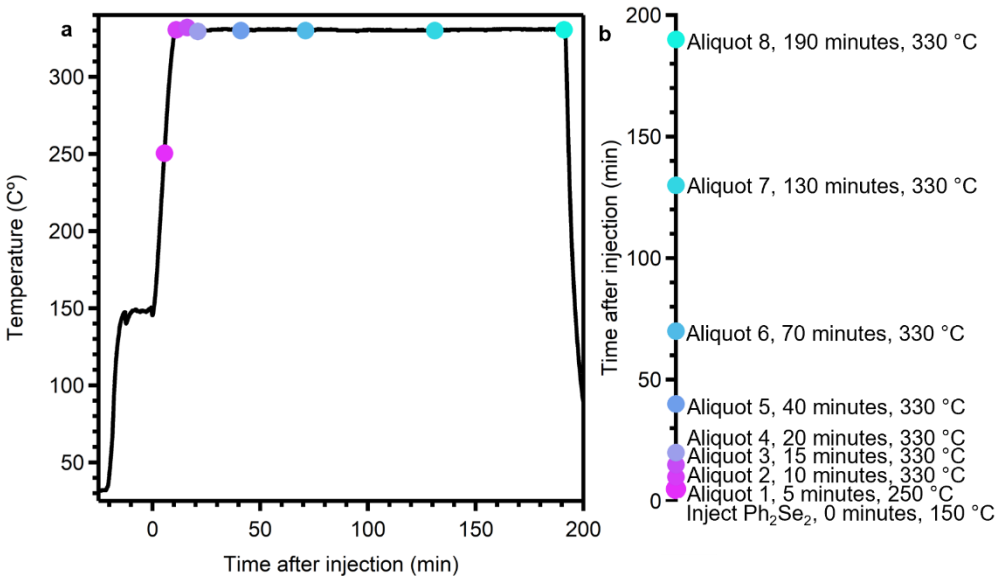

Figure S5. 2. (a) Typical heating curve of a standard reaction. Solution heated to 150 C to solubilize the tungsten hexacarbonyl, dip occurs after injection of Ph_2Se_2, then solution heated to 330 °C for 3 hours. Colored circles show points at which aliquots are taken. **(b)** Outline of time and temperature aliquots are taken.

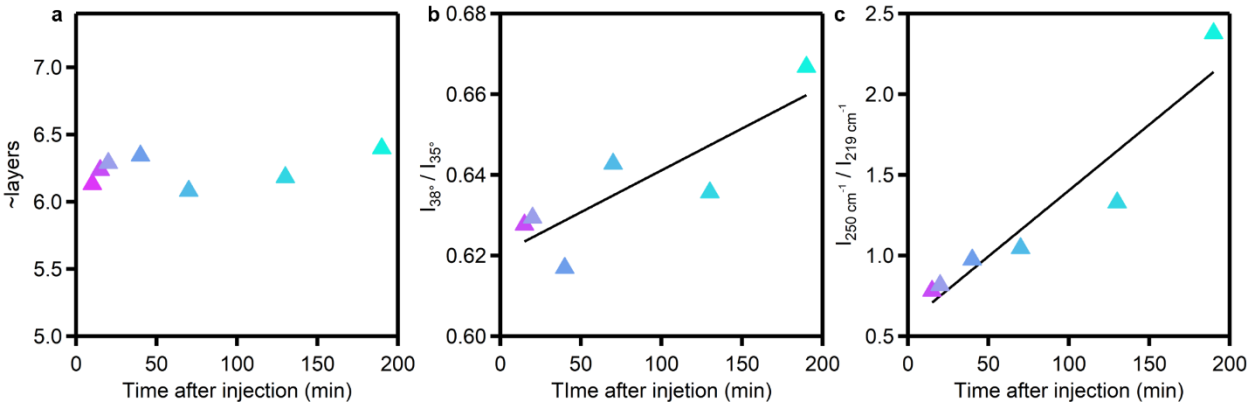

Figure S5. 3. (a) Number of layers calculated from the (002) FWHM for aliquots 2-8. (b) Ratio of intensities of the Raman mode at 250 cm^{-1} over the Raman mode at 219 cm^{-1} plotted over time for aliquots 3-8. (c) Ratio of intensities of pXRD patterns at 38 2θ over 35 2θ plotted over time for aliquots 3-8.

Table S5. 1. Time, temperature, (002) FWHM, I_{251}/I_{220}, and I_{38}/I_{35} summarized for aliquots taken during a synthesis using nanocrystals synthesized by injecting 0.3 mM Ph_2Se_2 in 1ml hexadecane into a solution of 0.06 mM $W(CO)_6$ in 4 ml TOPO at 150 °C, followed by a heat-up to 330 °C.

Aliquot	Time (min)	Temperature (°C)	(002) FWHM	Layers	I_{251}/I_{220}	I_{38}/I_{35}
1	7	300	N/A	N/A	N/A	N/A
2	10	330	2.40	6.1	N/A	N/A
3	15	330	2.36	6.2	0.64	0.63
4	20	330	2.34	6.3	0.77	0.63
5	40	330	2.32	6.3	0.97	0.62
6	70	330	2.42	6.1	1.02	0.64
7	130	330	2.38	6.2	1.33	0.64
8	190	330	2.30	6.4	2.32	0.67

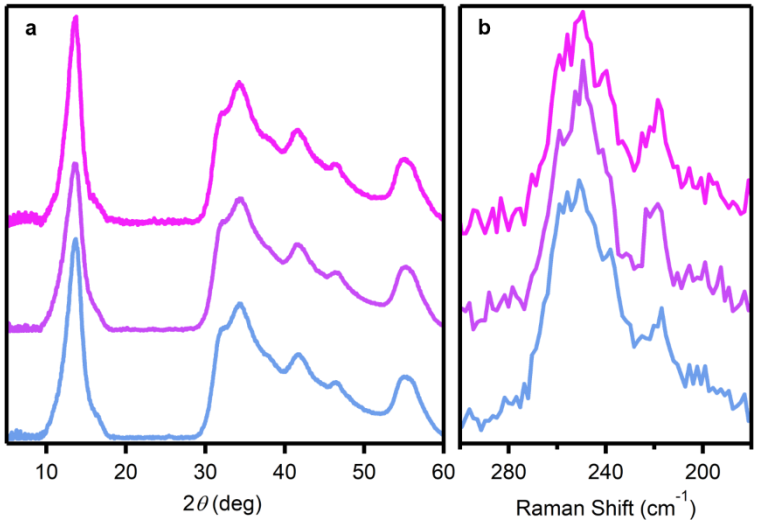

Figure S5. 4. (a) pXRD on aliquot 6 and **(b)** Raman spectra on aliquot 8 for repeated 5 eq reactions synthesized at total concentration of 73 mM.

Table S5. 2. Reaction parameters for repeated reactions synthesized with 5eq Ph_2Se_2 to $W(CO)_6$ at total concentration of 73 mM. (002) FWHM, I_{251}/I_{220}, and I_{38}/I_{35} from each reaction averaged.

$W(CO)_6$ (mmol)	Ph_2Se_2 (mmol)	Ph_2Se_2 /$W(CO)_6$	$[W(CO)_6]$ (mM)	$[Ph_2Se_2]$ (mM)	$[W(CO)_6]$+ $[Ph_2Se_2]$ (mM)	(002) FWHM	Layers	I_{251}/I_{220} (190 min)	I_{38}/I_{35} (70 min)
0.06	0.30	5	12	61	73	2.4	6.1	2.3	0.64
0.06	0.31	5	12	62	74	2.2	6.7	2.2	0.63
0.06	0.30	5	12	60	72	2.1	7.0	2.1	0.62
						2.2 ± 0.2	6.6 ± 0.4	2.2 ± 0.2	0.63 ± 0.01

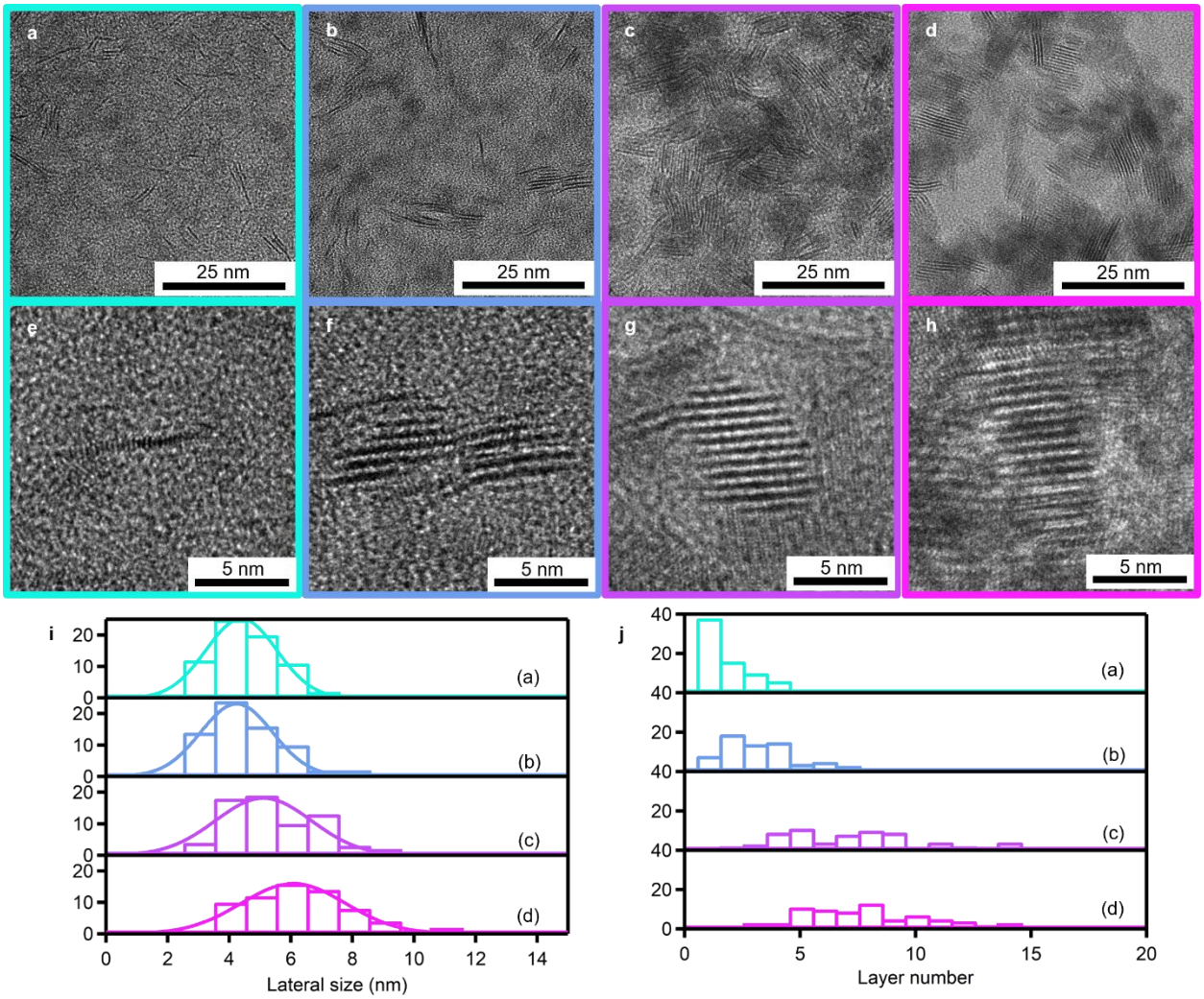

Figure S5. 5. TEM images for nanocrystals synthesized by keeping amount of $W(CO)_6$ added constant (0.06 mmol) in 4 ml TOPO and varying amount of Ph_2Se_2 injected in 1 ml hexadecane **(a)** 1eq (0.06 mmol), **(b)** 2eq (0.12 mmol), **(c)** 5 eq (0.30 mmol) and **(d)** 10 eq (0.62 mmol). And selected zoomed in images highlighting isolating nanocrystals (e), (f), (g), and (h) for same reactions respectively. Statistical analyses (n=70) of lateral sizes (i) and layer number (j) for corresponding reactions. TEM on aliquots taken after 1 hour at 330 °C, or 70 minutes after injection.

Table S5. 3. Reaction parameters for nanocrystals synthesized by keeping amount of $W(CO)_6$ added constant (0.056 mmol) in 4 ml TOPO and varying amount of Ph_2Se_2 injected in 1 ml hexadecane.

$W(CO)_6$ (mmol)	Ph_2Se_2 (mmol)	Ph_2Se_2 /$W(CO)_6$	$[W(CO)_6]$ (mM)	$[Ph_2Se_2]$ (mM)	$[W(CO)_6]$+ $[Ph_2Se_2]$ (mM)	(002) FWHM	Layers	I_{251}/I_{220} (190 min)	I_{38}/I_{35} (70 min)
0.06	0.06	1	12	12	24	N/A	N/A	11.3	1.1
0.06	0.12	2	12	24	36	2.6	5.6	4.8	0.74
0.06	0.30	5	12	61	73	2.4	6.1	2.3	0.64
0.06	0.62	10	12	123	132	2.0	7.4	1.3	0.56

Table S5. 4. Reaction parameters for nanocrystals synthesized by keeping the total concentration, $[W(CO)_6]+[Ph_2Se_2]$ the same and varying the equivalents of $Ph_2Se_2/W(CO_6$. Used 4 ml of TOPO and injection done in 1 ml hexadecane.

$W(CO)_6$ (mmol)	Ph_2Se_2 (mmol)	Ph_2Se_2 /$W(CO)_6$	$[W(CO)_6]$ (mM)	$[Ph_2Se_2]$ (mM)	$[W(CO)_6]+$ $[Ph_2Se_2]$ (mM)	(002) FWHM	Layers	I_{251}/I_{220} (final)	I_{38}/I_{35}
0.03	0.34	11	6	67	73	2.5	5.9	1.6	0.61
0.06	0.30	5	12	60	73	2.4	6.1	2.3	0.64
0.12	0.25	2	23	50	73	2.3	6.3	2.7	0.66
0.15	0.21	1	30	42	72	N/A	N/A	8.3	0.79

Table S5. 5. Reaction parameters for nanocrystals synthesized by keeping the equivalents of Ph_2Se_2 to $W(CO)_6$ constant and varying the total concentration. Used 4 ml of TOPO and injection done in 1 ml hexadecane.

$W(CO)_6$ (mmol)	Ph_2Se_2 (mmol)	Ph_2Se_2 /$W(CO)_6$	$[W(CO)_6]$ (mM)	$[Ph_2Se_2]$ (mM)	$[W(CO)_6]+$ $[Ph_2Se_2]$ (mM)	(002) FWHM		I_{251}/I_{220} (final)	I_{38}/I_{35}
0.02	0.10	6	3	20	23	3.7	4.0	4.9	0.74
0.03	0.15	5	6	29	35	3.1	4.7	3.0	0.65
0.06	0.30	5	12	60	73	2.4	6.1	2.3	0.64
0.13	0.61	5	25	122	147	2.0	7.4	1.4	0.52

Table S5. 6. Reaction parameters for nanocrystals synthesized by keeping the amount of Ph_2Se_2 injected constant and varying the amount of $W(CO)_6$ added. Used 4 ml of TOPO and injection done in 1 ml hexadecane.

$W(CO)_6$ (mmol)	Ph_2Se_2 (mmol)	Ph_2Se_2 /$W(CO)_6$	$[W(CO)_6]$ (mM)	$[Ph_2Se_2]$ (mM)	$[W(CO)_6]+$ $[Ph_2Se_2]$ (mM)	(002) FWHM		I_{251}/I_{220} (final)	I_{38}/I_{35}
0.03	0.30	11	5	60	66	3.1	4.7	2.0	0.64
0.06	0.30	5	12	60	73	2.4	6.1	2.3	0.64
0.16	0.30	2	32	60	92	1.9	7.7	1.9	0.65
0.30	0.30	1	60	60	120	N/A	N/A	9.1	0.91

Table S5. 7. (002) FWHM, I_{251}/I_{220}, and I_{38}/I_{35} values summarized at aliquots taken at 15, 70, and 190 minutes for both the standard 5eq reaction with a total concentration of 73 mM (standard), and the reaction diluted to 24 mM after 15 minutes of reaction time (dilution).

	Standard		Dilution	
Time (min)	(002) FWHM	I_{38}/I_{35}	(002) FWHM	I_{38}/I_{35}
15	2.36	0.63	2.44	0.63
70	2.42	0.64	2.51	0.61
190	2.30	0.67	2.48	0.67
			2.38	0.88

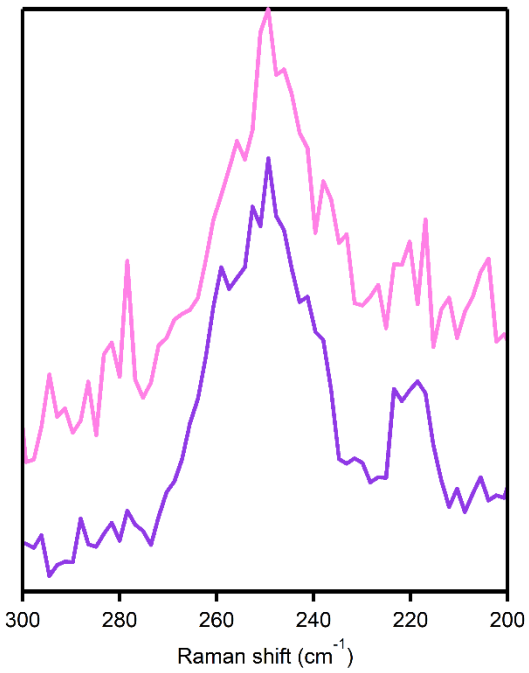

Figure S5. 6. Raman for 190 minute aliquot of 5 eq Ph_2Se_2 at 72 mM total concentration reaction (bottom purple) and same reactions condition, but diluted to 24 mM after 15 minutes (top pink). The intensity ratio of the dilution reaction is 2.3 and for the standard reaction it is 2.4.

Experimental methods

Chemical	**Purity**	**Manufacturer**
Trioctylphosphine oxide (TOPO)	99%	STREM
Hexadecane	>98%	TCI
Tungsten hexacarbonyl ($W(CO)_6$)	99%	Acros
Diphenyl diselenide (Ph_2Se_2)	>97%	TCI
Toluene	99.9%	Fischer
Methanol (MeOH)	99.9%	Fischer
Deuterated chloroform	99.8%	Cambridge Laboratories inc

All chemicals were used without further purification. TOPO, hexadecane, $W(CO)_6$ and Ph_2Se_2 were stored under nitrogen in a glove box and toluene MeOH and d-chloroform stored under ambient conditions. All reactions were carried out using a glass sheath to prevent contamination from the temperature probe.

Synthesis of WSe_2 nanocrystals with $[W(CO)_6]=12$, $[Ph_2Se_2]=60$, $[W(CO)_6]+[Ph_2Se_2]=73$, and $Ph_2Se_2/W(CO)_6=5$: Two 25 ml round bottom flasks (one 3 neck, one 4 neck) charged with glass covered stir bars, an air condenser and 2 flow adapters were dried in a 120 °C oven. Glassware, septa, ceramic sheaths, and flow adapter components were then pumped into the glove box. In the 4 neck 25 ml RB 21.1 mg $W(CO)_6$ and 3.6 g TOPO are combined. This flask is fitted with the two ceramic sheaths and condenser. In the other flask, a 2 ml stock solution is made consisting of 188 mg Ph_2Se_2 and 1.546 g hexadecane are combined. All glassware is appropriately fitted with flow adapters and septa, removed from box and placed on the Schlenk line. Space up to the flow adapters are evacuated and refilled with argon 3 times in quick succession. Chemicals are then opened to up to the line and are evacuated and refilled with argon 3 times over the course of an hour at room temperature. After final refilling of argon, mixture with $W(CO)_6$ is heated to 150 °C using a temperature controller and held at that temperature for 10 minutes. At about 70 °C gas evolution begins, and solution turns yellow. Meanwhile, the flask containing Ph_2Se_2 is heated to 70 °C with a variac and temperature is monitored using a thermometer outside the flask (this is done to ensure complete dissolution of the Ph_2Se_2 and to avoid large temperature drops after injection). After both solutions are appropriately heated, an injection of 1 ml of the Ph_2Se_2 solution into the $W(CO)_6$ solution is performed. After injection solution is heated to 330 °C, after reaching this temperature the solution is held there for the duration of the experiment. During heating rapid gas evolution is observed and solution changes color from yellow to a brown/black. Aliquots are taken from the reaction by removing about 0.1 ml of solution using a purged 1 ml syringe and needle, and immediately injecting that into a vial containing a small amount of toluene to prevent solidification of the TOPO. After the reaction is complete, solution is cooled by removing the heating mantle. At about 80 °C septa on the flask are

removed and some toluene is injected to avoid solidification of mixture. Aliquots and final reaction solutions are transferred to centrifuge tubes and methanol is added in 1:0.5 volume ratio to the mixture. These are centrifuged for 5 minutes at 8000 rpm. After initial crash NCs washed 2 more times by redispersing in toluene, adding MeOH and centrifuging for 5 minutes at 8000 rpm.

Synthesis of WSe_2 NCs with other conditions: To vary the [$W(CO)_6$], [Ph_2Se_2], [$W(CO)_6$]+[Ph_2Se_2], and Ph_2Se_2/$W(CO)_6$ conditions specified in Tables S2-S7. The reaction was performed in a similar manner as stated previously, but the amounts of Ph_2Se_2 and $W(CO)_6$ were varied to match the target concentrations.

Characterization

Raman spectroscopy: Samples were prepared by drop-casting a suspension of nanocrystals in hexanes onto a polished silicon substrate (Silicon Valley Microelectronics). Raman spectra were collected using a Renishaw inVia confocal Raman microscope with 532 nm laser excitation(10mW) and a 50× objective lens.

Powder X-ray diffraction: After washing nanocrystals, excess solvent was removed with vacuum or air drying. Dried samples were transferred to a loop. Powder X-ray diffraction patterns were collected using a D8 Smart diffractometer with a Pt 135 detector equipped with a Rigaku MicroMax-007HF High-intensity Microfocus rotating anode with Cu Kα radiation (λ= 1. 54184)at 40 kV, 30 mA and Varimax-HF double bounce optics. Diffraction images were merged/integrated in Diffrac.EVA V.4.3.0.1(Bruker).

Transmission electron microscopy. TEM grids were prepared by drop-casting a suspension of nanocrystals in toluene as a single drop onto a 100-mesh copper TEM grid coated with formvar and carbon (Electron Microscopy Sciences). Images were collected on a ThermoFisher Talos 200X TEM.

5.7 Acknowledgments

Chapter 5, in part, is currently being prepared for submission for publication of the material. The dissertation author was the primary author of this paper and gratefully acknowledges the contributions of coauthor Alina M. Schimpf.

5.8 References

1. Bennett, E.; Greenberg, M. W.; Jordan, A. J.; Hamachi, L. S.; Banerjee, S.; Billinge, S. J. L.; Owen, J. S., Size Dependent Optical Properties and Structure of ZnS Nanocrystals Prepared from a Library of Thioureas. *Chem Mater* **2022,** *34* (2), 706-717.

2. Campos, M. P.; Hendricks, M. P.; Beecher, A. N.; Wslravens, W.; Swain, R. A.; Cleyeland, G. T.; Hens, Z.; Sfeir, M. Y.; Owen, J. S., A Library of Selenourea Precursors to PbSe Nanocrystals with Size Distributions near the Homogeneous Limit. *J Am Chem Soc* **2017,** *139* (6), 2296-2305.

3. Hamachi, L. S.; Plante, I. J. L.; Coryell, A. C.; De Roo, J.; Owen, J. S., Kinetic Control over CdS Nanocrystal Nucleation Using a Library of Thiocarbonates, Thiocarbamates, and Thioureas. *Chem Mater* **2017,** *29* (20), 8711-8719.

4. Hendricks, M. P.; Campos, M. P.; Cleveland, G. T.; Jen-La Plante, I.; Owen, J. S., A tunable library of substituted thiourea precursors to metal sulfide nanocrystals. *Science* **2015,** *348* (6240), 1226-1230.

5. Yin, Y.; Alivisatos, A. P., Colloidal nanocrystal synthesis and the organic-inorganic interface. *Nature* **2005,** *437* (7059), 664-670.

6. Smith, J. D.; Scanlan, M. M.; Chen, A. N.; Ashberry, H. M.; Skrabalak, S. E., Kinetically Controlled Sequential Seeded Growth: A General Route to Crystals with Different Hierarchies. *Acs Nano* **2020,** *14* (11), 15953-15961.

7. Strach, M.; Mantella, V.; Pankhurst, J. R.; Iyengar, P.; Loiudice, A.; Das, S.; Corminboeuf, C.; van Beek, W.; Buonsanti, R., Insights into Reaction Intermediates to Predict Synthetic Pathways for Shape-Controlled Metal Nanocrystals. *J Am Chem Soc* **2019,** *141* (41), 16312-16322.

8. Zhao, M.; Chen, Z. T.; Shi, Y. F.; Hood, Z. D.; Lyu, Z. H.; Xie, M. H.; Chi, M. F.; Xia, Y. A., Kinetically Controlled Synthesis of Rhodium Nanocrystals with Different Shapes and a Comparison Study of Their Thermal and Catalytic Properties. *J Am Chem Soc* **2021,** *143* (16), 6293-6302.

9. Washington, A. L.; Foley, M. E.; Cheong, S.; Quffa, L.; Breshike, C. J.; Watt, J.; Tilley, R. D.; Strouse, G. F., Ostwald's Rule of Stages and Its Role in CdSe Quantum Dot Crystallization. *J Am Chem Soc* **2012,** *134* (41), 17046-17052.

10. Sokolikova, M. S.; Sherrell, P. C.; Palczynski, P.; Bemmer, V. L.; Mattevi, C., Direct solution-phase synthesis of 1T ' WSe2 nanosheets. *Nat Commun* **2019,** *10*.

11. Geisenhoff, J. Q.; Tamura, A. K.; Schimpf, A. M., Using ligands to control reactivity, size and phase in the colloidal synthesis of WSe2 nanocrystals. *Chem Commun* **2019,** *55* (60), 8856-8859.

12. Mahler, B.; Hoepfner, V.; Liao, K.; Ozin, G. A., Colloidal synthesis of 1T-WS2 and 2H-WS2 nanosheets: applications for photocatalytic hydrogen evolution. *J Am Chem Soc* **2014,** *136* (40), 14121-7.

13. Zhou, P. S.; Schiettecatte, P.; Vandichel, M.; Rousaki, A.; Vandenabeele, P.; Hens, Z.; Singh, S., Synthesis of Colloidal WSe2 Nanocrystals: Polymorphism Control by Precursor-Ligand Chemistry. *Cryst Growth Des* **2021,** *21* (3), 1451-1460.

14. Martinolich, A. J.; Neilson, J. R., Toward Reaction-by-Design: Achieving Kinetic Control of Solid State Chemistry with Metathesis. *Chem Mater* **2017,** *29* (2), 479-489.

15. Kanatzidis, M. G.; Poeppelmeier, K. R., Report from the third workshop on future directions of solid-state chemistry: The status of solid-state chemistry and its impact in the physical sciences. *Prog Solid State Ch* **2008,** *36* (1-2), 1-133.

16. Sokolikova, M. S.; Mattevi, C., Direct synthesis of metastable phases of 2D transition metal dichalcogenides. *Chem Soc Rev* **2020,** *49* (12), 3952-3980.

17. Tappan, B. A.; Brutchey, R. L., Polymorphic Metastability in Colloidal Semiconductor Nanocrystals. *Chemnanomat* **2020,** *6* (11), 1567-1588.

18. Cardew, P. T.; Davey, R. J., The Kinetics of Solvent-Mediated Phase-Transformations. *P Roy Soc Lond a Mat* **1985,** *398* (1815), 415-428.

19. Schutte, W. J.; Deboer, J. L.; Jellinek, F., Crystal-Structures of Tungsten Disulfide and Diselenide. *J Solid State Chem* **1987,** *70* (2), 207-209.

20. Sun, Y. J.; Wang, D.; Shuai, Z. G., Indirect-to-Direct Band Gap Crossover in Few-Layer Transition Metal Dichalcogenides: A Theoretical Prediction. *J Phys Chem C* **2016,** *120* (38), 21866-21870.

21. Mattheis.Lf, Energy-Bands for 2h-Nbse2 and 2h-Mos2. *Phys Rev Lett* **1973,** *30* (17), 784-787.

22. Ajayan, P.; Kim, P.; Banerjee, K., Two-dimensional van der Waals materials. *Phys Today* **2016,** *69* (9), 39-44.

23. Schaibley, J. R.; Yu, H. Y.; Clark, G.; Rivera, P.; Ross, J. S.; Seyler, K. L.; Yao, W.; Xu, X. D., Valleytronics in 2D materials. *Nat Rev Mater* **2016,** *1* (11).

24. Lai, Z.; He, Q.; Tran, T. H.; Repaka, D. V. M.; Zhou, D. D.; Sun, Y.; Xi, S.; Li, Y.; Chaturvedi, A.; Tan, C.; Chen, B.; Nam, G. H.; Li, B.; Ling, C.; Zhai, W.; Shi, Z.; Hu, D.; Sharma, V.; Hu, Z.; Chen, Y.; Zhang, Z.; Yu, Y.; Renshaw Wang, X.; Ramanujan, R. V.; Ma, Y.; Hippalgaonkar, K.; Zhang, H., Metastable 1T'-phase group VIB transition metal dichalcogenide crystals. *Nat Mater* **2021,** *20* (8), 1113-1120.

25. Fang, Y. Q.; Dong, Q.; Pan, J.; Liu, H. Y.; Liu, P.; Sun, Y. Y.; Li, Q. J.; Zhao, W.; Liu, B. B.; Huang, F. Q., Observation of superconductivity in pressurized 2M WSe2 crystals. *J Mater Chem C* **2019,** *7* (28), 8551-8555.

26. Fang, Y. Q.; Pan, J.; Zhang, D. Q.; Wang, D.; Hirose, H. T.; Terashima, T.; Uji, S.; Yuan, Y. H.; Li, W.; Tian, Z.; Xue, J. M.; Ma, Y. H.; Zhao, W.; Xue, Q. K.; Mu, G.; Zhang, H.; Huang, F. Q., Discovery of Superconductivity in 2M WS2 with Possible Topological Surface States. *Adv Mater* **2019,** *31* (30).

27. Qian, X. F.; Liu, J. W.; Fu, L.; Li, J., Quantum spin Hall effect in two-dimensional transition metal dichalcogenides. *Science* **2014,** *346* (6215), 1344-1347.

28. ten Wolde, P. R.; Frenkel, D., Homogeneous nucleation and the Ostwald step rule. *Phys Chem Chem Phys* **1999,** *1* (9), 2191-2196.

29. McHale, J. M.; Auroux, A.; Perrotta, A. J.; Navrotsky, A., Surface energies and thermodynamic phase stability in nanocrystalline aluminas. *Science* **1997,** *277* (5327), 788-791.

30. Wang, Y.; He, J.; Liu, C.; Chong, W. H.; Chen, H., Thermodynamics versus kinetics in nanosynthesis. *Angew Chem Int Ed Engl* **2015,** *54* (7), 2022-51.

31. Cardew, P. T.; Davey, R. J.; Ruddick, A. J., Kinetics of Polymorphic Solid-State Transformations. *J Chem Soc Farad T 2* **1984,** *80*, 659-668.

32. Niebur A, S. A., Haizmann P, Strolka O, Rudolph D, Peisert H, Lauth J, Untangling the Intertwined: Metallic to Semiconducting Phase Transition in Colloidal MoS2 Nanoplatelets and Nanosheets. *ChemRxiv* **2022,** (Cambridge: Cambridge Open Engage).

33. Hansen, L. P.; Johnson, E.; Brorson, M.; Helveg, S., Growth Mechanism for Single- and Multi-Layer MoS2 Nanocrystals. *J Phys Chem C* **2014,** *118* (39), 22768-22773.

34. Whitehead, C. B.; Ozkar, S.; Finke, R. G., LaMer's 1950 model of particle formation: a review and critical analysis of its classical nucleation and fluctuation theory basis, of competing models and mechanisms for phase-changes and particle formation, and then of its application to silver halide, semiconductor, metal, and metal-oxide nanoparticles. *Mater Adv* **2021,** *2* (1), 186-235.

Chapter 6: Tightly bound trioctylphosphine ligands for monolayer transition metal dichalcogenides nanocrystals

6.1 Abstract

Colloidal synthesis of monolayer transition metal dichalcogenide nanocrystals allows access to solution-processable monolayers in a scalable fashion. Syntheses in oleylamine have received much attention as they produce monolayer materials of the metastable phase of TMD materials. Herein we present a synthesis that results in trioctylphosphine ligands bound along the basal plane of the transition metal dichalcogenide materials producing monolayer nanocrystals. The bound ligands cause rapid phase conversion to the thermodynamically favored phase. Compared to syntheses that do not include trioctylphosphine and result in multi-layer nanocrystals, the monolayer nanocrystals have the expected change to their photophysical properties.

6.2 Introduction

Group IV transition metal dichalcogenides (TMDs) (ME_2, M = Mo, W; E = S, Se) are a class of two-dimensional materials that have gained intense research interest due to their unique layered crystal structure and subsequent layer-dependent properties. These materials also exhibit polymorphism and obtaining the different crystal structures can also greatly influence the properties of the material. For instance, the thermodynamically favored phase (2H) is a semiconductor[1] and the metastable phase (2M) is a small bandgap material.[2-3] In both cases isolation of few- to monolayer materials is of great importance as new properties emerge with two-dimensional electron confinement: the 2H phase shifts from an indirect to direct bandgap[4-5] and the 2M phase becomes a topological insulator.[6-7] Top-down approaches to obtaining monolayers

typically exploit the weak Van der Waals interactions and the layers are separated with some form of mechanical exfoliation.[8-10] These post-synthetic methods inherently require multiple steps, are often low yielding, and are therefore not scalable.[8] Synthesizing monolayers via a direct method is an attractive alternative to overcome these issues.

Colloidal synthesis has demonstrated itself as a useful tool for directly synthesizing thin, nanosheet materials,[11] with cadmium selenide (CdSe) being the seminal example. [12-18] Typically, thin CdSe nanosheets are grown in the presence of some coordinating ligand. In oleylamine a soft templating method is known, where magic-sized clusters first form lamellar structures with the ligand as a template.[12-14, 19] Then, with a low-temperature annealing step, nanosheets of CdSe are produced.[12-14] Alternatively, thin nanosheets of zinc blende CdSe can be grown in the presence of carboxylate ligands.[15-18] These ionic ligands strongly bind to cadmium terminated (001) or (111) facets directing two-dimensional growth.[15, 20] Thickness and lateral sizes of the nanosheets can be tuned with temperature, using multiple or slow injection procedures, or with the packing density of the ligands along the basal plane.[17-18]

Ideally, a similar methodology could be applied to the group VI TMDs to produce free-standing, solution-processable monolayers, however, in contrast to the CdSe example, the desired basal plane to bind ligands to is chalcogen terminated and does not possess any dangling bonds. Instead, the edges of TMDs should behave more analogously to traditional surface/ligand binding found in nanocrystal systems.[21-22] Indeed, exploiting the affinity for ligand binding at the edges has resulted in control over the lateral sizes as well as layer number.[23-24] Ligands that have a strong binding affinity to the edges result in nanocrystals with smaller lateral sizes and a greater number of layers, while ligands with a weak binding affinity lead to greater lateral growth and fewer

layers.[23-24] However, without anything to impede interlayer interactions these few-layer materials will be unstable to restacking forming a multilayer Van der Waals structure.

So far, the best colloidal monolayer TMD materials have been produced in oleylamine[25-31] or other alkylamine environments,[28, 32] or ionic liquids.[33] The oleylamine synthesis has mostly been applied to 2M(1T′) WS_2[25-31] but has recently been extended to the other TMDs.[30] In oleylamine many common sulfur precursors (CS_2, thiourea) will react with the excess oleylamine to generate H_2S gas.[29] This intermediate is highly reducing and results in excess electrons in the formed TMD nanosheets, which stabilize the metastable 2M phase.[25-26] To compensate for these excess electrons positively charged oleylammonium ligands coordinate to the basal plane of the TMDs via electrostatic interaction.[25-26] This leads to monolayer nanosheets that can agglomerate and form lamellar structures but can also be separated from one another using similar methods to isolate free-standing CdSe nanosheets.[25, 27] This ligand interaction is only available for the metastable 2M phase, as conversion to the thermodynamically favored 2H phase and loss of the excess electrons is accompanied by loss of the oleylammonium ligands.[26]

Ideally, a ligand could be chosen that will be generalizable to all TMDs and does not have a preference for phase. A good candidate is a phosphine as it is a very strong, soft base that makes strong adducts with both sulfur and selenium.[34-36] Recently we developed a simple synthetic method to synthesize tungsten diselenide (WSe_2), where tungsten hexacarbonyl ($W(CO)_6$) and diphenyl diselenide (Ph_2Se_2) were combined at low temperatures followed by a heat-up in excesses of trioctylphosphine oxide (TOPO). Herein we show that adding just a few equivalents of trioctylphosphine (TOP) to this reaction results in the TOP being bound to the nanocrystals. Furthermore, we verify that binding occurs at the chalcogen plane likely through a P–Se interaction. It is demonstrated that the TOP is tightly bound to the nanocrystal surface which

significantly improves colloidal stability compared to the TOPO-synthesized nanocrystals. After using WSe_2 as our case study the synthesis is extended to the other TMD materials $MoSe_2$, WS_2, and MoS_2. Finally, we discuss how the bound ligands impact the electronic structure of the TMDs.

6.3 Results and Discussion

WSe_2 nanocrystals were prepared via 2 methods: in TOPO as the main coordinating solvent, and then in a mixture of TOPO and TOP. The synthesis in all TOPO follows a modified procedure (chapter 5). Briefly, $W(CO)_6$ is heated in 180 eq of TOPO to 150 °C, then held at this temperature for 10 minutes, after which 2 eq Ph_2Se_2 is injected into the solution. Immediately following injection, the solution is heated to 330 °C and held at this temperature for 90 minutes. The reaction with TOP was performed in the same manner, however, the ligand mixture used was 180 eq TOPO and 10 eq TOP to the $W(CO)_6$.

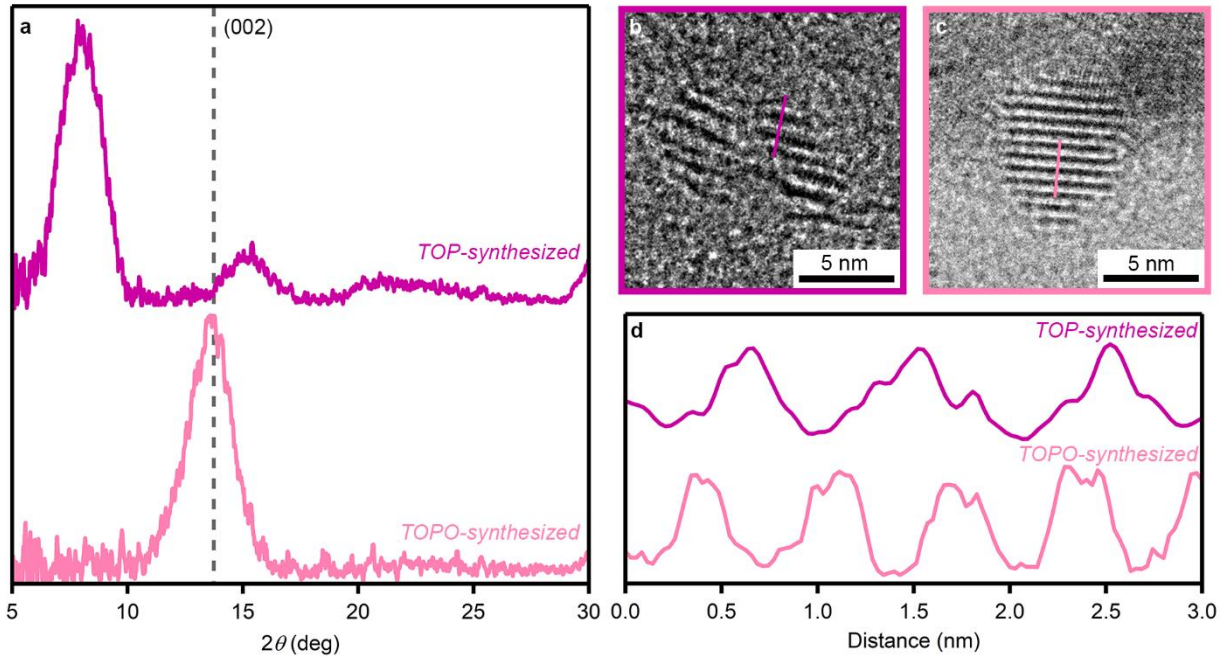

Figure 6. 1. (a) Powder X-ray diffraction patterns for WSe_2 nanocrystals synthesized with 0.06 mmol $W(CO)_6$ in 180 eq TOPO to the $W(CO)_6$ (pink, bottom) or a combination of 180 eq TOPO and 10 eq TOP (purple, top). Each reaction had an injection of 2 eq Ph_2Se_2 in 1 ml hexadecane performed at 150 °C followed by a heat-up to 330 °C where the reaction was held for 90 minutes. Reference patterns for the (002) reflection of the 2H phase are shown on the bottom.[37] **(b)** TEM images for nanocrystals synthesized with TOP and **(c)** without TOP. **(d)** Intensity profiles showing the distance between the individual WSe_2 layers for nanocrystal synthesized with TOP (purple, top) and without TOP (pink, bottom).

Figure 6.1a shows the powder X-ray diffraction patterns for WSe_2 synthesized with and without TOP. Interestingly, for the nanocrystals synthesized with TOP (purple, top trace) the principal reflection (00x) is shifted to a lower 2θ than is what is expected for bulk WSe_2 (7.8 2θ).[37] This corresponds to a d spacing of 1.1 nm which is 0.5 nm greater than bulk WSe_2, indicating an expansion between the layers. A new peak at 15 2θ is also observed which is the new (002x) reflection for this expanded lattice. The nanocrystals synthesized in all TOPO do not show any shift of the (002) reflection from bulk WSe_2, lying at 13.7 2θ or 0.6 nm. This difference in layer expansion can be directly visualized through TEM images. Figure 6.1b and c show representative particles for the TOP and no TOP synthesized samples respectively. Here the nanocrystals lie on

their side, where the individual layers can be distinguished. The distance between neighboring layers was determined by taking an intensity line scan perpendicular to the layers, Figure 6.1d. The distance between the TOPO synthesized reaction is 0.6 nm, which aligns with powder X-ray diffraction pattern and the expected distance for WSe_2 held together via its Van der Waals forces. For the nanocrystals synthesized with TOP, this spacing is increased to 1.1 nm which also aligns with the expansion observed in the powder patterns.

The powder patterns (Figure S6.1) indicate that the TOPO nanocrystals show a mixture of the 2M and 2H phase, while the nanocrystals synthesized with TOP show very good agreement with just the 2H phase. The TOPO synthesized nanocrystals have a peak at 35 2θ which aligns with the metastable 2M phase, while the nanocrystals synthesized with TOP have a decrease in intensity at 35 2θ and then a peak at 38 2θ aligning with the 2H phase. The observed mixture of 2M and 2H phase is expected for these reaction conditions for nanocrystals synthesized in all TOPO. For the TOP bound WSe_2 the layer expansion is always present, even at early reaction times (Figure S6.2a). The layer expansion is accompanied by very rapid phase conversion that is demonstrated in the Raman spectra of timed aliquots (Figure S6.2b). The spectra show more 2H phase at early times and any amount of 2M phase present at early times is rapidly converted to produce high-phase purity 2H nanocrystals. Bound TOP results in an interlayer expansion that weakens the interlayer interactions between the layers. This matches our previous observation that weakening the interlayer interactions causes rapid phase conversion to the 2H phase as weak interlayer interactions allow for facile atom migration in the lattice (chapter 5).

To confirm that ligand binding is causing the interlayer expansion in the TOP synthesized nanocrystals, the nanocrystals were investigated with FTIR spectroscopy (Figure 6.2a). In the CH stretching region TOP and TOPO both should exhibit the same stretches relating to the CH_3 and

CH_2 stretching of its octyl chains, TOP is chosen as the reference in Figure 6.1a. WSe_2 synthesized with TOP show these characteristic CH stretches even after multiple washing steps (purple). The CH stretches are shifted to lower wavenumbers than the TOP reference, which is consistent with a change from a liquid to a crystalline state,[38] further supporting that the ligand is bound rather than not washed away. In contrast, the nanocrystals synthesized in TOPO lack all CH stretching which suggests the TOPO does not bind to any nanocrystal surfaces and is easily removed via washing. The difference in ligand binding between the two samples is also observed using TGA (Figure S6.3) as the mass loss of the TOP-bound nanocrystals is 14 % greater than the nanocrystals synthesized in TOPO with no ligands bound.

To get further insight into the nature of the ligand binding FTIR stretches at low wavenumbers were investigated. The P=Se stretch is identified by using TOP=Se, synthesized by sonicating elemental Se in excess TOP, as a reference (Figure 6.1b). This P=Se stretch is at 500 cm^{-1}, matching previously reported P=Se compounds.[39] The TOP-bound nanocrystals show a similar stretch at this same frequency suggesting that the phosphine is bound through the chalcogen plane rather than binding to metal atoms. Again, the TOPO-synthesized nanocrystals lack any stretches further demonstrating the lack of ligands.

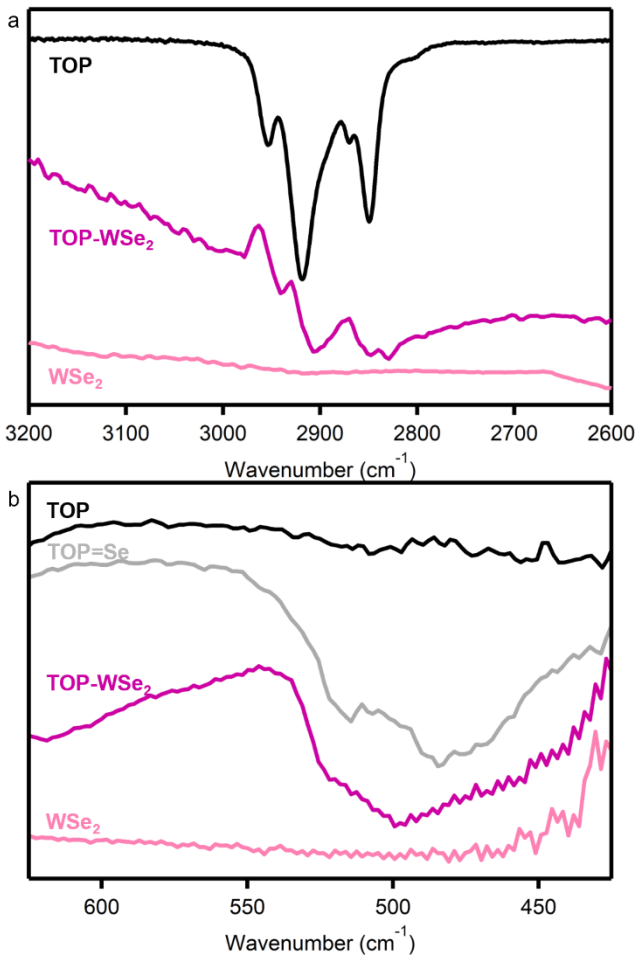

Figure 6. 2. FTIR spectra of TOP (black), TOP=Se (gray), WSe_2 synthesized with TOP (purple), and WSe_2 synthesized without TOP (pink) in the CH_x **(a)** and P=Se **(b)** stretching regions.

Qualitatively, the difference in ligand binding is observed by the fact that the nanocrystals synthesized in all TOPO form very poor suspensions that are not stable in solution, while those synthesized with TOP form stable suspensions in non-polar solvents like toluene. This colloidal stability allows for the TOP synthesized particles to be analyzed with ^{1}H NMR (Figure 6.3). The proton signals are all broadened, and downshifted compared to neat TOP, indicating the ligands are bound to the nanocrystal surfaces, and a significant portion is tightly bound.[40] Although these stretches and proton NMR signals should be similar in both TOP and TOPO, it can be concluded

that the ligand binding and interlayer expansion must be coming from TOP acting as a ligand in some form as it is the only difference between the two reactions.

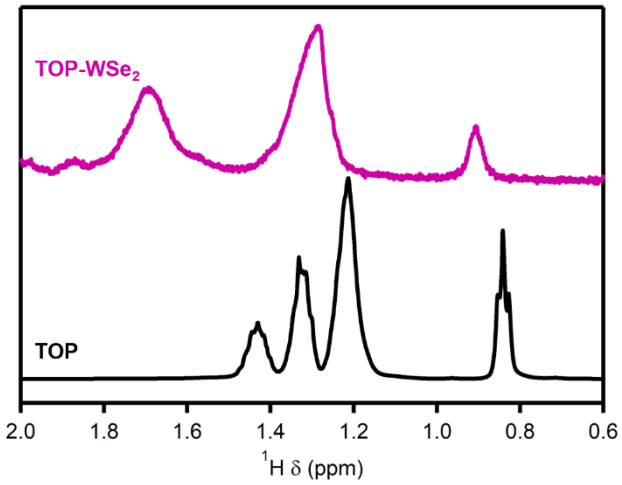

Figure 6. 3. ^{1}H-NMR spectra of WSe_2 nanocrystals synthesized with TOP (purple, top), and TOP (black, bottom).

To further investigate how the inclusion of TOP into the lattice occurs, the precursor chemistry is analyzed. In previous studies, we have identified the substitution products formed after heating $W(CO)_6$ in TOPO as the reactive intermediates $W(CO)_5TOPO$ and *cis*-$W(CO)_4(TOPO)_2$ (chapter 4). With the addition of 10 eq TOP *trans*-$W(CO)_4TOP_2$ is formed as an intermediate which is confirmed by ^{13}C-NMR and FTIR (Figure S6.4). Unlike the TOPO reaction, the addition of TOP also causes a change to the selenium precursor. In excess TOP, Se is stripped from Ph_2Se_2 forming TOP=Se (figure S6.5).

The inclusion of bound TOP within the lattice happens at very early times of the reaction as aliquots show a shift of the (002) to 7.8 2θ after just 5 minutes of the reaction, Figure S6.2a. We hypothesize that the precursor chemistry is vital in instilling the bound TOP as typically Lewis bases are hard to incorporate into the lattice of group IV TMDs post-synthetically.[41-42] For instance, we attempted to intercalate TOP post-synthetically by injecting 30 eq TOP into a TOPO-

synthesized sample at 330 °C after 1 hour of reaction time. After the TOP injection the reaction temperature was held at 330 °C for 24 hours. No change to the (002) reflection of WSe_2 was observed indicating that post-synthetic intercalation is not possible, at least on time scales comparable to a typical reaction time (Figure S6.6a). Additionally, after 2 washing steps, we do not observe any bound ligand in the FTIR (Figure S6.6b and c) suggesting this process does not even result in ligand interaction at the edges of the nanocrystals.

To explore what precursor change was important in instilling the bound TOP we ran reactions with only 2 and 4 eq of TOP to $W(CO)_6$/1 and 2 eq TOP to the Ph_2Se_2. Neither of these reactions shows any shift of the (002) reflection which suggests that there is no incorporation of the TOP into the lattice (Figure S6.7). Both reactions have enough TOP to form a TOP-coordinated tungsten carbonyl complex but do not leave much in excess to form TOP=Se. This suggests that the ability of the TOP to sequester Se from the Ph_2Se_2 is the limiting factor in the incorporation of TOP into the lattice. However, adding TOP in great excesses completely arrests the reactivity and no nanocrystals will be formed. What is collected from the reaction is a purple-colored solution (Figure S6.8), which we believe is formed from a tungsten-coordinated TOP/TOP=Se molecular species. We also note that this purple complex may be an intermediate formed during the synthesis. The solution always turns purple around 280 °C during the heat-up of the reaction, after which the solution turns brown when the nanocrystals begin nucleating and growing at higher temperatures.

To confirm that Top=Se is the necessary chalcogen precursor we synthesized TOP-bound WSe_2 with an injection of TOP=Se (Figure S6.9). This approach results in a synthesis that is low yields (8%) while the synthesis with Ph_2Se_2 gives a higher yield of 36%. The presence of other Se precursors from the diorganyl dichalcogenide may increase reactivity resulting in higher yields of nanocrystals.

Finally, to fully eliminate the possibility that TOPO plays a role in the ligand binding, we replaced the TOPO with, the more innocent, docosane. Interestingly, using the same heating rate as the TOPO reaction does not produce ligand-bound nanocrystals. Using the fast heat-up of 15 minutes no purple intermediate is observed and only a color change from yellow to brown is observed. Instead, the docosane reaction mixture was first heated to 280 °C and held at this temperature for 15 minutes to first form the purple intermediate, then the mixture is heated to 330 °C and held for 90 minutes like previous reactions. Doing the reaction with this intermediate heating step does produce nanocrystals with TOP bound, as the (002) is shifted in the powder X-ray diffraction pattern (Figure S6.11a) and CH stretches and P=Se stretches are visible in the FTIR (Figure S6.10b and c). We do note that the (002) reflection is slightly more shifted than the TOPO reactions, which is likely due to some incorporation of docosane between the sheets. The need for the longer heating step at lower temperatures with docosane is likely due to the removal of the TOPO. TOPO is good at CO labilization and likely facilitates the reactivity of the tungsten carbonyl in a catalytic manner.[43-44]

To see if this chemistry was generalizable to the other TMDs ($MoSe_2$, WS_2, and MoS_2) it was necessary to find analogous precursors. To expand to the Mo TMDs we find that $Mo(CO)_6$ has the same chemistry with TOP as $W(CO)_6$ forming *trans*-$Mo(CO)_4TOP_2$ (Figure S6.11). Reactions in all TOPO with $Mo(CO)_6$ and Ph_2Se_2 yield nanocrystals with an un-expanded (002) reflection at 13.2 2θ, or 0.7 nm, Figure 6.4a. While those synthesized with 10 eq TOP added to show a very similar shift as the TOP-WSe_2 nanocrystals do. For TOP-$MoSe_2$ the (002) reflection is at 8.1 nm 2θ, or 1.1 nm in d spacing, resulting in an expansion of 0.5 nm compared to that of un-expanded $MoSe_2$. This expansion is also confirmed with TEM images, as the TOP-$MoSe_2$ nanocrystals have

a spacing of 1.1 nm between the layers (Figure 6.4b), while the nanocrystals synthesized in all TOPO have a spacing of 0.7 nm.

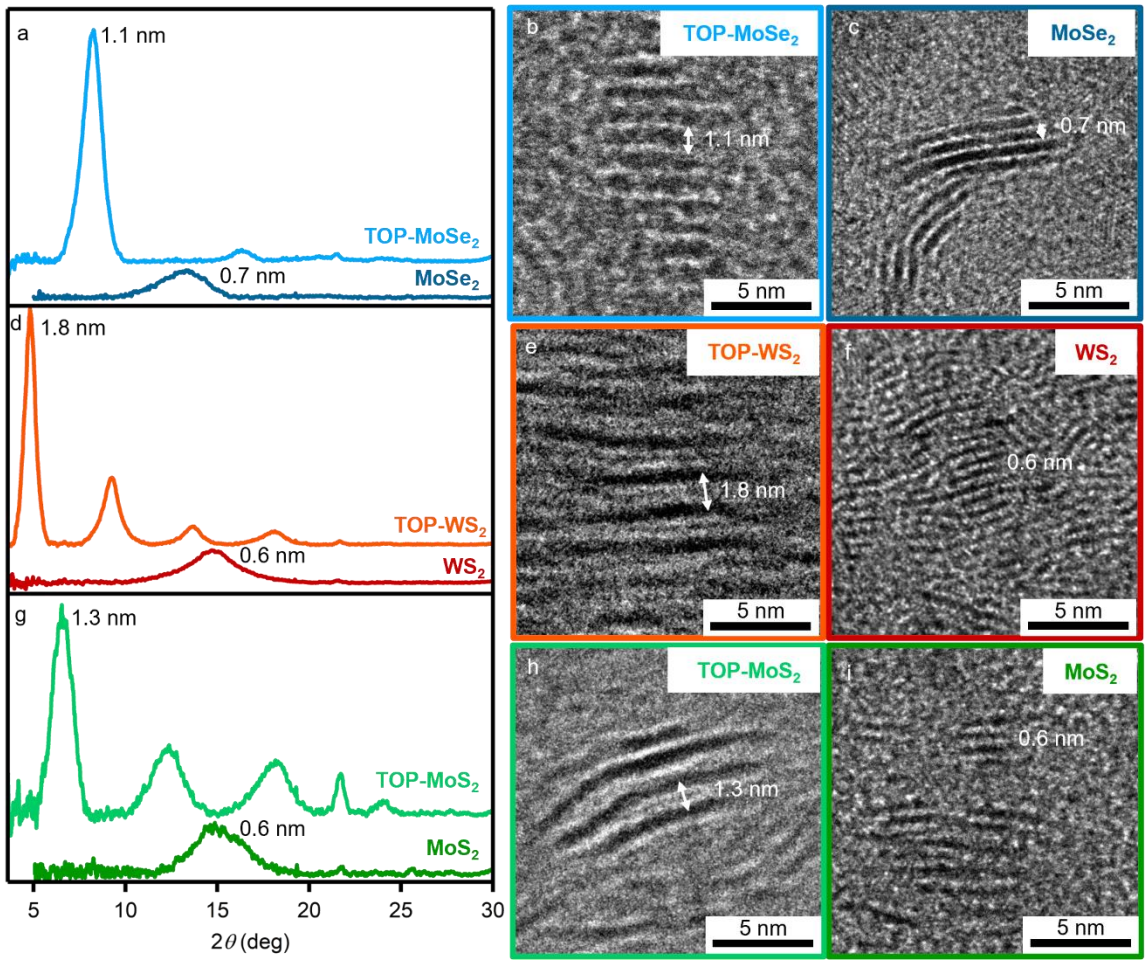

Figure 6. 4. (a) PXRD for $MoSe_2$ nanocrystals synthesized in all TOPO (bottom, dark blue) and with 10 eq TOP added (top, light blue), both reactions used a 2 eq Ph_2Se_2: $Mo(CO)_6$ injection at 150 °C, followed by heat-up to 330 °C, where the reactions were held for 90 minutes. TEM for TOP-$MoSe_2$ **(b)** and $MoSe_2$ **(c)** nanocrystals. **(d)** PXRD for WS_2 nanocrystals synthesized in all TOPO (bottom, red) and with 3 eq TOP added (top, orange), both reactions used a 2 eq Bn_2S_2:$W(CO)_6$ injection at 150 °C, followed by heat-up to 330 °C, where the reactions were held for 20 hours. TEM for TOP-WS_2 **(e)** and WS_2 **(f)** nanocrystals. **(g)** PXRD for MoS_2 nanocrystals synthesized in all TOPO (bottom, dark green) and with 3 eq TOP added (top, light green), both reactions used a 2 eq Bn_2S_2:$Mo(CO)_6$ injection at 150 °C, followed by heat-up to 330 °C, where the reactions were held for 20 hours. TEM for TOP-MoS_2 **(e)** and MoS_2 **(f)** nanocrystals.

To expand to the sulfides we first attempted reactions with Ph_2S_2 but found in all TOPO this did not lead to any nanocrystal formation, which is likely due to the greater C-E bond strengths compared to Ph_2Se_2. Similar reactivity has also been observed in the synthesis of CdS where no reaction takes place when using Ph_2S_2.[45] Lowering the C-E bond energy by using Bn_2S_2[46] rectifies this issue and we see nanocrystal formation in all TOPO for both WS_2 and MoS_2 (Figure 6.3d) and g. Here, as expected, the (002) of the TOPO-synthesized WS_2 and MoS_2 align with the unexpanded materials at 14.8 2θ or 0.6 nm (Figure 6.4d and e respectively). Use of Bn_2S_2 with added TOP results in the formation of TOP=S (Figure S6.12). Here the sequestration of S is facile due to the lower C-E bond energy[46] (similar to what is observed with Bn_2Se_2) as well as the increased bond dissociation energy of TOP=S compared to TOP=Se.[34-36] Due to the lower reactivity of TOP=S running reactions with 10 eq TOP for WS_2 and MoS_2 resulted in no reaction. After lowering the equivalents of TOP to 3 eq the reaction proceeds but still requires longer reaction times (19 hr) than the selenides. For TOP-WS_2 the (002) reflection is shifted to 4.8 2θ, or 1.8 nm in d spacing, resulting in an expansion of 1.2 nm compared to that of un-expanded WS_2 (Figure 6.3d). This is also confirmed with TEM where TOP-WS_2 shows 1.8 nm expansion (Figure 6.4e) and while nanocrystals synthesized in all TOPO show the expected expansion of 0.6 nm. With TOP-MoS_2 we see similar shifts where the (002) reflection is shifted to 6.5 2θ, or 1.3 nm in d spacing, resulting in an expansion of 0.7 nm compared to that of un-expanded MoS_2 (Figure 6.4g). The TEM also confirms this, where TOP-MoS_2 has an expansion of 1.3 nm between the layers (Figure 6.4h) and TOPO-synthesized nanocrystals have an expansion of 0.6 nm. Interestingly, the TOP-WS_2 and TOP-MoS_2 nanocrystals are expanded to a greater extent than compared to the Se analogs We believe this is likely due to the increased binding energy of the P-S bond compared to the P-Se bond, resulting in more TOP being bound to the basal plane of the sulfide materials.

Changes to the confinement of the nanocrystals and making monolayer materials should be accompanied by a change in the electronic structure.[5, 47] The exciton absorption features of the nanocrystals are explored with UV-vis spectroscopy (Figure 6.5). For all TMDs there is the excitonic absorbance features A and B that are from a direct transition at the K point in the band structure, where the valence band is split from spin-orbit coupling. Most TMDs have a third excitonic feature C that is from an indirect transition. WSe_2 has 2 more excitonic features C and D that are from excited states of the A and B transitions.[48] In all cases we see a blue shift in the excitonic transitions for the TOP-bound nanocrystals, which is expected as the nanocrystals are thinned to the monolayer limit, summarized in Table 1. The blue shift is lessened for the WS_2 and MoS_2 despite the greater interlayer spacing, which may be from the increased density of bound TOP on the sulfide nanocrystals affecting the band structure of the material.

Table 6. 1. Absorbance spectra for TOP bound and few-layer nanocrystals for (a) WSe_2, (b) $MoSe_2$, (c) WS_2, and (d) MoS_2.

	A (eV)	B (eV)	C (eV)	D (eV)
WSe_2	1.64	2.05	2.40	2.88
TOP-WSe_2	1.73	2.13	2.46	2.95
$MoSe_2$	1.53	1.72	2.27	--
TOP-$MoSe_2$	1.59	1.80	2.67	--
WS_2	1.99	2.38	2.83	--
TOP-WS_2	2.07	2.40	2.84	--
MoS_2	1.88	2.03	2.87	--
TOP-MoS_2	1.91	2.06	3.00	--

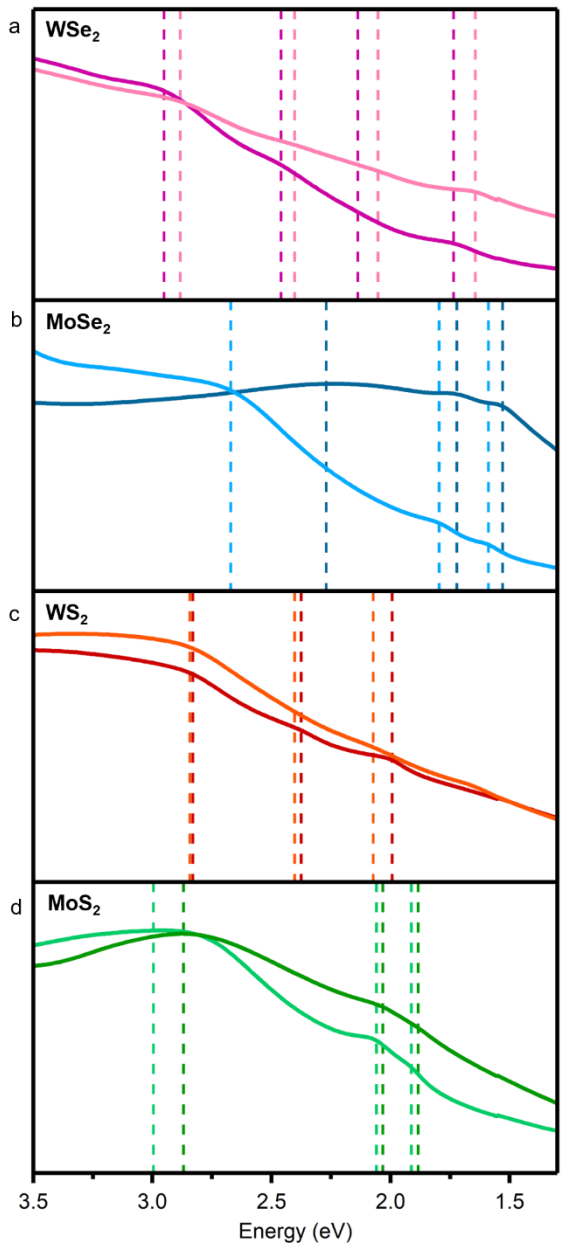

Figure 6. 5. Absorbance spectra for TOP bound and few-layer nanocrystals for (a) WSe_2, (b) $MoSe_2$, (c) WS_2, and (d) MoS_2. Shifts are highlighted with dashed vertical lines.

To investigate how the bound TOP impacts the properties of the material through chemical functionalization we performed X-ray photoelectron spectroscopy (XPS) on TOP-WSe_2 and TOP-WS_2. Figure 6.6a shows the W 4*f* XPS spectra. The dashed vertical gray lines at 32.3 and 34.4 eV

show the expected energies for the W 4*f*7/2 and W 4*f*5/2 for the 2H phase of both WSe_2 and WS_2. The TOP-WSe_2 nanocrystals do not show much shift from the expected position with the W 4*f*7/2 and W 4*f*5/2 energies lying at 32.2 and 34.3, only a shift of -0.1 eV. The TOP-WS_2 samples show a greater shift than the TOP WSe_2 samples, where the W 4*f*7/2 and W 4*f*5/2 energies lie at 31.9 and 34.0, resulting in a shift in the binding energy of -0.4 eV. Figure 6.6b shows the S 2*p* region for the TOP-WS_2 with the 2H reference as dashed vertical gray lines. The S 2*p*3/2 and 2*p*1/2 energies lie at 161.9 and 163.0 eV for the TOP-WS_2 nanocrystals which is a shift of -0.7 eV. Figure 6.6c shows the Se 3*d* region for the TOP-WSe_2 samples with the 2H reference as dashed vertical lines. A shift to lower binding energy in the Se region is also observed, where the TOP-WSe_2 Se 3*d*5/2 and Se 3*d*3/2 energies lie at 54.2 and 55.0 eV, which corresponds to a shift of -0.2 eV. Shifts to lower binding energy are expected when electron-donating ligands are present.[49] The shifts for the TOP-WS_2 samples are greater than the shifts for TOP-WSe_2, this is likely from the greater packing density of bound TOP for the TOP-WS_2 nanocrystals. For each set of nanocrystals shift to lower binding energy is greater for the chalcogen atoms, which indicates the binding of the ligand at the chalcogen plane.

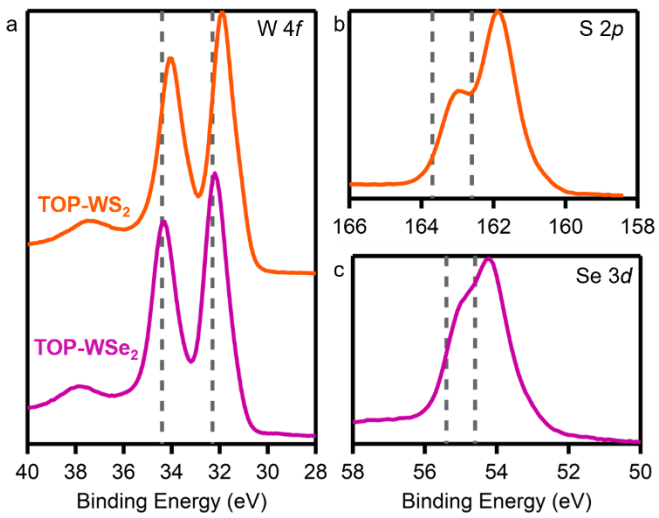

Figure 6. 6. (a) W 4*f*, (b) S 2*p* and (c) Se 3*d* X-ray photoelectron spectra for TOP-WSe_2 (purple) and TOP-WS_2 (orange) nanocrystals. 2H references are indicated with vertical dashed gray lines.

6.4 Discussion

The addition of phosphines to the synthesis of TMDs at early reaction times is vital in instilling them as tightly bound ligands across the basal plane of the TMDs. Although the exact nature of this bond is not fully understood we have identified some necessary aspects of the precursor chemistry. The phosphine must be added in great enough excesses that *trans*-$W(CO)_4(TOP)_2$ and TOP=E are formed as precursors, then these precursors react to form a purple intermediate. The identity of the purple intermediate is still undetermined and will be studied in future studies. We hypothesize that going through this purple intermediate is a necessary step in forming the ligand-bound nanocrystals. After forming this intermediate the reaction flask is further heated to decompose this intermediate into ligand-bound nanocrystals. The low-temperature injection and heat-up are necessary to allow these transformations to take place before nanocrystal formation.

Identifying ligands that can bind to the surfaces of TMDs is necessary to achieve monolayer growth in the solution phase. A combination of the P=Se stretch in the FTIR, increased shifts in

the chalcogen shifts compared to metal shifts in the XPS and an increased spacing for the sulfides rather than the selenides suggests that bonding is occurring through the chalcogen plane, rather than to a metal atom creating chalcogen defects. The binding of neutral phosphine to chalcogen-terminated neutral surfaces would be a unique binding motif for semiconducting nanocrystal systems. For instance, binding of L-type ligands to the surfaces of more traditional semiconductor nanocrystals, like CdSe, usually bind to open metal sites and are accompanied by X-type ligands that are necessary for charge compensation.[50] Additionally, oxidation of a low valent metal with TOP=E should result in the P=E bond cleaving.[35] Despite the known reactions of phosphines a neutral binding motif may be available due to the unique neutral basal plane of TMD systems.

Some insights can be gained by looking into the intercalation chemistry of TMDs. The group VI TMDs, in their 2H phase, have been notoriously resistant to the intercalation of neutral L-type ligands due to their low electron affinity.[41-42] However, group IV, V, and VII TMDs are all capable of this intercalation,[51] likely due to their small bandgap to metallic band structures that allow electron donation into empty *d*-orbitals.[52] The metastable 2M phase of the group VI TMDs should be more responsive to intercalation in a similar way. Likely, at early reaction times, all the TMDs investigated here go through this metastable phase facilitating bonding to the layers. The bounds are then preserved as phase conversion takes place. The monolayer-like nature of the TMDs produced here promotes phase conversion, but it might be possible that the electron donation from the phosphine ligands pins a certain amount of the metastable phase. Although we don't see many hallmarks of the metastable phase in the sulfide materials this could explain why the metal atoms remain more reduced in WS_2 compared to WSe_2.

Summary and Conclusions

The solution phase synthesis and processing of monolayer group IV TMD materials are highly desired yet remain complex due to the chemistry and available binding sites along the neutral, chalcogenide-terminated basal planes. The data presented herein demonstrate that with the addition of phosphines, ligands can bind to these planes and permanently separate the layers from one another. This separation of the layers is accompanied by expected changes to the electronic structure.

6.5 Supplementary Information

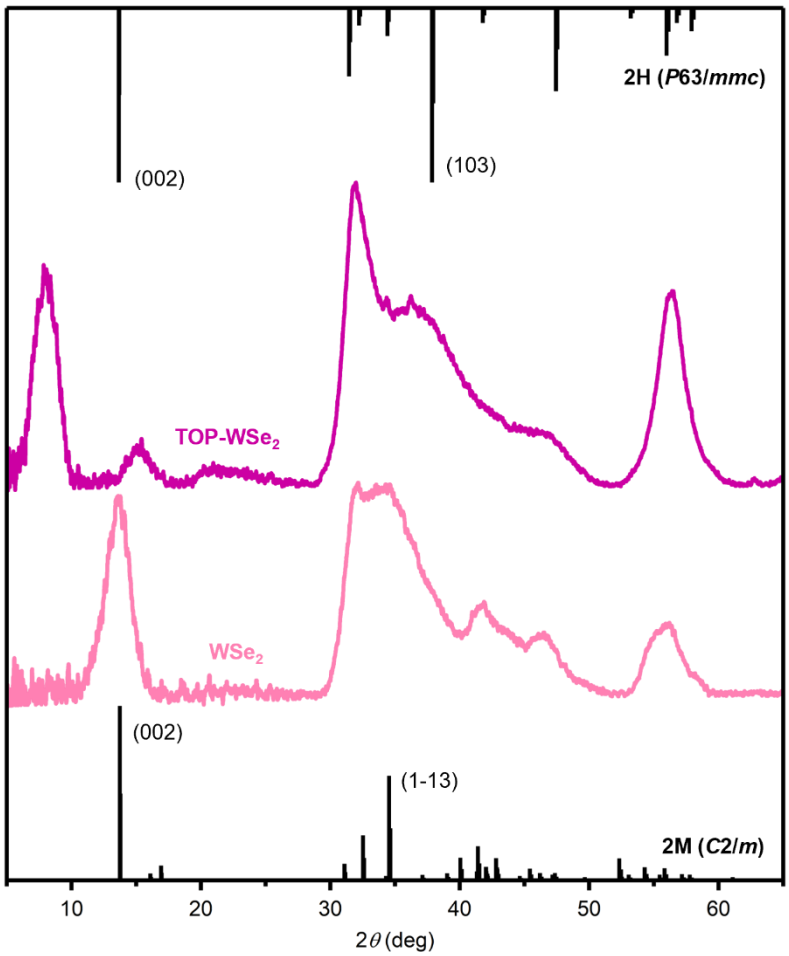

Figure S6. 1. Powder X-ray diffraction patterns for TOP-(purple TOP) and TOPO-(pink, bottom) synthesized WSe_2. Reference patterns for the 2H phase[37] and 2M phase[3] are shown on the top and bottom respectively.

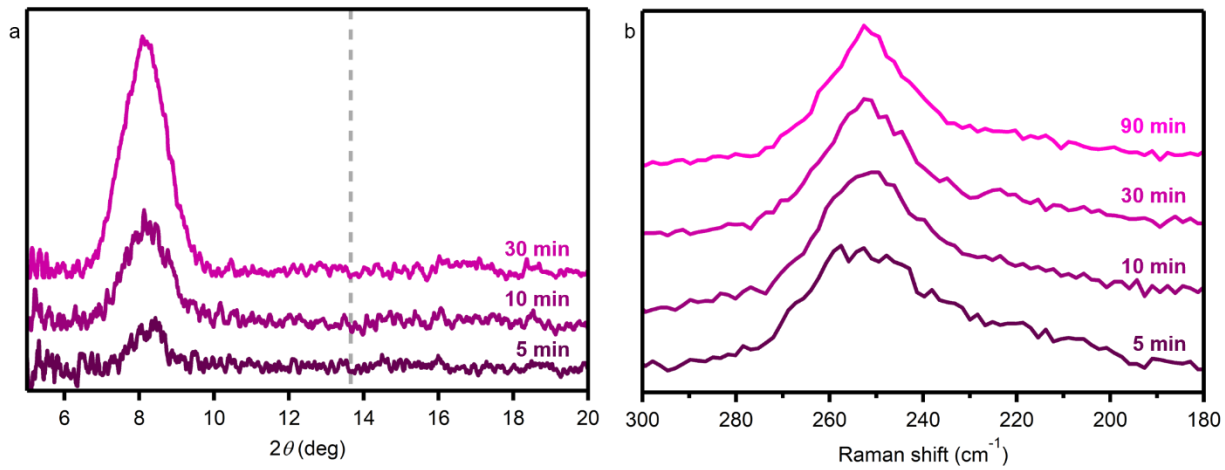

Figure S6. 2. (a) Powder X-ray diffraction patterns of aliquots taken from WSe_2 reaction synthesized ion 180 eq TOPO with 10 eq TOP added. **(b)** Raman spectra of aliquots. The peak at 250 cm^{-1} aligns with the 2H phase.

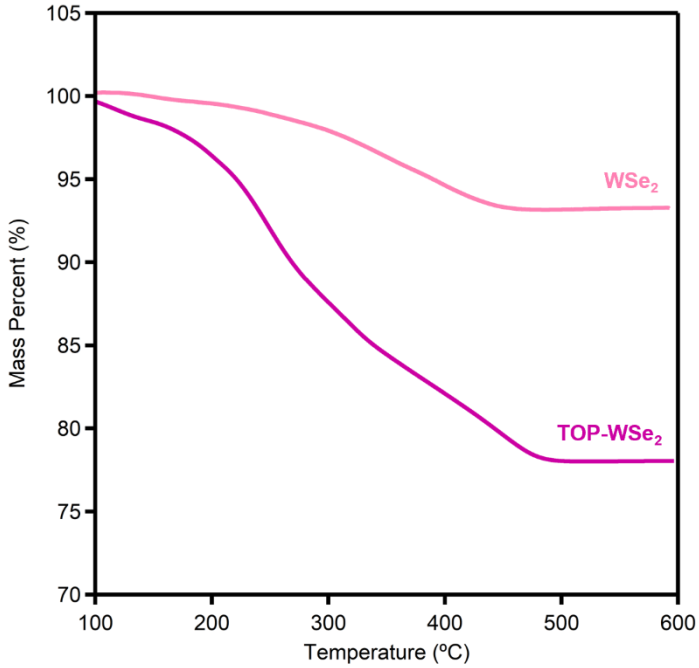

Figure S6. 3. TGA of WSe_2 nanocrystals synthesized in 180 eq TOPO (pink, top) and with 10 eq TOP added to the reaction (purple, bottom).

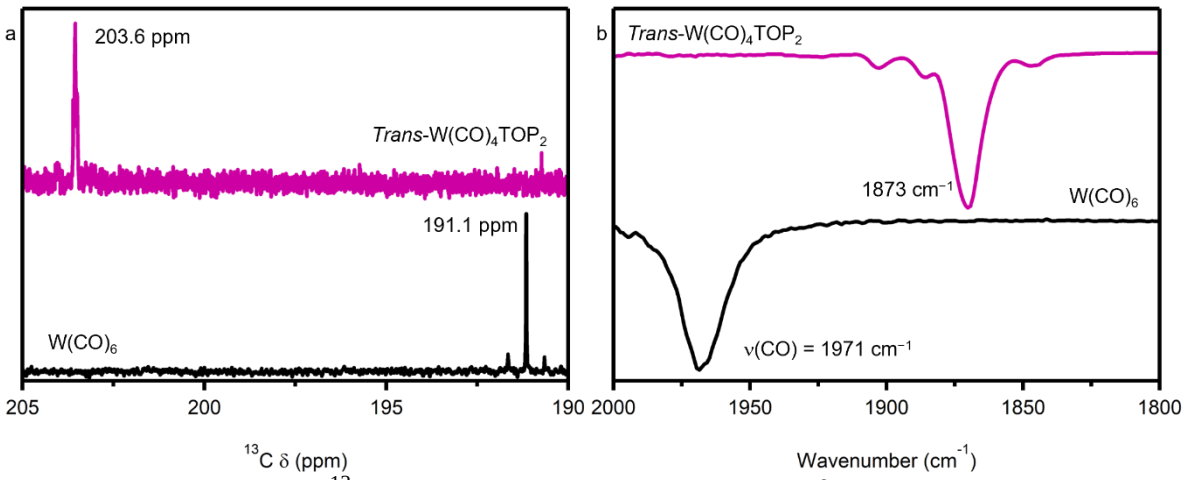

Figure S6. 4. (a) ^{13}C NMR and **(b)** FTIR spectra of *Trans*-$W(CO)_4TOPO$ synthesized via heating $W(CO)_6$ in >2eq TOP (purple, top) and comparison to pure $W(CO)_6$ (black, bottom). CO peak downfield shifted from 191.1 to 203.6 ppm and CO stretching frequency shifted to a lower wavenumber from 1971 cm^{-1} to 1873 cm^{-1}. Both these shifts align with previously reported di-substituted phosphine tungsten carbonyls.[53-54] The phosphorus NMR shows a singlet with triplet splitting and the FTIR shows one stretching mode, confirming trans substitution.

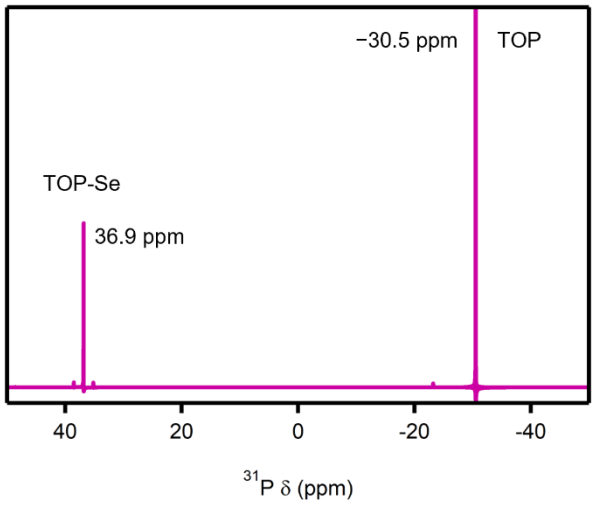

Figure S6. 5. ^{31}P-NMR after heating Ph_2Se_2 with 10 eq TOP at 150 °C for 10 minutes. The emergence of the peak at 36.9 ppm confirms the formation of TOP-Se.

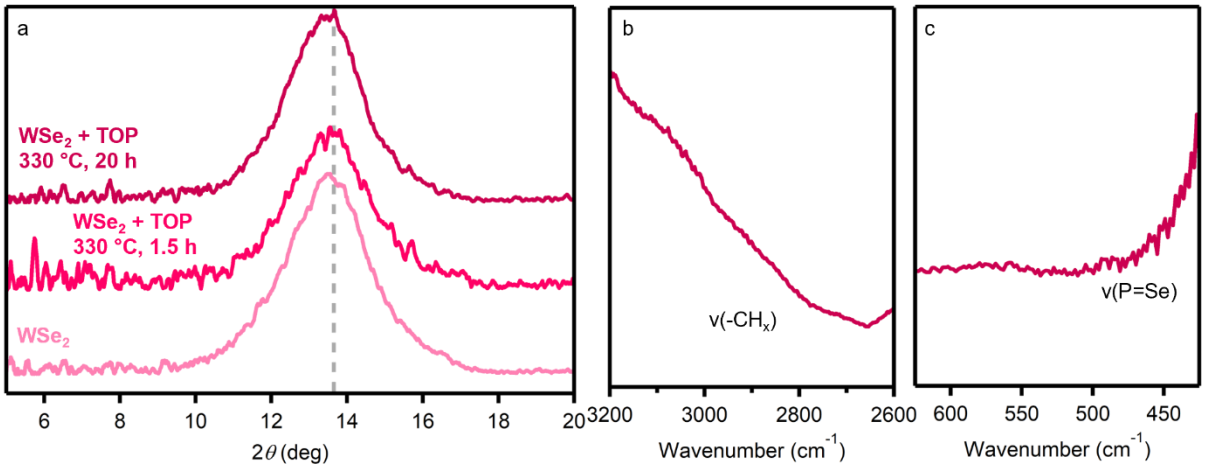

Figure S6. 6. PXRD of nanocrystals synthesized without TOP, and same nanocrystals stirred in 30 eq TOP at 330 °C for 1.5 hr and 20 hr (a). FTIR of nanocrystals after heating with TOP in the CH stretching region (b) and the P=Se stretching region (c).

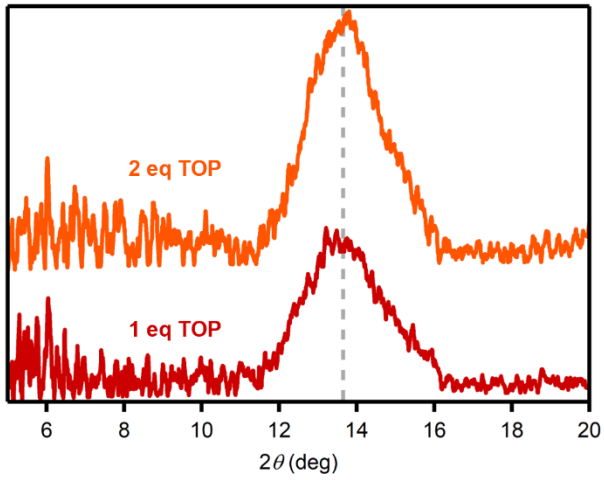

Figure S6. 7. PXRD of WSe_2 nanocrystals synthesized in 180 eq TOPO with 2 eq TOP added (orange, top) and 1 eq TOP added (red, bottom). The Gray dashed line is (002) of WSe_2 with no increased interlayer distance.

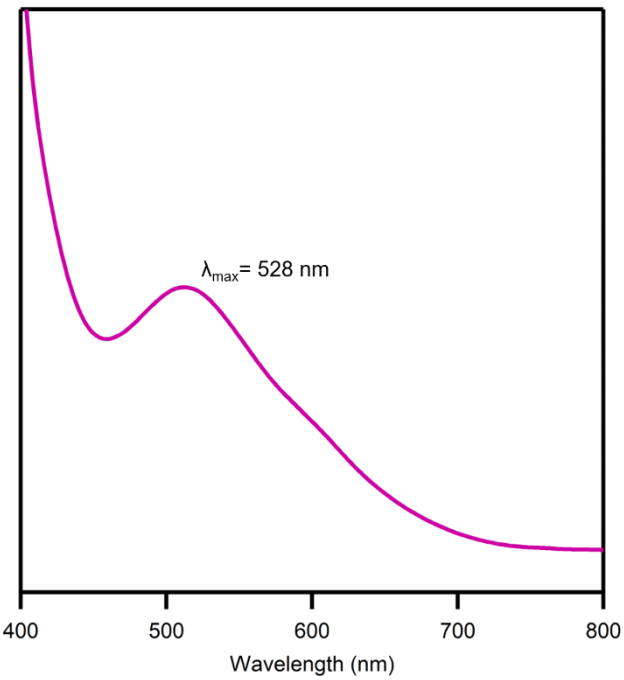

Figure S6. 8. Absorbance spectra of complex formed from reaction performed in 200 eq TOP and no TOPO.

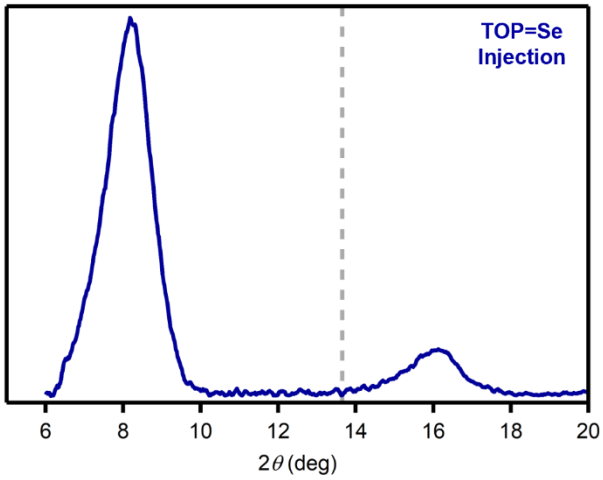

Figure S6. 9. PXRD of WSe_2 nanocrystals synthesized with 10 eq TOP with TOP=Se injection

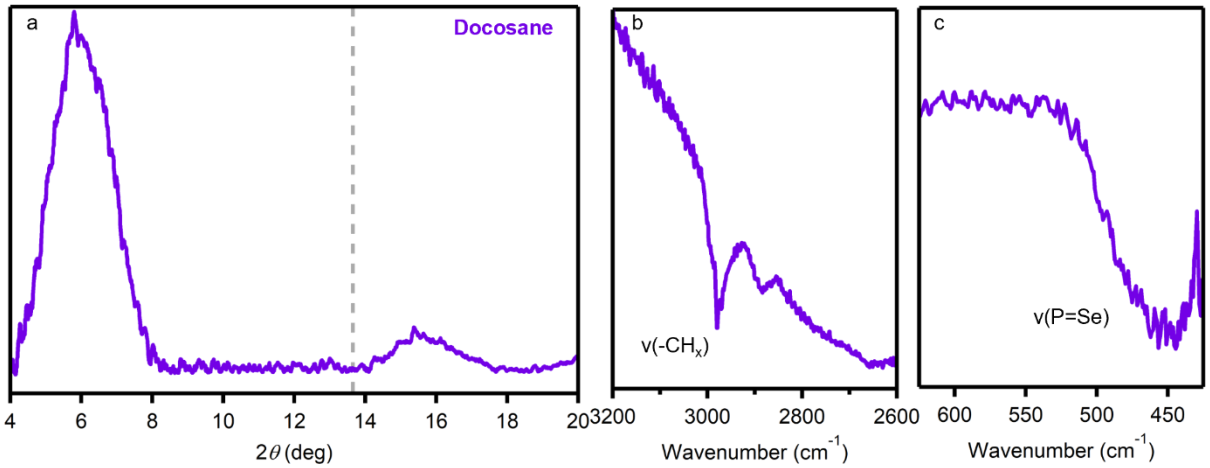

Figure S6. 10. PXRD of WSe_2 nanocrystals synthesized with 10 eq TOP and 2eq injection of Ph_2Se_2 in 180 eq docosane. FTIR of nanocrystals after heating with TOP in the CH stretching region (b) and the P=Se stretching region (c).

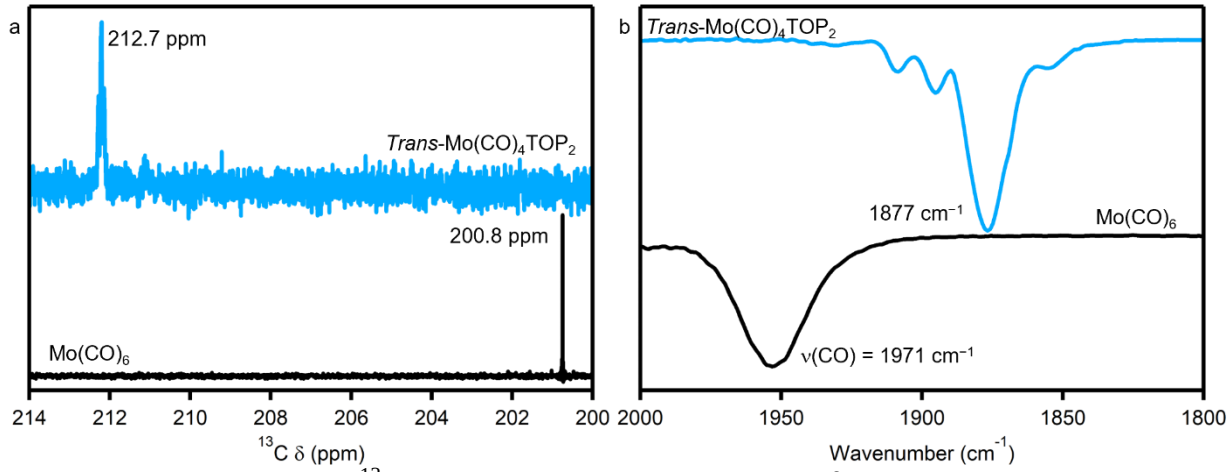

Figure S6. 11. (a) ^{13}C NMR and **(b)** FTIR spectra of *Trans*-Mo(CO)$_4$TOPO synthesized via heating Mo(CO)$_6$ in >2eq TOP (purple, top) and comparison to pure Mo(CO)$_6$ (black, bottom). CO peak downfield shifted from 200.8 to 212.7 ppm and CO stretching frequency shifted to a lower wavenumber from 1971 cm^{-1} to 1873 cm^{-1}. Both these shifts align with previously reported di-substituted phosphine molybdenum carbonyls.[53-54] The phosphorus NMR shows a singlet with triplet splitting and the FTIR shows one stretching mode, confirming trans substitution.

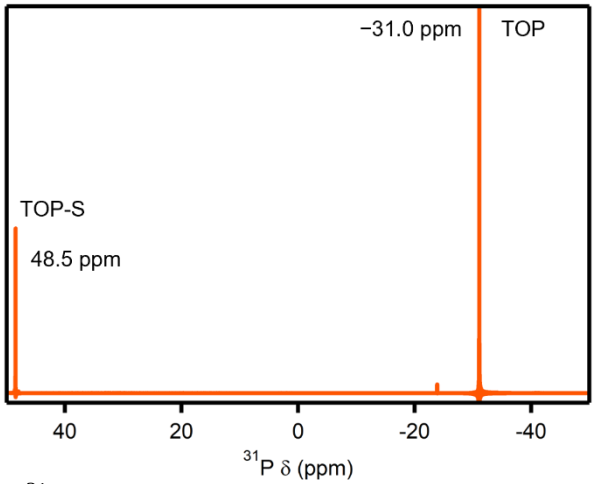

Figure S6. 12. ^{31}P-NMR after heating Bn_2S_2 with 10 eq TOP at 150 °C for 10 minutes. The emergence of the peak at 48.5 ppm confirms the formation of TOP-S.

Experimental methods

Table S6. 1. Chemicals

Chemical	**Purity**	**Manufacturer**
Trioctylphosphine oxide (TOPO)	99%	STREM
Trioctylphosphine (TOP)	98%	STREM
Hexadecane	>98%	TCI
Tungsten hexacarbonyl ($W(CO)_6$)	99%	Acros
Molybdenum hexacarbonyl ($Mo(CO)_6$)	98%	Acros
Diphenyl diselenide (Ph_2Se_2)	>97%	TCI
Dibenzyl disulfide (Bn_2S_2)	>98%	Alfa Aesar
Toluene	99.9%	Fischer
Methanol (MeOH)	99.9%	Fischer
Deuterated chloroform	99.8%	Cambridge Laboratories inc

All chemicals were used without further purification. All chemicals were stored in a nitrogen-filled glove box except the toluene, MeOH, and d-chloroform which were stored under ambient conditions. All reactions were carried out using a glass sheath to prevent contamination from the temperature probe.

Synthesis of NCs: Two 25 ml round bottom flasks charged with glass-covered stir bars, an air condenser, and 2 flow adapters were dried in a 120 °C oven. Glassware, septa, glass sheath,

and flow adapter components were then pumped into the glove box. One 25 ml round bottom is referred to as the “main flask” where the metal carbonyl is combined with different ligands+solvent. This flask is fitted with a glass sheath and condenser. The other 25 ml round bottom is referred to as the “side flask” where the chalcogen source is combined with hexadecane. All glassware is appropriately fitted with flow adapters and septa, removed from the box, and placed on the Schlenk line. Space up to the flow adapters is evacuated and refilled with argon 3 times in quick succession. Chemicals are then opened to the line and are evacuated and refilled with argon 3 times over the course of an hour at room temperature. After the final refilling of argon, the main flask is heated to 150 °C using a temperature controller and held at that temperature for 15 minutes. At about 70 °C gas evolution begins, and the solution turns yellow. Meanwhile, the side flask is heated to 70 °C with a variac, and temperature is monitored using a thermometer outside the flask (this is done to ensure complete dissolution of the diorganyl dichalcogenide and to avoid large temperature drops after injection). After both solutions are appropriately heated, 1 ml of the solution from the side flask is injected into the main flask. After the injection, the solution is heated to 330 °C, and after reaching temperature the solution is held there. After the reaction is complete, the solution is cooled by removing the heating mantle. At about 80 °C septa on the flask are removed and some toluene is injected to avoid solidification of the mixture. The solution is then transferred to centrifuge tubes and methanol is added in a 1:1 volume ratio to the mixture. These are centrifuged for 5 minutes at 15000 rpm. After the initial crash, NCs washed 2 more times by redispersing in toluene, adding MeOH, and centrifuging for 5 minutes at 8000 rpm.

Table S6. 2. Details for reaction conditions and parameters.

Reaction	Main flask		Side flask		Heating rate	Reaction time at 330 °C
	Metal carbonyl	Ligand mixture	Chalcogen	hexadecane		
Multilayer WSe_2	20 mg $W(CO)_6$	3.495 g TOPO	71 mg Ph_2Se_2	1.54 g	15-minute heat-up to 330 °C	90 min
TOP-bound WSe_2	20 mg $W(CO)_6$	3.495 g TOPO + 210 mg TOP	71 mg Ph_2Se_2	1.54 g	15 minute heat-up to 330 °C	90 min
TOP-bound WSe_2 with TOP=Se	20 mg $W(CO)_6$	3.495 g TOPO	18 mg Se + 420 mg TOP	1.16g	15-minute heat-up to 330 °C	90 min
TOP-bound WSe_2 in docosane	20 mg $W(CO)_6$	2.98 g docosane + 210 mg TOP	71 mg Ph_2Se_2	1.54 g	Heat to 280 °C for 15 minutes, then heat to 330 °C	90 min
Multilayer $MoSe_2$	15 mg $Mo(CO)_6$	3.495 g TOPO	71 mg Ph_2Se_2	1.54 g	15-minute heat-up to 330 °C	90 min
TOP-bound $MoSe_2$	15 mg $Mo(CO)_6$	3.495 g TOPO + 210 mg TOP	71 mg Ph_2Se_2	1.54 g	15 minute heat-up to 330 °C	90 min
Multilayer WS_2	20 mg $W(CO)_6$	3.495 g TOPO	56 mg Bn_2S_2	1.54 g	15-minute heat-up to 330 °C	90 min
TOP-bound WS_2	20 mg $W(CO)_6$	3.495 g TOPO + 63 mg TOP	56 mg Bn_2S_2	1.54 g	15 minute heat-up to 330 °C	90 min
Multilayer MoS_2	15 mg $Mo(CO)_6$	3.495 g TOPO	56 mg Bn_2S_2	1.54 g	15-minute heat-up to 330 °C	90 min
TOP-bound MoS_2	15 mg $Mo(CO)_6$	3.495 g TOPO + 63 mg TOP	56 mg Bn_2S_2	1.54 g	15 minute heat-up to 330 °C	90 min

Characterization

^{13}C NMR spectroscopy: Samples were prepared by adding 0.5 grams d-chloroform to 0.5 grams combined mixture of tungsten+ligand. ^{13}C NMR spectra were collected on a JEOL ECA 500 MHz spectrometer with ^{1}H decoupling (1024 scans, relaxation delay = 1 s) and processed in Mestrenova.

Fourier transformed infrared spectroscopy: Infrared spectroscopy performed by directly transferring solid samples as-prepared to the crystal of ATR accessory on an Agilent Cary 630 ATR-FTIR.

Raman spectroscopy: Samples were prepared by drop-casting a suspension of nanocrystals in hexanes onto a polished silicon substrate (Silicon Valley Microelectronics). Raman spectra were

collected using a Renishaw inVia confocal Raman microscope with 532 nm laser excitation(10mW) and a 50× objective lens.

Powder X-ray diffraction: After washing nanocrystals, the excess solvent was removed with a vacuum or air drying. Dried samples were transferred to a loop. Powder X-ray diffraction patterns were collected using a D8 Smart diffractometer with a Pt 135 detector equipped with a Rigaku MicroMax-007HF High-intensity Microfocus rotating anode with Cu Kα radiation (λ= 1. 54184)at 40 kV, 30 mA, and Varimax-HF double bounce optics. Diffraction images were merged/integrated in Diffrac.EVA V.4.3.0.1(Bruker).

Transmission electron microscopy. TEM grids were prepared by drop-casting a suspension of nanocrystals in toluene as a single drop onto a 100-mesh copper TEM grid coated with formvar and carbon (Electron Microscopy Sciences). Images were collected on a ThermoFisher Talos 200X TEM.

6.6 Acknowledgments

Chapter 6, in part, is currently being prepared for submission for publication of the material. The dissertation author was the primary author of this paper and gratefully acknowledges the contributions of coauthors Hang Yin, Natacha Oget, and Alina M. Schimpf.

6.7 References

1. Mattheis.Lf, Energy-Bands for 2h-Nbse2 and 2h-Mos2. *Phys Rev Lett* **1973,** *30* (17), 784-787.

2. Fang, Y.; Pan, J.; Zhang, D.; Wang, D.; Hirose, H. T.; Terashima, T.; Uji, S.; Yuan, Y.; Li, W.; Tian, Z.; Xue, J.; Ma, Y.; Zhao, W.; Xue, Q.; Mu, G.; Zhang, H.; Huang, F., Discovery of Superconductivity in 2M WS2 with Possible Topological Surface States. *Adv Mater* **2019,** *31* (30), e1901942.

3. Fang, Y. Q.; Dong, Q.; Pan, J.; Liu, H. Y.; Liu, P.; Sun, Y. Y.; Li, Q. J.; Zhao, W.; Liu, B. B.; Huang, F. Q., Observation of superconductivity in pressurized 2M WSe2 crystals. *J Mater Chem C* **2019,** *7* (28), 8551-8555.

4. Sun, Y. J.; Wang, D.; Shuai, Z. G., Indirect-to-Direct Band Gap Crossover in Few-Layer Transition Metal Dichalcogenides: A Theoretical Prediction. *J Phys Chem C* **2016,** *120* (38), 21866-21870.

5. Pandey, S. K.; Das, R.; Mahadevan, P., Layer-Dependent Electronic Structure Changes in Transition Metal Dichalcogenides: The Microscopic Origin. *Acs Omega* **2020,** *5* (25), 15169-15176.

6. Qian, X. F.; Liu, J. W.; Fu, L.; Li, J., Quantum spin Hall effect in two-dimensional transition metal dichalcogenides. *Science* **2014,** *346* (6215), 1344-1347.

7. Ugeda, M. M.; Pulkin, A.; Tang, S. J.; Ryu, H.; Wu, Q. S.; Zhang, Y.; Wong, D.; Pedramrazi, Z.; Martin-Recio, A.; Chen, Y.; Wang, F.; Shen, Z. X.; Mo, S. K.; Yazyev, O. V.; Crommie, M. F., Observation of topologically protected states at crystalline phase boundaries in single-layer WSe2. *Nat Commun* **2018,** *9*.

8. Liu, F.; Wu, W. J.; Bai, Y. S.; Chae, S. H.; Li, Q. Y.; Wang, J.; Hone, J.; Zhu, X. Y., Disassembling 2D van der Waals crystals into macroscopic monolayers and reassembling into artificial lattices. *Science* **2020,** *367* (6480), 903-+.

9. Zhang, Q. Y.; Mei, L.; Cao, X. H.; Tang, Y. X.; Zeng, Z. Y., Intercalation and exfoliation chemistries of transition metal dichalcogenides. *J Mater Chem A* **2020,** *8* (31), 15417-15444.

10. Li, H.; Wu, J. M. T.; Yin, Z. Y.; Zhang, H., Preparation and Applications of Mechanically Exfoliated Single-Layer and Multi layer MoS2 and WSe2 Nanosheets. *Accounts Chem Res* **2014,** *47* (4), 1067-1075.

11. Nasilowski, M.; Mahler, B.; Lhuillier, E.; Ithurria, S.; Dubertret, B., Two-Dimensional Colloidal Nanocrystals. *Chem Rev* **2016,** *116* (18), 10934-10982.

12. Wang, Y. Y.; Zhang, Y.; Wang, F. D.; Giblin, D. E.; Hoy, J.; Rohrs, H. W.; Loomis, R. A.; Buhro, W. E., The Magic-Size Nanocluster (CdSe)(34) as a Low-Temperature Nucleant for Cadmium Selenide Nanocrystals; Room-Temperature Growth of Crystalline Quantum Platelets. *Chem Mater* **2014,** *26* (7), 2233-2243.

13. Liu, Y. H.; Wang, F. D.; Wang, Y. Y.; Gibbons, P. C.; Buhro, W. E., Lamellar Assembly of Cadmium Selenide Nanoclusters into Quantum Belts. *J Am Chem Soc* **2011,** *133* (42), 17005-17013.

14. Son, J. S.; Wen, X. D.; Joo, J.; Chae, J.; Baek, S. I.; Park, K.; Kim, J. H.; An, K.; Yu, J. H.; Kwon, S. G.; Choi, S. H.; Wang, Z. W.; Kim, Y. W.; Kuk, Y.; Hoffmann, R.; Hyeon, T., Large-Scale Soft Colloidal Template Synthesis of 1.4 nm Thick CdSe Nanosheets. *Angew Chem Int Edit* **2009,** *48* (37), 6861-6864.

15. Li, Z.; Peng, X. G., Size/Shape-Controlled Synthesis of Colloidal CdSe Quantum Disks: Ligand and Temperature Effects. *J Am Chem Soc* **2011,** *133* (17), 6578-6586.

16. Ithurria, S.; Tessier, M. D.; Mahler, B.; Lobo, R. P. S. M.; Dubertret, B.; Efros, A., Colloidal nanoplatelets with two-dimensional electronic structure. *Nat Mater* **2011,** *10* (12), 936-941.

17. Jiang, Y.; Ojo, W. S.; Mahler, B.; Xu, X. Z.; Abecassis, B.; Dubertret, B., Synthesis of CdSe Nanoplatelets without Short-Chain Ligands: Implication for Their Growth Mechanisms. *Acs Omega* **2018,** *3* (6), 6199-6205.

18. Bouet, C.; Mahler, B.; Nadal, B.; Abecassis, B.; Tessier, M. D.; Ithurria, S.; Xu, X. Z.; Dubertret, B., Two-Dimensional Growth of CdSe Nanocrystals, from Nanoplatelets to Nanosheets. *Chem Mater* **2013,** *25* (4), 639-645.

19. Wang, Y. Y.; Liu, Y. H.; Zhang, Y.; Kowalski, P. J.; Rohrs, H. W.; Buhro, W. E., Preparation of Primary Amine Derivatives of the Magic-Size Nanocluster (CdSe)(13). *Inorg Chem* **2013,** *52* (6), 2933-2938.

20. Koster, R. S.; Fang, C. M.; van Blaaderen, A.; Dijkstra, M.; van Huis, M. A., Acetate ligands determine the crystal structure of CdSe nanoplatelets - a density functional theory study. *Phys Chem Chem Phys* **2016,** *18* (32), 22021-22024.

21. Kim, M.; Park, G. H.; Seo, S.; Bui, V. Q.; Cho, Y.; Hong, Y.; Kawazoe, Y.; Lee, H., Uncovering the Role of Countercations in Ligand Exchange of WSe2: Tuning the d-Band Center toward Improved Hydrogen Desorption. *Acs Appl Mater Inter* **2021,** *13* (9), 11403-11413.

22. Tsai, C.; Chan, K. R.; Abild-Pedersen, F.; Norskov, J. K., Active edge sites in MoSe2 and WSe2 catalysts for the hydrogen evolution reaction: a density functional study. *Phys Chem Chem Phys* **2014,** *16* (26), 13156-13164.

23. Jung, W.; Lee, S.; Yoo, D.; Jeong, S.; Miro, P.; Kuc, A.; Heine, T.; Cheon, J., Colloidal synthesis of single-layer MSe2 (M = Mo, W) nanosheets via anisotropic solution-phase growth approach. *J Am Chem Soc* **2015,** *137* (23), 7266-9.

24. Cho, Y.; Le, T. A.; Kim, H.; Hong, Y.; Hwang, H.; Park, G. H.; Seo, S.; Lee, H., Unveiling surface charge on chalcogen atoms toward the high aspect-ratio colloidal growth of two-dimensional transition metal chalcogenides. *Nanoscale* **2021,** *13* (2), 1291-1302.

25. Mahler, B.; Hoepfner, V.; Liao, K.; Ozin, G. A., Colloidal synthesis of 1T-WS2 and 2H-WS2 nanosheets: applications for photocatalytic hydrogen evolution. *J Am Chem Soc* **2014,** *136* (40), 14121-7.

26. Liu, Z. Q.; Li, N.; Su, C.; Zhao, H. Y.; Xu, L. L.; Yin, Z. Y.; Li, J.; Du, Y. P., Colloidal synthesis of 1T ' phase dominated WS2 towards endurable electrocatalysis. *Nano Energy* **2018,** *50*, 176-181.

27. Shahmanesh, A.; Romanin, D.; Dabard, C.; Chee, S. S.; Greboval, C.; Methivier, C.; Silly, M. G.; Chaste, J.; Bugnet, M.; Pierucci, D.; Ouerghi, A.; Calandra, M.; Lhuillier, E.; Mahler, B., 2D Monolayer of the 1T' Phase of Alloyed WSSe from Colloidal Synthesis. *J Phys Chem C* **2021,** *125* (20), 11058-11065.

28. Jiang, M.; Zhang, J. J.; Wu, M. H.; Jian, W. J.; Xue, H. T.; Ng, T. W.; Lee, C. S.; Xu, J., Synthesis of 1T-MoSe2 ultrathin nanosheets with an expanded interlayer spacing of 1.17 nm for efficient hydrogen evolution reaction. *J Mater Chem A* **2016,** *4* (39), 14949-14953.

29. Scarfiello, R.; Cesari, A.; Altamura, D.; Masi, S.; Nobile, C.; Balzano, F.; Giannini, C.; Grillo, V.; Tavabi, A. H.; Dunin-Borkowski, R. E.; Uccello-Barretta, G.; Cozzoli, P. D.; Rizzo, A., Mechanistic insight into the formation of colloidal WS2 nanoflakes in hot alkylamine media. *Nanoscale Adv* **2019,** *1* (7), 2772-2782.

30. Liu, Z. Q.; Nie, K. K.; Qu, X. Y.; Li, X. H.; Li, B. J.; Yuan, Y. L.; Chong, S. K.; Liu, P.; Li, Y. G.; Yin, Z. Y.; Huang, W., General Bottom-Up Colloidal Synthesis of Nano-MonolayerTransition-Metal Dichalcogenides with High 1T '-Phase Purity. *J Am Chem Soc* **2022,** *144* (11), 4863-4873.

31. Pippia, G.; Van Hamme, D.; Martin-Garcia, B.; Prato, M.; Moreels, I., A colloidal route to semiconducting tungsten disulfide nanosheets with monolayer thickness. *Nanoscale* **2022,** *14* (42), 15859-15868.

32. Liu, Q.; Li, X. L.; Xiao, Z. R.; Zhou, Y.; Chen, H. P.; Khalil, A.; Xiang, T.; Xu, J. Q.; Chu, W. S.; Wu, X. J.; Yang, J. L.; Wang, C. M.; Xiong, Y. J.; Jin, C. H.; Ajayan, P. M.; Song, L., Stable Metallic 1T-WS2 Nanoribbons Intercalated with Ammonia Ions: The Correlation between Structure and Electrical/Optical Properties. *Advanced Materials* **2015,** *27* (33), 4837-4844.

33. Yang, J. N.; Xu, Q. C.; Zheng, Y. T.; Tian, Z. M.; Shi, Y. Y.; Ma, C. X.; Liu, G. Y.; Peng, B.; Wang, Z.; Zheng, W. J., Phase Engineering of Metastable Transition Metal Dichalcogenides via Ionic Liquid Assisted Synthesis. *Acs Nano* **2022**.

34. Alvarado, S. R.; Shortt, I. A.; Fan, H. J.; Vela, J., Assessing Phosphine-Chalcogen Bond Energetics from Calculations. *Organometallics* **2015,** *34* (16), 4023-4031.

35. Garcia-Rodriguez, R.; Hendricks, M. P.; Cossairt, B. M.; Liu, H. T.; Owen, J. S., Conversion Reactions of Cadmium Chalcogenide Nanocrystal Precursors. *Chem Mater* **2013,** *25* (8), 1233-1249.

36. Sandblom, N.; Ziegler, T.; Chivers, T., A density functional study of the bonding in tertiary phosphine chalcogenides and related molecules. *Can J Chem* **1996,** *74* (11), 2363-2371.

37. Schutte, W. J.; Deboer, J. L.; Jellinek, F., Crystal-Structures of Tungsten Disulfide and Diselenide. *J Solid State Chem* **1987,** *70* (2), 207-209.

38. Peters, J. L.; de Wit, J.; Vanmaekelbergh, D., Sizing Curve, Absorption Coefficient, Surface Chemistry, and Aliphatic Chain Structure of PbTe Nanocrystals. *Chem Mater* **2019,** *31* (5), 1672-1680.

39. Zingaro, R. A., Phosphine Sulfides and Selenides - Phosphorus-Sulfur and Phosphorus-Selenium Stretching Frequencies. *Inorg Chem* **1963,** *2* (1), 192-&.

40. Hens, Z.; Martins, J. C., A Solution NMR Toolbox for Characterizing the Surface Chemistry of Colloidal Nanocrystals. *Chem Mater* **2013,** *25* (8), 1211-1221.

41. Kuo, D. Y.; Cossairt, B. M., Direct intercalation of MoS2 and WS2 thin films by vacuum filtration. *Mater Horiz* **2022,** *9* (1), 360-367.

42. Chhowalla, M.; Shin, H. S.; Eda, G.; Li, L. J.; Loh, K. P.; Zhang, H., The chemistry of two-dimensional layered transition metal dichalcogenide nanosheets. *Nat Chem* **2013,** *5* (4), 263-275.

43. Darensbourg, D. J., Mechanistic Pathways for Ligand Substitution Processes in Metal Carbonyls. *Adv Organomet Chem* **1982,** *21*, 113-150.

44. Darensbourg, D. J.; Darensbourg, M. Y.; Walker, N., Studies Using (n-Bu)$_3$P=O as a Carbon Monoxide Labilizing Ligand in the Synthesis of Metal Carbonyl Complexes Highly Enriched in ^{13}CO. *Inorg. Chem.* **1981,** *20* (6), 1918-1921.

45. Guo, Y. J.; Alvarado, S. R.; Barclay, J. D.; Vela, J., Shape-Programmed Nanofabrication: Understanding the Reactivity of Dichalcogenide Precursors. *Acs Nano* **2013,** *7* (4), 3616-3626.

46. Rhodes, J. M.; Jones, C. A.; Thal, L. B.; Macdonald, J. E., Phase-Controlled Colloidal Syntheses of Iron Sulfide Nanocrystals via Sulfur Precursor Reactivity and Direct Pyrite Precipitation. *Chem Mater* **2017,** *29* (19), 8521-8530.

47. Lezama, I. G.; Arora, A.; Ubaldini, A.; Barreteau, C.; Giannini, E.; Potemski, M.; Morpurgo, A. F., Indirect-to-direct band gap crossover in few-layer MoTe(2). *Nano Lett* **2015,** *15* (4), 2336-42.

48. Zhao, W. J.; Ghorannevis, Z.; Chu, L. Q.; Toh, M. L.; Kloc, C.; Tan, P. H.; Eda, G., Evolution of Electronic Structure in Atomically Thin Sheets of WS2 and WSe2. *Acs Nano* **2013,** *7* (1), 791-797.

49. Feltham, R. D.; Brant, P., Xps Studies of Core Binding-Energies in Transition-Metal Complexes .2. Ligand Group Shifts. *J Am Chem Soc* **1982,** *104* (3), 641-645.

50. Anderson, N. C.; Hendricks, M. P.; Choi, J. J.; Owen, J. S., Ligand Exchange and the Stoichiometry of Metal Chalcogenide Nanocrystals: Spectroscopic Observation of Facile Metal-Carboxylate Displacement and Binding. *J Am Chem Soc* **2013,** *135* (49), 18536-18548.

51. Gamble, F. R.; Osiecki, J. H.; Cais, M.; Pisharody, R.; Disalvo, F. J.; Geballe, T. H., Intercalation complexes of lewis bases and layered sulfides: a large class of new superconductors. *Science* **1971,** *174* (4008), 493-7.

52. Golub, A. S.; Zubavichus, Y. V.; Slovokhotov, Y. L.; Nikovikov, Y. N., Monolayer dispersions of transition metal dichalcogenides in the synthesis of intercalation compounds. *Usp Khim+* **2003,** *72* (2), 138-158.

53. Bodner, G. M., Fourier-Transform C-13 Nuclear Magnetic-Resonance Study of Group 6b Transition-Metal Carbonyl-Complexes. *Inorg Chem* **1975,** *14* (11), 2694-2699.

54. Cotton, F. A.; Kraihanzel, C. S., Vibrational Spectra and Bonding in Metal Carbonyls .1. Infrared Spectra of Phosphine-Substituted Group Vi Carbonyls in Co Stretching Region. *J Am Chem Soc* **1962,** *84* (23), 4432-+.